Algorithmes de super-résolution pour la microscopie à balayage laser avec modelage de faisceau par diffraction conique

Anne-Sophie Macé

UNIVERSITÉ PARIS DESCARTES

École doctorale 386 : Sciences Mathématiques de Paris Centre

Laboratoire MAP5 (CNRS UMR 8145)

Algorithmes de super-résolution pour la microscopie à balayage laser avec modelage de faisceau par diffraction conique

Super-resolution algorithms for laser scanning microscopy with illumination patterns shaped by conical diffraction

Par Anne-Sophie Macé

Thèse de doctorat de Mathématiques Appliquées

Présentée et soutenue publiquement le 5 juillet 2018, devant le jury composé de

Sylvain Durand	Université Paris Descartes	Examinateur
Jean-François Giovannelli	Université de Bordeaux	Examinateur
Jérôme Idier	CNRS/École Centrale de Nantes	Rapporteur
Charles Kervrann	INRIA Rennes	Rapporteur
Cécile Louchet	Université d'Orléans	Examinatrice
Lionel Moisan	Université Paris Descartes	Directeur de thèse
Gabriel Sirat	BioAxial	Examinateur
Jean-Yves Tinevez	Institut Pasteur	Examinateur

Résumé

Cette thèse s'intéresse à des techniques non linéaires de reconstruction d'images, appliquées au problème de la super-résolution en microscopie, qui vise à dépasser la limite de résolution de Abbe en combinant des techniques de mesure et de traitement d'images. Nous considérons un système à fluorescence avec une méthode d'*Image Scanning Microscopy* (ISM), produisant des micro-images obtenues en scannant un échantillon biologique et en y projetant une distribution lumineuse. La forme de cette distribution peut être assez singulière lorsqu'elle est créée par un modelage de faisceau laser, rendu possible grâce à un phénomène optique appelé diffraction conique. Un cadre mathématique s'appuyant sur la transformée de Fourier à quatre dimensions est proposé, permettant de comparer théoriquement les méthodes ISM, en quantifiant leur impact en terme de résolution. Nous considérons également la modélisation mathématique exacte de ces méthodes et en particulier les questions de discrétisation, permettant ensuite de simuler un système ISM. Cette modélisation est indispensable lorsque l'on cherche à résoudre le problème inverse induit par la super-résolution. Nous abordons sa résolution avec des contraintes très faibles, à savoir uniquement la positivité de l'image recherchée. Nous mettons en évidence un artefact, appelé *night sky*, produit par l'estimateur du Maximum A Posteriori (MAP). Nous montrons néanmoins que cet artefact peut être évité en imposant à l'image super-résolue d'être à bande limitée, contrainte convexe qui peut être ajoutée à la positivité moyennant un algorithme de projection adapté. Nous introduisons ensuite un nouvel estimateur, le E-LSE, pour *Emitters-Least-Square Error*, qui minimise l'erreur quadratique moyenne a posteriori et qui est adapté aux images parcimonieuses, une caractéristique souvent satisfaite par les images biologiques obtenues en microscopie à fluorescence. Nous montrons qu'en dépit de la dimension élevée et du caractère non convexe de la contrainte de parcimonie, cet estimateur E-LSE peut-être évalué numériquement par un algorithme de type MCMC (*Markov chain Monte Carlo*). L'estimateur E-LSE permet de limiter certains artefacts spécifiques du MAP et, sur plusieurs exemples, produit une image mieux résolue.

Abstract

This thesis focuses on non-linear image reconstruction methods applied to super-resolution in microscopy, which aims to overcome Abbe resolution limit by combining specific acquisition and image processing techniques. We consider a fluorescence Image Scanning Microscopy (ISM) system, which scans a biological sample with a particular light distribution and records a micro-image at each scan position. This specific light distribution is created by shaping a laser beam thanks to an optical phenomenon called conical diffraction. We propose a mathematical framework based on a four-dimensional Fourier transform, which enables us to provide a theoretical comparison of the different ISM methods in terms of resolution gain. We also address the exact mathematical modelling of these methods, and in particular the discretization issues involved in the simulation of an ISM system. These questions indeed play an essential role for the super-resolution system we study, naturally written as an inverse problem. We first consider a formulation with very little constraints by imposing only the positivity of the reconstructed image. We show that in that case, the Maximum A Posteriori (MAP) estimate suffers from an artifact called *night sky*, but it can be avoided by imposing an additional band-limitedness constraint on the reconstructed image. The two resulting convex constraints can be simultaneously handled by means of a specific projection algorithm. We then introduce a new estimator, called E-LSE (for Emitters-Least-Square Error), which minimizes the a posteriori mean square error and is particularly suited to sparse samples, which are often encountered in fluorescence microscopy. Despite the very high dimension of the problem and the non-convexity of the sparsity constraint, this E-LSE estimator can be numerically computed with an MCMC (Markov Chain Monte Carlo) algorithm. We show that it outperforms the MAP estimate in terms of artifacts and, on several examples, produces a better-resolved image.

Contents

Chapitre 1

Introduction

En 1873, Ernest Abbe évoquait l'impossibilité pour un microscope optique de visualiser des éléments plus petits qu'environ la moitié de la longueur d'onde utilisée pour illuminer l'échantillon biologique. Le domaine des longueurs d'onde du spectre visible étant compris entre 400 et 800 nanomètres environ, des détails plus petits qu'environ 200 nanomètres ne pourront donc pas être distingués lors de l'utilisation d'un microscope optique. En 2014 le prix Nobel de chimie est remis à Eric Betzig, Stefan W. Hell et William E. Moerner, pour leurs différentes techniques de super-résolution "repoussant les limites de la science", utilisant les propriétés des molécules fluorescentes. Aujourd'hui, la plupart des microscopes à fluorescence sont équipés d'un module de super-résolution, indispensable pour visualiser des phénomènes biologiques dont l'ordre de grandeur est la centaine de nanomètres. En effet si la taille des cellules biologiques est plutôt de l'ordre de la dizaine de micromètres, celle des virus et des protéines est de l'ordre de la dizaine de nanomètres, rendant impossible la visualisation de leurs interactions avec une cellule sans technique de super-résolution. La microscopie électronique, différente de la microscopie optique car elle éclaire l'échantillon avec un faisceau d'électrons, permet de dépasser sans difficulté cette limite, mais requiert de fixer, c'est-à-dire tuer les cellules constituant l'échantillon. Elle n'offre donc pas la possibilité d'observer des échantillons et phénomènes vivants, ce qui explique l'utilisation toujours actuelle des microscopes optiques. Pour autant, l'observation de la dynamique des processus biologiques nanoscopiques permettrait de mieux comprendre leurs étapes et la durée de chacune, afin d'être capable d'agir sur celle-ci (par exemple dans le cas d'une contamination par un virus, être capable de visualiser les différentes étapes par lequel le virus passe avant d'infecter une cellule pourrait permettre de stopper la contamination en rendant impossible une des étapes).

La microscopie à fluorescence utilise des fluorophores, c'est-à-dire des protéines émettant de la lumière suite à une excitation (à l'aide un laser par exemple) par un photon d'une longueur d'onde adaptée à ce fluorophore. Au moment de retourner dans son état fondamental, le fluorophore libère un photon, appelé photon de fluorescence, créant une lumière qui est ensuite enregistrée par une détecteur (caméra, PMT etc.), par exemple. Les longueurs d'onde d'émission et d'excitation d'un fluorophore sont différentes, permettant de visualiser uniquement, au moyen d'un filtre, les photons émis par les fluorophores.

Plusieurs techniques, et en particulier celles traitées dans cette thèse, dans les chapitres 3 et 6, utilisent un microscope à balayage laser ; il s'agit d'un système où le laser se déplace sur l'échantillon, le plus souvent par l'intermédiaire de miroirs galvanométriques. Une mesure ne correspond donc pas à l'image complète de l'échantillon biologique mais à une petite partie uniquement. À chaque mouvement du laser, une mesure est effectuée et l'ensemble de ces mesures permet, après traitement des données, de créer ensuite l'image finale. On les appelle souvent méthodes ISM, pour *Image Scanning Miscroscopy*.

Dans cette thèse, on s'intéresse particulièrement aux images parcimonieuses, *sparses* en anglais. Dans [64], la parcimonie est définie comme suit : "une représentation sparse est une représentation dans laquelle un petit nombre de coefficients contient une large proportion d'énergie". La création même des images en microscopie de fluorescence induit une notion de sparsité dans le domaine de l'image, puisqu'on illumine des sources ponctuelles de lumière, les fluorophores. Les représentations *sparses* sont de plus en plus présentes dans la littérature, notamment grâce au développement du *compressed sensing* [36], qui cherche, étant donné un système linéaire, une base dans laquelle, la représentation de la solution du système linéaire soit la plus *sparse* possible.

1.1 Formation de l'image et modélisation du bruit lié à la mesure

Une image numérique (monochromatique) est modélisée par un tableau de nombres, dont chaque case est appelée un pixel. Les valeurs de ces pixels sont appelés les niveaux de gris, le 0 représentant le noir absolu. On revient sur la création de ce tableau

et en particulier sur la notion de capteur. Ensuite, on s'intéresse aux différents bruits intervenant lors de la création d'une image sur le capteur de la caméra, en s'appuyant sur l'article de Aguerrebere et al. [6]. On décrit ici les deux principales sources de bruit : le bruit dit de "grenaille" (photon shot en anglais), dû au caractère quantique de la lumière et caractérisé par un processus de Poisson, et le bruit de lecture de la caméra, dû par exemple à son électronique. Ce dernier est le plus souvent modélisé par un bruit additif gaussien, dont la déviation standard est spécifiée dans les caractéristiques de la caméra.

1.1.1 Formation de l'image sur le capteur

Une caméra numérique est composée d'éléments électroniques appelés capteurs photographiques ou photosites, qui sont photosensibles et qui convertissent un rayonnement électromagnétique (pouvant être dans le domaine du visible, c'est-à-dire entre 400 et 800 nanomètres environ, mais également dans l'infra-rouge ou l'ultra-violet) en un signal électrique analogique. Dans le cas d'un capteur CMOS, pour Complementary Metal Oxide Semi-Conductor en anglais, ce signal passe par un amplificateur puis un convertisseur analogique-numérique créant l'image numérique en sortie. Sur ce type de capteur, la lecture se fait ligne par ligne, c'est-à-dire que toutes les colonnes sont lues en même temps, chacune étant associée à un amplificateur ; chaque amplificateur étant différent, un motif de colonne se crée alors à la lecture de plusieurs lignes (représenté sur la figure 1.1), qu'il faudra ensuite intégrer dans le modèle pour qu'il n'altère pas la qualité de l'image finale.

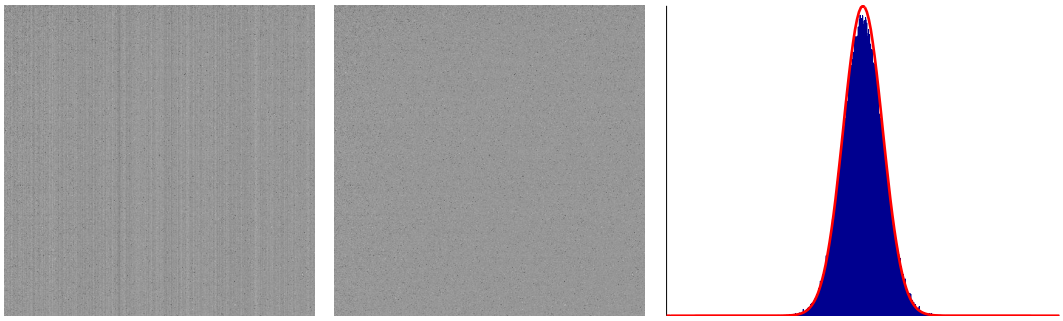

Figure 1.1: Exemple d'image "noire" (pas de lumière projetée, temps d'exposition d'environ 1 ms) à gauche obtenue sur un capteur de type CMOS. En raison du processus de lecture, avec un amplificateur par colonne, on voit apparaître un motif de colonne ; sur la seconde image, on a retiré à chaque colonne sa moyenne, laissant apparaître une image uniformément bruitée, sans motif. À droite, l'histogramme des niveaux de gris de l'image du milieu. L'histogramme de cette image est très proche d'une courbe Gaussienne (représenté en rouge), la modélisation du bruit de lecture par un bruit Gaussien semble donc cohérente.

Si l'on note C la surface d'un photosite, le signal récupéré sur le photosite imageant l'échantillon biologique u est donné par

$$\int\int_C u(k\delta + x, l\delta + y)dxdy,$$

où δ est le pas d'échantillonnage ; il s'agit alors d'un échantillon de la discrétisation de la convolution entre l'échantillon u et et la fonction indicatrice de la surface collectrice C.

1.1.2 Analyse des bruits prédominants

Bruit de grenaille Comme expliqué, par exemple dans [118], la lumière peut être vue comme une série de particules, appelés photons. D'après les lois de la physique, chaque photon possède une énergie définie par hc/λ, où λ est la longueur d'onde, c la vitesse de la lumière et h la constante de Planck. La physique quantique permet de décrire l'émission de photons par une source lumineuse selon un processus statistique de Poisson. Le nombre de photons observés durant un intervalle de temps T (appelé temps d'exposition) suit une loi de Poisson de paramètre ρT où ρ est le flux de photons. La figure 1.2 illustre ce phénomène.

Bruit de lecture Le bruit de lecture est dû à deux phénomènes : la conversion analogique-numérique au sein du capteur et un bruit intrinsèque à chaque pixel. Plus ce bruit de lecture est faible, plus les changements faibles d'intensités peuvent être observés sur la caméra, ce qui prend particulièrement sens pour les applications biologiques où l'éclairement des échantillons est le plus limité possible, afin d'éviter de tuer les cellules ou de faire perdre aux fluorophores leurs propriétés de fluorescence. Il est de coutume de modéliser ce bruit de lecture comme un bruit additif Gaussien [109]. Une expérience faite en prenant une image constante (sans lumière) confirme cette hypothèse : sur la figure 1.1, la répartition des valeurs prises par les pixels est très proche d'une courbe Gaussienne. L'image étant obtenue sur une caméra avec un capteur CMOS, le motif de colonne mentionné ci avant est visible, on retire donc à chaque colonne sa moyenne, laissant apparaître une image similaire à du bruit pur, et dont les pixels ont été utilisés pour la comparaison avec la gaussienne.

Dans le cas d'une acquisition en faible lumière, comme la microscopie à fluorescence, on considère uniquement le bruit de grenaille, analysé prédominant [7]. Ce n'est pas la seule application où l'on considère uniquement ce type de bruit ; c'est également le cas en tomographie par émission [110] ou en astronomie [12]. Cette

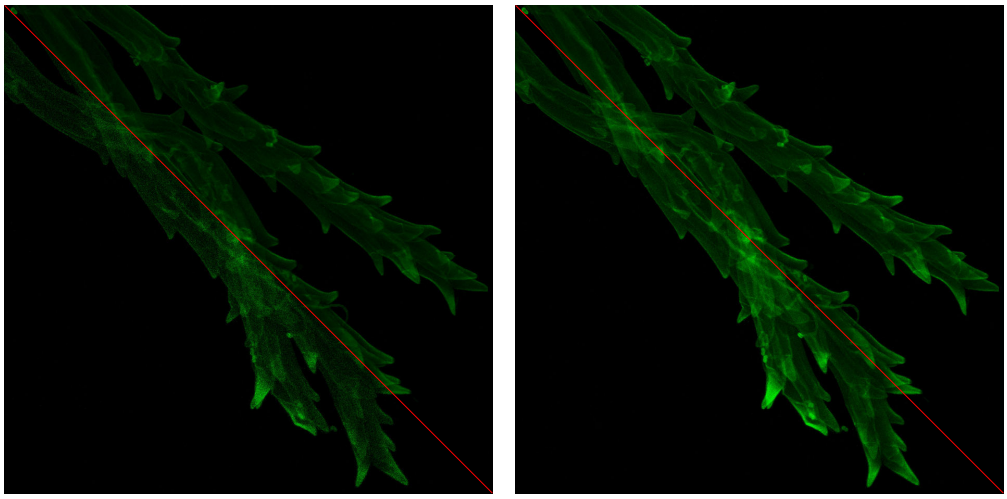

(a) Maximum à 50 photons : originale et bruitée

(b) Maximum à 500 photons : originale et bruitée

Figure 1.2: Illustration du bruit de Poisson sur deux images de dynamiques différentes : l'image originale est représentée dans la moitié supérieure, au dessus de la séparation rouge dans les deux cas. À partir de cette image, on a généré du bruit de Poisson, pour un maximum de photons de 50 en (a), 500 en (b), dont les représentations sont dans les moitiés inférieures, sous la séparation rouge. Visuellement l'effet du bruit de Poisson est bien plus fort lorsque le nombre de photons est plus faible (à gauche). La valeur des pixels bruités étant liée au nombre de photons sur l'image, et non additive, comme dans le cas Gaussien, des algorithmes spécifiques pour ce type de bruit doivent être mis en place. *Image de cellule fongique (le canal vert est le seul représenté sur cette image) par Fernan Federici et Anna Gordon pour le concours Olympus BioScapes Digital Imaging 2011, licence CC BY-NC-ND 3.0*

hypothèse est aussi valide car les caméras utilisées dans ces applications sont performantes et donc limitent le bruit Gaussien. Pour plus d'informations sur un modèle prenant en compte également le bruit Gaussien, le lecteur peut se référer à [72]. A contrario, lorsque le nombre de photons est plus important, le bruit Gaussien additif est souvent le seul considéré.

Les images obtenues sur la caméra doivent donc être débruitées, à l'aide d'algorithmes adaptés au bruit de Poisson, mais aussi déconvoluées car l'image par un système optique d'un point très petit n'est pas un point mais une tâche ; ceci est dû à un phénomène physique, appelé diffraction : l'étalement de l'énergie d'un point par tout système optique fini.

1.2 Limitation fréquentielle d'un système optique

En 1873, Abbe [1] définit la limite de diffraction, d, c'est-à-dire la plus petite période représentable par le système optique, comme une fonction de la longueur d'onde utilisée λ et l'ouverture numérique de l'objectif NA, donnée par

$$d = \frac{\lambda}{2NA}. \tag{1.1}$$

L'ouverture numérique, NA, est une caractéristique capitale d'un objectif décrivant le cône de lumière entre le foyer et la lentille. Elle est proportionnelle à l'indice de réfraction du milieu et au demi-angle d'ouverture, angle entre l'axe optique et le plus grand rayon pouvant pénétrer dans la lentille. Plus NA est grand, plus la résolution est bonne (en effet, d dans (1.1) est inversement proportionnel à NA). Une grande ouverture numérique limite cependant la profondeur de champ, c'est-à-dire la zone sur l'axe z contenant des objets nets est plus restreinte. Dans la suite de cette introduction, on se référera à d quand on parlera du pouvoir de résolution d'un système optique.

Cette limite de diffraction peut aussi s'exprimer dans le domaine de Fourier comme expliqué par Goodman [44] : les transformées de Fourier des images générées par un microscope sont à support borné, contenues dans $[-f_{max}, f_{max}]^2$, où f_{max}, appelée la fréquence de coupure, est donnée par

$$f_{max} = \frac{2\pi}{d} = \frac{4\pi NA}{\lambda}. \tag{1.2}$$

On revient plus précisément dans le chapitre 2 sur la définition de la transformée de Fourier, définie pour toute fonction $\tilde{f} \in L^1(\mathbb{R}^n)$ par

$$\forall \xi \in \mathbb{R}^n,\ \mathcal{F}(f) : \xi \longmapsto \int_{\mathbb{R}^n} \tilde{f}(x) e^{-i\langle \xi, x\rangle} dx.$$

Le détecteur de la caméra étant pixelisé, il faut introduire la Transformée de Fourier Discrète, DFT ; étant donnés N échantillons $(f(k))_{k=0,\dots,N-1}$, tels que $f(k) = \tilde{f}(kT)$, où T est le pas d'échantillonnage, la DFT de f s'écrit

$$\forall p \in \mathbb{Z},\ \hat{f}(p) = \sum_{k=0}^{N-1} f(k) e^{-\frac{2i\pi pk}{N}}$$

La DFT est un outil très intéressant numériquement car sa complexité est en $O(N \log N)$, pour tout N positif.

On présente sur la figure 1.3 une image numérique et sa transformée de Fourier discrète. Puisque cette dernière est complexe, on ne peut la représenter directement ; dans cette thèse, on représente toujours son module, car on s'intéresse au poids des composantes les unes par rapport aux autres. L'utilisation de l'échelle logarithmique pour son observation est assez fréquente car l'étendue des intensités est en générale assez grande.

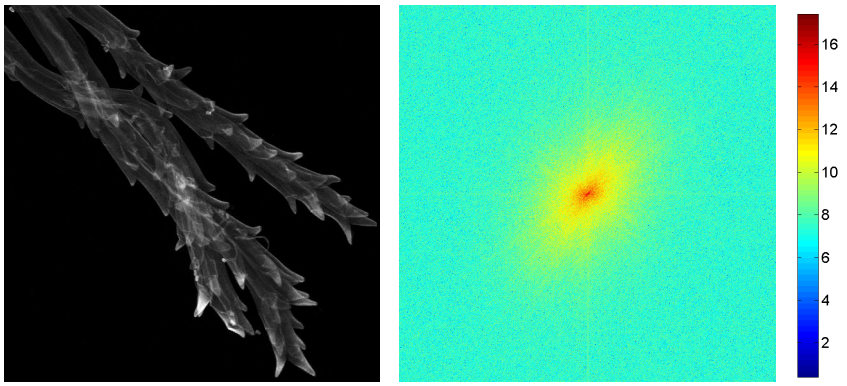

Figure 1.3: Représentation d'une image numérique et de sa transformée de Fourier discrète. À gauche, image de la figure 1.2, représentée cette fois en niveau de gris, à droite l'image du module de sa transformée de Fourier discrète, en échelle logarithmique. On remarque que l'énergie est plus condensée dans l'espace de Fourier, en particulier autour des basses fréquences, situées près du centre. L'image de départ étant réelle, le module de sa transformée de Fourier est une fonction paire, ce qui explique la symétrie centrale observée dans l'image de droite.

Le fait que tout système optique soit limité en fréquence signifie qu'au-delà de la fréquence f_{max} donnée par la Formule (1.2), les coefficients capturés sont théoriquement nuls, donc dans la pratique, uniquement dus au bruit. Cela signifie également que, dans le domaine spatial, c'est-à-dire dans le domaine de l'image, par opposition au domaine de Fourier [1], un point plus petit que la limite de résolution du système d apparaît comme une tache. Dans le cas d'une source ponctuelle, cette tache est appelée PSF, pour Point Spread Function en anglais, fonction d'étalement du point en français et notée φ. Pour un échantillon u, en deux dimensions, on observe non pas u mais $u * \varphi$, où $*$ dénote la convolution, sur laquelle on revient dans la suite. Pour un microscope, lorsque l'ouverture est circulaire et la lumière considérée monochromatique et incohérente, la PSF est modélisée par la tache d'Airy. Cette "tache d'Airy" est représentée dans le domaine spatial et de Fourier sur la figure 1.4.

1. cette définition du domaine spatial sera celle utilisée dans le reste de cette introduction ainsi que dans les différents chapitres

On note r_a, pour rayon d'Airy, le premier zéro du profil vertical de la fonction d'Airy ; sa valeur est fonction de la longueur d'onde λ, de l'ouverture numérique NA et est donnée par

$$r_a \simeq 0.61 \frac{\lambda}{NA}.$$

On remarque sur la figure 1.4 que la majorité de l'énergie de la PSF est concentrée dans le cercle de rayon r_a. Cela signifie qu'en plus d'être à bande limitée, c'est-à-dire que sa transformée de Fourier est bornée, la PSF est aussi très condensée dans le domaine spatial.

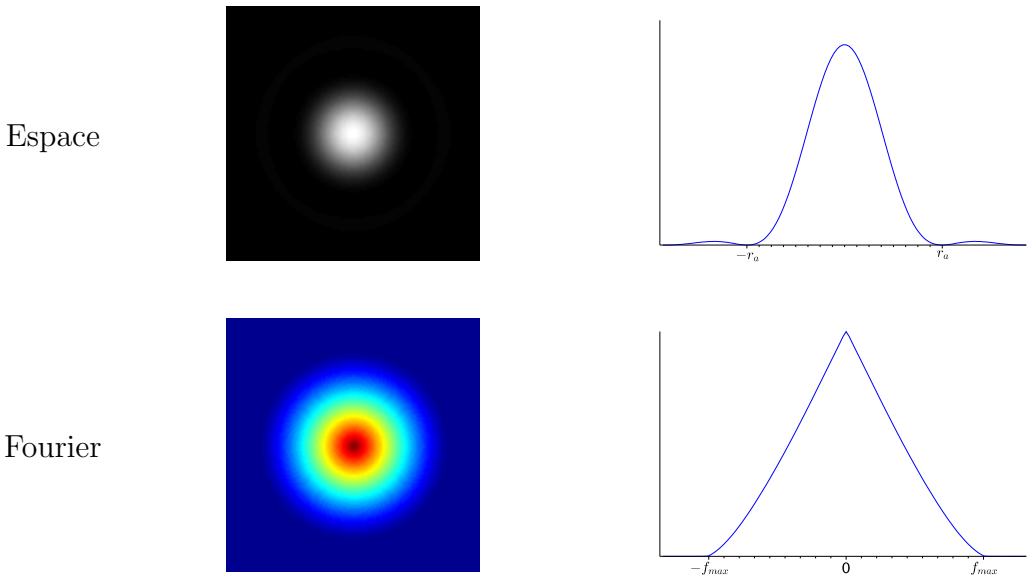

Figure 1.4: Illustration de la tache d'Airy, modélisant la tache optique du microscope, en espace (en haut) et dans le domaine de Fourier (en bas). Un profil vertical est représenté pour les deux images. En espace, on voit qu'une grande proportion de l'énergie est située dans le cercle centré en 0 et de rayon r_a. Dans le domaine de Fourier, on remarque que les coefficients discrets plus grands que f_{max} ont des valeurs nulles, ce qui est dû au fait que le système optique crée des signaux à bande limitée.

Pour comprendre le problème de cette limitation dans le domaine de Fourier, il est important de comprendre ce que représentent les hautes et basses fréquences d'une image. L'énergie des fréquences hautes d'une image correspond dans la majorité des cas aux changements brusques d'intensité, par exemple les contours mais également

le bruit ; a contrario, celle des basses fréquences représente les parties homogènes, avec des changements de contraste assez lents, comme présenté sur la figure 1.5. Pour séparer ces composantes, on utilise un filtre dit passe-haut (*i.e*, laissant passer les fréquences hautes) et un passe bas (*i.e*, laissant passer les basses fréquences). Sur la figure 1.5, l'application des deux filtres témoigne des caractéristiques recensées ci-avant : l'image résultat du filtre passe-bas est quasiment identique avec ou sans bruit contenant les parties homogènes, donnant une version floue de l'image originale. L'image résultat du filtre passe-haut contient les détails fins, à savoir les contours et le bruit pour l'image bruitée.

Figure 1.5: Illustration des hautes et basses fréquences de la transformée de Fourier d'une image. Sur la première colonne sont représentées les images "originales", en haut, l'image usuelle de Lena, en bas, cette même image dégradée par un bruit Gaussien. Sur les deux colonnes suivantes : l'image de la première colonne filtrée avec un filtre de Butterworth [19] passe-bas (fréquence de coupure à 3% de la taille de l'image), image originale filtrée avec un filtre passe-haut (fréquence de coupure à 10% de la taille de l'image). Le filtre passe-bas atténue les contours et détails de l'image (la rendant plus floue) et produit un résultat similaire que l'image de base soit bruitée ou non. Au contraire, le filtre passe-haut contient tous les contours et détails précis (par exemple les plumes du chapeau ou les cils) mais également le bruit.

En microscopie, lors de la convolution du signal avec la tâche d'Airy, les hautes fréquences perdues peuvent par exemple éliminer des séparations (de taille inférieure à d) entre les éléments biologiques, des filaments de très faible épaisseur ou encore des éléments ponctuels de très petite taille. Cependant, ces caractéristiques peuvent permettre au biologiste de mieux appréhender les phénomènes qu'il étudie. C'est

pourquoi de nombreuses techniques de super-résolution se sont développées au cours des dernières années.

1.3 Techniques de super-résolution en microscopie à fluorescence

Dans le cas de la microscopie à fluorescence, la protéine GFP (pour Green Fluorescent Protein, dont le prix Nobel de Chimie 2008 a récompensé la découverte et les applications), utilisée dans la préparation de nombreux échantillons car peu toxique sur les cellules vivantes, possède un maximum d'excitation autour de 480 nm. Les meilleurs objectifs ont une ouverture numérique autour de $NA = 1.5$, nous donnant donc une limite de diffraction de

$$d = \frac{480}{2 \times 1.5} \simeq 160 \text{ nm},$$

signifiant qu'aucun élément plus petit que 160 nm ne peut-être résolu dans ces circonstances. Pour pallier cette limite, de nombreuses techniques dites de "super-résolution" ont été créées, exploitant les propriétés des molécules fluorescentes, notamment la possibilité de les allumer/éteindre sélectivement dans une scène donnée. De nombreux articles recensent les différentes techniques de super-résolution actuelles, parmi lesquels on peut citer en 2009 l'article de Chi [25] ou encore celui de Huang at al. [59] et en 2011 celui de Leung et Chou [73]. Les techniques de super-résolution peuvent être divisées en deux catégories : les méthodes plein champ comme le SIM, pour Structured Illumination Microscopy, et le PALM/ STORM, pour Photo-Activated Localization Microscopy et STochastic Optical Reconstruction Microscopy, et les méthodes plus locales, utilisant le plus souvent un microscope de fluorescence à balayage laser. Le chapitre suivant de cette thèse traite du SIM et des méthodes dites ISM, pour Image Scanning Microscopy. Pour ces deux méthodes, les valeurs des coefficients fréquentiels entre f_{max} et $2f_{max}$ (voir formule (1.2)) existent dans la transformée de Fourier des images acquises. De plus, l'hypothèse de positivité sur les données pourrait permettre de repousser cette limite [100]. Dans la suite on appelle widefield l'image obtenue avec le système optique sans traitement, en plein champ.

Plusieurs paramètres doivent être pris en compte pour caractériser une méthode de super-résolution, comme souligné par Schermelleh, Heintzmann et Leonhardt-dans [99]. En effet, si le gain de résolution est évidemment un point très important (séparation de points, épaisseurs de filaments, etc.), d'autres critères sont à respecter.

En particulier la phototoxicité, très particulièrement liée à la possibilité d'étudier des phénomènes vivants ; en effet la projection d'une forte lumière sur l'échantillon peut tuer celui-ci, et donc empêcher ou altérer une mesure sur plusieurs minutes ou heures. Deux autres points sont importants, comme la facilité à créer les échantillons et aussi à utiliser la technique ainsi que la possibilité de faire de la colocalisation ; en effet il peut arriver de vouloir étudier l'interaction entre deux objets biologiques, marqués alors par des fluorophores répondant à des longueurs d'onde différentes, (on utilise le système de super-résolution deux fois, une fois avec chaque longueur d'onde). On souhaite alors que les deux images obtenues puissent être comparées spatialement, afin de caractériser le lien entre les deux objets biologiques.

Il est important de souligner également que les systèmes de super-résolution ont souvent pour but de valider ou non une hypothèse formulée par un biologiste, il est donc important que ce dernier ait "confiance" dans les résultats, connaisse les limites du système et en particulier que ce système ne l'induise pas en erreur quant à la validité de ses hypothèses. Ceci est encore plus vrai lorsque le biologiste utilise le système pour émettre une hypothèse, établie d'après l'observation des données. La connaissance et la gestion des artefacts est donc un point très important pour la super-résolution.

1.3.1 STED

La microscopie STED, en français Déplétion par Émission STimulée, a été publiée en 1994 dans [56] par Hell, et réalisée physiquement pour la première fois en 2000. Cette technique utilise le fait qu'il existe en fait un autre moyen pour le fluorophore de retourner dans son état fondamental : l'émission stimulée. On illumine le fluorophore juste après l'excitation par une longueur d'onde correspondant à son énergie de transition, ce qui le désexcite sans libérer de photon.

Le STED est utilisé avec un microscope à balayage laser, et utilise l'émission simulée ; on utilise d'abord le système normalement (avec la PSF usuelle), puis on projette juste après, par l'intermédiaire d'un autre laser, un faisceau dit "STED" ou d'émission stimulée dont la longueur d'onde appartient au spectre d'émission de la molécule. Ce faisceau a la forme d'un anneau, permettant de ne laisser excités que les fluorophores au centre (cf figure 1.6). Il est à noter que les fluorophores en périphérie (dans l'anneau) ont été doublement éclairés par rapport au confocal et saturés. Comme spécifié dans [39], l'anneau de déplétion est obtenu le plus souvent grâce à un masque de phase placé sur le chemin optique du faisceau STED même si

des alternatives sont possibles [123]. Comme expliqué dans [37], plus on augmente l'intensité du faisceau d'émission stimulée, plus la zone de fluorescence finale est diminuée, sans réelle limite et surtout de manière non linéaire. Il est à noter que les deux lasers ont le plus souvent un chemin optique différent, afin que l'un ait la forme usuelle de la PSF et le second la forme d'anneau.

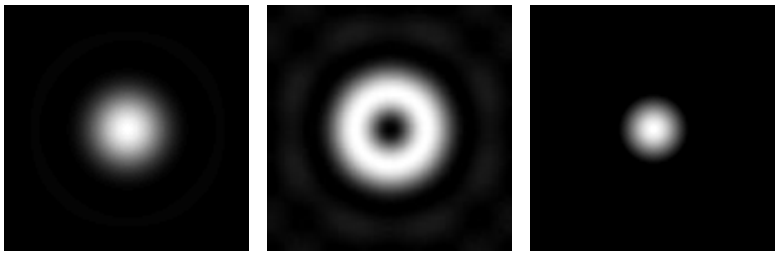

Figure 1.6: Illustration simplifiée du principe du STED ; de gauche à droite : illumination projetée sur l'échantillon (tache optique conventionnelle, PSF) - faisceau de déplétion STED, de la forme d'un anneau - illumination excitatrice équivalente qui en résulte. Sans aucun doute le faisceau de déplétion a permis de réduire la taille de la PSF, en désexcitant les photons en périphérie de la PSF conventionnelle ; ces derniers ont par contre été doublement éclairés : une fois par la PSF usuelle à gauche et une fois par le faisceau de déplétion (au milieu).

Une image obtenue sur des microtubules est présentée sur la figure 1.7 où l'on peut clairement voir que le STED permet de dépasser la limite de résolution du widefield.

D'autres comparaisons peuvent être vues par exemple dans [99] ou [25], où la forme du neurone est mise en avant grâce au STED. Dans [54], Hell et al. prouvent que la limite de diamètre atteinte par le STED est décrite par la formule

$$\frac{\lambda}{2NA\sqrt{1+I_S/I}},$$

où λ est la longueur d'onde utilisée, NA l'ouverture numérique de l'objectif, I_S l'intensité du faisceau de déplétion et I l'intensité des fluorophores. D'après cette formule, le moyen d'augmenter la résolution (en réduisant ce diamètre) est donc d'augmenter l'intensité du faisceau de déplétion I_s, pouvant mener à la destruction des cellules, rendant donc plus difficiles les mesures du vivant à très haute résolution.

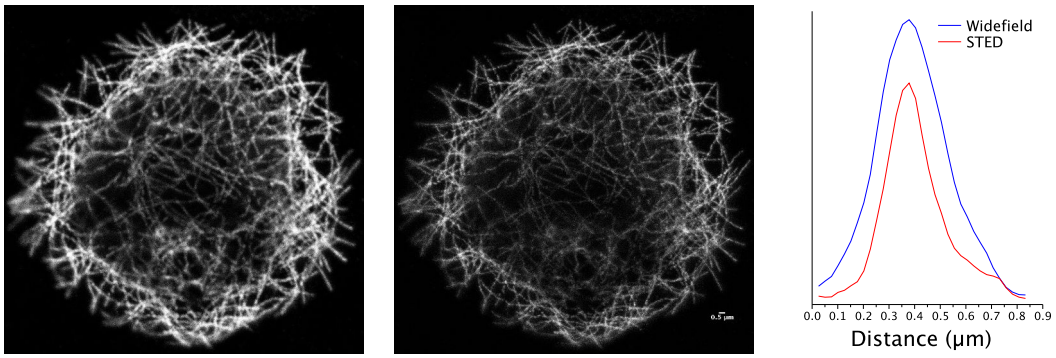

(a) Imagerie conventionnelle (b) STED (c) Profil microtubule

Figure 1.7: Exemple de super-résolution par méthode STED : (a) image obtenue par un microscope widefield (et donc limité par la formule de Abbe), (b) image obtenue par un microscope Leica avec technologie STED (taille du pixel ∼25 nm). Les protéines fixées sur les microtubules ont été excitées avec une longueur d'onde de 488 nm. On peut voir que l'image de droite est plus résolue (comme montré sur le profil d'une microtubule en (c)) et laisse apparaître des séparations non visibles sur celle de gauche.
Image de microtubules dans une cellule de drosophile par Cazares-Chao-Andlauer-J. et C. Galbraith disponible sur cellimagelibrary.org, licence CC BY-NC-ND 3.0

1.3.2 Microscopie à molécule unique

Il existe différentes techniques de la microscopie à molécule unique, parmi les plus connues, le PALM [17] et le STORM [98]. Ces deux techniques ont été créées en 2006 par deux laboratoires différents mais reposent sur le même principe : seul un petit nombre de fluorophores sont excités, stochastiquement, à chaque prise d'image, de manière à ce que deux fluorophores très proches aient une très faible probabilité d'être excités (et donc d'émettre de la lumière) au même moment. Une caméra enregistre ensuite un très grand nombre d'images obtenues par ce processus, avec activation de différents fluorophores. Comme précisé auparavant, toute source ponctuelle plus petite que la limite de diffraction renvoie une tache de la forme de la PSF. Sur chaque image enregistrée, on retrouve donc une somme de PSFs, isolées, créées par les sources ponctuelles éclairées. La forme de la PSF étant connue, on peut déterminer la position et l'intensité de chacun des fluorophores avec une bonne précision. Ce processus est effectué pour chaque image et finalement l'ensemble des positions et intensités permet de créer l'image finale, super-résolue. La figure 1.8 présente des résultats obtenus dans [106], les structures détectées par le PALM n'auraient pu être devinées sans super-résolution, en particulier sur l'image widefield, les deux canaux, vert et

rouge, semblent se recouvrir l'un l'autre alors que l'un se révèle plutôt constitué de structures continues (en rouge) et l'autre de structures ponctuelles (en vert).

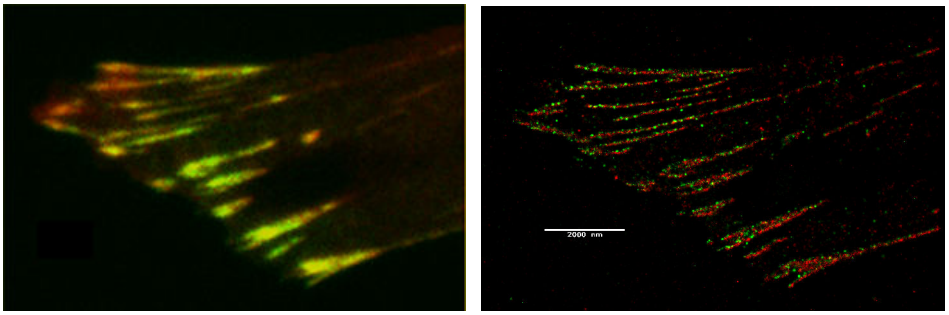

(a) Microscope optique (b) Résultat PALM

Figure 1.8: Illustration du PALM sur une image réelle : l'image (a), limitée par la diffraction, l'image (b) représente la même structure imagée par un système de super-résolution PALM. Les images originales ne sont pas à la même résolution (le pixel est plus petit sur l'image PALM). Le gain en super-résolution est indéniable, et les structures qui semblaient se recouvrir complètement en (a) s'avèrent en fait assez différentes, les protéines vertes formant des sources beaucoup plus ponctuelles que les rouges.
Image par Catherine et James Galbraith, correspondant à la figure 4 de l'article [106] et rendue disponible par les auteurs sur cellimagelibrary.org, licence CC BY-NC-ND 3.0

Dans [84], Mortensen et al. prouvent que la précision de la position du fluorophore est donnée par

$$\sqrt{\frac{\sigma_k + r_c^2/12}{N}\left(\frac{16}{9} + \frac{8\pi\sigma_k b^2}{r_c^2 N}\right)}, \tag{1.3}$$

avec N le nombre de photons collectés par fluorophore, σ_k la variance de la PSF, souvent approximée Gaussienne, r_c la taille du pixel de la camera et b le nombre de photons dans le fond de l'image, considéré constant.

Il est à noter que la super-résolution obtenue par cette méthode repose sur le fait que les molécules sont excitées stochastiquement. En effet, si par hasard deux molécules séparées par une distance plus petite que (1.1) étaient allumées simultanément, l'ajustement avec la PSF ne ferait pas apparaître les deux molécules mais situerait le fluorophore au milieu de la tache créée par la somme des deux spots. Cela signifie qu'il faudrait que très peu de molécules soient excitées en même temps, ce qui requiert un grand nombre d'images et donc un temps d'acquisition assez long.

Très récemment, en 2014 et 2016, deux articles ont développé des méthodes variationnelles autour des techniques à molécules uniques, par exemple l'algorithme FALCON - pour FAst Localization algorithm based on a CONtinuous-space formulation en anglais [82] ou l'algorithme SPIDER - pour Sparse Image DEconvolution and Reconstruction en anglais [63]. Dans le premier article, un algorithme en trois étapes est proposé pour traiter des données de PALM/STORM assez denses (et donc où plusieurs points sources pourraient interagir) : une déconvolution avec pénalisation au sens de la norme L1, suivie d'une localisation grossière des différentes molécules puis une recherche précise de position et intensité pour chacune d'entre elles, cherchant la PSF translatée la plus proche des données obtenues. Pour le second article, une pénalité de type L_0 (c'est-à-dire sur le nombre de pixels non nuls) est utilisée ; si le problème n'a pas de solution explicite, un schéma itératif peut être créé, donnant des résultats concluants sur des données simulées mais pour l'instant très peu de résultats sur données réelles existent. Il est à noter que la création d'échantillons utilisables avec cette technique est assez compliquée et requiert des experts dans le domaine, rendant plus difficile son utilisation.

1.3.3 Structured Illumination Microscopy - SIM

Dans le SIM, publié en 2000 par Gustafsson [46] et inspiré par Heintzmann [55], un ensemble de grilles est projeté sur l'échantillon biologique u. Ces grilles s'écrivent sous la forme

$$\forall x \in \mathbb{R}^2,\ m^{i,\theta}(x) = M_0\left(1 + \alpha\cos(\langle k_\theta, x\rangle + \phi_i)\right).$$

La transformée de Fourier de $m^{i,\theta}$ se formule comme une somme pondérée de distributions de Dirac, en 0 et $\pm k_\theta$. Soit $I_u^{i,\theta}$ l'image créée par l'utilisation de la grille $m^{i,\theta}$, sa transformée de Fourier est donnée par

$$\widehat{I_u^{i,\theta}}(\xi) = \left(M_0\hat{u}(\xi) + M_0\alpha'\left(\hat{u}(\xi + k_\theta)e^{i\phi_i} + \hat{u}(\xi - k_\theta)e^{-i\phi_i}\right)\right)\widehat{\varphi}(\xi) + \widehat{n^{i,\theta}}(\xi),$$

où φ est la PSF du système, à bande-limitée, vérifiant donc

$$\forall \xi \in \mathbb{R}^2 \mid\ \xi \in \mathcal{B}(0, f_{max}),\ \widehat{\varphi}(\xi) = 0,$$

où $\mathcal{B}(0, f_{max})$ est la boule de rayon f_{max} centrée sur la fréquence 0. Cela signifie que $\forall \xi \in \mathbb{R}^2 \mid\ |\xi| > f_{max},\ \widehat{I_u^{i,\theta}}(\xi) = 0$. Cependant, on peut voir que la transformée de Fourier de la mesure à la fréquence ξ contient les valeurs de la transformée de Fourier de l'échantillon pour des fréquences entre $\xi - k_\theta$ et $\xi + k_\theta$, c'est-à-dire supérieures à

f_{max}. Ces composantes peuvent être séparées si le nombre de phases ϕ_i pour chaque θ est supérieur à 3 puis la fusion de toutes les composantes est faite grâce à un filtre de Wiener. La figure 1.9 résume le principe du SIM.

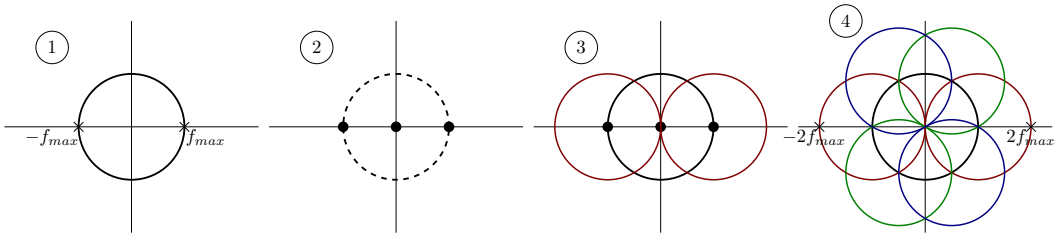

Figure 1.9: Illustration du SIM avec $|k_\theta| = f_{max}$: (1) les fréquences des images créées au sein du microscope sont à bande limitée, de fréquence maximale f_{max}, les coefficients fréquentiels présents dans la mesure sont donc ceux contenus à l'intérieur du cercle noire (2) transformée de Fourier de la grille $m^{i,0}$ utilisée par le SIM, constituée de 3 distributions de Dirac, (3) les coefficients fréquentiels de l'image obtenue grâce à l'acquisition $m^{i,0}$ sont contenues dans un domaine plus grand que celui des images initiales, mais uniquement dans une direction provilégiée ; le nouveau domaine est celui à l'intérieur de l'union des cercles rouges et noirs, (4) grâce aux acquisitions $m^{i,\theta}$ pour $\theta \in \{0, \frac{\pi}{3}, \frac{2\pi}{3}\}$, le domaine des fréquences de l'échantillon representés dans les mesures est élargi dans différentes directions. Ce domaine est délimité par les cercles colorés. On peut voir que grâce à la forme particulière de la grille, des fréquences contenues entre f_{max} et $2f_{max}$ peuvent être calculées.
La figure présentée s'inspire de la figure de l'article de Gustafsson [46] présentant la technique SIM.

L'avantage du SIM est qu'il s'agit d'une technique plein champ et linéaire. Uniquement 9 images sont nécessaires : 3 valeurs de ϕ_i pour chaque angle θ, et 3 valeurs de θ, rendant la méthode très rapide. Cependant une erreur d'estimation des paramètres (notamment ϕ_i, $|k_\theta|$, à cause du bruit ou d'un mauvais alignement des optiques par exemple) pour une des mesures peut très fortement altérer le résultat final. C'est pourquoi les méthodes d'Illumination Scanning Microscopy, qui scannent localement l'échantillon semblent plus adaptées car chaque image concerne une petite partie de l'échantillon (et altère donc moins le résultat final) et la redondance d'informations apporte plus de confiance quant au résultat obtenu.

1.3.4 Interprétation des méthodes ISM

Dans les méthodes ISM, l'échantillon biologique, u, est scanné à un certain nombre de positions, notées $(X_s)_{s\in\{1,\dots,S\}}$, en utilisant une distribution lumineuse, pouvant être dépendante de la position, D^s ; l'image observée sur la caméra est une fonction en quatre dimensions, les deux premières correspondant au pixel caméra, X_c, les deux

autres à la position X_s :

$$I_u(X_s, X_c) = \left((u(\cdot) \times D^s(\cdot - X_s)) * \varphi(\cdot)\right)(X_c). \tag{1.4}$$

Dans le chapitre 3, on prouve que, comme dans le SIM, il est possible de doubler le domaine des fréquences mesurées avec les méthodes ISM. En effet, la transformée de Fourier 4-dimensions de (1.4) s'écrit, comme nous le verrons dans le chapitre 2, sous la forme

$$\widehat{I_u}(\eta) = \widehat{\varphi}(\eta_{34})\widehat{D^s}(-\eta_{12})\hat{u}(\eta_{12} + \eta_{34}),\ \eta = \begin{pmatrix}\eta_{12}\\ \eta_{34}\end{pmatrix} \tag{1.5}$$

avec $\eta_{12} \in \mathcal{B}(0, f_{max}),\ \eta_{34} \in \mathcal{B}(0, f_{max})$ et donc $\eta_{12} + \eta_{34} \in \mathcal{B}(0, 2f_{max})$, ce qui signifie que les fréquences de l'échantillon u dans la boule $\mathcal{B}(0, 2f_{max})$ sont présentes dans les acquisitions $\widehat{I_u}$.

La discrétisation d'un problème de type (1.4) est le sujet du chapitre 3 ; pour les méthodes ISM en microscopie, il est assez rare de trouver une description détaillée de la discrétisation, mais pour les techniques de super-résolution plus générales, sur images naturelles, utilisant plusieurs images basse résolution, avec, parfois, un mouvement de la caméra, pour créer une image super-résolue, la bibliographie est plus dense [92]. On peut voir que l'opérateur ISM peut se décomposer en opérations simples, à savoir

$$I_u = DMHu,$$

où la matrice de convolution H est une matrice de Toeplitz dont chaque ligne est composée du noyau (ou plus exactement ici la PSF) translaté, celle de multiplication M est une matrice diagonale et D est la matrice de sous-échantillonnage. Dans [79], Marquina et Osher choisissent une matrice D, décomposée en D_x et D_y, avec

$$D_x = \begin{pmatrix} 1 & 1 & 0 & 0 & \dots & 0 & 0 \\ 0 & 0 & 1 & 1 & \dots & 0 & 0 \\ \vdots & & & & \ddots & & \vdots \\ 0 & 0 & 0 & 0 & \dots & 1 & 1 \end{pmatrix},$$

et D_y défini symétriquement, c'est-à-dire D effectue la moyenne des pixels super-résolus correspondant au pixel sous-résolu. Dans [26], une méthode d'interpolation bilinéaire est utilisée et dans [40], le sous-échantillonnage est choisi en prenant un point sur z, où z est le facteur de zoom entre l'image caméra et l'image super-résolue. Dans notre cas, on verra que le fait que le signal créé soit bande limitée permet un

sous-échantillonnage sans perte d'information, en "coupant" l'image du spectre discret, la fréquence de coupure étant donnée par la valeur discrète de f_{max}.

Il est important de noter que les techniques de super-résolution citées ci-avant s'appuient sur l'*aliasing*, c'est-à-dire le mélange des hautes et basses fréquences de l'image recherchée, obtenu en choisissant un pas d'échantillonnage trop grand (par rapport à celui requis par le théorème de Shannon), comme expliqué par Simpkins et Stevenson dans [107]. En microscopie, au contraire, le pas d'échantillonnage est choisi de manière à éviter de phénomène d'*aliasing*. Cette hypothèse de bon échantillonnage nous a motivés à choisir l'interpolation de Shannon pour modéliser le lien entre l'image continue et sa discrétisation ; cette interpolation proposée par Abergel et Moisan [3] découle directement du théorème de Shannon, supposant que l'image super-résolue à retrouver est à bande limitée. Ce formalisme nous permet, puisque la PSF φ et les illuminations D^s sont à bande limitée, de définir la distance minimale nécessaire entre deux points de scan. De plus, une définition des opérations de type translation (nécessaire car les distributions lumineuses ne sont pas nécessairement projetées au même endroit de la caméra), zoom et zoom arrière, dans le cas de signaux à bande limitée, dérive de la définition de l'interpolée de Shannon. Il faut néanmoins se rappeler que l'utilisation de la transformée de Fourier discrète induit une hypothèse de périodicité implicite qui requiert d'être attentif aux opérations de convolution (qui avec l'utilisation de la DFT est par définition une convolution périodique) et de multiplication (puisqu'il s'agit d'une convolution dans le domaine de Fourier). Un algorithme complet est donc proposé dans le chapitre 3.

Parmi les méthodes ISM les plus connues, on peut citer

— l'imagerie conventionnelle : l'image obtenue par ce système est créée en sommant les images obtenues sur la caméra ; on démontre dans le chapitre 3 que la PSF d'un tel système est en fait la même que celle du microscope ;

— le pixel-reassignement : consiste à assigner le signal enregistré pour une acquisition à une position entre la position laser et la position caméra, le plus souvent au milieu. Cette technique est aujourd'hui utilisé par le système Airyscan [61], [62]. Depuis 2017, [68], [67], ce module est utilisé sur des cellules vivantes et a montré sur des mitochondries ses performances en terme de résolution, sans altérer ni tuer la cellule. Dans [62], une comparaison entre le SIM et le système Airyscan est effectuée ; dans les meilleures conditions, le SIM semble plus performant en terme de résolution. Cependant les "meilleures conditions" ne sont pas toujours réunies en microscopie (échantillon fin, bien marqué, avec

un nombre de photons assez élevé etc), et dans ce cas le système AiryScan reconstruit des images plus précises, avec moins d'artefacts ;

— l'imagerie confocale : un faisceau laser scanne l'échantillon et filtre la lumière renvoyée au moyen d'un sténopé, c'est-à-dire un trou de très faible diamètre. Comme présenté sur la figure 1.10, la tache d'Airy est très concentrée spatialement au plan focal et s'étale dans les plans suivants ; les photons capturés assez loin du rayon d'Airy proviennent alors vraisemblablement des plans défocalisés et sont donc éliminés grâce au diaphragme.

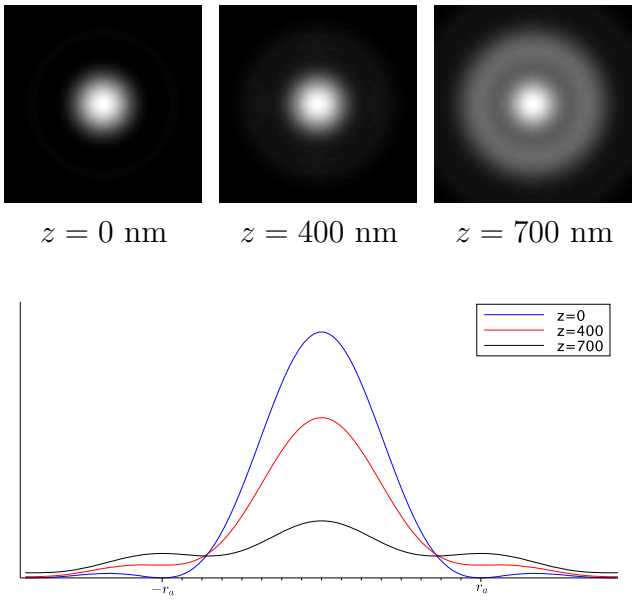

Figure 1.10: Sections xy normalisées de la tache d'Airy, modélisant la tache optique du microscope optique, pour 3 valeurs de z : 0, 400 et 700 nanomètres ; en dessous, on peut voir les profils verticaux des 3 taches. Les images étant normalisées, la différence entre 0 et 400 nanomètres est peu visible à l'œil nu, mais le profil montre la différence de répartition de l'énergie ; à 700 nanomètres, la forme même de la tache est modifiée. Les profils défocalisés, à 400 et 700 nanomètres, ont une plus grande proportion d'énergie en dehors du cercle centré sur le milieu de l'image et de rayon r_a.

Remarque. Le diaphragme du confocal est placé devant le détecteur créant l'image, ce qui signifie que la quantité de lumière projetée sur l'échantillon est la même qu'avec l'utilisation d'un système conventionnel.
Plus le diaphragme est petit, plus l'image semble nette, mais plus l'intensité recueillie est faible. Il faut donc éclairer l'échantillon avec un laser plus fort pour obtenir une même intensité finale. Sur la figure 1.11, on peut voir une

comparaison entre les systèmes widefield et confocal, avec un diaphragme égal à 1.3 fois le rayon d'Airy. Sans nul doute la résolution obtenue est meilleure.

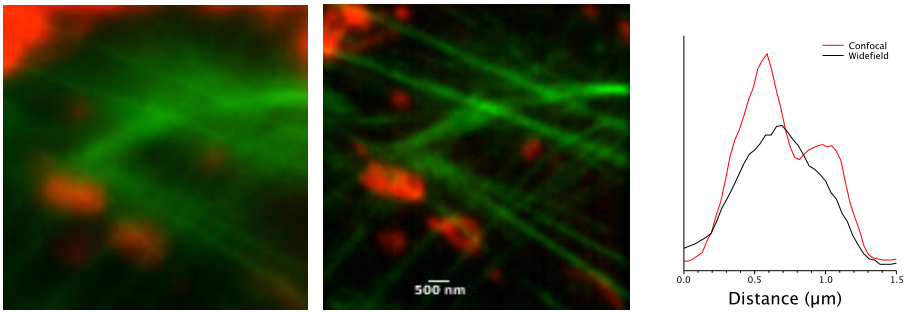

(a) Widefield (b) Confocal (c) Profil du "donut"

Figure 1.11: Comparaison entre widefield et confocal : (a) image obtenue par un microscope optique widefield en plein champ, dont la résolution est définie par la limite de Abbe (1.1), (b) même image obtenue grâce à un système confocal. Le gain obtenu par le confocal est indéniable : sur le canal vert les filaments sont plus fins, mieux séparés, sur le canal rouge, la forme "donut" d'un des éléments apparaît (dont le profil est représenté en (c)). Le confocal est aujourd'hui une des techniques les plus répandues en microscopie à fluorescence.
Image obtenue sur un échantillon de type FluoCells de ThermoFisher, le canal rouge représente les mitochondries et le vert l'actine.

1.3.5 Comparaison des méthodes ISM

Pour comparer les méthodes, dans le chapitre 2, on compare les Fonctions de Transfert Optiques, notées OTF, des systèmes associés à ces méthodes, c'est-à-dire les transformées de Fourier des PSF équivalentes. En particulier, on s'intéresse aux valeurs des OTF autour de la fréquence $\pm 2f_{max}$: plus ces coefficients sont élevés, plus les composantes fréquentielles de l'échantillon autour de $2f_{max}$ sont capturées dans les acquisitions produites par la technique. Le calcul des OTFs pour les 3 méthodes est détaillé dans le chapitre 3, on présente ici simplement les profils du module des OTF, sur la figure 1.12, avec une comparaison avec un (hypothétique) conventionnel de double résolution ; deux tailles de diaphragme pour le confocal sont présentées. On peut voir que les coefficients des OTF autour de $2f_{max}$ sont bien moins bons que ceux de ce conventionnel hypothétique à résolution double. Les méthodes du confocal et du pixel-reassignement présentent néanmoins un réel gain par rapport au conventionnel réel.

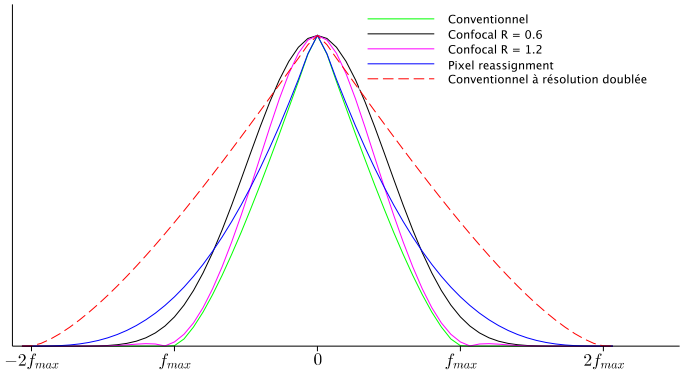

Figure 1.12: Comparaison des profils des OTF pour les trois reconstructions linéaires : conventionnelle, confocale (pour deux valeurs de diaphragme), pixel-reassignement ainsi que celui d'un hypothétique système conventionnel de résolution doublée. Pour le conventionnel, on a exactement la PSF, donc le signal est limité à f_{max} ; pour les autres techniques, des fréquences entre f_{max} et $2f_{max}$ sont non nulles. Les meilleurs résultats sont obtenus pour le pixel-reassignement ; quant au confocal, plus le diaphragme se réduit, plus le support des coefficients fréquentiels non nuls s'agrandit, mais on rappelle que plus le diaphragme se réduit, plus le nombre de photons compté est faible, ce qui peut nécessiter d'éclairer l'échantillon plus intensément. On note cependant qu'on n'atteint pas les performances d'un conventionnel de fréquence maximale $2f_{max}$.

Ces techniques sont des techniques de reconstruction linéaire. D'autres types de reconstructions peuvent être obtenues en considérant le problème ISM comme un problème inverse.

1.4 Résolution de problèmes inverses par méthodes non linéaires

Étant donné un signal $x : \Omega \to \mathbb{R}$, avec $\text{card}(\Omega) = p$, on observe $y : \Omega' \to \mathbb{R}$, avec $\text{card}(\Omega') = n$. Formellement, on définit un problème inverse linéaire par

$$Hx = y, \tag{1.6}$$

— $y \in C_y \subset \mathbb{R}^n$ les données observées,
— $H \in \mathcal{M}_{p,n}$ un opérateur linéaire connu,
— $x \in C_x \subset \mathbb{R}^p$ le vecteur inconnu que l'on cherche à retrouver.

Les problèmes inverses sont très présents autour de nous : par exemple en géophysique pour chercher l'origine d'un séisme grâce aux ondes émises lors de ce dernier, en

chimie pour déterminer des constantes de réactions, en météorologie pour prédire le temps, etc. On rappelle qu'un problème inverse est bien posé au sens d'Hadamard si la solution existe, est unique et dépend continûment de la donnée y [49] ; ce n'est, en général, pas le cas de la déconvolution ; en particulier, la solution n'est pas toujours stable par rapport à de légères perturbations du signal de départ y.

Remarque. Dans (1.6), le problème est considéré en une dimension ; dans cette thèse on s'intéresse plus particulièrement aux images, en deux dimensions. Le passage d'une image x à un vecteur équivalent se fait en concaténant les lignes ou les colonnes de l'image x. On notera parfois $x \in \mathbb{R}^\Omega$, où $\mathbb{R}^\Omega$ représente les fonctions de Ω dans $\mathbb{R}$, avec $\Omega = \{0, \dots, p_x - 1\} \times \{0, \dots, p_y - 1\}$, et $\text{card}(\Omega) = p_x \times p_y = p$; les notations $\mathbb{R}^p$ et $\mathbb{R}^\Omega$ sont alors équivalentes.

Dans le cas de la super-résolution et des méthodes à balayage laser, le problème inverse est le suivant : retrouver la distribution des marqueurs fluorescents placés sur le spécimen biologique à partir d'images acquises en scannant l'échantillon (avec éventuellement un faisceau projetant une distribution lumineuse particulière). Les images d'entrée y sont enregistrées sur une caméra dont les pixels forment ce que l'on appelle la grille "sous-résolue", alors que l'image super-résolue x est calculée sur une grille plus fine, afin de pouvoir reconstruire des structures à plus petite échelle. Dans cette thèse, on considère uniquement une grille k fois plus fine que celle de la caméra, avec $k \in \mathbb{N}^*$. L'ensemble C_x auquel appartient la solution est $C_x = \mathbb{R}_+^p$. L'opérateur H, dans la définition du problème inverse (1.6), modélise toutes les étapes permettant de passer de l'image x super-résolue aux images scannées y, c'est-à-dire les I_x de la Formule (1.4) ; il doit modéliser notamment la multiplication avec la distribution de lumière projetée par le faisceau laser, la convolution par la PSF et le changement de résolution.

Afin de tester les méthodes proposées sur un problème plus simple, on s'intéresse également dans cette thèse au problème de déconvolution sous contrainte de positivité, dans les chapitres 4 et 5. On rappelle donc la définition de la convolution. L'opérateur H représente dans ce cas le noyau de convolution uniquement, y est une version convoluée et bruitée de x, l'image recherchée. L'écriture du problème est cependant identique ; c'est pourquoi dans la suite (hormis sur la figure 1.14 où l'on traite de la déconvolution), l'opérateur H peut représenter de la même manière l'opérateur de déconvolution ou de super-résolution, sauf si précisé autrement.

Remarque. Le modèle utilisé dans cette thèse est le modèle "complet", c'est à dire que toutes les images mesurées sont utilisées et intégrées dans le modèle. D'autres

techniques utilisent les images mesurées pour, dans un premier temps, créer une image de la zone complète scannée (image équivalente à un système conventionnel ou confocal par exemple), puis cette image est déconvoluée en utilisant des méthodes de déconvolution traditionnelles. En particulier, on peut noter l'utilisation de la méthode de Richardson-Lucy [77][95], qui date des années 70 mais qui est très utilisée dans le domaine de la microscopie, principalement car elle a été développée pour des images bruitées par bruit de Poisson. En 1990, Bertero l'utilise sur l'image d'un système confocal [13] avec la régularisation de Tikhonov, et plus récemment, en 2006, on peut noter son utilisation avec la régularisation par variation totale dans [32].

En traitement d'image, les problèmes inverses sont également nombreux : le débruitage, l'*inpainting*, l'estimation du flou de bougé etc. Dans cette thèse, on s'intéresse particulièrement à la déconvolution. Soit h un noyau de convolution (généralement positif et à support limité), la formulation continue de ce problème inverse est donnée sur $\mathbb{R}^d$, avec $d = 2$ dans le cas des images, par

$$\forall t \in \mathbb{R}^d,\ y(t) = \int_{\mathbb{R}^d} x(s)h(t-s)ds \tag{1.7}$$

et sa formulation discrète par

$$\forall m \in \mathbb{Z}^d,\ y(m) = \sum_{n\in\mathbb{Z}^d} x(n)h(m-n).$$

Un exemple d'image convoluée avec un noyau gaussien est présenté sur la figure 1.13. L'effet de cette opération est de flouter l'image. L'image convoluée est la somme pondérée des noyaux recentrés en chaque pixel de l'image originale, la pondération étant la valeur initiale du pixel. Les détails vraiment fins de l'image sont donc perdus, comme la séparation de certains filaments (en vert) ou de certaines billes (en bleu). Dans cette configuration, le problème inverse est : étant donnés l'image floutée et le noyau de flou, retrouver l'image originale. Dans le cas de la déconvolution, la transformée de Fourier joue un rôle très important car le problème (1.7) peut s'exprimer (en gérant correctement le calcul au bord du domaine de l'image) dans l'espace de Fourier comme une simple multiplication. Puisque les noyaux (gaussiens ou la tâche d'Airy) sont des noyaux passe-bas, l'image convoluée contient essentiellement les basses fréquences de l'image originale, ce qui explique le résultat cohérent avec la figure 1.5.

Une approche très utilisée pour résoudre un problème inverse de type (1.6), avec H connu, consiste à lui associer une énergie, que l'on cherche à minimiser. Cette

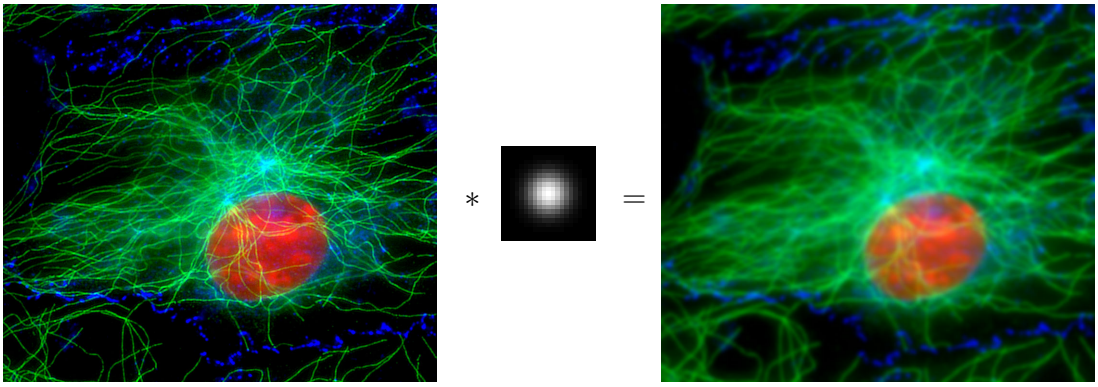

(a) Image originale (b) Noyau (c) Image convoluée

Figure 1.13: Illustration de la convolution : (a) image originale, représentant des fibroblastes, (b) noyau de convolution gaussien d'écart type $\sigma = 3$ (représenté avec des pixels plus gros pour plus de visibilité), (c) résultat de la convolution. On peut voir que la convolution a rendu l'image de départ floue ; en particulier on ne distingue plus toutes les séparations, entre les filaments sur le canal vert ou entre les billes sur le canal bleu.
Image de fibroblaste (l'image présentée est un extrait de l'image originale) par Jan Schmoranzer pour l'Olympus BioScapes Digital Imaging Competition 2007, rendue disponible sur le site cellimagelibrary.org, licence CC BY-NC-ND 3.0.

énergie cherche à évaluer la différence entre les données mesurées y et le modèle appliqué à l'image proposée comme solution, Hx. Son expression est directement liée au modèle de bruit considéré pour la mesure ; comme précisé avant, on s'intéresse plus particulièrement, dans cette introduction, au bruit de Poisson.

1.4.1 Estimateur MAP sous contrainte de positivité

En reprenant les notations de (1.6), on considère que la valeur de y au pixel i, notée y_i, est la réalisation d'une variable aléatoire Y_i de Poisson de paramètre $(Hx)_i$ (on a alors $C_y = \mathbb{N}^{\Omega'}$, d'après la définition de la loi de Poisson), c'est-à-dire

$$\forall i \in \{1 \dots n\},\ \mathbb{P}(Y_i = y_i | (Hx)_i) = \frac{(Hx)_i^{y_i} e^{-(Hx)_i}}{y_i!}.$$

L'hypothèse de bruit de Poisson induit une hypothèse de positivité sur la donnée à retrouver. Une méthode assez usuelle, appelée Maximum A Posteriori, MAP, consiste à chercher le signal (l'image en deux dimensions) le plus probable ayant engendré les données obtenues. L'estimateur MAP est alors donné par

$$\underset{x \in \mathbb{R}_+^{\Omega}}{\operatorname{argmax}}\, p(x|y),$$

qui peut être calculé par la formule de Bayes,

$$x_{MAP} = \underset{x\in\mathbb{R}_+^\Omega}{\operatorname{argmax}}\, p(x|y) = \underset{x\in\mathbb{R}_+^\Omega}{\operatorname{argmax}}\, \frac{p(x)}{p(y)} p(y|x) \tag{1.8}$$

En supposant l'indépendance de tous les Y_i, on peut écrire la log-vraisemblance

$$L(x) = \log\left(\prod_{i=1}^{n} \mathbb{P}(Y_i = y_i|(Hx)_i)\right) = \sum_{i=1}^{n} y_i \log((Hx)_i) - (Hx)_i - \log(y_i!), \tag{1.9}$$

et on associe au problème l'énergie

$$E_y(x) = \sum_i (Hx)_i - y_i \log((Hx)_i), \tag{1.10}$$

(on élimine le dernier terme $\log(y_i!)$ qui ne dépend pas de x). Il y a donc équivalence entre le calcul de l'estimateur du Maximum a Posteriori et la résolution d'un problème variationnel, la minimisation de E_y :

$$x_{MAP} = \underset{x\in\mathbb{R}_+^\Omega}{\operatorname{argmax}}\, p(x|y) = \underset{x\in\mathbb{R}_+^\Omega}{\operatorname{argmin}}\, E_y(x)$$

Un algorithme de gradient projeté, accéléré par Nesterov [87] et amélioré par Weiss [122], permet une convergence effective en pratique (contrairement à beaucoup d'autres algorithmes) tout en restant très simple d'implémentation, puisqu'il nécessite uniquement de connaître l'opérateur adjoint de H, H^*. Cependant, l'estimateur MAP produit un artefact appelé *night sky* par Bertero et al. dans [14] : toute continuité est perdue dans le signal final, constitué de points isolés. Cela est dû au fait que lors de la déconvolution, l'estimateur crée des hautes fréquences, qui, à cause de la contrainte de positivité, deviennent, dans le domaine spatial, des oscillations entre valeurs positives, plus élevées que le signal de base, et nulles. Sur la figure 1.14, ce phénomène de *night sky* est bien mis en évidence.

1.4.2 Algorithmes d'approximation du MAP

L'étude du *night sky*, présentée dans le chapitre 4, montre que cet artefact apparaît au cours des itérations, au fur et à mesure de la convergence vers le minimum exact de la fonctionnelle ; des déformations progressives des structures continues sont visibles avant que l'image ne soit compose que de sources totalement isolées. Il est intéressant de noter que l'utilisation d'un simple algorithme de gradient projeté, qui

était pendant longtemps la technique utilisée pour résoudre ce problème, à nombre d'itérations fixé (de manière à obtenir un temps de calcul raisonnable) présente très rarement cet effet de *night sky*, sauf si l'image est très petite ou le nombre d'itérations très important. Cet algorithme est en fait beaucoup moins efficace pour minimiser l'énergie que l'algorithme optimisé de Nesterov, à cause de la dimension élevée du problème (donnée par le nombre de pixels de l'image), et ce manque d'efficacité a donc paradoxalement un effet positif. Ainsi, les algorithmes couramment utilisés bénéficient aussi de leur relative inefficacité à converger. Comme nous le montrons dans le chapitre 4, seule l'utilisation d'un algorithme accéléré (de type Nesterov) permet de mettre en évidence ce défaut majeur de l'estimateur MAP.

Une méthode non satisfaisante mathématiquement (car on ne sait pas décrire précisément le résultat obtenu) consiste à stopper les itérations au cours de l'algorithme. Cela permet d'obtenir une image sans *night sky* mais avec les effets de la déconvolution ; cependant, il faut trouver un critère d'arrêt de l'algorithme pour avoir une image convenable. L'algorithme de Richardson-Lucy par exemple, couramment utilisé en microscopie, est très souvent stoppé après une dizaine d'itérations, car ensuite il est connu pour décrire de plus en plus, au cours des itérations, le bruit altérant l'image originale que l'image elle-même. Dans le chapitre 4, on propose, dans le cas du bruit additif Gaussien, un critère d'arrêt qui soit cohérent avec les statistiques de ce bruit.

De nos jours, les algorithmes d'approximation du MAP sont le plus souvent utilisés avec une régularisation, permettant d'ajouter une contrainte sur la solution, et par là même, de limiter le *night sky*.

1.4.3 Régularisation

Dans ce cas, on minimise l'énergie E_y, mais en y ajouttant un terme, appelé *prior*, caractérisant une propriété de l'image x à retrouver. On présente 2 priors assez connus et utilisés en microscopie, comme précisé avant, Tikhonov et la Variation Totale (TV en anglais). On cherche alors à résoudre le problème suivant

$$\underset{x \in C}{\operatorname{argmin}} \quad E_y(x) + \lambda R(x),$$

le second terme $R(x)$ étant le terme de régularisation, pondérée par un paramètre $\lambda > 0$. Une régularisation de type Tikhonov [115] consiste à prendre la fonction $R(x)$ égale à la norme ℓ^2 du vecteur recherché

$$R(x) = \|x\|^2$$

et la régularisation TV est donnée par la formulation

$$R(x) = TV(x) = \sum_{i \in \Omega} \|\nabla x(i)\|,$$

où ∇ représente l'opérateur discrétisé du gradient (approché généralement par un schéma aux différences finies). La première solution favorise les solutions de faible norme ; en présence de bruit de Poisson, l'algorithme est présenté dans [71] et combine une méthode de Newton et un gradient conjugué projeté pour l'estimation du minimum de la fonctionnelle. Quant à la seconde, elle favorise les solutions constantes par morceaux comme cela peut être vu sur la figure 1.14, dernière ligne. Plus λ est grand, plus les zones lisses sont étendues. La recherche du minimum se fait grâce à l'algorithme de Chambolle-Pock [24]. La variation totale a été introduite en 1992 par Rudin, Osher et Fatemi dans [96] dans le cadre du débruitage et est un a priori très utilisé depuis en traitement d'images. C'est une méthode très efficace pour débruiter les images dites "cartoon" c'est-à-dire contenant des zones très lisses séparées par des frontières régulières. Sur les images réelles, par contre, on voit souvent apparaître un artefact appelé *staircasing*, remarqué par Dobson et Santosa en 1996 [33] et décrit notamment dans [21] par Buades, Coll et Morel comme la "création de régions uniformes séparées par des bords artificiels", le plus souvent les transitions d'intensité se font sous forme de marches d'escalier, même dans les zones initialement lisses.

La figure 1.14 réunit des résultats obtenus sur une image convoluée avec un noyau Gaussien et perturbée par du bruit de Poisson. Une image biologique a été utilisée. Comme précisé précédemment, le MAP présente l'artefact de *night sky* : l'image est constituée de points isolés, et l'on observe que les structures continues ont été perdues. Les deux régularisations sont présentées avec 3 pondérations λ différentes, afin de mesurer l'influence de son paramètre. Dans le cas de la régularisation Tikhonov, une valeur très faible dédouble les structures et crée certaines valeurs ponctuelles dans le fond, initialement noir. Une valeur trop grande donne un aspect encore flou à l'image et augmente sa dynamique. Pour la régularisation TV, pour un faible λ on remarque l'apparition du *night sky* alors qu'une grande valeur donne un effet "cartoon" à l'image, constituée alors de zones constantes par morceaux.

Même si les résultats sont plutôt intéressants, la régularisation est assez peu satisfaisante dans le cas des images produites par un microscope à fluorescence ; la régularisation de Tikhonov altère les intensités initiales et l'hypothèse de données constantes par morceaux n'est pas tout à fait cohérente avec la microscopie, du fait que les éléments biologiques visualisés peuvent être très diversifiés (certains constants,

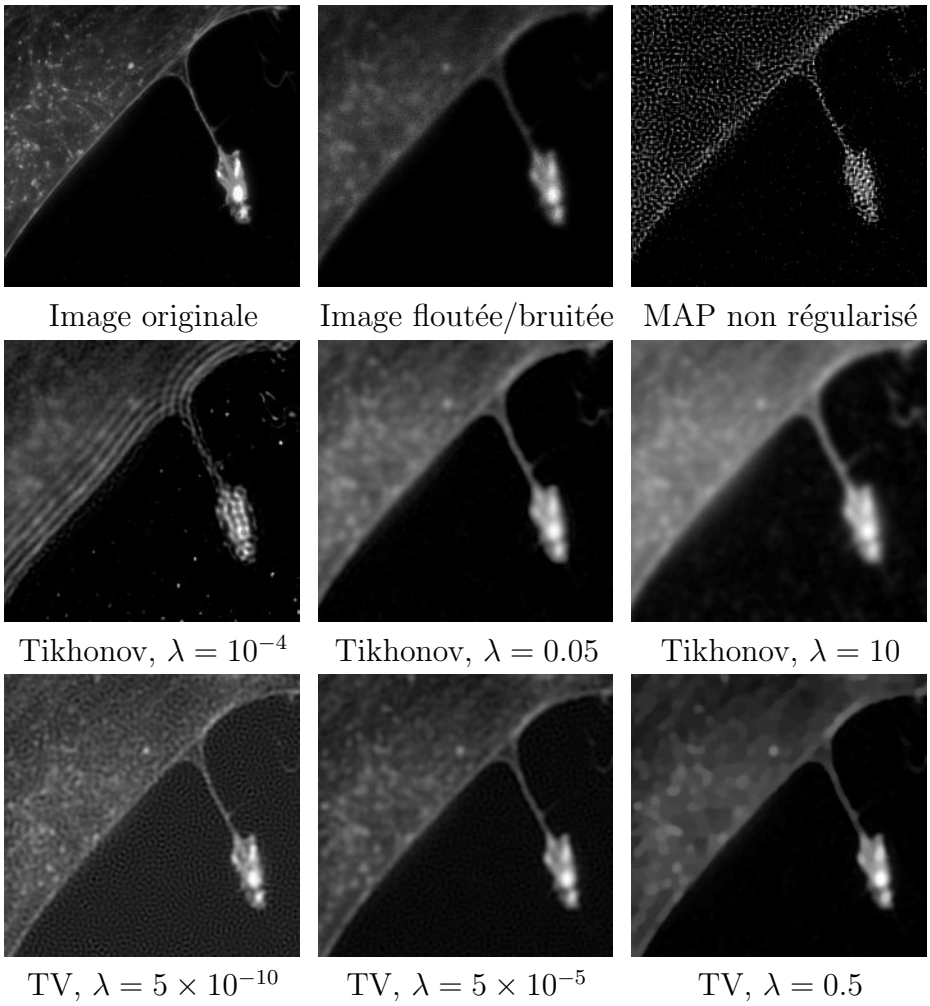

Figure 1.14: Comparaison des méthodes de déconvolution en présence de bruit de Poisson ; sur la première ligne, l'image originale, à gauche sa convolution avec un noyau Gaussien de déviation standard 2 avec un bruit de Poisson généré sur chaque pixel. L'estimateur MAP obtenu avec un algorithme de type Nesterov, arrivé à convergence, est présenté à droite. Sur la deuxième ligne, l'estimateur MAP avec régularisation de Tikhonov pour 3 valeurs de λ est présenté et sur la troisième, l'estimateur MAP avec régularisation TV pour 3 valeurs de λ. L'estimateur MAP non régularisé présente un artefact appelé *night sky* : l'image finale est essentiellement constituée de points isolés. La régularisation Tikhonov crée une image de contraste différent de celle de départ ; une valeur de λ trop faible entraîne une répétition des contours, avec des valeurs dans le fond parfois aléatoires ; une trop grande valeur crée une image assez floue. $\lambda = 0.05$ donne des résultats assez intéressants sur cet échantillon, recréant parfaitement la structure en haut à droite sous la cellule qui avait quasiment disparu dans l'image convoluée et bruitée. La variation totale crée une image constante par morceaux ; plus λ est grand, plus les zones lisses sont étendues, comme on peut le voir pour $\lambda = 0.5$; une trop faible valeur fait apparaître un artefact assez proche du *night sky*, et une valeur intermédiaire offre des résultats intéressants : l'image est un peu déconvoluée, et le contraste mieux conservé qu'avec la régularisation de Tikhonov.
Image de cellules de veines ombilicales humaines (HUVEC) par Ana M. Pasapera - Clare M. Waterman disponible sur cellimagelibrary.org.

d'autres très ponctuels). De plus, la variation totale est connue pour ne pas toujours reconstruire correctement la texture dans les images, car cette dernière peut être considérée comme du bruit (selon la valeur de λ). Pour limiter le *night sky* dans le cas de la super-résolution, on a ajouté une contrainte sur l'image recherchée : elle doit être à bande limitée ; plus exactement son support doit être choisi tel que sa fréquence maximale soit égale à kf_{max} avec $k \in \mathbb{N}^*$. L'estimateur de l'image super-résolue x^{SR}_{MAP} est alors donné par

$$x^{SR}_{MAP} = \underset{x\in\mathcal{K}}{\operatorname{argmax}}\ p(x|y) = \underset{x\in\mathcal{K}}{\operatorname{argmin}} (Hx)_i - y_i \log((Hx)_i), \tag{1.11}$$

avec

$$\mathcal{K} = \left\{ x \,\middle|\, x \in \mathbb{R}^\Omega,\ \operatorname{supp}(\hat{x}) \in \mathcal{B}(0, kf_{max}) \right\}.$$

L'estimateur MAP est aujourd'hui très majoritairement utilisé car le problème se ramène à une minimisation d'énergie, dont l'estimation peut se faire assez rapidement, grâce aux algorithmes d'optimisation développés spécifiquement pour ce calcul. Cette solution n'est cependant pas entièrement satisfaisante, en particulier car la distribution du MAP est connue pour ne pas être représentative de la loi a posteriori [88]. Cela signifie que les images tirées aléatoirement selon une distribution de probabilité en très grande dimension n'ont souvent pas la propriété de maximiser la densité a posteriori.

On peut noter que l'estimateur MAP peut aussi être vu comme le minimum d'une fonction de risque

$$x_{MAP} = \underset{x\in\mathbb{R}^\Omega}{\operatorname{argmin}} R(x) \text{ avec } R(x) = \int_{\mathbb{R}^\Omega} L(x, x') p(x'|y) dx',$$

pour la fonction de perte L donnée par

$$L(x, x') = \begin{cases} 0 \text{ si } x = x' \\ 1 \text{ sinon} \end{cases}.$$

Cette écriture sous forme de minimisation de fonction de risque permet alors de créer de nombreux autres estimateurs, par des choix variés pour la fonction de perte L [97]. Depuis 1989, avec Besag [16] par exemple, une autre fonction de perte, L', dite quadratique, est particulièrement utilisée en traitement d'images, et définie par $L'(x, x') = \|x - x'\|_2^2$. La fonction de risque R' associée est donc égale à

$$R'(x) = \int_{\mathbb{R}^\Omega} \|x' - x\|_2^2\ p(x'|y) dx',$$

dont le minimum x_{LSE}, LSE pour Least-Square Error, est donné par l'espérance de la loi a posteriori

$$x_{LSE} = \underset{x \in \mathbb{R}^\Omega}{\operatorname{argmin}} R'(x) = \int_{\mathbb{R}^\Omega} p(x'|y) x' dx' = \mathbb{E}(x'|y). \tag{1.12}$$

Cet estimateur est souvent appelé MMSE, pour Minimum Mean Square Error. Il a été montré que, dans le cas d'images binaires [42], l'estimateur LSE est plus représentatif de la loi a posteriori que le MAP. Dans le cas de la déconvolution simple avec un noyau connu, pour un a priori gaussien, l'estimateur LSE est explicite et en fait équivalent à l'application du filtre de Wiener sur les mesures. Une généralisation à un système multi-image peut-être faite, décrite par exemple par Huang [60] dans le cas d'image ultrasons. Dans la suite, on s'intéresse à un estimateur proche du LSE, que l'on reformule différemment pour y intégrer une contrainte de parcimonie. En utilisant la fonction de perte L' plutôt que L pour ce problème inverse, on espère être capable de mieux représenter la densité a posteriori, et plus précisément éviter le *night sky*.

1.4.4 E-LSE : un nouvel estimateur parcimonieux pour les problèmes inverses

Dans [75], Louchet propose d'utiliser l'estimateur LSE, defini par (1.12) comme alternative au MAP dans le cas du débruitage Gaussien (c'est-à-dire $y \sim \mathcal{N}(x, \sigma^2 Id_\Omega)$, σ fixé) avec régularisation TV. L'estimateur peut être adapté au cas où l'image est déteriorée par du bruit de Poisson [2] et au problème de la déconvolution, donnant

$$x_{LSE} = \int_{\mathbb{R}^\Omega} p(x|y) x dx = \frac{\displaystyle\int_{\mathbb{R}^\Omega} e^{-E_y(x)} x dx}{\displaystyle\int_{\mathbb{R}^\Omega} e^{-E_y(x)} dx}, \tag{1.13}$$

où E_y est la fonction énergie définie en (1.10). En débruitage avec régularisation TV, l'estimateur MAP présente, comme mentionné ci-avant, un artefact de *staircasing*. Le calcul de l'estimateur LSE permet d'effacer cet artefact sur le résultat [75]. Cette constatation nous motive donc à développer l'estimateur LSE pour le problème de la déconvolution.

Cependant, comme précisé auparavant, on souhaite intégrer l'hypothèse de parcimonie dans l'image recherchée ; c'est pourquoi on propose un modèle plus adapté aux

images parcimonieuses, l'estimateur E-LSE, pour Emitters-Least-Square Error. D'un point de vue mathématique, la différence entre l'estimateur LSE et cet estimateur réside dans le domaine d'intégration : pour le LSE, il s'agit de R^{Ω}, pour le E-LSE, il s'agit d'un espace plus restreint, dans lequel les images peuvent s'écrire comme la somme pondérée de distributions de Dirac. L'estimateur E-LSE s'écrit alors

$$\hat{x}_{E-LSE} = \frac{\int_C e^{-E_y(x)} x dx}{\int_C e^{-E_y(x)} dx} \text{ avec } C = \left\{ x \in \mathbb{R}^{\Omega} \,\middle|\, x = \sum_{e=1}^{N_e} \lambda_e \delta_{p_e} \,, \lambda_e \in \mathbb{R}_+, p_e \in \Omega \right\}. \tag{1.14}$$

L'ajout de cette contrainte a cependant un impact algorithmique très important et l'algorithme utilisé pour l'estimation du E-LSE diffère très sensiblement de celui du LSE. L'estimateur E-LSE, mais également le LSE, calculent une intégrale en très grande dimension et nécessitent donc l'utilisation d'outils adaptés ; on a choisi les méthodes MCMC, méthode de Monte-Carlo par Chaînes de Markov, avec un algorithme de Metropolis-Hastings [51] [80]. Dans le cas du LSE, on rappelle qu'une chaîne représente l'image, dont la valeur des pixels évolue au cours des itérations, et la moyenne des états successifs est utilisé comme estimateur LSE. Dans le cas du E-LSE, une chaînes représente une population de N_e émetteurs (N_e fixé par l'utilisateur). Ces émetteurs sont caractérisés par leurs intensités et par leurs positions, définies sur la grille de pixels de l'image résultat, Ω. A chaque itération, une proposition de nouvel état est considérée ; ce nouvel état se caractérise par un changement de position et/ou d'intensité d'un seul des émetteurs, choisi uniformément parmi l'un des N_e. Cette proposition respecte la contrainte de positivité sur l'intensité de l'émetteur et l'appartenance à Ω et est acceptée ou refusée selon le critère de Metropolis Hastings : si l'énergie décroît, elle est acceptée d'office ; sinon la probabilité d'acceptation s'écrit comme une fonction (décroissante) de la différence d'énergie entre les deux états, de manière à ce qu'un changement augmentant fortement l'énergie ait très peu de chances de se produire.

L'image produite par une chaîne s'écrit comme la somme pondérée de distributions de Dirac aux positions des émetteurs, les poids étant donnés par l'intensité des émetteurs. Les théorèmes d'approximation d'intégrales stipulent que l'intégrale (1.14) peut être approximée par la moyenne (calculée à partir d'un nombre infini d'états) des images successives produites par une seule chaîne. Cependant, plusieurs ajustements sont faits dans le cas de l'estimateur E-LSE, inspirés par [75] et liés au modèle. Concernant les états conservés dans le calcul de la moyenne, deux états consécutifs

de la chaîne différent au maximum d'un émetteur, on décide donc qu'entre deux états moyennés, N_e propositions d'états ont été effectuées par l'algorithme de Metropolis-Hastings. Pour éviter que l'initialisation n'influence trop le résultat, on n'utilise pas les premiers états de la chaîne dans la chaîne, mais seulement ceux obtenus à partir d'un certain rang, choisi de manière à ce que le régime stationnaire soit plus ou moins atteint. Un moyen de contrôler la convergence de l'estimateur LSE est d'utiliser deux chaînes, et de s'arrêter lorsque les estimateurs donnés par ces deux chaînes sont "assez proches". Pour le E-LSE la démarche est un peu différente car l'ensemble C n'est pas convexe (contrairement à l'espace $\mathbb{R}^\Omega$) ; la convergence est plus délicate et certaines chaînes peuvent rester bloquées dans une certaine configuration d'émetteurs correspondant à un minimum local de l'énergie (voir la Figure 1.15, montrant le résultat d'une chaîne). C'est pourquoi nous avons décider d'utiliser un nombre important de chaînes dans le calcul de la moyenne, afin de considérer les différentes configurations d'émetteurs. Le E-LSE possède un paramètre supplémentaire par rapport au LSE, il s'agit du nombre d'émetteurs N_e. Les images étudiées étant considérées parcimonieuses, on veut que $N_e \ll |\Omega|$, mais ce nombre doit être suffisant pour représenter tous les éléments constituant l'image en moyennant les différentes chaînes. En particulier, si N_e est trop petit, certaines séparations ou certains éléments moins intenses peuvent disparaître de l'image résultat.

L'image résultat obtenue est la moyenne de différentes images appartenant à l'ensemble C. Puisque ces images ne sont ni naturelles (elles ne peuvent être produites par un appareil optique, tel qu'un microscope), ni interpolables, un post-traitement de convolution est effectué. Ce dernier permet de simuler l'image équivalente qui pourrait être théoriquement obtenue avec un microscope de très grande résolution (irréalisable en pratique à cause des contraintes physiques d'ouverture numérique et de longueurs d'ondes du spectre visible). Le noyau doit être choisi de manière à ne pas trop dégrader l'effet de la déconvolution ; le résultat de l'estimateur présenté sur la figure 1.15, créée en moyennant les résultats de 2500 chaînes a été post-traité par une gaussienne de faible écart type. Dans les chapitres 5 et 6, on revient sur le choix de ce noyau dans le cas de la déconvolution et de la super-résolution.

Dans le cas de la déconvolution, l'estimateur E-LSE (tout comme le LSE) n'élimine pas l'effet de *night-sky* ; de nombreuses chaînes moyennées contiennent cet artefact. La mise en place d'un estimateur utilisant non plus E_y mais λE_y (dans le terme exponentiel de la formule (1.13)) a permis d'effacer cet artefact mais les résultats ne sont pas vraiment meilleurs que les résultats d'un estimateur MAP non convergé. En super-résolution l'estimateur E-LSE, sans pondération de l'énergie, fournit des résultats vraiment intéressants (comme présenté sur la figure 1.15, pas de *night sky*

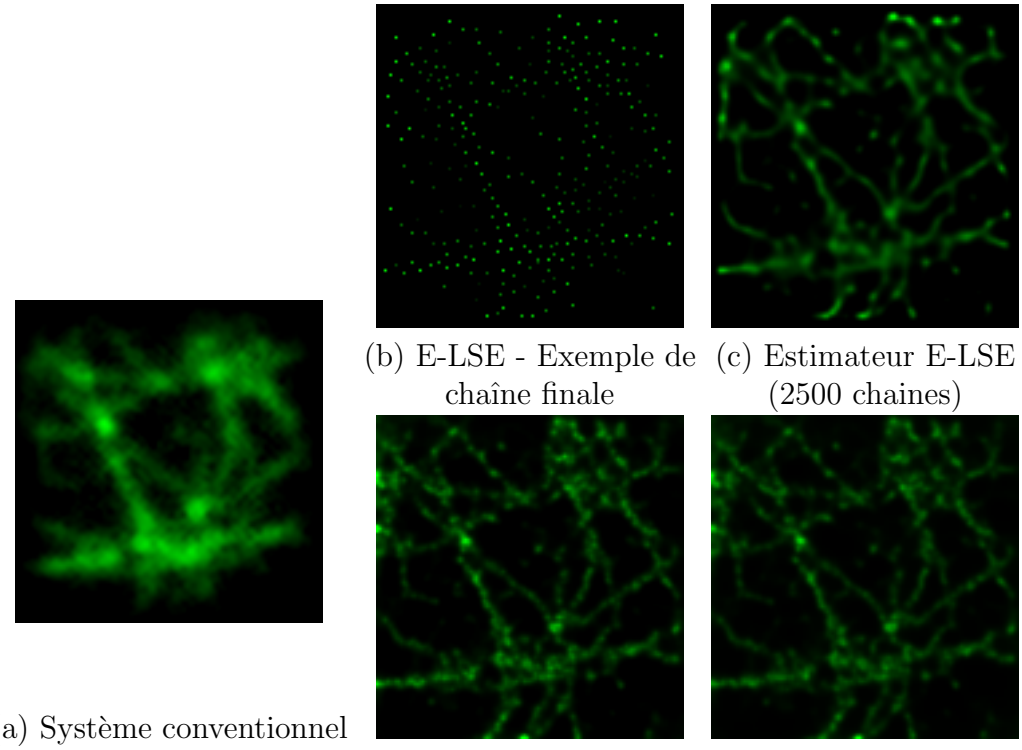

(a) Système conventionnel (Image zoomée)

(b) E-LSE - Exemple de chaîne finale

(c) Estimateur E-LSE (2500 chaines)

(d) LSE - Exemple de chaîne finale

(e) Estimateur LSE (2 chaines)

Figure 1.15: Calcul du E-LSE : sur une image de filaments, acquise par le système BioAxial, on présente l'image d'un système conventionnel en (a) (somme de toutes les images replacées où elles ont été acquises), zoomée (par *zero-padding*) pour atteindre la même résolution que celle des chaînes représentées, puis les résultats obtenus lors de l'algorithme E-LSE. En (b) est représenté le résultat final d'une des chaînes (avec saturation des couleurs, afin de rendre plus visibles les émetteurs) ; la plupart des chaînes obtenues ressemblent à celle représentée en (b), avec des positions et intensités différentes pour les émetteurs. En (c), le résultat de l'estimateur E-LSE est obtenu en moyennant les résultats de 2500 chaînes, convolué avec une gaussienne de faible écart-type. On peut remarquer que chaque chaîne individuellement n'est pas représentative du signal complet mais que leur moyenne permet de créer une image bien mieux résolue que l'image obtenue grâce à un système conventionnel. Au contraire, dans le cas du LSE, une chaîne finale, comme celle représentée en (d), est très proche du résultat final (e), puisque tous les pixels de l'image sont modifiés au cours de l'algorithme MCMC, permettant de n'utiliser que 2 chaînes.

sur la reconstruction finale), l'image produite possède beaucoup moins d'artefacts et dans certains cas présente un meilleur pouvoir de séparation que l'estimateur MAP. On revient sur ces résultats dans la section suivante.

1.5 Applications au système Bioaxial

Avant de présenter les résultats en microscopie, on présente les illuminations, c'est-à-dire les D^s dans l'équation (1.4), qui correspondent à la forme du faisceau laser projetée sur l'échantillon. Dans l'expression de la transformée de Fourier, (1.5), on voit que ces illuminations doivent être choisies intelligemment, puisque que les valeurs de leurs transformées de Fourier pondèrent les valeurs de la transformée de Fourier de l'image recherchée. Le système de super-résolution sur lequel s'appuient les expériences de cette thèse, dans le chapitre 6, est celui commercialisé par l'entreprise BioAxial qui utilise des illuminations dites *singulières* ; on présente comment celles-ci sont créées, leurs avantages et certains résultats obtenus avec leur utilisation.

1.5.1 Illuminations singulières par diffraction conique

La diffraction conique est un phénomène décrit par Michael Berry dans [10] en 2004, d'après une étude théorique de Hamilton [50] et des expériences de LLoyd [74] dans les années 1830. Elle caractérise la propagation d'un faisceau de lumière dans un cristal dit biaxe (voir [11] pour une définition et les propriétés de ce cristal), modifiant en particulier la polarisation et la répartition de l'énergie du faisceau lumineux. Cette reprise du phénomène par Berry a été un tremplin à de nombreuses applications de la diffraction conique. Dans [116], Turpin et al. évoquent son utilité par exemple dans les communications optiques, la création de meilleurs polarimètres et de nouveaux lasers. L'application qui nous intéresse particulièrement a été proposée par Gabriel Sirat dans [108] et mise en application pour la super-résolution dans [22].

On décrit brièvement le modèle mathématique associé, nécessaire à la création d'un algorithme générant des distributions lumineuses créées par ce phénomène. On suppose que la lumière se propage dans le cristal selon un cône, dont R_0 est le rayon à la sortie du cristal. Dans le cas où le rayon incident est à symétrie circulaire, Berry prouve [10] que l'écriture exacte du champ électrique est donnée, en utilisant les coordonnées polaires, $\mathbf{R} = R\begin{pmatrix}\cos(\theta) & \sin(\theta)\end{pmatrix}$, et le vecteur d'onde $\mathbf{P} = P\begin{pmatrix}\cos(\theta_P) & \sin(\theta_P)\end{pmatrix}$, par

$$E(\mathbf{R}, z) = B_0(R, R_0, z)\begin{pmatrix}V_x\\V_y\end{pmatrix} + B_1(R, R_0, z)\underbrace{\begin{pmatrix}\cos(\theta_P) & \sin(\theta_P)\\ \sin(\theta_P) & -\cos(\theta_P)\end{pmatrix}}_{M}\begin{pmatrix}V_x\\V_y\end{pmatrix}, \quad (1.15)$$

avec

$$B_0(r, R_0, z) = k \int_0^\infty P \cos(kR_0P)a(P)J_0(kPR)e^{-\frac{ikP^2z}{2}}dP,$$
$$B_1(r, R_0, z) = k \int_0^\infty P \sin(kR_0P)a(P)J_1(kPR)e^{-\frac{ikP^2z}{2}}dP,$$

où J_0 et J_1 sont les fonctions de Bessel de première espèce, d'ordre 0 et 1, $a(P)$ est la transformée de Fourier du champ électrique du rayon lumineux entrant dans la pupille, $k \in \mathbb{R}$ est une caractéristique du cristal. $\begin{pmatrix} V_x & V_y \end{pmatrix}^T$ représente la polarisation de l'onde lumineuse en entrée, la polarisation décrivant l'orientation des oscillations de l'onde.

L'équation (1.15) nous montre que la première composante, B_0, possède à la sortie la même polarisation que celle d'entrée. Il s'agit de la composante correspondant au "Fondamental", présentée à gauche sur la figure 1.16. A contrario, la polarisation de la deuxième composante, B_1, appelée "Vortex", au milieu sur la figure 1.16, est modifiée par la matrice M.

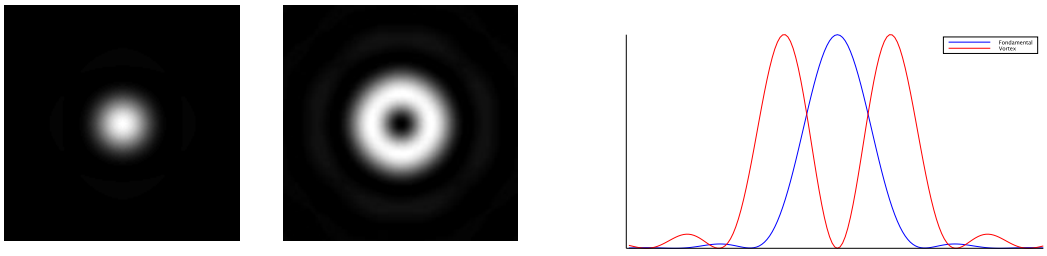

Composante fondamentale | Composante vortex | Profils verticaux

Figure 1.16: Représentation de la composante "Fondamental" (B_0) à gauche, de la composante "Vortex" (B_1) au milieu et comparaison de leurs profils horizontaux à droite. Le fondamental est très similaire à la tache d'Airy (figure 1.4) alors que le Vortex est assez atypique, contenant un trou au milieu. On peut remarquer que la distance entre les deux pics du Vortex est plus petite que la distance entre les deux zéros qui délimitent le lobe principal du fondamental, permettant donc a priori une détection d'objets plus petits.

Il est possible, grâce à cette différence de polarisation entre les deux composantes, de les séparer mais aussi de les mixer, de différentes manières, dépendant de $\begin{pmatrix} V_x & V_y \end{pmatrix}^T$ et de M, créant des distributions lumineuses très différentes ; on parle de modelage de faisceau. Sur la figure 1.17 sont représentées les distributions obtenues grâce à différentes polarisations en entrée et en sortie ; cette liste n'est pas exhaustive.

Remarque. On peut remarquer que la forme d'anneau utilisée pour le faisceau de déplétion du STED (figure 1.6) pourrait être obtenue grâce à la diffraction conique, en utilisant une polarisation de sortie, par exemple, laissant passer uniquement la composante Vortex, dont la forme est très similaire à celle du faisceau STED.

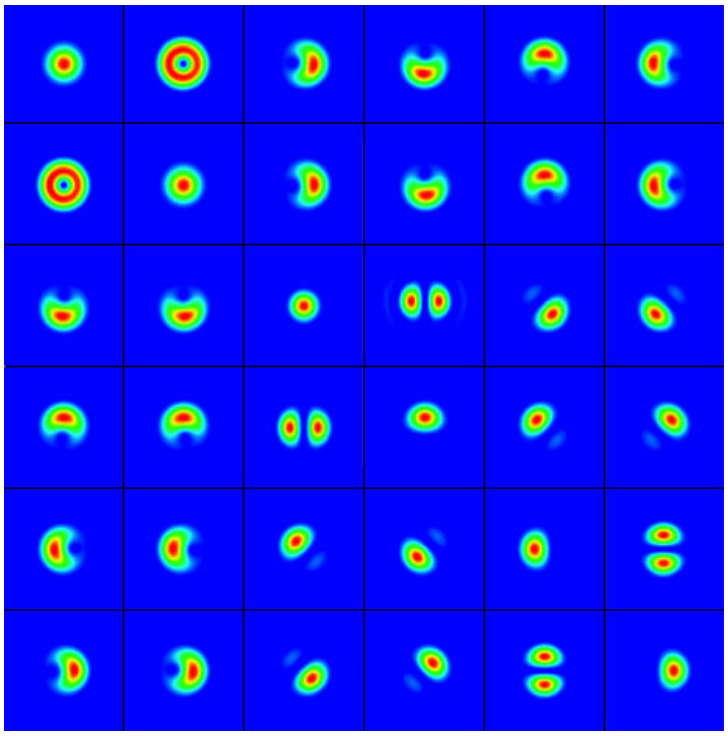

Figure 1.17: Exemples de distributions lumineuses obtenues par la diffraction conique ; ces dernières sont générées en changeant les polarisations d'entrée et de sortie du faisceau laser. On remarque que les deux premières images, en haut à gauche, correspondent aux composantes Fondamentale et Vortex. On peut voir également que de nombreuses formes sont similaires à une rotation près ; on peut en effet les produire avec n'importe quel angle d'inclinaison, en choisissant les polarisations correspondantes.

Dans le système Bioaxial [22], qui est celui utilisé pour les données réelles et simulées sur des images d'échantillon biologique (obtenues avec un microscope à fluorescence par exemple), plusieurs demi-lunes, avec des orientations différentes, sont projetées sur l'échantillon au cours de l'acquisition. Il s'agit de celles représentées sur la figure 1.18, constituées de deux lobes et symétriques. Il est clair que, spatialement, le creux entre les deux lobes est intéressant car ne renverra, en théorie, aucun photon

sur un fond noir ; dans le domaine de Fourier, les coefficients des fréquences en-dessous mais proches de f_{max} ont des valeurs plus élevées que la tache d'Airy, qui peuvent permettre de mieux capturer les composantes fréquentielles de cette zone, comme le montre le profil sur la figure 1.19. De plus il a été montré, par exemple par Soskin [111], que le zéro du vortex, et donc des demi-lunes (qui utilisent le zéro de la composante vortex puisqu'elles sont obtenues par la formule (1.15)), est stable : même dans des conditions non optimales (élément optique imparfait, changements de température par exemple), la forme singulière du vortex est conservée.

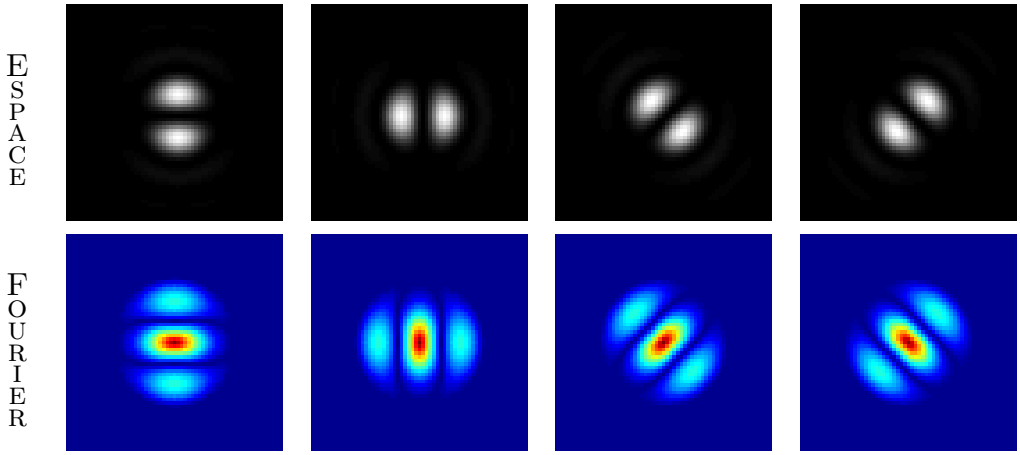

Figure 1.18: Représentation, dans le domaine spatial sur la première ligne et dans celui de Fourier sur la deuxième (représentation du module), des quatre demi-lunes (dont les orientations sont $\{0, \pi/2, \pi/4, -\pi/4\}$), générées par un modelage du faisceau laser et utilisées par le système BioAxial. On peut voir que la représentation dans le domaine de Fourier est assez atypique avec deux lobes autour du centre, orientés dans la même direction que la demi-lune. Le nombre de demi-lunes et leurs angles ont été choisis dans le système Bioaxial de manière à bien couvrir le domaine de Fourier en les sommant. Sur la figure 1.19, une comparaison de profil avec la tache d'Airy est présentée.

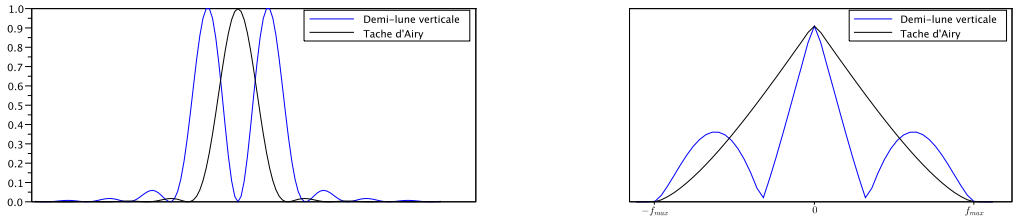

Domaine spatial Domaine fréquentiel

Figure 1.19: Comparaison des profils horizontaux de la tache d'Airy et de la deuxième demi-lune de la figure 1.18 dans les domaines spatial et fréquentiel. La représentation spatiale permet de voir que, à une même résolution, la distribution est plus grosse que la tache d'Airy, mais son zéro particulier au centre permet de détecter une absence de fluorophore. Leur représentation dans le domaine de Fourier montre que les images sont toutes deux à bande limitée, de fréquence maximale f_{max} ; les demi-lunes présentent cependant des coefficients fréquentiels d'énergie plus élevée autour de f_{max}. D'après la Formule (1.5), on peut donc espérer capturer les composantes fréquentielles de l'échantillon entre f_{max} et $2f_{max}$ plus précisément.

1.5.2 Estimateurs MAP et E-LSE pour le système BioAxial

Les deux modèles de la section précédente ont été adaptés à la super-résolution pour un système ISM, l'estimateur MAP étant celui donné par (1.11)

$$x_{MAP}^{SR} = \underset{\substack{x\in\mathbb{R}_+^{\Omega} \\ \mathrm{supp}(\hat{x})\in\mathcal{B}(0,kf_{max})}}{\operatorname{argmin}} \sum_{i<|\Omega'|} (Hx)_i - y_i \log((Hx)_i)$$

et l'estimateur E-LSE

$$x_{E-LSE} = \frac{\displaystyle\int_C e^{-E_y(x)} x dx}{\displaystyle\int_C e^{-E_y(x)} dx} \text{ avec } C = \left\{ x \in \mathbb{R}^{\Omega} \,\middle|\, x = \sum_{e=1}^{N_e} \lambda_e \delta_{p_e} \,, \lambda_e \in \mathbb{R}_+, p_e \in \Omega \right\},$$

c'est-à-dire que l'image super-résolue est supposée appartenir à C, s'écrivant donc comme $x = \sum_e \lambda_e \delta_{p_e}$.

Les y_i représentent, dans le cas d'une méthode ISM, les images obtenues à chaque point de scan avec potentiellement une illumination particulière, créée par exemple par modelage de faisceau. Ces images sont mesurées sur une caméra, et ne contiennent, en théorie, pas de structures de taille plus petite que d définie dans (1.1). L'ensemble de définition Ω' est alors de taille $n \times m \times S$ où n et m sont le nombre de pixels constituant l'image dans chaque direction et S est le nombre de positions de

scan. L'opérateur H modélise les différentes étapes permettant, à partir d'une image discrète, ici x, super-résolue, c'est-à-dire représentée sur une grille plus fine que les images mesurées, de calculer les S images correspondant aux mêmes paramètres que chacune des images mesurées constituant y_i (même taille $n \times m$, même illumination projetée, même position laser).

L'algorithme de Nesterov pour calculer l'estimateur MAP est aujourd'hui l'algorithme de reconstruction implémenté sur le système BioAxial [22] et a été utilisé pour des études de phénomènes biologiques dans [43][93][91]. Son implémentation en code C calcule 50 itérations sur une zone 10µm×10µm en environ 30 secondes. Comme dans le cas du MAP en déconvolution sous contrainte de positivité, le calcul du gradient de l'énergie nécessite uniquement le calcul de la transposée de l'opérateur H, obtenu en transposant chacune des opérations le constituant. Dans le cas de la déconvolution, la projection sur l'ensemble des images positives correspondait à un simple seuillage. Dans le cas de la super-résolution, comme précisé par la formulation de x^{SR}_{MAP}, la projection est effectuée sur l'ensemble des images positives ($x \in \mathbb{R}^{\Omega}_{+}$) et à bande limitée ($x|\text{supp}(\widehat{x}) \in \mathcal{B}(0, kf_{max})$) (afin d'éviter le *night sky* en particulier). Le chapitre 6 présente la méthode *Dual Backward*, choisie après étude de plusieurs méthodes proposées par Combettes et al. [28] ; le schéma proposé converge assurément vers la projection si la solution existe. Sur la figure 1.20, on présente les résultats de cet algorithme sur des chromatides, dont la séparation entre les deux brins est de l'ordre d'une centaine de nanomètres. Cette séparation est invisible sans super-résolution (car plus petit que le pouvoir de résolution défini en (1.1)), comme cela peut être remarqué sur l'image d'un système conventionnel, présenté en comparaison.

Pour l'estimateur E-LSE, le principe est le même que celui présenté ci-avant, la seule différence étant que les positions pour les émetteurs sont choisies sur les pixels de la grille sur-résolue. Chaque chaîne x étant un élément de C, l'écriture de l'énergie peut être simplifiée, donnant

$$\forall x = \sum_{e=1}^{N_e} \lambda_e \delta_{p_e},\ E_y(x) = \sum_{i \in |\Omega'|} \sum_{e=1}^{N_e} (H\lambda_e\delta_{p_e})_i + B - y_i \log\left(\sum_{e=1}^{N_e} (H\lambda_e\delta_{p_e})_i + B\right),$$

où la constante B est un terme modélisant le fond constant dans chaque micro-image, ajouté en particulier pour que le terme dans le logarithme ne s'annule pas. La proposition d'un nouvel état modifiant uniquement un émetteur f (position et/ou intensité), la formulation de l'énergie nous prouve qu'il suffit de calculer l'opérateur

(a) Système conventionnel (b) Système BioAxial (Estimateur MAP) (c) Richardson-Lucy

Figure 1.20: Système Bioaxial avec estimateur MAP : en (a) l'image produite par un système conventionnel, c'est à dire en sommant les images à l'endroit où elles ont été enregistrées sur la caméra en (b) l'image produite par le système BioAxial grâce à l'estimateur MAP sous contrainte de positivité et de transformée de Fourier bornée. L'image (a) est par définition limitée par la diffraction ; on peut remarquer que le système BioAxial a réussi à dépasser cette limite de diffraction, puisque des séparations non visibles en (a) sont apparues. En effet la distance entre les deux brins de la chromatide ($\simeq$ 100 nm) est plus petite que le pouvoir de résolution selon Abbe (1.1) ($\simeq$ 200 nm). En (c), on présente une comparaison avec l'algorithme de Richardson-Lucy, qui effectue une simple déconvolution sur l'image (a) à partir de la PSF calibrée du système ; le nombre d'itérations a été choisi manuellement, pour représenter l'image avec le meilleur effet de déconvolution, mais avant l'apparition du *night sky*. Sans aucun doute, l'utilisation de l'opérateur H avec toutes les micro-images apporte plus d'information et donc de résolution dans l'image finale.

H appliqué à la contribution de cet émetteur dans x, c'est-à-dire $\lambda_f \delta_{p_f}$, pour évaluer sa contribution dans l'énergie. Les détails complets d'implémentation sont présentés dans le chapitre 6. Afin d'accélérer la convergence, les positions initiales des émetteurs sont tirées aléatoirement selon la distribution de probabilité de l'image (normalisée) correspondant au système conventionnel ; ainsi la grande majorité des positions initiales des émetteurs correspond à une zone contenant du signal.

Bien évidemment, pour obtenir des résultats performants avec un système tel que le système Bioaxial, avec l'un ou l'autre des estimateurs, plusieurs calibrations préalables sont indispensables. La première concerne les positions lasers ; ces dernières doivent pouvoir être estimées précisément (quasiment au nanomètre près) afin que l'estimation de l'impact laser soit la plus juste possible. Généralement, le balayage se fait au moyen de miroirs galvanométriques contrôlés électriquement par des changements de voltages. Il faut donc connaître précisément, par une relation affine ou

plus complexe, l'équivalence entre ces voltages envoyés aux miroirs et le point d'impact sur la caméra. Une autre information très importante à connaître est la forme exacte des illuminations projetées sur l'échantillon biologique. En effet, bien que les illuminations, les demi-lunes ici, soient assez proches visuellement de celles créées grâce aux équations présentées ci-avant, utiliser leurs définitions théoriques n'est pas vraiment satisfaisant, car pas assez précis. Sur la figure 1.21, on présente une comparaison entre une demi-lune réelle et une théorique, les formes sont très proches, mais on peut voir que les deux lobes peuvent avoir une intensité différente et que la forme n'est pas tout à fait symétrique ; parfois l'angle n'est pas exactement celui souhaité (en particulier pour les demi-lunes à 45°) etc. Cette calibration peut être effectuée, par exemple, en déconvoluant les illuminations obtenues à partir d'un échantillon de billes de rayon plus petit que la limite d'Abbe d définie par (1.1). Elle peut également permettre de définir la PSF réelle du système.

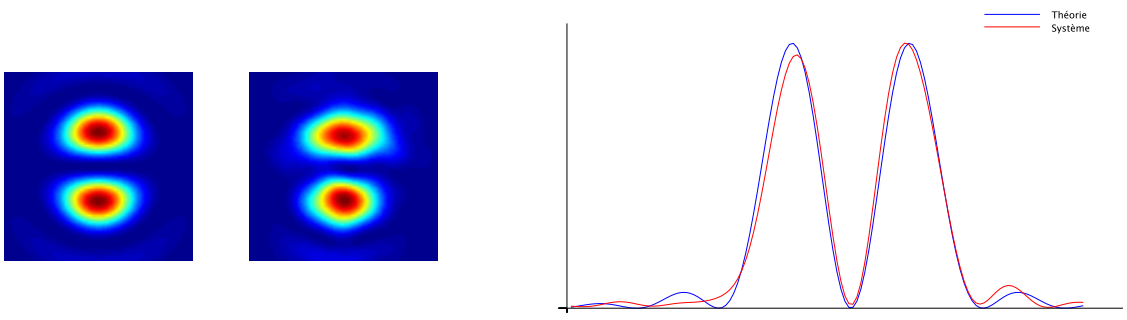

(a) Demi-lune théorique

(b) Demi-lune obtenue en pratique

(c) Cross-section sur les lobes des deux demi-lunes

Figure 1.21: Comparaison entre une demi-lune théorique et une demi-lune obtenue par calibration. On peut remarquer visuellement que les formes sont assez proches, mais la symétrie de la demi-lune calibrée n'est pas parfaite (contrairement à l'illumination théorique), ses lobes sont un peu plus alongés. C'est pourquoi il est important d'utiliser les illuminations réelles (et non les théoriques) dans le calcul de l'opérateur H, modélisant les opérations composant une acquisition obtenue par un microscope à balayage laser, afin d'utiliser des paramètres les plus proches possible des micro-images mesurées.

La figure 1.22 présente les résultats des deux estimateurs, MAP et E-LSE, sur des images réelles de chromosomes, sur lesquelles a été simulé le système BioAxial, avec les 4 demi-lunes de la figure 1.18 projetées en chaque point du scan. La forme en X bien connue pour représenter les chromosomes apparaît clairement sur la reconstruction de l'estimateur E-LSE, tandis que l'estimateur MAP est incapable de trouver la séparation entre les chromatides. Les résultats sont très encourageants pour le E-LSE, même si les zones traitées doivent être d'assez petite surface afin d'obtenir le résultat en un temps raisonnable. L'acquisition de cartes Intel phi a permis de paralléliser les calculs (en particulier le calcul des chaînes qui sont totalement indépendantes) et réduire ce temps, mais une implémentation en GPU (par exemple) est maintenant nécessaire pour rendre l'algorithme industrialisable. Un autre avantage de cet algorithme, qui n'est pas présenté ici mais dans le chapitre 6, est que l'estimateur E-LSE reconstruit un fond constant noir correctement, alors que le résultat de l'estimateur MAP n'est pas constant mais constitué d'artefacts. Ces artefacts ont un niveau de signal beaucoup plus faible que le signal étudié, et ne sont en fait visibles que lorsque les niveaux de gris de l'image sont saturés. Ils ne gênent donc pas la visualisation mais peuvent être problématiques si l'image résultat est ensuite utilisée pour une autre application, car peuvent mener à la conclusion que le fond n'est pas constant mais constitué de petites particules.

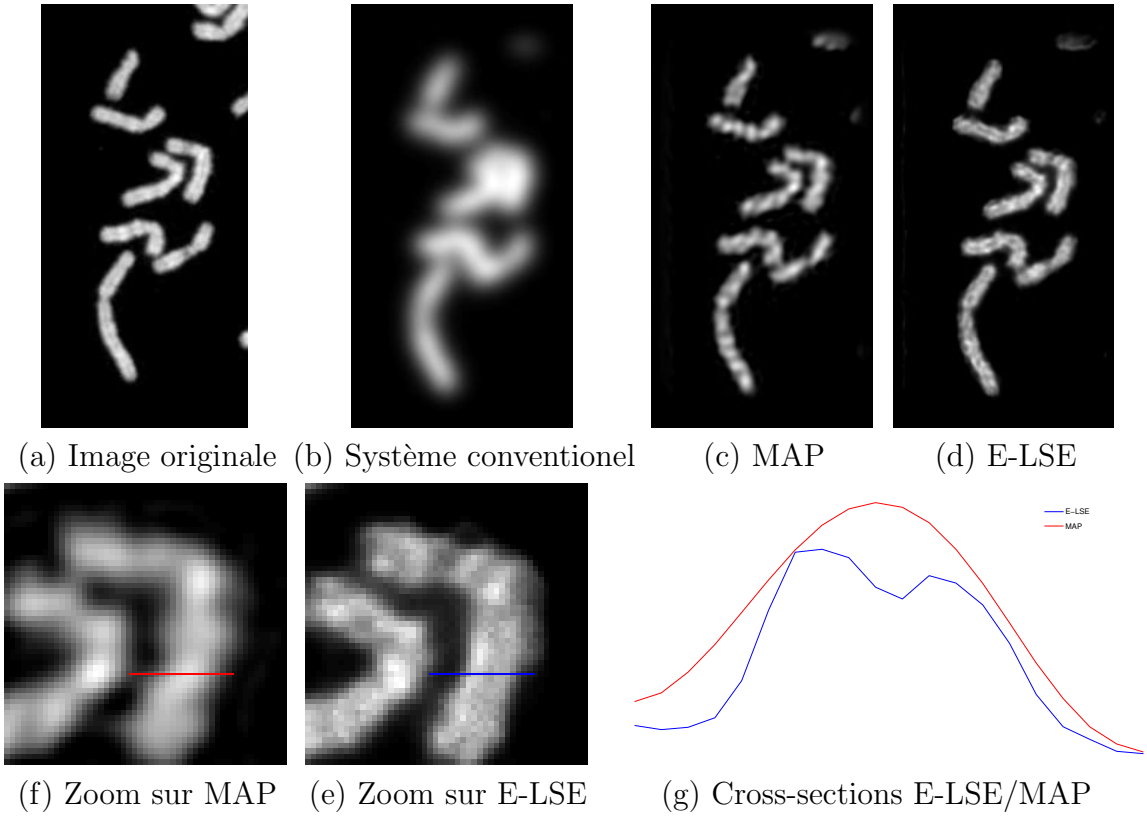

(a) Image originale (b) Système conventionel (c) MAP (d) E-LSE

(f) Zoom sur MAP (e) Zoom sur E-LSE (g) Cross-sections E-LSE/MAP

Figure 1.22: Comparaison des estimateurs MAP (c) et E-LSE (d) sur une image de chromosomes (a). L'image est une image réelle ; on a simulé le système BioAxial, consistant en un scan avec les 4 demi-lunes représentées sur la figure 1.18. En (b) l'image conventionnelle, c'est-à-dire l'image de la somme de toutes les micro-images à l'endroit où elles ont été enregistrées sur la caméra (et donc à la résolution de la caméra), zoomée, est présentée pour comparaison (b). Des zooms et une cross-section sont présentées en (e)-(f)-(g). La forme originale en X des chromosomes n'est pas du tout reconstruite par l'estimateur MAP, qui de plus crée une texture oscillante le long des chromosomes ; au contraire, l'estimateur E-LSE, même s'il ne retrouve pas complètement la structure des chromosomes laisse apparaître leur forme originale, comme le montrent le zoom et la cross-section.

La suite de cette introduction est dédiée au résumé et contribution des différents chapitres qui composent cette thèse. Des premiers résultats ont été présentés en mai 2016 au cours de la conférence IPMS - Inverse Problems : Modeling and Simulation - pendant un symposium sur le sujet “Inverse Problems in Computer Vision”.

Chapitre 2 Dans ce chapitre, nous présentons le phénomène de diffraction amenant à la limite de résolution de Abbe. Nous revenons en détail sur la méthode SIM, les différents calculs et estimations, et nous présentons quelques simulations. Il s'agit d'une des techniques de super-résolution les plus rapides car elle opère sur tout le champ à imager, mais le modèle est très sensible aux aberrations locales et donc très difficile à calibrer. Nous nous intéressons ensuite aux techniques ISM qui scannent progressivement toute la zone à imager, projetant localement une distribution lumineuse au moyen d'un laser ; chaque point de scan produit alors une mesure (une intensité globale ou une image) et l'image super-résolue est ensuite reconstruite grâce aux données récoltées sur l'ensemble des points de scan. Nous proposons une nouvelle formulation du problème ISM, en 4 dimensions, dans l'espace de Fourier, permettant de comparer la résolution théorique effective des différentes méthodes de reconstruction linéaires.

Chapitre 3 Dans ce chapitre, nous proposons un schéma de discrétisation précis pour les systèmes d'imagerie utilisant un microscope à balayage laser. Toutes les méthodes ISM peuvent s'écrire comme des opérateurs linéaires sur l'image super-résolue, dont les étapes sont : multiplication/convolution/sous-échantillonnage. Bien que la modélisation dérive de l'écriture du problème, il est assez rare d'en trouver une description détaillée. Pour comprendre les subtilités associées à la discrétisation de l'opérateur ISM, nous revenons sur la définition mathématique de l'échantillonnage, créant le lien entre l'image continue et sa discrétisée mais aussi entre leurs transformées de Fourier respectives. Toutes ces relations doivent être maîtrisées afin de définir les outils permettant d'effectuer correctement les opérations basiques contenues dans l'opérateur et donc permettre sa discrétisation exacte. Les questions d'optimisation de pas d'échantillonnage et de quantités de données générées par les méthodes ISM sont également traitées. Cette étude à notamment permis de proposer un nouveau schéma de scan, adapté à la forme des distributions lumineuses projetées, ce qui permet de diminuer sensiblement le temps d'acquisition sans sacrifier la résolution finale. A la fin du chapitre, nous nous intéressons aux distributions lumineuses singulières qui peuvent être produites grâce à la diffraction conique et en particulier à leur avantage pour les méthodes ISM.

Dans les deux chapitres suivants, nous avons décidé d'étudier un problème inverse un peu plus simple, la déconvolution, dans le cas de contraintes très faibles sur la solution : uniquement sa positivité.

Chapitre 4 La déconvolution sous contrainte de positivité par maximisation de la densité a posteriori, définissant l'estimateur MAP, peut être vue comme la minimisation d'une énergie dans un cadre bayésien et peut être calculée grâce à l'algorithme itératif de Nesterov accéléré. Nous mettons en évidence que l'estimateur final, à convergence, présente un artefact appelé *night sky*, caractérisé par une discontinuité totale des structures. Cet artefact est également visible sur le résultat de la méthode de Richardson-Lucy, lorsqu'un nombre d'itérations important est utilisé. Ces algorithmes sont itératifs, faisant apparaître progressivement le *night sky*. L'arrêt des itérations au cours de l'algorithme permet donc d'obtenir un résultat convenable. Ceci nécessite, dans l'hypothèse d'un traitement automatique, de définir un critère d'arrêt adapté. Dans le cas du bruit Gaussien, nous introduisons un critère basé sur les statistiques du bruit pour stopper les itérations, créant un estimé sans *night sky*.

Chapitre 5 Pour éviter les artefacts de *night sky* de l'estimateur MAP, nous nous intéressons à des estimateurs différents et en particulier le LSE, pour Least-Square Error, consistant à minimiser l'erreur quadratique moyenne a posteriori. Nous adaptons cet estimateur à la déconvolution, sous seule contrainte de positivité et nous introduisons un nouvel estimateur, le E-LSE, pour Emitters-Least-Square Error, adaptation du LSE aux images parcimonieuses. Le calcul de ces estimateurs exige un calcul d'intégrales en très grande dimension, ce qui est néanmoins possible en utilisant des méthodes MCMC avec un algorithme de Metropolis-Hastings, adapté à la formulation de chacun des estimateurs. En raison de la non-convexité du domaine d'intégration du E-LSE, la convergence est plus délicate et les chaînes peuvent se figer dans une configuration correspondant à un minimum local, ce qui nécessite le recours à un grand nombre de chaînes. Malheureusement, dans le cas de la déconvolution, ces deux estimateurs n'évitent pas complètement le phénomène de *night sky*. Une pondération de l'énergie permet néanmoins d'y remédier mais les résultats sont alors sensiblement équivalents à ceux du MAP non convergé, stoppé par le critère proposé dans le chapitre 4 par exemple.

Chapitre 6 Dans ce dernier chapitre, nous étudions l'adaptation des estimateurs MAP et E-LSE au problème inverse de la super-résolution, dans le cas des méthodes ISM. En raison d'un faible flux de photons utilisé en pratique, uniquement le bruit de Poisson est considéré et nous nous intéressons à des échantillons très parcimonieux.

Pour éviter le *night sky*, une contrainte supplémentaire est ajoutée lors du calcul de l'estimateur MAP : la solution doit être à bande limitée (avec une fréquence de coupure supérieure à celle imposée par l'optique). L'algorithme utilisé est classique (gradient projeté, accélération de Nesterov), mais l'ajout d'une contrainte supplémentaire (bande limitée) nécessite une étape non triviale de projection sur l'intersection convexe des contraintes, pour laquelle nous proposons une solution par la méthode *Dual forward-backward splitting*. Pour le E-LSE, aucune contrainte supplémentaire ne se révèle nécessaire, l'image reconstruite ne présentant pas les artefacts de *night sky* observés en déconvolution, sûrement grâce à la redondance d'informations, très présente dans les méthodes ISM. Nous présentons également des techniques mises en place pour accélérer le calcul de l'estimateur et le moyen d'éviter les effets de bord (accumulation des émetteurs au bord du domaine). Nous présentons plusieurs simulations pour lesquelles la reconstruction obtenue par E-LSE surpasse en qualité et en résolution celle du MAP.

Chapter 2

Super-Resolution Microscopy

Contents

In this Chapter, we present the diffraction effect more precisely. This physical phenomenon happens each time the light goes through an obstacle or aperture and explains that a fluorescence microscope cannot resolve too small structures. This

limitation can also be observed in the Fourier domain: the output signals are band-limited, meaning that their Fourier Transform equals zero beyond a cut-off frequency noted f_{max}, depending on the emission wavelength, supposed monochromatic.

The impulse response of the microscope is called Point Spread Function (PSF) and noted φ. It corresponds to the imaging response of a point source by the optical device. Its representation in Fourier domain, $\widehat{\varphi}$, is called the Optical Transfer Function (OTF).

For a long time now, scientists have tried to go beyond this f_{max} limit. We here present two families of well-known super-resolution techniques, that both enable to retrieve frequency components until $2f_{max}$. The first one, called Structured Illumination Microscopy (SIM), is a wide-field technique because it operates on the whole sample. The main idea is to project a grid on the sample; the specific formulation in the Fourier space of this grid theoretically enables super-resolution. The second technique is a more local technique called Illumination Structured Microscopy (ISM) where the sample is scanned with a particular distribution of light; the acquisition is performed gradually, each scanned area after another, and the reconstruction is computed afterwards on the whole data.

2.1 Diffraction phenomenon and notion of resolution

2.1.1 General definitions

Let us recall the definition of the convolution in $\mathbb{R}^n$, between two functions f and g defined in $\mathbb{R}^n$, as

$$\forall x \in \mathbb{R}^n,\ (f * g)(x) = \int_{\mathbb{R}^n} f(x-t)g(t)dt = \int_{\mathbb{R}^n} g(x-t)f(t)dt.$$

Given $f \in L^1(\mathbb{R}^n)$ ($\int_{\mathbb{R}^n} |f(x)|dx < \infty$), its Fourier transform is defined as

$$\forall \xi \in \mathbb{R}^n,\ \mathcal{F}(f) : \xi \longmapsto \int_{\mathbb{R}^n} f(x)e^{-i\langle \xi, x\rangle}dx,$$

also noted $\hat{f}(\xi)$. The inverse Fourier transform of f, defined if $\hat{f} \in L^1(\mathbb{R}^n)$, is then

$$\forall x \in \mathbb{R}^n,\ \mathcal{F}^{-1}(\hat{f}) : x \longmapsto \frac{1}{(2\pi)^n} \int_{\mathbb{R}^n} \hat{f}(\xi)e^{i\langle \xi, x\rangle}d\xi.$$

A function f is said to be band-limited if there exists a δ such that

$$\mathrm{supp}(\hat{f}) = \left[-\frac{\pi}{\delta}, \frac{\pi}{\delta}\right]^n.$$

For $f \in L^1(\mathbb{R}^n)$, $g \in L^1(\mathbb{R}^n)$ we recall that

$$\begin{aligned}
\forall (a,b) \in \mathbb{R}^2,\ \mathcal{F}(af+bg)(\xi) &= a\mathcal{F}(f)(\xi) + b\mathcal{F}(g)(\xi),\\
\forall a \in \mathbb{R},\ \mathcal{F}(f(a\cdot))(\xi) &= \frac{1}{|a|^n}\mathcal{F}(f)\left(\frac{\xi}{a}\right),\\
\forall t \in \mathbb{R}^n,\ \mathcal{F}(f(\cdot+t))(\xi) &= \mathcal{F}(f)(\xi)e^{i\langle \xi, t\rangle},\\
\forall \mu \in \mathbb{R}^n,\ \mathcal{F}(f(\cdot)e^{-i\langle \cdot, \mu\rangle})(\xi) &= \mathcal{F}(f)(\xi+\mu), \qquad (2.1)\\
\mathcal{F}(f*g)(\xi) &= \mathcal{F}(f)(\xi) \times \mathcal{F}(g)(\xi). \qquad (2.2)
\end{aligned}$$

The Parseval identity specifies that for $f \in L^2(R^n)$ we have

$$\int_{\mathbb{R}^n} |f(x)|^2\, dx = \frac{1}{(2\pi)^n}\int_{\mathbb{R}^n} \left|\hat{f}(\xi)\right|^2 d\xi. \qquad (2.3)$$

Thanks to the distribution theory, the notion of Fourier transform can be extended, in particular to the space of tempered distributions, $\mathcal{S}$', dual of $\mathcal{S}$ where $\mathcal{S}$ is defined as

$$\mathcal{S} = \left\{ \varphi : \mathbb{R}^n \longrightarrow \mathbb{C} \,\middle|\, \varphi \in C^\infty(\mathbb{R}^n), \forall (\alpha,\beta) \in \mathbb{N}^2 \ \sup_{x\in\mathbb{R}^n} |x^\alpha \partial^\beta \varphi(x)| < \infty \right\}.$$

Let us remind that the Fourier transform in $\mathcal{S}'$ is defined as

$$\forall T \in \mathcal{S}', \forall \varphi \in \mathcal{S}, \left\langle \widehat{T}, \varphi \right\rangle = \langle T, \hat{\varphi} \rangle .$$

This space enables to introduce the Dirac distribution in a, δ_a, element of $\mathcal{S}'$, defined for each $\varphi \in \mathcal{S}$ by $< \delta_a, \varphi >= \varphi(a)$. The convolution of any distribution $T \in \mathcal{S}'$ by δ_a corresponds to a translation of T by a, that is, noting τ_a the translation function $\tau_a : x \mapsto x - a$,

$$\forall T \in \mathcal{S}',\ \forall \varphi \in \mathcal{S},\ \langle T * \delta_a, \varphi\rangle = \langle \tau_a T, \varphi\rangle.$$

We can then notice that δ_0 is the identity element of the convolution.

Moreover, the Fourier transform of a complex exponential function is a Dirac distribution. Indeed let us consider $T \in \mathcal{S}'$ defined for $x \in \mathbb{R}^n$, as $T : x \longmapsto e^{i\langle \omega, x\rangle}$,

$\omega \in \mathbb{R}^n$ then $\forall \varphi \in \mathcal{S}, \left\langle \widehat{T}, \varphi \right\rangle = (2\pi)^n \langle \delta_\omega, \varphi \rangle$.

In the following, most of the time, for ease of reading, we will improperly use a functional notation for distributions, writing for example $\int \varphi(x)\delta_a(x)dx$ instead of $\langle \delta_a, \varphi \rangle$.

2.1.2 Fluorophores

In the case of fluorescence microscopy, fluorescent compounds called fluorophores are used to label a specimen. The fluorophores are chemical composites made of between 20 and 100 atoms and are usually described by their emission and excitation wavelength, noted λ_{em} and λ_{ex}. A fluorophore absorbs light energy around its excitation wavelength and emits light at its emission wavelength. The time between absorption and emission depends on the fluorophore but it is usually quantified in picoseconds. This emission of light is then recorded by a captor and enables to create the image. A filter that blocks the excitation wavelength is used so that the collected light only corresponds to the emission. The quantity of light emitted by a fluorophore is fading progressively when exciting it several times, leading to the phenomenon of photo-bleaching: the fluorophore cannot emit light anymore. In that case, it is no longer possible to create an image since no light is collected.

The range of excitation wavelength in nanometers of most fluorophores is around $[400, 750]$. The emission is always a bit higher than the excitation (5 to 10%) but we will consider that $\lambda_{em} \simeq \lambda_{ex}$ in the following. It will make easier the explanation in Fourier of both SIM and ISM methods in the Fourier domain. However remarks 3 and 5 reconsider the difference between those two wavelengths and explain its influence in the case of SIM and ISM.

A well known fluorophore used in fluorescence microscopy is GFP, for Green Fluorescent Protein, that was first discovered in 1962 [105] and has been used by lots of biologists since then (see [124] for instance). This protein, that comes from a jellyfish called Aequorea victoria, presents two excitation peaks (at 395 nanometers and 475 nanometers) and is really less phototoxic than other proteins, making the analysis of live cells possible. Numerous derivatives of GFP were developed in the following years, for instance in [53], a mutation of GFP was proposed, so that it presents only on peak, at 488, making the protein more stable and more adapted to filters used by fluorescence microscopes.

2.1.3 Diffraction phenomenon

The two following parts, the description in space and in Fourier domain of an optical device using circular pupil, are inspired by [44].

A convolution in the space domain

Under the hypothesis that the observation distance (located on the focal plan) is quite far, the diffraction phenomenon can be modeled using Fraunhofer diffraction. For a monochromatic and incoherent light, the representation of the real scene u, $\tilde{u}$, created by a device of focal length f, aperture $\mathcal{A}$ and using wavelength λ, is modeled as a convolution

$$\tilde{u} = K * u, \quad \text{with } K = |\mathcal{U}_0|^2, \tag{2.4}$$

$\mathcal{U}_0$ being the field distribution on $\mathcal{A}$ at focal plan, that is at $z = 0$. In the case of a circular aperture of radius R, we have

$$\forall z \in \mathbb{R},\ \forall x \in \mathbb{R}^2,\ \mathcal{U}_z(x) = \frac{ke^{ikf}}{if} e^{i\frac{k}{2f}|x|^2} \int_{\mathcal{B}(0,R)} e^{-\frac{ikz}{2f^2}|\xi|^2} e^{-\frac{i}{\lambda f}\langle x,\xi\rangle} d\xi, \tag{2.5}$$

with $\mathcal{B}(0,R) = \{\xi \in \mathbb{R}^2 |\, |\xi| < R\}$ and $k = 2\pi/\lambda$ the wave number.

Setting $z = 0$, introducing polar coordinates for x, (r,θ), and ξ, (ρ,ϕ) and the function c_R defined by

$$c_R(r) = \begin{cases} 1 \text{ if } (r < R) \\ 0 \text{ otherwise} \end{cases}$$

leads to

$$\mathcal{U}_0(r) = \frac{e^{ikf}}{i\lambda f} e^{i\frac{k}{2f}r} \mathcal{F}\left(c_R(\rho)\right)\left(\frac{r}{\lambda f}\right).$$

The Fourier transform of the function c_R is known: it is a Bessel function J_1. We have $\mathcal{F}\left(c_R(r)\right)(\rho) = RJ_1(2\pi R\rho)/\rho$. And then using Fourier Transform properties it comes

$$\mathcal{U}_0(r) = \frac{e^{ikf}}{i\lambda f} e^{i\frac{k}{2f}r} \frac{J_1\left(2\pi R\left(\frac{r}{\lambda f}\right)\right)}{\frac{r}{\lambda f}} R.$$

Finally, we can compute

$$|\mathcal{U}_0(r)|^2 = \frac{1}{(\lambda f)^2}\left(\frac{J_1\left(2\pi R\left(\frac{r}{\lambda f}\right)\right)}{\frac{r}{\lambda f}} R\right)^2 = \left(\frac{\pi R^2}{\lambda f}\right)^2 \left(2\frac{J_1(2\pi R\left(\frac{r}{\lambda f}\right))}{2\pi R\left(\frac{r}{\lambda f}\right)}\right)^2,$$

and what is called the Airy disk K is given, according to the diameter of the pupil $D = 2R$ by

$$K(x) = C \times \left(2\frac{J_1(y)}{y}\right)^2, \; y = \pi D\frac{|x|}{\lambda f}, \; C \text{ constant.}$$

Its representation in two dimensions and its radial section can be seen in Figure 2.1. We call r_a the first zero of this function, whose value is a function of λ, R and f

$$r_a \simeq 1.22\frac{\lambda f}{D}$$

and we can notice that most of the energy (almost 95%) of the spot is located between $-r_a$ and r_a.

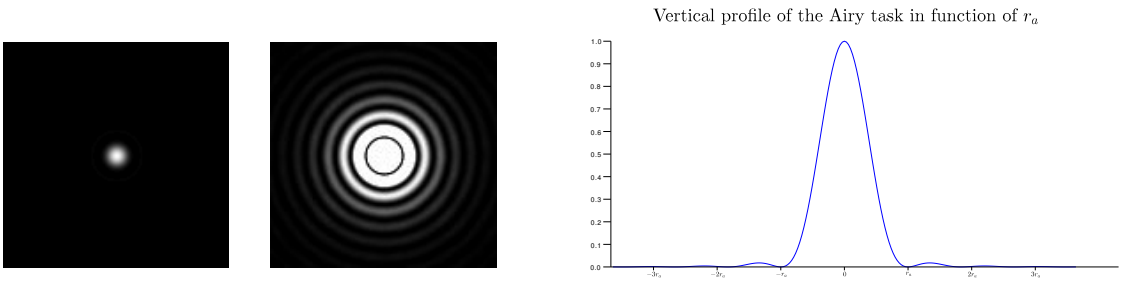

(a) (b) (c)

Figure 2.1: Representation of the Airy spot: (a) normalized Airy disk, (b) saturation of the disk to show all the rings. On the bottom (c) a radial section of the disk shows that more than 94% of the energy of the disk is contained in the center and first ring.

In the following, if no contradictory information is given, φ, the PSF of the optical device, corresponds to K with $\lambda = \lambda_{em}$. In other words, we consider that the aperture of our device is a circle of diameter D. We recall that the PSF is the image of point source by the optical device

An expression of the PSF for any plan $z = c$ (with c a constant) can be obtained taking the square of the absolute value of (2.5) with $z = c$. We present in Figure 2.2 the result for 3 values of z: 0, 400 and 700 nanometers. We can notice that the spot really spreads in the lateral direction when the depth increases.

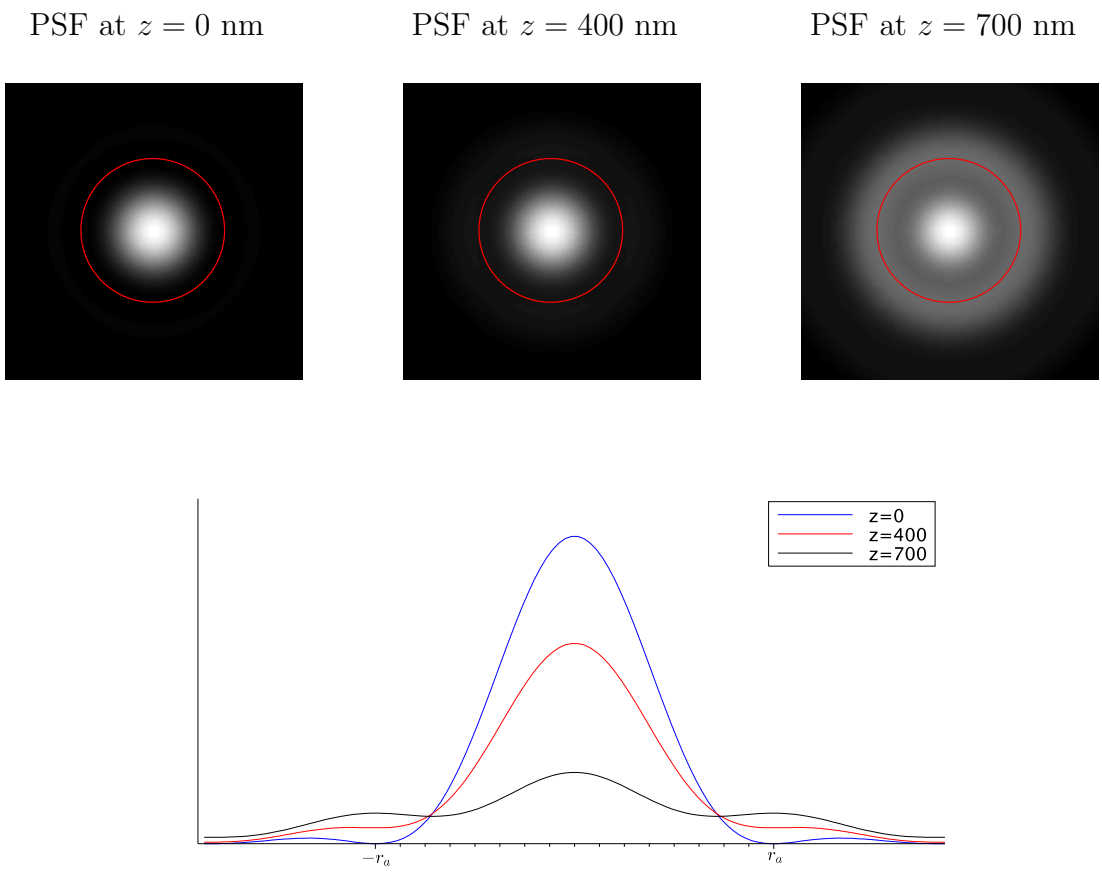

Figure 2.2: Representation of normalized sections (x, y) of the Airy spot modeling the PSF for different values of z (0, 400 and 700 nm) ant their vertical profiles; in red is drawn the circle centered on the middle of the spot and of radius r_a: for the focused spot very few signal is outside the circle, and the most z increases the most signal is spreading, as shown on the plot.

A band limited Fourier transform

A consequence of (2.4) is that the OTF, Fourier transform of the PSF, of an optical system can be obtained, for an Aberration-Free System of pupil function $\mathcal{P}$, by the computation of the ratio between the area of overlapping between two displaced functions $\mathcal{P}$ and the area total of the pupil, meaning

$$OTF = \frac{\text{Area overlap between two pupils } \mathcal{P}}{\text{Total area of the pupil } \mathcal{P}}.$$

This definition enables to understand why the PSF is band limited: when no overlapping between the two pupils, the values of the OTF will be zero. The calcu-

lation for an optical device of focal length f with a circular pupil of radius R and using wavelength λ gives that

$$OTF(\xi) = \begin{cases} C\left(\arccos(\rho) - \rho\sqrt{1-\rho^2}\right) & \text{if } \rho = \frac{\lambda f}{4\pi R}\|\xi\| \leq 1 \\ 0 & \text{otherwise} \end{cases}, \ C \text{ a constant.} \tag{2.6}$$

The representation of the modulus of this function in two dimensions can be seen in Figure 2.3 as well as a plot of the radial section. The highest non zero frequency f_{max} is then defined by

$$\frac{\lambda f}{4\pi R} f_{max} = 1 \Leftrightarrow f_{max} = \frac{4\pi R}{\lambda f}. \tag{2.7}$$

In the following, we will use the notation $\mathcal{B}(0, f_{max})$ for the ball of radius f_{max} centered at frequency 0.

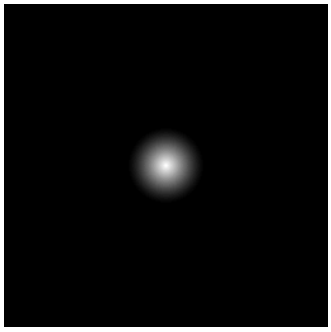

Fourier Transform of the Airy disk

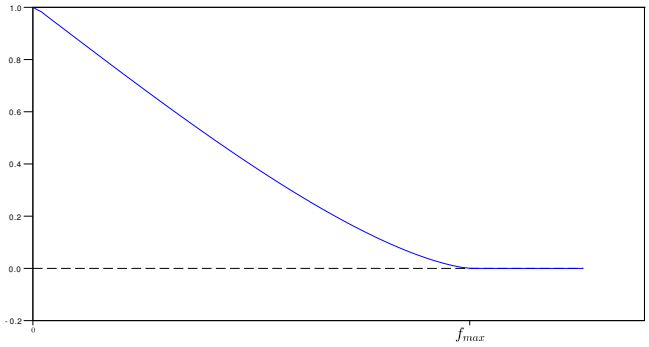

Radial section of the Fourier Transform of the Airy disk

Figure 2.3: Representation of the Airy spot in the Fourier domain: on the left, the image of the absolute value of the Fourier transform of the Airy disk in 2 dimensions, that is, $|OTF|$ as defined in (2.6); on the right the intensity profile of the normalized OTF in function of $\|\xi\|$: the support of the OTF is included in $[-f_{max}, f_{max}]$, with f_{max} the cut-off frequency.

2.1.4 Limit of resolution for a microscope

For a microscope it is more common to use the Numerical Aperture (NA) to characterize the objective. It is defined as a function of n, the index of refraction

and α, the half-angle of the maximal cone of light entering or exiting the lens, by $NA = n \sin \alpha$. For a thin lens the angle α can be approximated with $\tan \alpha = R/f$ giving $\alpha = \arctan(R/f)$ and for small angles we can approximate $\sin \alpha \sim R/f$ and then $NA \sim nR/f$.

Relation (2.7) in the case of microscopy using wavelength λ and using an objective with numerical aperture NA is given by

$$f_{max} = 2\pi \cdot \frac{2NA}{\lambda}.$$

It means that no detail smaller than $\lambda/(2NA)$ can be imaged by an optical device of numerical aperture NA using wavelength λ. This is the definition of resolution proposed by Abbe and so called the Abbe limit [1].

With this formula, we can think about two ways to improve resolution, that is increase f_{max} or equivalently reduce $\lambda/(2NA)$): either reduce λ or increase NA. Concerning λ as said before it cannot be smaller than 400/450 nm. Concerning the numerical aperture, the air objectives have a numerical aperture around 1, and the best ones (oil objectives) around 1.5. The computation of the Abbe limit then gives 130 nm: no detail smaller than 130 nm can be imaged with a standard microscope.

Another vision of resolution has been proposed by Rayleigh and can be seen in Figure 2.4: the resolution of an optical system is the minimal distance of separation between two points. Indeed for two very close sources, the diffraction patterns interfere and when the central peaks overlap, it is impossible to distinguish the two sources. The minimal distance is then the distance between the peak and the first zero of the diffraction patter. In the case of an Airy disk, the Rayleigh criterion is equal to the Airy radius, whose expression using the numerical aperture is given by $r_a \sim 0.61\lambda/NA$.

Of course the gain of resolution in microscopy is not only lateral but also axial, that is, in the z-direction; indeed we gave before the expression of the PSF as a function of z and the biological sample is most of the time a three dimensional function. The Rayleigh criterion can be extended to the z-direction, saying that the z-resolution is defined as the minimal distance between two points (in the z-direction) that the optical system can separate. The definition of this resolution r_z is a function of the numerical aperture, the refractive index and the wavelength given

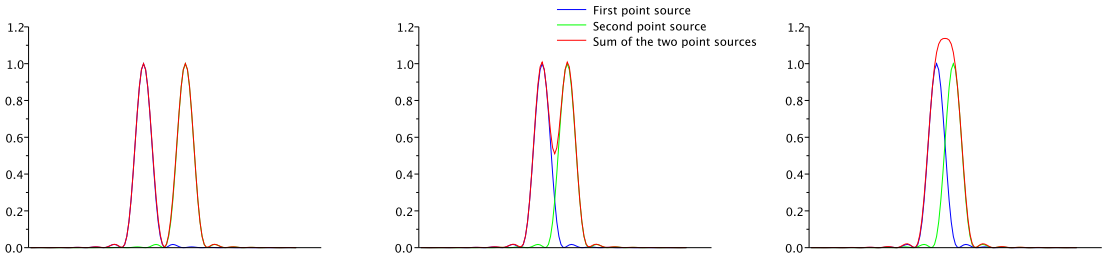

Figure 2.4: Illustration of Rayleigh criteria: the sum of two point sources, whose image by the system is modeled by the Airy disk, is performed in 3 situations. First the sources are completely separated, their sum makes them appear separately with no doubt; secondly, the sources are quite close so that the sum contains both of them at some point but the separation is still visible. On the last image, the sources are so close that the separation is not visible anymore on the sum: the distance between those two is smaller than r_a.

by

$$r_z = \frac{2\lambda n}{NA^2}.$$

This limit can be found computing (2.5) with $|x| = 0$. However, in the following, we will focus on the gain of resolution in the xy-direction.

2.2 Structured Illumination Microscopy

2.2.1 Presentation

The Structured Illumination Microscopy (SIM) technique is a wide-field technique projecting a grid pattern on the whole sample. In 1999 in [55], Heintzmann comes with the idea of using a diffraction grating on the laser beam because of its particular Fourier Transform made of Diracs. The result image is obtained by simple operations (addition/subtraction) on the images taken with a grid with different orientations (three were used in the experiments proposed in this article).

One year later in [46], Gustafsson explains the concept of Structured Illumination Microscopy using the Fourier space. In [48] a more precise mathematical presentation of the problem and an algorithm for processing the data with a Wiener filter are proposed. In this article, we can also see that a real advantage of the SIM technique is that it can also be used to improve the z-resolution.

Other methods than Wiener filters can be used to reconstruct the images; in [78] for example, a Bayesian approach leads to the minimization of an energy. If the SIM is supposed to be limited to a factor of two for retrieving frequencies, in [47], Gustafsson presents a technique of non linear microscopy, called SSIM, for Saturated Structured Illumination Microscopy, and claims that it can theoretically produce "infinite" frequencies. However this technique is quite limited because it requires a large amount of light (in relation to the first S of the name, saturated), leading most of the time to photo-bleaching of the sample.

The following is based on a simplification of [70], article published in 2016 and giving a full algorithm to reconstruct the super-resolved SIM image. In this model and most of the time for the SIM, the noise is assumed to be Gaussian, which is quite rare in microscopy applications; the Poisson assumption is more often used.

2.2.2 Mathematical model

Given $u \in L^1(\mathbb{R}^2)$ a fluorophore density, that is a function from $\mathbb{R}^2$ to $\mathbb{R}^+$, also called sample, illuminated by m a pattern function from $\mathbb{R}^2$ to $\mathbb{R}^+$ and φ the PSF of the optical device, we suppose that the emitted signal arriving on the camera can be written for each 2D-position x of the plan as

$$\forall x \in \mathbb{R}^2, \quad x \longmapsto \big((u(\cdot) \times m(\cdot)) * \varphi(\cdot)\big)(x). \tag{2.8}$$

In the case of SIM, the pattern function is supposed to be a grid modeled as

$$\forall x \in \mathbb{R}^2, \quad m^{i,\theta}(x) = M_0 \left(1 + \alpha \cos(\langle k_\theta, x\rangle + \phi_i)\right), \tag{2.9}$$

where $M_0 \in \mathbb{R}$ is the peak illumination intensity, $k_\theta = (|k|\cos\theta, |k|\sin\theta)$ the illumination frequency vector of orientation θ, α the modulation factor, such that $|\alpha| \leq 1$ and ϕ_i the phase of the pattern.

Let us consider $I_u^{i,\theta}$ a noisy version of the acquisition with grid $m^{i,\theta}$. Under Gaussian noise assumption, (2.8) and (2.9) give

$$\forall x \in \mathbb{R}^2,\ I_u^{i,\theta}(x) = \big(\big(u(\cdot) \times m^{i,\theta}(\cdot)\big) * \varphi(\cdot)\big)(x) + n^{i,\theta}(x),\ n^{i,\theta}(x) \sim \mathcal{N}(0, \sigma^2). \tag{2.10}$$

2.2.3 Fourier transform of the acquired images $I_u^{i,\theta}$

Due to the Fourier transform properties, the Fourier transform of $I_u^{i,\theta}$ defined by (2.10) is given by

$$\forall \xi \in \mathbb{R}^2,\ \widehat{I_u^{i,\theta}}(\xi) = \widehat{u \times m^{i,\theta}}(\xi) \times \widehat{\varphi}(\xi) + \widehat{n^{i,\theta}}(\xi). \tag{2.11}$$

Using that $\forall x \in \mathbb{R}^2,\ \omega \in \mathbb{R},\ \phi \in \mathbb{R}^2,\ \cos(\omega x + \phi) = \frac{1}{2}\left(e^{iwx+\phi} + e^{-(iwx+\phi)}\right)$, we remind that the Fourier transform of a cosine function with a phase is written as

$$\forall \xi \in \mathbb{R}^2,\ \mathcal{F}(\cos(\omega x + \phi))(\xi) = \frac{1}{2} \times (2\pi)^2 \left(e^{i\phi}\delta_\omega(\xi) + e^{-i\phi}\delta_{-\omega}(\xi)\right),$$

which permits to develop $\widehat{u \times m^{i,\theta}}(\xi)$, with $\alpha' = 2\pi^2\alpha$, as

$$\begin{aligned}\widehat{u \times m^{i,\theta}}(\xi) &= M_0\hat{u}(\xi) + M_0\alpha'\left((\hat{u}(\cdot) * \left(\delta_{k_\theta}(\cdot)e^{i\phi_i} + \delta_{-k_\theta}(\cdot)e^{-i\phi_i}\right))(\xi)\right) \\ &= M_0\hat{u}(\xi) + M_0\alpha'\left(\hat{u}(\xi + k_\theta)e^{i\phi_i} + \hat{u}(\xi - k_\theta)e^{-i\phi_i}\right).\end{aligned}$$

Equation (2.11) becomes then

$$\widehat{I_u^{i,\theta}}(\xi) = \left(M_0\hat{u}(\xi) + M_0\alpha'\left(\hat{u}(\xi + k_\theta)e^{i\phi_i} + \hat{u}(\xi - k_\theta)e^{-i\phi_i}\right)\right)\widehat{\varphi}(\xi) + \widehat{n^{i,\theta}}(\xi). \tag{2.12}$$

We remind that the PSF φ is band limited so that

$$\forall\ \xi \quad \text{s.t.} \quad |\xi| > f_{max},\ \widehat{\varphi}(\xi) = 0,$$

meaning that

$$\forall\ \xi \quad \text{s.t.} \quad |\xi| > f_{max},\ \widehat{I_u^{i,\theta}}(\xi) = \widehat{n^{i,\theta}}(\xi). \tag{2.13}$$

However the Fourier transform (2.12) computed in ξ ($|\xi| < f_{max}$) contains frequencies coefficients of the sample u in ξ, $\xi - k_\theta$ and $\xi + k_\theta$. This means that using $m^{i,\theta}$ pattern, we can recover higher frequencies than f_{max}: $f_{max} \pm k_\theta$.

Remark 1. *Equation (2.12) shows, as said before, that with a constant illumination (that is for instance $\alpha = 0$ in (2.9)), we have*

$$\widehat{I_u^{i,\theta}}(\xi) = M_0\hat{u}(\xi)\widehat{\varphi}(\xi) + \widehat{n^{i,\theta}}(\xi),$$

and then $\widehat{I_u^{i,\theta}}$ only depends on the coefficients of $\hat{u}$ contained in $\mathcal{B}(0, f_{max})$.

Concerning the illumination vector k_θ, since the pattern also goes through the optical device, it also is band-limited. We have that $k_\theta \in \mathcal{B}(0, f_{max})$, meaning that in Equation (2.12) $\widehat{I_u^{i,\theta}}(\xi)$ theoretically depends on frequencies of u contained in $\mathcal{B}(0, 2f_{max})$

Remark 2. *To reach frequency $2f_{max}$ in (2.12), one needs that $\xi = |k_\theta| = f_{max}$. However $\varphi(\xi) = \varphi(f_{max}) = 0$, meaning that we cannot get the information corresponding to $2f_{max}$. This is a theoretical value and cannot be exactly reached.*

Remark 3. *The difference between the emission and excitation wavelengths gives that the cut-off frequency of the PSF, f_{max}^{em} is smaller than the cut-off frequency of the grid, f_{max}^{ex}, this means that $|k_\theta|$ can take a value higher than f_{max}^{em} (but smaller than f_{max}^{ex}). Theoretically, the final resolution is then $f_{max}^{em} + f_{max}^{ex}$.*

As shown in Equation (2.13), the frequencies higher than f_{max} are only characterizing the noise; this means that the spectrum of $I_u^{i,\theta}$ in $\mathcal{B}(0, f_{max})$ "mixes" for each frequency (whose absolute value is smaller than f_{max}) its real value and some of the ones created thanks to the special pattern. In [46], Gustafsson shows that it is sufficient to use 3 values of ϕ_i, $\left\{0, \frac{2\pi}{3}, -\frac{2\pi}{3}\right\}$, to recover the frequencies corresponding to k_θ and separate them. Equation (2.12) with those three values gives

$$\begin{cases} \widehat{I_u^{0,\theta}}(\xi) = M_0 \left[\hat{u}(\xi) + \alpha'\hat{u}(\xi + k_\theta) + \alpha'\hat{u}(\xi - k_\theta)\right] \times \varphi(\xi) + \widehat{n^{0,\theta}}(\xi) \\ \widehat{I_u^{1,\theta}}(\xi) = M_0 \left[\hat{u}(\xi) + \alpha'\hat{u}(\xi + k_\theta)e^{\frac{2i\pi}{3}} + \alpha'\hat{u}(\xi - k_\theta)e^{-\frac{2i\pi}{3}}\right] \times \varphi(\xi) + \widehat{n^{1,\theta}}(\xi)\,. \\ \widehat{I_u^{2,\theta}}(\xi) = M_0 \left[\hat{u}(\xi) + \alpha'\hat{u}(\xi + k_\theta)e^{-\frac{2i\pi}{3}} + \alpha'\hat{u}(\xi - k_\theta)e^{\frac{2i\pi}{3}}\right] \times \varphi(\xi) + \widehat{n^{2,\theta}}(\xi) \end{cases}$$

When $\alpha' \neq 0$, we can then compute an estimation of $\hat{u}(\xi)\widehat{\varphi}(\xi)$, $\hat{u}(\xi + k_\theta)\widehat{\varphi}(\xi)$ and $\hat{u}(\xi - k_\theta)\widehat{\varphi}(\xi)$ (linear system of 3 equations, with 3 unknowns). Setting $\hat{v}^\theta(\xi, k_\theta)$ as the estimate of $\hat{u}(\xi + k_\theta)\widehat{\varphi}(\xi)$ created thanks to the acquisition with angle θ, we have

$$\begin{cases} \hat{v}^\theta(\xi, 0) \propto \left(e^{\frac{4i\pi}{3}} - e^{-\frac{4i\pi}{3}}\right)\widehat{I_u^{0,\theta}}(\xi) - \left(e^{\frac{2i\pi}{3}} - e^{-\frac{2i\pi}{3}}\right)\left(\widehat{I_u^{1,\theta}}(\xi) - \widehat{I_u^{2,\theta}}(\xi)\right) \\ \hat{v}^\theta(\xi, k_\theta) \propto \left(e^{-\frac{2i\pi}{3}} - e^{\frac{2i\pi}{3}}\right)\widehat{I_u^{0,\theta}}(\xi) + \left(e^{\frac{2i\pi}{3}} - 1\right)\widehat{I_u^{1,\theta}}(\xi) - \left(e^{-\frac{2i\pi}{3}} - 1\right)\widehat{I_u^{2,\theta}}(\xi). \\ \hat{v}^\theta(\xi, -k_\theta) \propto \left(e^{-\frac{2i\pi}{3}} - e^{\frac{2i\pi}{3}}\right)\widehat{I_u^{0,\theta}}(\xi) - \left(e^{-\frac{2i\pi}{3}} - 1\right)\widehat{I_u^{1,\theta}}(\xi) + \left(e^{\frac{2i\pi}{3}} - 1\right)\widehat{I_u^{2,\theta}}(\xi) \end{cases} \quad (2.14)$$

Obtaining the values of $\hat{u}$ at the different frequencies from this system is done by a Wiener filter. Let us remind the principle of this filter.

2.2.4 Wiener filter for estimating the signal in ξ, $\xi \pm k_\theta$

Given a noisy observation $v : \mathbb{R}^n \mapsto \mathbb{R}$ of a signal $u : \mathbb{R}^n \mapsto \mathbb{R}$ convolved with a kernel $\varphi : \mathbb{R}^n \mapsto \mathbb{R}$, the observation can be written, assuming Gaussian noise, as

$$\forall t \in \mathbb{R}^n, v(t) = (\varphi * u)(t) + n(t),\ n(t) \sim \mathcal{N}(0, \sigma^2).$$

The filter g, also called Wiener filter, whose Fourier Transform is defined as

$$\forall \xi \in \mathbb{R}^n,\ \hat{g}(\xi) = \frac{\widehat{\varphi^*}(\xi)}{\frac{P_N(\xi)}{P_U(\xi)} + |\widehat{\varphi}(\xi)|^2}, \tag{2.15}$$

with $P_U(\xi) = \mathbb{E}(|\hat{u}(\xi)|^2)$ and $P_N(\xi) = \mathbb{E}(|\hat{n}(\xi)|^2)$, minimizes the mean square error between $g * v$ and u. This can be proven assuming independence between the noise n and the signal u and computing $g = \underset{h}{\operatorname{argmin}}\, \mathbb{E}(\|h*v-u\|^2)$, which is totally equivalent by Parseval equality (2.3) to find $\hat{g} = \underset{\hat{h}}{\operatorname{argmin}}\, \mathbb{E}(\|\hat{h}\hat{v} - \hat{u}\|^2)$.

To be able to compute the filter (2.15) on the SIM data (2.14) we first need to compute P_U, for the fluorophore density and P_N, for the noise.

For the noise the assumption $n \sim \mathcal{N}(0, \sigma^2)$ directly gives that $P_N = \sigma^2$. We then need to estimate the variance of the noise. Using (2.13), we notice that we can use the values of the frequency coefficients higher than the cut-off frequency to estimate σ^2; more precisely one can compute $\tilde{\sigma}^2$, an estimate of σ^2, as the average of all the squared frequencies higher than f_{max}, using all $(n^{i,\theta})_{i,\theta}$.

For computing P_U, [70] considers that $P_{v^\theta}(\xi) = \mathbb{E}(|\hat{v}^\theta(\xi, 0)|^2)$ (computed with the result of the first equation of (2.14)) can be written as:

$$\forall \xi \in \mathbb{R}^n,\ P_{v^\theta}(\xi) = |\varphi(\xi)|^2 P_U(\xi) + P_N(\xi) = |\varphi(\xi)|^2 \mathcal{A}^2 |\xi|^{-2\gamma} + P_N(\xi), \tag{2.16}$$

where $\mathcal{A}$ and γ estimated by curve fitting are constants characterizing the spectrum: $\mathcal{A}$ its amplitude, γ how fast the Fourier transform decreases. Once $\tilde{\sigma}^2$, $\mathcal{A}$ and γ estimated, the Wiener filter on (2.14) can be computed. We note $\tilde{\hat{u}}^\theta$, the estimate of $\hat{u}$ that is computed in ξ, $\xi + k_\theta$ and $\xi - k_\theta$ from acquisition with angle θ

$$\begin{cases} \tilde{\hat{u}}^\theta(\xi) = \dfrac{\widehat{\varphi^*}(\xi)}{|\widehat{\varphi}(\xi)|^2 + \frac{\tilde{\sigma}^2}{\mathcal{A}^2|\xi|^{-2\gamma}}} \hat{v}^\theta(\xi, 0) \\ \tilde{\hat{u}}^\theta(\xi + k_\theta) = \dfrac{\widehat{\varphi^*}(\xi)}{|\widehat{\varphi}(\xi)|^2 + \frac{\tilde{\sigma}^2}{\mathcal{A}^2|\xi+k_\theta|^{-2\gamma}}} \hat{v}^\theta(\xi, k_\theta) \\ \tilde{\hat{u}}^\theta(\xi - k_\theta) = \dfrac{\widehat{\varphi^*}(\xi)}{|\widehat{\varphi}(\xi)|^2 + \frac{\tilde{\sigma}^2}{\mathcal{A}^2|\xi-k_\theta|^{-2\gamma}}} \hat{v}^\theta(\xi, -k_\theta) \end{cases}.$$

The values from the two last equations need to be shifted afterwards to their correct positions on the spectrum of the image result, that is centered respectively on k_θ and $-k_\theta$. To perform this shift, we compute the translation in the reciprocal space using property (2.1) (that is we multiply by $e^{i\langle x,\pm k_\theta\rangle}$ in the space domain). We note them $\tau_{k_\theta}\tilde{\hat{u}}(\xi+k_\theta)$ and $\tau_{-k_\theta}\tilde{\hat{u}}(\xi-k_\theta)$

$$\tau_{k_\theta}\tilde{\hat{u}}^\theta(\xi+k_\theta) = \mathcal{F}\left(\mathcal{F}^{-1}\left(\tilde{\hat{u}}^\theta(\xi+k_\theta)\right)(x)\times e^{i\langle x,k_\theta\rangle}\right)(\xi),$$
$$\tau_{-k_\theta}\tilde{\hat{u}}^\theta(\xi-k_\theta) = \mathcal{F}\left(\mathcal{F}^{-1}\left(\tilde{\hat{u}}^\theta(\xi+k_\theta)\right)(x)\times e^{-i\langle x,k_\theta\rangle}\right)(\xi).$$

2.2.5 Creation of the SIM image

In [89], the authors present that 3 values of θ, $\{0, \frac{\pi}{3}, \frac{2\pi}{3}\}$, are sufficient for creating the SIM image. Looking at Figure 2.5 where k_θ equals f_{max}, we see that, indeed, with those three values almost all the frequencies in $\mathcal{B}(0, 2f_{max})$ are recovered. The merging of the frequencies coming from the different θ is computed using a generalized Wiener filter. This filter enables to merge the results of different views of the same object with different parameters, still minimizing the mean square error.

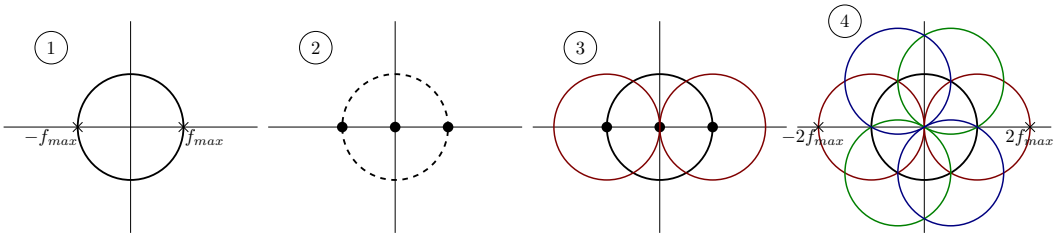

Figure 2.5: Principle of Structured Illumination Microscopy with $|k_\theta| = f_{max}$: (1) the spectrum of an image going through a microscope, band-limited, with maximal frequency f_{max}, (2) the Fourier transform of a grid $m^{i,0}$, used by the SIM, made of Dirac distributions (3) the Fourier spectrum recovered by an acquisition with $m^{i,0}$, (4) the Fourier spectrum recovered by an acquisition with 3 values of θ: $\{0, \frac{\pi}{3}, \frac{2\pi}{3}\}$. One grid enables to recover frequency coefficients in one direction, the three values of θ enable to almost double the spectrum, that is to go until $2f_{max}$. However as mentioned before, since $\widehat{\varphi}(f_{max}) = 0$, the value for $|k_\theta|$ has to be smaller than f_{max}, so that the support of the reconstruction cannot be exactly $\mathcal{B}(0, 2f_{max})$.

The result of this generalized filter, $\widehat{U}_{SIM}$ is the Fourier Transform of the final super-resolved image. The result produced by the SIM algorithm described is then $\mathcal{F}^{-1}(\widehat{U}_{SIM})$; it should contain details smaller than $\frac{\lambda}{2NA}$.

2.2.6 Discussion on the SIM method

One big advantage of the SIM is its speed because it is working on the whole field. However, it also presents drawbacks. For instance lenses produce much more aberrations far from the optical axis, in particular coma and astigmatism aberrations, that modifies the shape of a point source; the first one can create distortions like tail on one point source and the second one can enlarge/modify the shape of the spot, making a circle look like an ellipse for example.

On top of that, if the principle of the SIM is quite "simple": the Fourier Transform of the projected grid enables to obtain higher frequencies mixing them with the lower ones and Wiener filters are used to separate the frequency components, the different parameters of the grid are in fact not defined by the experimental protocol and need to be estimated: M_0, k_θ, α, ϕ_i. This makes the real processing of the data a more complex procedure than just Wiener filters. These estimations (as well as $\mathcal{A}$ and γ in (2.16)) could be done in various ways (because of the redundancy of the data) (see [70] for an example of a full algorithm). As it can be seen in Figure 2.6, a wrong value for one of the k_θ for instance clearly deteriorates the resolution and creates artifacts such as the duplication of some structures. This is particularly an issue for biological interpretations.

Moreover, as we mentioned before, the sample is most of the time three-dimensional, meaning that not only the focal plane is illuminated but also the plans below and above, with a bigger PSF (see Figure 2.2); this can impact the whole reconstruction. This phenomenon is easier to control with local approaches, for instance by using a pinhole (real or virtual) to suppress out of focus photons.

Numerous articles were published in the last few years concerning artifacts produced by the SIM ([114] and [30] for instance), in order to prevent wrong interpretations from biological experiments or to optimize the performances of the method. This can be done either by a better protocol for samples creation [30], by controlling each step of the processing [8] to be able to detect inconsistencies (about parameters values for instance) or or by trying to remove the out of focus light in the SIM reconstruction [90]. Some alternatives to Wiener filtering have also been proposed using the Bayesian framework, for instance in [78] where a prior using the derivative of the gradient of the reconstructed image is taken to assure its smoothness ([69] proposes a free tool to process data from a SIM acquisition and compare the reconstructions) or in [89] where the posterior law is defined as a function of the data but also parameters of the model, with also a prior promoting smooth features, using Gaussian

fields.

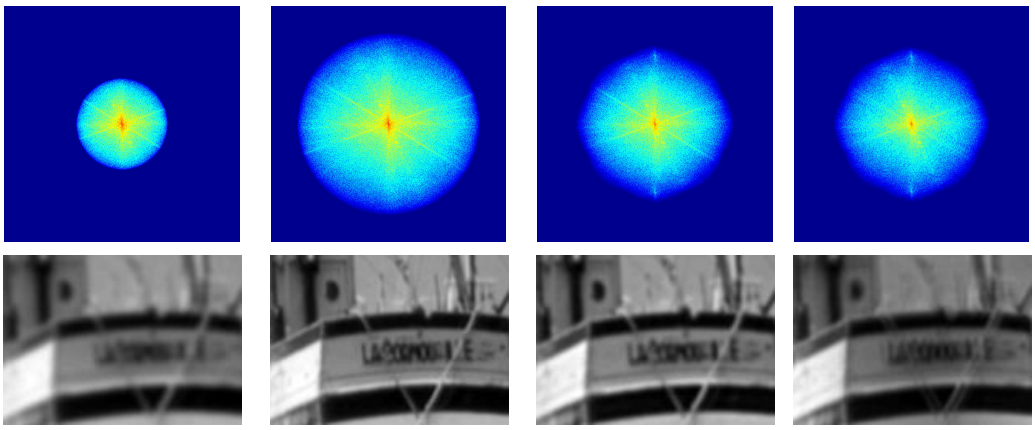

(a) Conventional microscope (b) Doubled conventional microscope (c) SIM image (perfect) (d) SIM image (wrong parameter)

Figure 2.6: Simulation of the SIM reconstruction (with no noise on the acquired data and $k_\theta \sim 3/4 f_{max}$): the first line represents the modulus of the Fourier spectra in logarithmic scale and the second line a crop on a significant region of interest of the image; they correspond to: (a) image obtained with a conventional microscope - (b) image that would be obtained with a (simulated) conventional microscope of double resolution - (c) SIM image obtained with correct parameters (4 values of θ and 3 of ϕ_i) - (d) SIM image obtained by assigning a wrong value to k_θ for one of the angle (less than 5% error). First we can notice that the SIM result is very good with the correct parameters, clearly presenting a better resolution than the widefield image, with a spectra close to the real one, with non null frequency coefficients between f_{max} and $2f_{max}$. However a bad estimation of one parameter can create artifacts (duplication of some structures) and deteriorate the resolution, as well as lead to false conclusion on the observed image.

2.3 Image Scanning Microscopy

2.3.1 General presentation

In the case of Image Scanning Microscopy, ISM, a laser emits light with a specified pattern at a given position on the fluorescent sample and the response of the sample is observed around this position. The laser then moves on the whole sample to collect data from different positions. In the following, we present a new general framework developed with Julien Caron that can describe every ISM method in four dimensions and enables to interpret the most popular existing methods (conventional

imaging, confocal microscopy and pixel reassignment).

Given u, a fluorophore density as before, we now suppose that a specific distribution of light D^s is projected on the sample, at position $X_s = (x_s, y_s)$ (the distribution can vary according to the position on the sample). The scanned image, I_u, captured on a camera of pixel $X_c = (x_c, y_c)$ is a four dimensions function written as

$$\forall (X_c, X_s) \in (\mathbb{R}^2)^2,\ I_u^s(X_s, X_c) = \left((u(\cdot) \times D^s(\cdot - X_s)) * \varphi(\cdot)\right)(X_c). \tag{2.17}$$

Remark 4. *D^s is created within the optical device and then, like the PSF φ, limited by the diffraction meaning that*

$$\forall \xi \ s.t.\ |\xi| > f_{max},\ D^s(\xi) = 0.$$

We can compute the four-dimensional Fourier transform of (2.17), $\forall \eta \in \mathbb{R}^4 = (\eta_{12}, \eta_{34})$, $(\eta_{12} \in \mathbb{R}^2, \eta_{34} \in \mathbb{R}^2)$,

$$\widehat{I_u^s}(\eta) = \int_{\mathbb{R}^2} \int_{\mathbb{R}^2} (u(\cdot) D^s(\cdot - X_s) * \varphi)(X_c) e^{-i\langle X_s, \eta_{12}\rangle} e^{-i\langle X_c, \eta_{34}\rangle} dX_c dX_s. \tag{2.18}$$

Replacing the convolution by its definition and swapping the integrals, we can isolate the Fourier Transform of φ in η_{34} and Equation (2.18) becomes

$$\widehat{I_u^s}(\eta) = \widehat{\varphi}(\eta_{34}) \int_{\mathbb{R}^2} \int_{\mathbb{R}^2} u(y) D^s(y - X_s) e^{-i\langle X_s, \eta_{12}\rangle} e^{-i\langle y, \eta_{34}\rangle} dy dX_s.$$

By swapping integrals again, we can see the Fourier Transform of translated and dilated D^s

$$\widehat{I_u^s}(\eta) = \widehat{\varphi}(\eta_{34}) \int_{\mathbb{R}^2} u(y) e^{-i\langle y, \eta_{34}\rangle} \underbrace{\left(\int_{\mathbb{R}^2} D^s(y - X_s) e^{-i\langle X_s, \eta_{12}\rangle} dX_s \right)}_{\widehat{D^s}(-\eta_{12}) e^{-i\langle y, \eta_{12}\rangle}} dy.$$

And finally the 4-D Fourier transform can be written as

$$\begin{aligned} \widehat{I_u^s}(\eta) &= \widehat{\varphi}(\eta_{34}) \widehat{D^s}(-\eta_{12}) \int_{\mathbb{R}^2} u(y) e^{-i\langle y, \eta_{34}\rangle} e^{-i\langle y, \eta_{12}\rangle} dy \\ &= \widehat{\varphi}(\eta_{34}) \widehat{D^s}(-\eta_{12}) \hat{u}(\eta_{12} + \eta_{34}), \end{aligned} \tag{2.19}$$

which means that an ISM method can double the range of frequencies (since $\widehat{I_u^s}(\eta) \neq 0$ when $\eta_{12} \in \text{supp}(\widehat{D^s}) \subset \mathcal{B}(0, f_{max})$ and $\eta_{34} \in \text{supp}(\widehat{\varphi}) \subset \mathcal{B}(0, f_{max})$) and that the weight for each frequency coefficient of the real image u in $\widehat{I_u^s}$ depends on specific frequencies of both the illumination and excitation patterns.

2.3.2 Overview of some linear reconstruction methods

In the following, we present several well-known ISM methods which can be written as Equation (2.17). An interesting way to compare those methods is to compare their theoretical OTF (to compare the recovered frequencies). To do that, given a reconstruction i, function of $I_u^s(X_s, X_c)$, we can either directly find the OTF of the system, that is $\widehat{\varphi}$ such that $\widehat{i} = \widehat{\varphi}\widehat{u}$, or find the PSF φ such that $i = \varphi * u$.

Conventional image

Going back to (2.17), we call the *conventional image*, noted u_{conv}, the integration of this expression over X_s replaced at position X_c. We then have

$$\begin{aligned}
\forall X_c \in \mathbb{R}^2, u_{\text{conv}}(X_c) &= \int_{\mathbb{R}^2} I_u^s(X_c, X_s) dX_s \qquad (2.20)\\
&= \int_{\mathbb{R}^2} \left((u(\cdot) \times D^s(\cdot - X_s)) * \varphi(\cdot)\right)(X_c) dX_s \\
&= \int_{\mathbb{R}^2}\int_{\mathbb{R}^2} \left(u(y) \times D^s(y - X_s)\right) \varphi(X_c - y) dy dX_s \\
&= \int_{\mathbb{R}^2} u(y)\varphi(X_c - y) \left(\int_{\mathbb{R}^2} D^s(y - X_s) dX_s\right) dy \\
&= \widehat{D^s}(0) \int_{\mathbb{R}^2} u(y)\varphi(X_c - y) dy \\
&= \widehat{D^s}(0) \left(u(\cdot) * \varphi(\cdot)\right)(X_c). \qquad (2.21)
\end{aligned}$$

Supposing that the total mass of the illumination pattern is 1, that is $\widehat{D^s}(0) = 1$, the PSF of an optical device creating the conventional image, u_{conv}, is φ and equivalently its OTF is

$$\text{OTF}_{u_{\text{conv}}} = \widehat{\varphi}.$$

Even if it seems less natural, this definition of the conventional image on the four dimensions function gives the idea of a "dual" conventional image, u^d_{conv}, which consists in integrating over the camera points, X_c, for each laser position and replacing it at the laser position, X_s. With similar steps and defining

$$\forall x \in \mathbb{R}^2,\ \check{D}^s(x) = D^s(-x),$$

we have

$$\begin{aligned}\forall X_s \in \mathbb{R}^2, u^d_{\text{conv}}(X_s) &= \int_{\mathbb{R}^2} I^s_u(X_c, X_s) dX_c, \\ &= \int_{\mathbb{R}^2}\int_{\mathbb{R}^2} \left(u(y) \times D^s(y - X_s)\right) \varphi(X_c - y) dy dX_c \\ &= \widehat{\varphi}(0) \left(u(\cdot) * \check{D}^s(\cdot)\right)(X_s). \end{aligned} \tag{2.22}$$

Most of the time, the illumination pattern is symmetrical, meaning that the PSF of an optical system computing the dual conventional image is the illumination pattern, under the assumption that $\widehat{\varphi}(0) = 1$. The OTF of u^d_{conv} is then

$$OTF_{u^d_{\text{conv}}} = \widehat{D^s}.$$

Remark 5. *The PSF of those two systems are respectively φ and D^s; these functions are band limited with higher frequency f_{max}. This means that these two reconstructions are also band limited with cut-off frequency f_{max}. However, if we consider the difference between the emission and excitation wavelengths the two methods are not exactly equivalent; indeed, we have that $supp(\widehat{\varphi}) \subset \mathcal{B}(0, f^{em}_{max})$ and $supp(\widehat{D^s}) \subset \mathcal{B}(0, f^{ex}_{max})$ and since $f^{ex}_{max} > f^{em}_{max}$, the support of $OTF_{u^d_{conv}}$ is a bit bigger than the support of $OTF_{u_{conv}}$.*

Comparing (2.21) and (2.22) to (2.19), we see that the creation of the conventional images correspond to a slice of $\widehat{I^s_u}(\eta)$ on the subspaces defined respectively by $\{\eta_{34} = 0\}$ and $\{\eta_{12} = 0\}$.

Confocal image

In the case of confocal microscopy (see [15] and the series of derivated articles by Bertero), the projected pattern is an Airy disk for each scanning point, meaning that $\forall s, D^s = \varphi$. For each scanning position X_s, the integration of (2.17) is computed on a disk of radius R, called pinhole, centered on X_s, and the number of collected photons on the camera pixels X_c within this pinhole is attributed to X_s. Let us call u_{conf} the created image, we have

$$\begin{aligned}\forall X_s \in \mathbb{R}^2,\ u_{\text{conf}}(X_s) &= \int_{\mathcal{B}(X_s,R)} I^s_u(X_s, X_c) dX_c \\ &= \int_{\mathbb{R}^2} I^s_u(X_s, X_c) \mathbb{1}_{\mathcal{B}(0,R)}(X_s - X_c) dX_c. \end{aligned} \tag{2.23}$$

Remark 6. *Due to the shape of the Airy spot (see Figure 2.1), a very small number of photons should be collected beyond the circle of radius r_a. In practice, this is not exactly the case because the fluorophore density is distributed in the three-dimensional space. It can be seen in Figure 2.2 that the support of the Airy spot in the space domain depends in fact on the 3^{rd} coordinate. Limiting the photons with a pinhole is then also a way to eliminate some of the out of focus light. Although a too small pinhole ($R \to 0$) would in practice collect too few photons, we shall here consider the limiting case of the Dirac centered on X_s for its interesting properties.*

We compute the Fourier transform of u_{conf}, given by

$$\begin{aligned}
\forall \xi \in \mathbb{R}^2,\ \widehat{u_{\text{conf}}}(\xi) &= \int_{\mathbb{R}^2} u_{\text{conf}}(X_s) e^{-i\langle X_s, \xi\rangle} dX_s \\
&= \int_{\mathbb{R}^2}\int_{\mathbb{R}^2} I_u^s(X_s, X_c) \mathbb{1}_{\mathcal{B}(0,R)}(X_s - X_c) e^{-i\langle X_s, \xi\rangle} dX_c dX_s \\
&= \int_{(\mathbb{R}^2)^3} u(x)\varphi(x - X_s)\varphi(X_c - x)\mathbb{1}_{\mathcal{B}(0,R)}(X_s - X_c) e^{-i\langle X_s, \xi\rangle} dx dX_c dX_s.
\end{aligned}$$

Swapping the order of integration, we notice that

$$\begin{aligned}
\int_{\mathbb{R}^2} \varphi(X_c - x)\mathbb{1}_{\mathcal{B}(0,R)}(X_s - X_c) dX_c &= \int_{\mathbb{R}^2} \varphi(X_s - y - x)\mathbb{1}_{\mathcal{B}(0,R)}(y) dy \\
&= \left(\varphi * \mathbb{1}_{\mathcal{B}(0,R)}\right)(X_s - x),
\end{aligned}$$

giving

$$\begin{aligned}
\widehat{u_{\text{conf}}}(\xi) &= \int_{\mathbb{R}^2}\int_{\mathbb{R}^2} u(x)\varphi(x - X_s)\left(\varphi * \mathbb{1}_{\mathcal{B}(0,R)}\right)(X_s - x) e^{-i\langle X_s, \xi\rangle} dx dX_s \\
&= \int_{\mathbb{R}^2}\int_{\mathbb{R}^2} u(x)\varphi(x - X_s)\left(\varphi * \mathbb{1}_{\mathcal{B}(0,R)}\right)(X_s - x)\, dx e^{-i\langle X_s, \xi\rangle} dX_s \\
&= \int_{\mathbb{R}^2} \left(u * \left(\check{\varphi} \cdot (\varphi * \mathbb{1}_{\mathcal{B}(0,R)})\right)\right)(X_s) e^{-i\langle X_s, \xi\rangle} dX_s \\
&= \mathcal{F}\left(u * \left(\check{\varphi} \cdot \left(\varphi * \mathbb{1}_{\mathcal{B}(0,R)}\right)\right)\right)(\xi) \\
&= \left(\hat{u} \times \left(\widehat{\check{\varphi}} * \left(\widehat{\varphi} \cdot \widehat{\mathbb{1}}_{\mathcal{B}(0,R)}\right)\right)\right)(\xi).
\end{aligned}$$

This means that the OTF of a confocal imaging system with pinhole of radius R is $\text{OTF}_{u_{\text{conf}}} = \widehat{\check{\varphi}} * \left(\widehat{\varphi} \cdot \widehat{\mathbb{1}}_{\mathcal{B}(0,R)}\right)$.

To explicit this OTF, we can use that

$$\widehat{\mathbb{1}}_{\mathcal{B}(0,R)}(\xi) = \frac{2\pi R}{\|\xi\|} J_1(R\|\xi\|)$$

and finally we can write the optical transfer function of the confocal system as

$$\mathrm{OTF}_{u_{\mathrm{conf}}}(\xi) = \left(\widehat{\check{\varphi}}(\cdot) * \left(\widehat{\varphi}(\cdot) \times \frac{2\pi R}{\|\cdot\|} J_1(R\|\cdot\|)\right)\right)(\xi).$$

In the particular case where the pinhole is reduced to a Dirac centered on X_s, Equation (2.23) gives, since $D^s = \varphi$,

$$\begin{aligned} u_{\mathrm{conf}}(X_s) &= \int_{\mathbb{R}^2} I_u^s(X_s, X_c)\delta_{X_s}(X_c)dX_c \\ &= \int_{\mathbb{R}^2} u(x)\varphi(x - X_s)\varphi(X_s - x)dx \\ &= \left(u(\cdot) * \left(\check{\varphi} \times \varphi\right)(\cdot)\right)(X_s). \end{aligned}$$

The OTF is then $\widehat{\check{\varphi}} * \widehat{\varphi}$ and we can see that it corresponds to an integration of (2.19) on the plane defined by $\{\eta_{12} + \eta_{34} = \xi\}$.

Most of the time the pinhole size is expressed as a proportion of the first zero of the Airy disk r_a, sometimes noted UA for "Unit of Airy". Figure 2.7 represents the vertical profiles in space and Fourier domains of the PSF produced by the formula above for three pinhole values and the Dirac distribution. The Dirac pinhole gives the best results in terms of high frequencies. But we can also see on Figure 2.7 that all the frequencies between $[f_{max}, 2f_{max}]$ are computed more efficiently in the case of small pinholes, that is the coefficients corresponding to those frequencies are higher. As in [104], we present also the normalized and unnormalized OTFs to keep in mind that a smaller pinhole gives better resolution but requires more light to get the same amount of photons, which can be a limiting factor in some biological applications.

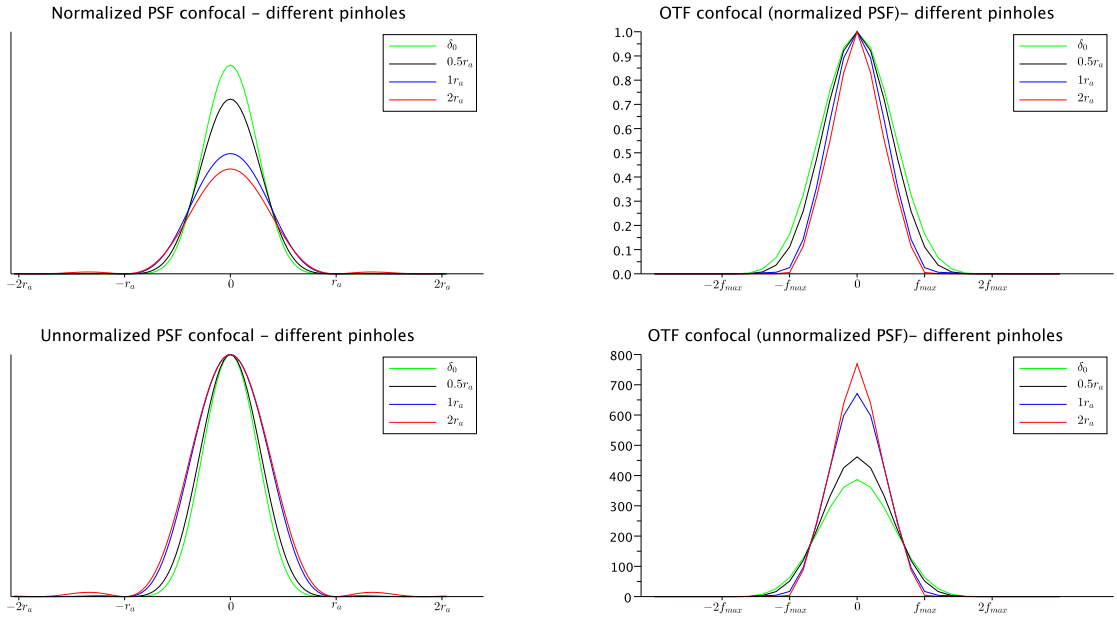

Figure 2.7: Comparison of different OTF for confocal imaging with different pinholes: radial profiles of theoretical normalized PSF and corresponding OTF (first line) and unnormalized PSF and corresponding OTF (second line) obtained with pinhole size of 0.5 UA, 1 UA, 2 UA (that is almost φ) and reduced to a Dirac in X_s. We see, on the first line, that in the Fourier domain the cut-off frequency is higher when the pinhole is smaller but also that the frequencies between f_{max} and $2f_{max}$ are better represented with a smaller pinhole. However, this better resolution is not without a consequence, as seen on the second line where the unnormalized profiles show that the number of photons needed to reach the same intensity that the pinhole equal to 2 UA for a Dirac pinhole is more than twice bigger.

Pixel reassignment method

In 1988, in [102], Sheppard presents the theoretical principle of pixel reassignment, proposing to create an image reassigning the signal from one scanning point to an intermediate position instead of putting it directly at the scanning point. However, this technique was implemented more than twenty years ago, in 2010, as it can be seen in [85].

Developing (2.17) with the definition of the convolution, we have

$$I_u^s(X_c, X_s) = \int_{\mathbb{R}^2} u(x) \times D^s(x - X_s)\varphi(X_c - x)dx.$$

As described in [103], the pixel reassignment method reassigns the signal from

X_c to the point $x_r = (1-a)X_c + aX_s$, $a \in [0,1]$. The case $a = \frac{1}{2}$, where the signal is reassigned to the middle position between X_s and X_c, gives

$$\begin{aligned} u_{\text{pr}}(x_r) &= \int_{\mathbb{R}^2} I_u^s(X_s, 2x_r - X_s) dX_s \\ &= \int_{\mathbb{R}^2} \int_{\mathbb{R}^2} u(y) \times D^s\left(y - X_s\right) \varphi\left(2x_r - X_s - y\right) dy dX_s \\ &= 4 \int_{\mathbb{R}^2} u(y) \int_{\mathbb{R}^2} D^s(2z) \varphi\left(2x_r - 2y + 2z\right) dz dy \\ &= 4 \int_{\mathbb{R}^2} u(y) (\check{D}^s\left(2\cdot\right) * \varphi\left(2\cdot\right))(x_r - y) dy \\ &= 4 \left(u * \left(\check{D}^s\left(2\cdot\right) * \varphi\left(2\cdot\right)\right)\right)(x_r). \end{aligned}$$

This also means that the Fourier transform of u_{pr} is

$$\forall \xi \in \mathbb{R}^2,\ \widehat{u_{\text{pr}}}(\xi) \propto \hat{u}(\xi) \times \left(\widehat{\check{D}^s}\left(\frac{1}{2}\xi\right) \widehat{\varphi}\left(\frac{1}{2}\xi\right)\right),$$

and the OTF in the case of pixel reassignment is then

$$\text{OTF}_{u_{\text{pr}}}(\xi) \propto \widehat{\check{D}^s}\left(\frac{\xi}{2}\right) \widehat{\varphi}\left(\frac{\xi}{2}\right). \tag{2.24}$$

Taking $D^s = \varphi$, Formula (2.24) gives that $\text{supp}(\text{OTF}_{u_{\text{pr}}}) = \mathcal{B}(0, 2f_{max})$. A representation of this OTF can be seen in Figure 2.8; we can notice that the frequencies between f_{max} and $2f_{max}$ are not as well represented as in the case of a (theoretical) conventional imaging system with double resolution, and that the frequency coefficients after $1.8f_{max}$ are quite low. This method consists in a slice of (2.19) on the subspace defined by $\{\eta_{12} = \eta_{34}\}$.

A summary of the action of the four methods in the 4D-Fourier space is presented in Figure 2.9. In Figure 2.10 and 2.11, some simulations on real data were made by using the theoretical definition of each OTF. We can clearly see the improvement of resolution in the space domain by analyzing the separation between filaments but also in the Fourier domain where the support of the OTFs varies depending on the methods. The best result is with no doubt obtained by a system using pixel reassignment; however the resolution is not as good as the one of a system producing a conventional image with a PSF twice smaller, that is with cut-off frequency $2f_{max}$.

Remark 7. *As mentioned before, this study implies that* $\lambda_{em} = \lambda_{ex}$ *which is not exactly the case. More precisely, we have that* φ *is limited by* $f'_{max} = \pi \cdot 2NA/\lambda_{em}$ *and the illumination vector* k_θ *of the grid* $m^{i,\theta}$ *for the SIM in (2.9) as well as* D^s *for the ISM are limited by* $f_{max} = \pi \cdot 2NA/\lambda_{ex}$*. This means that the frequencies in (2.10) and (2.19) are not exactly contained in the interval* $[-2f_{max}; 2f_{max}]$ *but in the interval* $[-f_{max} - f'_{max}; f_{max} + f'_{max}]$

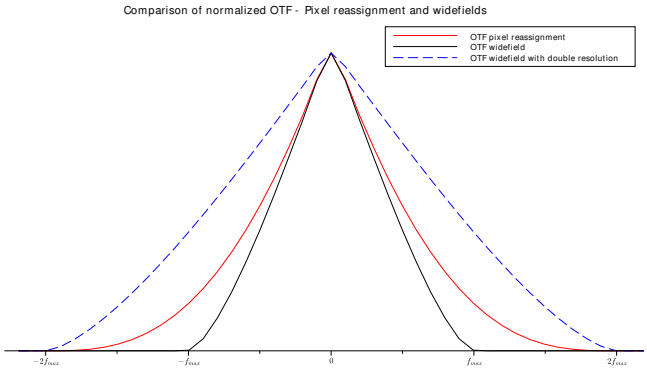

Figure 2.8: Comparison of the radial profiles of the OTF of a pixel reassignment technique and conventional imaging systems: in black the OTF of a widefield system ($\widehat{\varphi}$), in red the OTF got by formula (2.24) for the pixel reassignment system and in blue the OTF of a widefield system whose resolution is doubled compared to the black one ($\widehat{\varphi}(\cdot/2)$). The support of the $\mathrm{OTF}_{u_{\mathrm{pr}}}$ is larger than the support of $\mathrm{OTF}_{u_{\mathrm{conv}}}$, giving a better resolution to this technique in comparison to a system performing conventional imaging. However we can see that it is not equivalent at all to an OTF for a conventional system with double resolution: the coefficients of the OTF are very lower in the case of pixel reassignment and especially if it could theoretically retrieve frequencies coefficients until $2f_{max}$, we can see that the weight on theses frequencies is close to zero.

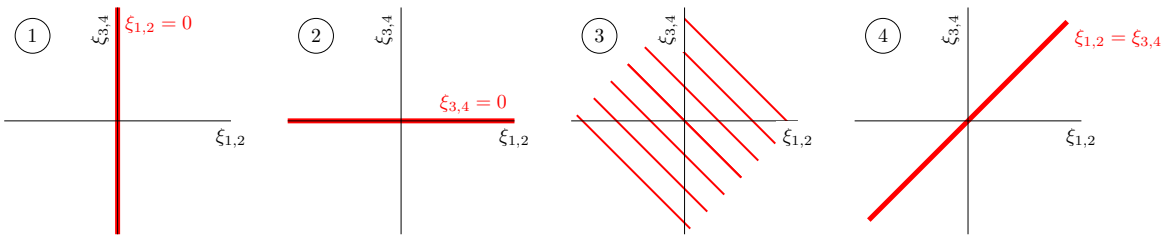

Figure 2.9: Comparison of the 4 methods in the Fourier (4D-)domain: in 1 and 2 conventional and dual conventional slice the 4D Fourier transform on each axis, in 3 the confocal technique with a Dirac as a pinhole integrates the 4D Fourier transform on $\{\eta_{12} + \eta_{34} = \xi\}$, in 4 the pixel reassignment slices the 4D Fourier transform on the subspace $\{\eta_{12} = \eta_{34}\}$.

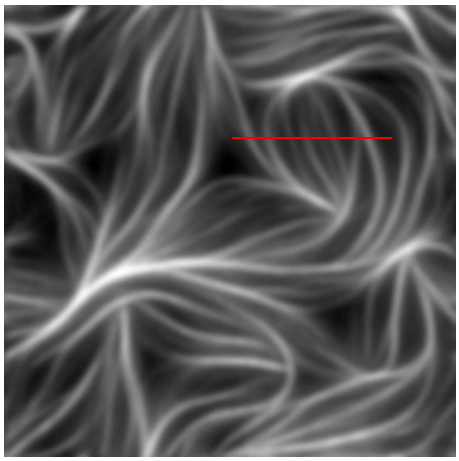

Conventional with double resolution

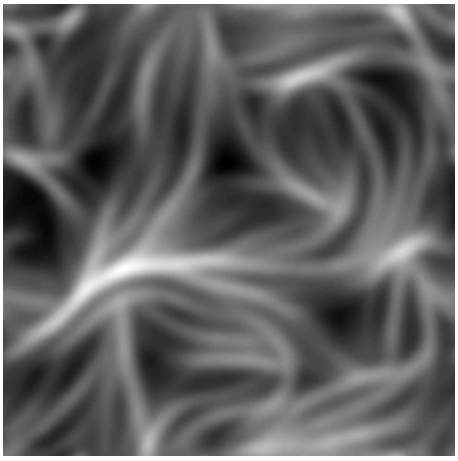

Conventional image

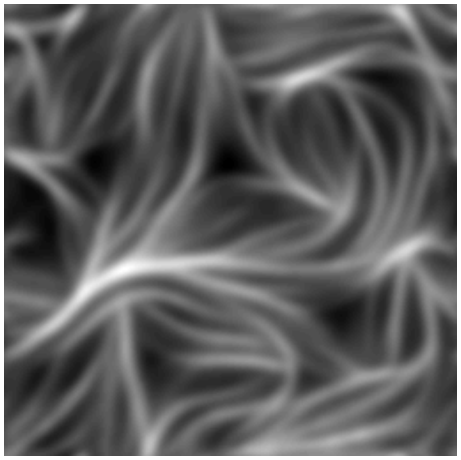

Confocal image (pinhole $0.6r_a$)

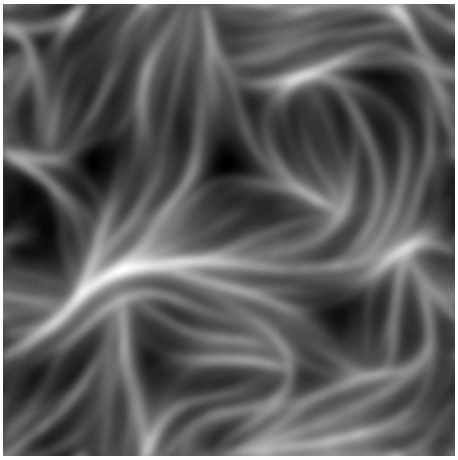

Pixel reassignment

Figure 2.10: Comparison of a conventional image with real doubled resolution with 3 ISM techniques on an image of filamentous actin. The results are from left to right: conventional image with a PSF twice smaller than the original PSF - conventional image with constant illumination - confocal image with a pinhole of $0.6r_a$ - pixel reassignment image. The images were generated computing the product of the Fourier transform of the original image and the theoretical OTF computed above. We can gradually see some filaments separation appearing with the different methods; the red profile on the original image is shown for the 4 images in Figure 2.12. It is clear that the pixel reassignment has a better resolution than the other two techniques but we can see that it does not reach exactly the factor 2 (contrary to the first image).
Image from cellimagelibrary.org by Dennis Breitsprecher for 2010 Olympus BioScapes Digital Imaging Competition is licensed under CC BY-NC-ND 3.0 - a frequency cut (explained in Chapter 3) as well as a periodic plus smooth decomposition [83] was performed on the image; the ground truth image is the periodic component.

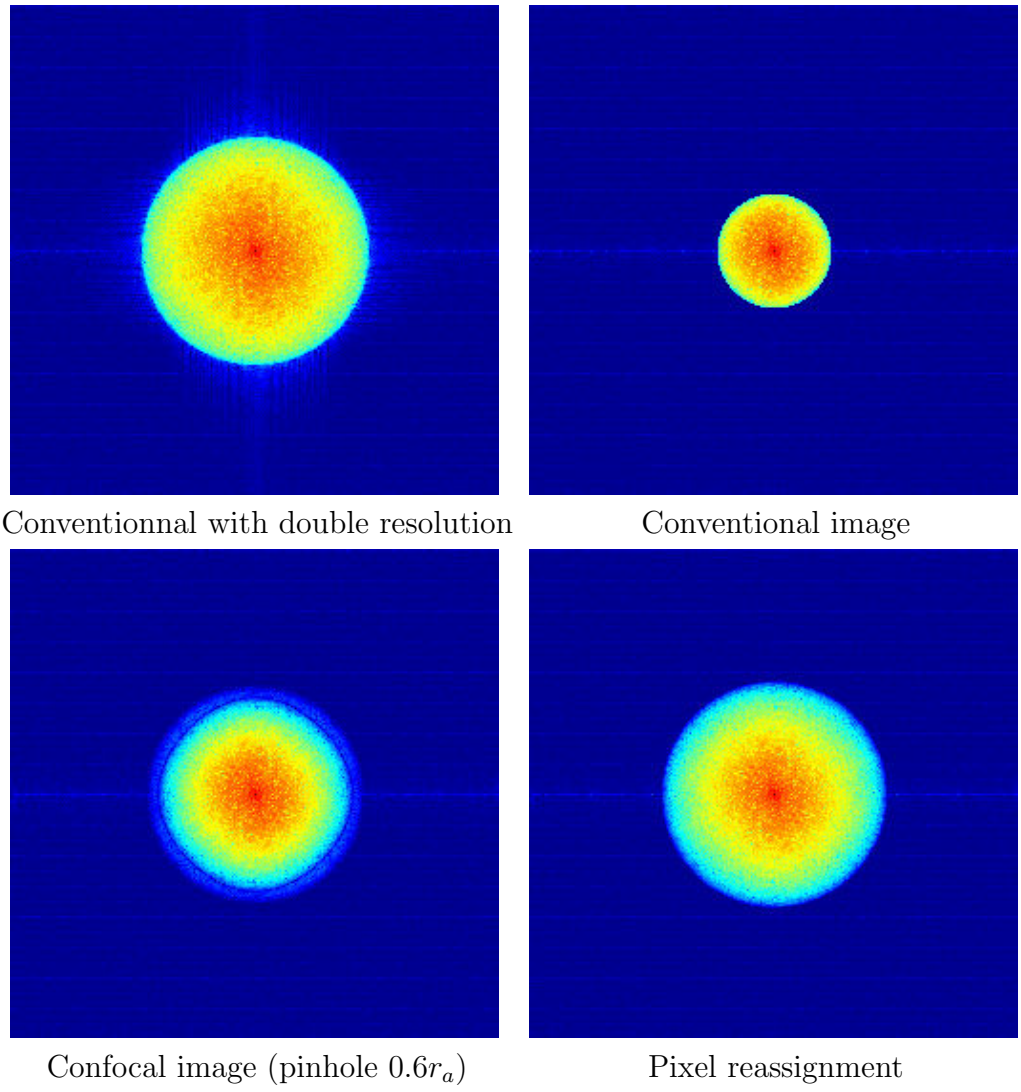

Figure 2.11: Comparison of Fourier transforms of images from Figure 2.10; the modulus of the Fourier transform is represented, in logarithmic scale, corresponding to from left to right: conventional image with an OTF twice bigger than the original one - conventional image with constant illumination - confocal image with a pinhole of $0.6r_a$ - pixel reassignment image. We clearly see the support of the Fourier transform increasing with the methods, but as said before, none of the method retrieves the frequency coefficients until $2f_{max}$ and none of them reach the resolution of an hypothetical system with a PSF twice smaller than the real one.

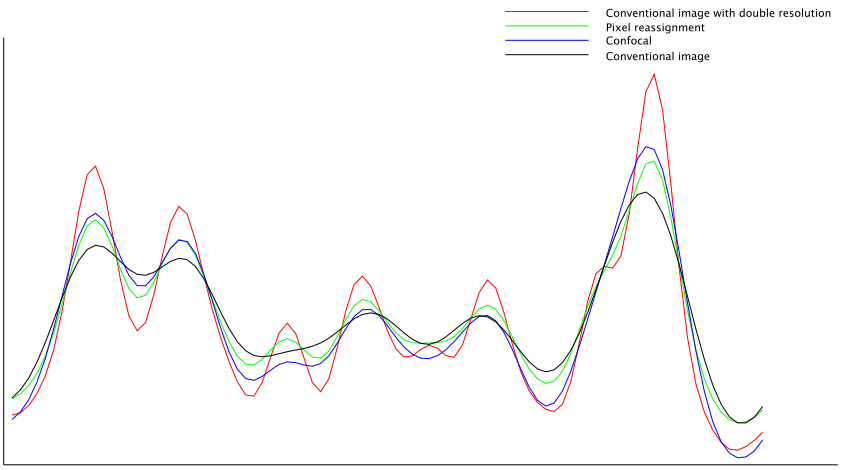

Figure 2.12: Cross-sections from Figure 2.10 (in red on the first image): in red a conventional with resolution twice better enables to see the separation of each filament and to compare the different methods. As explained before, the conventional has the worst resolution, and we can see that confocal and pixel reassignment techniques separate more or less the filaments but this separation is stronger for the pixel reassignment (in green). Once again, we can notice that not all details are retrieved: the last part of the profile is made of two peaks, as shown on the conventional with double resolution, but none of the methods could resolve the separation between those peaks.

Remark 8. *The comparison we present is considering a non-noisy acquisition but, in practice, this never happens. It would be interesting to also measure the amount of noise produced by this methods to be totally impartial in their comparison.*

2.3.3 Non linear reconstruction methods for an ISM acquisition

The image formation (2.17) can be written as $HM^s u(X_c)$, where H is the convolution operator and M^s the operator of multiplication with D^s centered on X_s. The MAP estimate, that computes the more plausible image knowing the data (a more precise definition of this estimate can be found in the following, in Chapter 4), of an acquisition of noisy realizations noted $(v_s)_{s=1,\dots,S}$ is given by

$$u_{MAP} = \underset{u}{\operatorname{argmax}}\, p(u|(v_s)_s) = \underset{u}{\operatorname{argmax}}\, p((v_s)_s|u)p(u). \tag{2.25}$$

In the case of fluorescence microscopy, usual prior on u is its positivity. Indeed the number of photons reaching the sensor is always a positive value.

Supposing Gaussian noise assumption, we have

$$p((v_s)_s|u) \propto \exp\left(-\frac{\|v_s - HM^s u\|}{\sigma^2}\right).$$

However due to the quantized nature of light, the assumption used in microscopy is more often the presence of Poisson noise (see for instance [94]). The number of collected photons, which is always an integer value, is a Poisson variable, meaning each v_s is a realization of V_s with

$$V_s \sim \mathcal{P}\left(HM^s U\right) \Leftrightarrow \mathbb{P}(V_s = v_s \,|U = u\,) = \frac{(HM^s u)^{v_s}}{v_s!} e^{-HM^s u},$$

and assuming independence between the (V_s), we have

$$p((v_s)_s|u) = \prod_s \frac{(HM^s u)^{v_s}}{v_s!} e^{-HM^s u}.$$

We can then replace in (2.25) using one or the other probability. With a positivity prior on u, the problem using the negative logarithm of the expression for Poisson noise can be written as an energy minimization

$$u_{MAP} = \underset{u\geq 0}{\operatorname{argmin}} \sum_s HM^s u - v_s \log(HM^s u) = \underset{u\geq 0}{\operatorname{argmin}}\, E(u). \tag{2.26}$$

The function $E(u)$ is convex and differentiable; a projected gradient descent can estimate the solution of (2.26). This requires the computation of the gradient of the energy, but also the discretization of the problem as precisely as possible, in particular the operators H and M^s. These points are presented in Chapter 3.

Chapter 3

Discretization of the Imaging Scanning Microscopy model

Contents

Given a continuous function from $\mathbb{R}^d$ to $\mathbb{R}$, choosing the proper samples to be able to reconstruct correctly the initial signal is not an easy task (see Figure 3.1). We present the link between a continuous function, its continuous Fourier transform and the discrete samples of the function, as well as the Discrete Fourier Transform associated to these samples. From Shannon's theorem can be derivated the Shannon interpolate, which will define the relation between the discrete and continuous images all along this chapter.

With all those considerations, we can define how to perform accurately basic operations on the discrete images; these operations are composing the operator H characterizing the ISM model. An algorithm of discretization is then proposed.

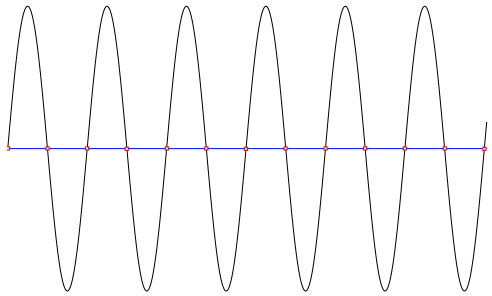

Figure 3.1: Illustration of discretization issues: two very different functions, a sine function (black) and a constant function (blue) can have the same samples (red dots); we then cannot expect to reconstruct the initial signals with those samples. *In which conditions can we precisely recover the original signal from its samples?*

3.1 Discrete representation of a signal

Given $\tilde{u}$ a continuous function from $\mathbb{R}$ to $\mathbb{R}$, we present the operation of sampling it into a set of finite samples. This part refers to [3] where a synthesis of the tools used in Shannon theory is well described. This part is written with one-dimension signals for an ease of read (with some examples in two-dimensions, with images) but it can easily be transposed to higher dimensions.

3.1.1 Definition of sampling in space and Fourier domains

We recall the definition of the Dirac comb and its Fourier transform,

$$\Pi_l = \sum_{j\in\mathbb{Z}} \delta_{jl}, \ \widehat{\Pi}_l = \frac{2\pi}{l} \times \Pi_{\frac{2\pi}{l}}.$$

The sampled version of $\tilde{u}$, with sampling rate T, is denoted u. It verifies for all k in $\mathbb{Z}$, $u(k) = \tilde{u}(kT)$, which can be written using a Dirac comb as

$$u = \tilde{u} \cdot \Pi_T. \tag{3.1}$$

Thanks to Fourier transform property (2.2), we know that (3.1) is equivalent, using the Fourier transform of the Dirac comb, to

$$\widehat{u} = \frac{1}{T}\left(\widehat{\tilde{u}} * \Pi_{\frac{2\pi}{T}}\right), \tag{3.2}$$

meaning that the Fourier transform of u, is a periodization, of period $2\pi/T$, of the Fourier transform of $\tilde{u}$.

3.1.2 Shannon theorem

Shannon Theorem [101] states that, given $T > 0$, if $\tilde{u} \in \mathcal{S}$ and the support of $\widehat{\tilde{u}}$ is included in $\left[-\frac{\pi}{T}, \frac{\pi}{T}\right]$, that is

$$\forall \xi \ s.t. \ |\xi| \ > \frac{\pi}{T}, \ \widehat{\tilde{u}} = 0,$$

then

$$\forall x \in \mathbb{R}, \ \tilde{u}(x) = \sum_{k\in\mathbb{Z}} \tilde{u}(kT)\mathrm{sinc}\left(\frac{x}{T} - k\right), \tag{3.3}$$

with

$$\forall t \in \mathbb{R}^*, \ \mathrm{sinc}(t) = \frac{\sin(\pi t)}{\pi t} \text{ and } \mathrm{sinc}(0) = 1.$$

This is a very powerful theorem because it means that a band-limited signal can be recovered exactly thanks to a set of (infinite) discretized samples, computing a convolution between the sampled signal and a cardinal sine function. As we said in the previous Chapter, the signal created within a microscope is band-limited so that this hypothesis suits the signals that we study. However it is impossible to get

an infinite number of samples. We have to make an hypothesis on the values of $u(k)$ outside of its set if definition, here defined as the range $\{0, ..., N-1\}$. In the following, we choose the N-periodicity hypothesis, meaning that the sampled signal u is defined by

$$\forall k \in \mathbb{Z},\ u(k+N) = u(k).$$

The computations are then performed on one period. Since we supposed that $u = \tilde{u}\Pi_T$, the N-periodicity hypothesis is also true for $\tilde{u}$.

Remark 9. *Using the periodicity hypothesis is more appropriate than for instance supposing that the signal is zero outside of the domain because according to* (3.3) *a discrete signal with constant values would be interpolated by an oscillating function (due to the sine cardinal function).*

Remark 10. *The condition on the Fourier spectrum for Shannon theorem is quite intuitive: since a sampling at rate T creates a duplication of the spectrum at a period of $2\pi/T$ (Equation* (3.2)*) in the Fourier domain, the condition $\mathcal{F}(\tilde{u}) \subset \left[-\frac{\pi}{T}, \frac{\pi}{T}\right]$ ensures that the original spectrum does not interfere with its periodization (see Figure 3.2 (a) for instance). Thus, this theorem also means that having a band-limited signal, with cut-off frequency f_{max}, sampling at frequency $2f_{max}$ is enough to recover the whole signal with Formula* (3.3)*; this frequency is sometimes called the Nyquist frequency. Choosing a smaller frequency (and then a higher sampling step) does not guarantee the equality given by Equation* (3.3) *anymore.*

3.1.3 Discrete Fourier Transform

The periodicity hypothesis is also quite convenient because it enables to use the Discrete Fourier Transform, DFT. We recall that the definition of the Discrete Fourier Transform, $\widehat{u}$, of a N-periodic signal u is

$$\forall p \in \mathbb{Z},\ \widehat{u}(p) = \sum_{k=0}^{N-1} u(k) e^{-\frac{2i\pi pk}{N}} \tag{3.4}$$

and that the inverse transform is defined as follows

$$\forall k \in \mathbb{Z},\ u(k) = \frac{1}{N} \sum_{p=0}^{N-1} \widehat{u}(p) e^{\frac{2i\pi pk}{N}}.$$

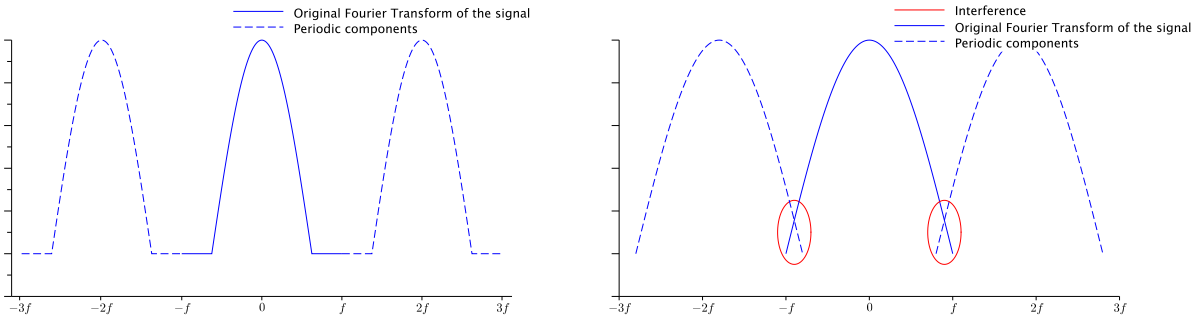

(a) DFT of a signal sampled at a correct frequency f

(b) DFT of a signal sampled at a frequency f too small

Figure 3.2: Periodization of the spectrum of band limited signals due to sampling: in (a), the sampling rate was correctly chosen (frequency higher or equal to Nyquist frequency), the periodic components do not interfere with the initial spectrum; in (b), the sampling rate was chosen too big so that there is an interference between the initial spectrum and its periodic components.

Setting $\widehat{U} = (\widehat{u}(p))_{p=0,\dots,N-1}$ and $U = (u(p))_{p=0,\dots,N-1}$, we have $\widehat{U} = FU$ with

$$F = \begin{pmatrix} 1 & 1 & \cdots & 1 \\ 1 & e^{-\frac{2i\pi}{N}} & \cdots & e^{-\frac{2i\pi(N-1)}{N}} \\ \vdots & & \ddots & \vdots \\ 1 & e^{-\frac{2i\pi(N-1)}{N}} & & e^{-\frac{2i\pi(N-1)(N-1)}{N}} \end{pmatrix}, \tag{3.5}$$

and we can see that $U = \frac{1}{N} F^* \widehat{U}$, where F^* is the transposed conjugate matrix of F.

The DFT is also N-periodic. Defining the convolution for two N-periodic signals u and v by

$$\forall j \in \{0, \dots, N-1\}, \; u * v(j) = \sum_{i=0}^{N-1} u(i) v(j-i), \tag{3.6}$$

we have, as in the continuous case, $\widehat{u * v} = \widehat{u} \cdot \widehat{v}$. The term $\frac{1}{N}$ in the definition of the inverse DFT gives that $\widehat{u \cdot v} = \frac{1}{N}(\widehat{u} * \widehat{v})$.

This means that performing the multiplication of the discrete spectra, obtained by the DFT, produces the result of the periodic convolution. We should keep this consideration in mind because in some cases, the convolution to perform is not a periodic one.

This periodization of $\tilde{u}$ enables to define the distribution $U \in \mathcal{S}'$ (see [3]) such that

$$U = \sum_{k=0}^{N-1} \tilde{u}(kT) \sum_{l\in\mathbb{Z}} \delta_{(k+lN)T} = \sum_{k=0}^{N-1} u(k) \sum_{l\in\mathbb{Z}} \delta_{(k+lN)T}.$$

Its Fourier transform is then given by

$$\begin{aligned}\forall \varphi \in \mathcal{S},\ \left\langle \widehat{U}\ ,\ \varphi \right\rangle &= \sum_{k=0}^{N-1} u(k) \left\langle \sum_{l\in\mathbb{Z}} \delta_{(k+lN)T}\ ,\ \widehat{\varphi} \right\rangle \\ &= \sum_{k=0}^{N-1} u(k) \left\langle \sum_{l\in\mathbb{Z}} \delta_{lNT}\ ,\ \tau_{kT}\widehat{\varphi} \right\rangle.\end{aligned}$$

Setting $g_k : x \longmapsto e^{-ikx}\varphi(x)$, we have

$$\begin{aligned}\forall \varphi \in \mathcal{S},\ \left\langle \widehat{U}\ ,\ \varphi \right\rangle &= \sum_{k=0}^{N-1} u(k) \left\langle \widehat{\sum_{l\in\mathbb{Z}} \delta_{lNT}}\ ,\ g_{kT} \right\rangle \\ &= \left\langle \frac{2\pi}{NT} \Pi_{\frac{2\pi}{NT}}\ ,\ \sum_{k=0}^{N-1} u(k) g_{kT} \right\rangle \\ &= \left\langle \frac{2\pi}{NT} \sum_{p\in\mathbb{Z}} \delta_{\frac{2\pi p}{NT}}\ ,\ \sum_{k=0}^{N-1} u(k) g_{kT} \right\rangle \\ &= \frac{2\pi}{NT} \sum_{p\in\mathbb{Z}} \sum_{k=0}^{N-1} e^{-ikT\frac{2\pi p}{NT}} \varphi\left(\frac{2\pi p}{NT}\right) u(k) \\ &= \frac{2\pi}{NT} \sum_{p\in\mathbb{Z}} \varphi\left(\frac{2\pi p}{NT}\right) \sum_{k=0}^{N-1} e^{-ik\frac{2\pi p}{N}} u(k).\end{aligned}$$

Using the definition $\widehat{u}(p) = \sum_{k=0}^{N-1} e^{-ik\frac{2\pi p}{N}} u(k)$, we obtain

$$\begin{aligned}\left\langle \widehat{U}\ ,\ \varphi \right\rangle &= \frac{2\pi}{NT} \sum_{p\in\mathbb{Z}} \varphi\left(\frac{2\pi p}{NT}\right) \widehat{u}(p) \\ &= \left\langle \frac{2\pi}{NT} \sum_{p\in\mathbb{Z}} \delta_{\frac{2\pi p}{NT}} \widehat{u}(p)\ ,\ \varphi \right\rangle,\end{aligned}$$

and we can see that

$$\widehat{U} = \frac{2\pi}{NT} \sum_{p \in \mathbb{Z}} \delta_{\frac{2\pi p}{NT}} \widehat{u}(p). \tag{3.7}$$

This means that the Fourier transform of U can be described with the values of $\widehat{u}(p)$, weighted by $2\pi/NT$. This formula establishes the link between the frequency coefficients of the periodic continuous signal and the coefficients of the DFT, computed with the samples of the continuous signal.

3.1.4 Aliasing

Developing the formula of periodization due to a sampling at rate T leads to

$$\forall \xi \in \mathbb{R},\ \widehat{u}(\xi) = \frac{1}{T} \left(\widehat{\tilde{u}} * \Pi_{\frac{2\pi}{T}} \right)(\xi) = \frac{1}{T} \sum_{n \in \mathbb{Z}} \widehat{\tilde{u}} \left(\xi - \frac{2\pi}{T} n \right), \tag{3.8}$$

so that in the case where $\text{supp}(\widehat{\tilde{u}}) \subset \left[-\frac{\pi}{T}, \frac{\pi}{T} \right]$, the frequencies of the sampled signal correspond to the real ones since

$$\forall \xi \in \mathbb{R},\ \forall n \in \mathbb{Z},\ n \neq 0,\ \widehat{\tilde{u}} \left(\xi - \frac{2\pi}{T} n \right) = 0.$$

However if the assumption $\text{supp}(\widehat{\tilde{u}}) \subset \left[-\frac{\pi}{T}, \frac{\pi}{T} \right]$ is not satisfied, the discretized frequency coefficients contain their real values but also "aliases" (shown in red in Figure 3.2) because the high frequencies components (higher than $\frac{\pi}{T}$) interfere with the low ones, more precisely, according to Formula (3.8), their energy will be added to the energy of the low discrete coefficients.

An operation like the sub-sampling should be performed carefully because it can create aliasing. Indeed, the "naive" method consists in taking one point over s of the discretized signal, s the sub-sampling step ($s > 1$). Given a band-limited signal $\tilde{u}$, with $\text{supp}(\tilde{u}) \subset \left[-\frac{\pi}{T}, \frac{\pi}{T} \right]$, and u its sampling at rate T, we can compute the Fourier transform of the signal created with 1 point over s, u_s, $\widehat{u_s}$,

$$u_s = u \times \Pi_s = \tilde{u} \times \Pi_{sT} \Longleftrightarrow \widehat{u_s} = \frac{1}{sT} \left(\widehat{\tilde{u}} * \Pi_{\frac{2\pi}{sT}} \right).$$

The Fourier transform is then periodized with a period of $2\pi/sT$, which is smaller than $2\pi/T$, producing aliasing. An example of this phenomenon is presented in

Figure 3.3 where a sub-sampling of $s = 2$ has been performed on the original image containing energy in the high frequency components. The aliasing effect is clearly visible on the Fourier transform (red arrows). In comparison, we present the result cutting half of the spectrum (to obtain the same size and resolution), that is

$$\widehat{u_s} = \widehat{u}\mathbb{1}_{\left[-\frac{\pi}{s};\frac{\pi}{s}\right]}.$$

However, this multiplication in Fourier by a rectangular function means a convolution in the space domain with a cardinal sine function, which can create artifacts called ringing, characterized by a duplication of the edges (in the space domain). A convolution of the image with a small Gaussian kernel can attenuate the effects of ringing, but of course it modifies the spectrum of the final image.

3.2 Operations on discretized signals using DFT

Because sampling a signal at a rate T is equivalent to periodize its spectrum at a period $2\pi/T$, any operation on the discrete image must be performed carefully. Thanks to Shannon theorem, we can define an interpolation called the Shannon interpolate [3], from which derives definitions of basic operations on images, such as zoom or translation.

3.2.1 Discrete Shannon interpolation

We now focus on the two-dimensional case, because it slightly differs from the one-dimensional one. All this part is inspired by [3], with a sampling step $T \neq 1$. Given $\Omega = \{0, \dots, N-1\} \times \{0, \dots, M-1\}$, we recall that u is the Ω-periodic discretization of $\tilde{u}$ with a sampling step value of T, $u : \Omega \to \mathbb{R}$. In the following, we suppose that N and M are odd numbers. We set U such that

$$\begin{aligned}
\forall (x,y) \in \mathbb{R}^2,\ U(x,y) &= \sum_{(k,l)\in\mathbb{Z}^2} u(k,l)\mathrm{sinc}\left(\frac{x}{T}-k\right)\mathrm{sinc}\left(\frac{y}{T}-l\right) \\
&= \sum_{(p,q)\in\mathbb{Z}^2}\sum_{(k,l)\in\Omega} u(k,l)\mathrm{sinc}\left(\frac{x}{T}-k-pN\right)\mathrm{sinc}\left(\frac{y}{T}-l-qM\right) \\
&= \sum_{(k,l)\in\Omega} u(k,l)\mathrm{sincd}_N\left(\frac{x}{T}-k\right)\mathrm{sincd}_M\left(\frac{y}{T}-l\right), \qquad (3.9)
\end{aligned}$$

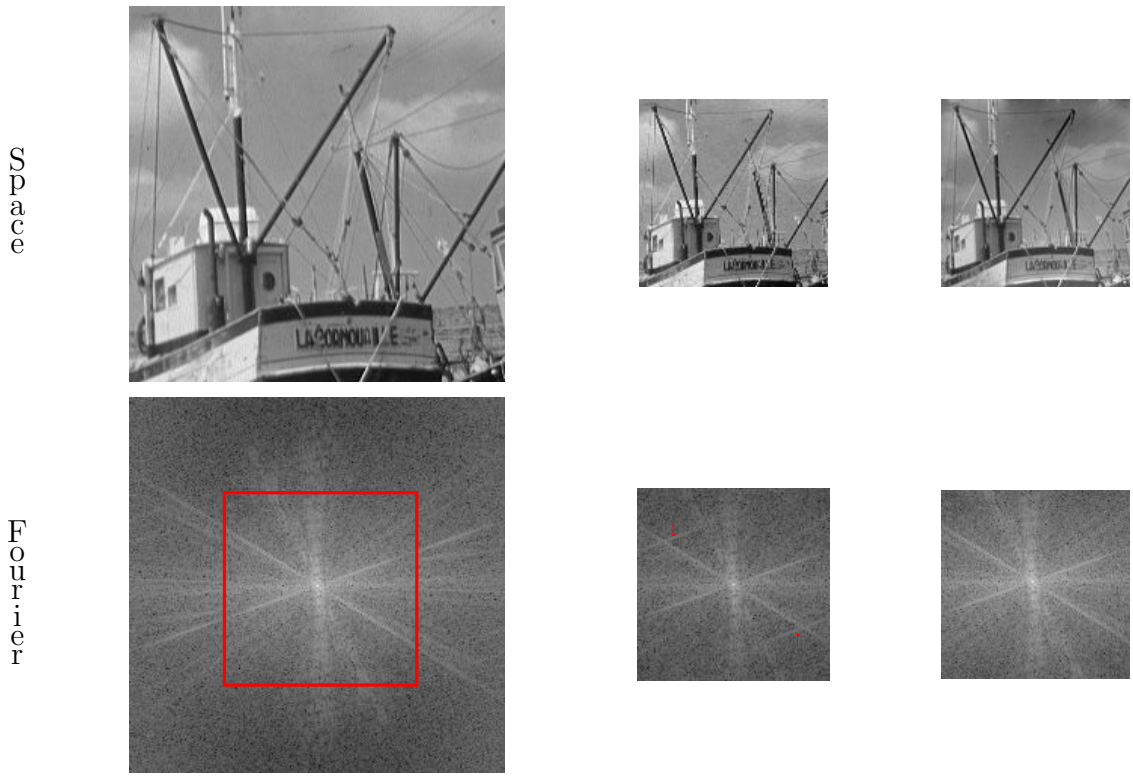

Figure 3.3: Illustration of aliasing in the case of sub-sampling; first row in the space domain, second row in the Fourier domain (modulus in logarithmic scale), from left to right: original image - sub-sampled image obtained by taking one point over two in the space domain - sub-sampled image obtained by spectrum cut. In red corresponds half of the spectrum of the original image, that is exactly the spectrum of (c). On the second column, we clearly distinguish the aliasing pointed by the red arrows. On the last image, this artifact has been avoided by cutting directly the spectrum. We can notice, in the space domain, the ringing artifact, that is the replication of some edges, due to the fact that a crop in Fourier domain corresponds to a multiplication by a cardinal sine function in the space domain.

with $\mathrm{sincd}_N(x) = \lim_{n\to+\infty} \sum_{p=-n}^{n} \mathrm{sinc}(x - pN)$. It is proven in [3] that

$$\mathrm{sincd}_N(x) = \frac{1}{N} \sum_{\alpha=-\lfloor N/2 \rfloor}^{\lfloor N/2 \rfloor} e^{2i\pi \frac{\alpha x}{N}}. \tag{3.10}$$

Formula (3.9) becomes for all $(x, y) \in \mathbb{R}^2$

$$U(x,y) = \sum_{(k,l)\in\Omega} u(k,l)\frac{1}{N}\sum_{\alpha=-\lfloor N/2\rfloor}^{\lfloor N/2\rfloor} e^{2i\pi\frac{\alpha\left(\frac{x}{T}-k\right)}{N}}\frac{1}{M}\sum_{\beta=-\lfloor M/2\rfloor}^{\lfloor M/2\rfloor} e^{2i\pi\frac{\beta\left(\frac{y}{T}-l\right)}{M}}$$
$$= \frac{1}{NM}\sum_{\alpha=-\lfloor N/2\rfloor}^{\lfloor N/2\rfloor}\sum_{\beta=-\lfloor M/2\rfloor}^{\lfloor M/2\rfloor}\sum_{(k,l)\in\Omega} u(k,l)e^{-2i\pi\left(\frac{\alpha k}{N}+\frac{\beta l}{M}\right)}e^{2i\pi\left(\frac{\alpha x}{TN}+\frac{\beta y}{TM}\right)}, \quad (3.11)$$

where we can recognize the two-dimensional discrete Fourier transform of u, $\widehat{u}$,

$$U(x,y) = \frac{1}{NM}\sum_{\alpha=-\lfloor N/2\rfloor}^{\lfloor N/2\rfloor}\sum_{\beta=-\lfloor M/2\rfloor}^{\lfloor M/2\rfloor}\widehat{u}(\alpha,\beta)e^{2i\pi\left(\frac{\alpha x}{TN}+\frac{\beta y}{TM}\right)}. \quad (3.12)$$

U is called the discrete Shannon interpolate, and is constructed with the DFT coefficients of u. From now on, it will represents the link between the discrete sampled image, and more especially its discrete Fourier transform, and the continuous image. We denote $\widehat{\Omega}$ the set of discretization of the frequencies; we have $\widehat{\Omega} = \left\{ -\lfloor\frac{N}{2}\rfloor, \ldots, \lfloor\frac{N}{2}\rfloor\right\} \times \left\{ -\lfloor\frac{M}{2}\rfloor, \ldots, \lfloor\frac{M}{2}\rfloor\right\}$.

3.2.2 Sub-pixel translation

Using (3.9), the translation of a signal of $t = (t_1, t_2) \in \mathbb{R}^2$, represented by the linear operator τ_t, is defined by

$$\forall (k,l) \in \Omega,\ \tau_t(U)(k,l) = \sum_{(i,j)\in\Omega} u(i,j)\mathrm{sincd}_N\left(\frac{k-t_1}{T}-i\right)\mathrm{sincd}_M\left(\frac{l-t_2}{T}-j\right),$$

which can be written if N and M are odd numbers, using (3.11), as

$$\forall t \in \mathbb{R}^2,\ \forall (p,q) \in \widehat{\Omega},\ \widehat{\tau_t(u)}(p) = e^{-2i\pi\left(\frac{pt_1}{TN}+\frac{qt_2}{TM}\right)}\widehat{u}(p,q). \quad (3.13)$$

It satisfies $\lim\limits_{t\longrightarrow 0}\frac{1}{t}\|\tau_t - Id\|_2$ is minimal (see [3] for a demonstration of this property).

This defines a way to compute invertible non-integer translations, which only consists in a multiplication by a complex exponential in the Fourier domain. Figure 3.4 summaries how a sub-pixel translation can be performed with this method; the steps are: compute the DFT of the image, multiply it by the exponential defined in (3.13) and compute the inverse DFT to obtain the translated image. It should be kept in mind that we set the hypothesis that the images are Ω-periodic; this explains that the translated image in Figure 3.4 presents a recopy of pixels from the bottom to the top and from the left to the right of the image.

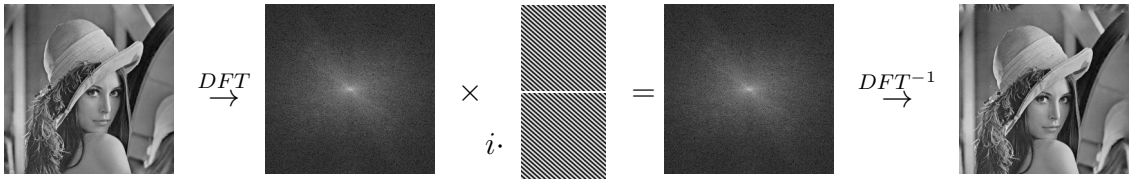

(a) Initial image | (b) DFT of (a) | (c) Exponential | (d) Multiplication | (e) Translated image

Figure 3.4: Illustration of the non-integer translation described by Formula (3.13): a translation of $t = (-16.9, 19.3)$ is performed on the image (a). The steps are: (b) computation of the Discrete Fourier Transform of the original image, (c) creation of the complex exponential defined in (3.13) with the correct value of t, (d) multiplication of (b) by (c) and (e) computation of the inverse discrete Fourier transform of the multiplication. The periodic assumption explains that the pixels from the bottom were copied on the top and the pixels from the right to the left.

3.2.3 Multiplication of discretized images

We recall the a multiplication in the space domain is equivalent to a convolution in the Fourier domain. The convolution, by its definition, produces a signal whose support is bigger than the initial signals. Due to periodicity of the Fourier transform induced by the discretization, the Fourier Transform of the signal obtained by direct multiplication can be inexact. This phenomenon is presented in Figure 3.5; we chose to multiply in the space domain the images of two Gaussian kernels with standard deviation σ, chosen so that the discrete Fourier transform, which is also a Gaussian function, vanishes quite slowly (meaning that the Gaussian signal in the space domain is quite compact, which is why we present the kernel and results only in the Fourier domain). The multiplication can be explicitly computed (it is still a Gaussian function, but not normalized) and we can compare the direct pixel-wise multiplication to the theoretical result. We can see that the computation is not exact, due to the fact that the support of the convolution of the two spectra is bigger than the size of the final image and therefore aliasing is created. The multiplication needs to be performed with another method.

According to Formula (3.12), adding zeros to the discrete Fourier transform of u does not change the value of its Shannon interpolate U. This method is called zero-padding and we will see that it enables to zoom any signal. For $M' > M$, $N' > N$, such that $M/M' = N/N'$, let us define $\widehat{u}^{zp}$ on $\widehat{\Omega}' = \left\{ -\lfloor \frac{N'}{2} \rfloor, \dots, \lfloor \frac{N'}{2} \rfloor \right\} \times$

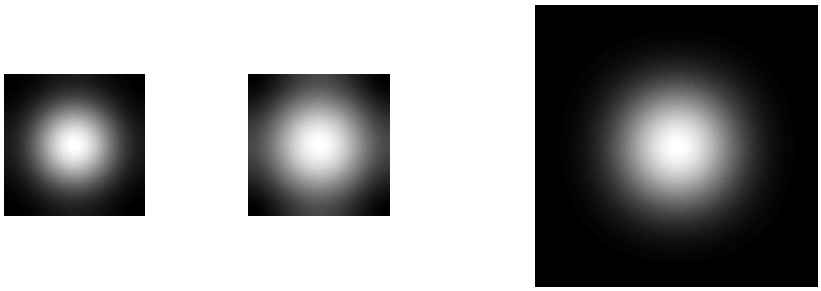

(a) DFT original signal (b) DFT direct multiplication (c) DFT multiplication after zero-padding

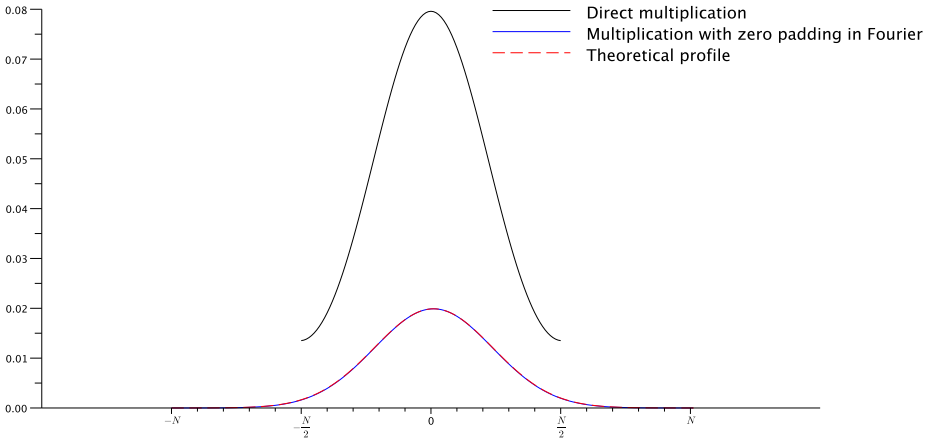

Figure 3.5: Illustration of the apparition of aliasing in the spectrum in the case of multiplication of two discrete images: (a) modulus of the discrete Fourier transform of the original image (a Gaussian function with $\sigma = 1$), (b) modulus of the discrete Fourier transform of the (direct) pixel-wise multiplication of this image by itself, (c) modulus of the discrete Fourier transform of the multiplication of the image (a) by itself using zero-padding (of factor 2), described by Formula (3.14), before pixel-wise calculation. On the images, we can guess that, in the case of direct calculation, the support is too small but the conclusion is clear looking at the horizontal section below, where the theoretical result is compared to both methods. Due to a support too small for the spectrum of the final image, the periodic convolution creates artifacts, due to the mix of the energy of the correct frequency components and the one created outside of $\widehat{\Omega}$ because of the convolution. On the contrary, using zero-padding in Fourier domain before multiplying the images creates an image with no artifacts, the values are correct, compared to the theory. The final image with zero-padding is twice bigger than the input image and has a twice thinner sampling rate.

$\left\{ -\lfloor \frac{M'}{2} \rfloor, \ldots, \lfloor \frac{M'}{2} \rfloor \right\}$ by

$$\forall (p,q) \in \widehat{\Omega}', \ \widehat{u}^{zp}(p,q) = \begin{cases} \widehat{u}(p,q) \text{ if } |p| < N/2, |q| < M/2 \\ 0 \quad \text{otherwise} \end{cases}. \tag{3.14}$$

The inverse discrete Fourier transform of $\widehat{u}^{zp}$ is

$$\forall k \in \Omega',\ u^{zp}(k,l) = \frac{1}{N'M'} \sum_{(p,q)\in\Omega'} \widehat{u}^{zp}(p,q) e^{-\frac{2i\pi kp}{N'}} e^{-\frac{2i\pi kq}{M'}},$$

which is the DFT of u, weighted by a factor $MN/M'N'$. We recall that u was chosen so that $u(k,l) = \tilde{u}(kT, lT)$ and whose DFT coefficients are defined as in Formula (3.4). Therefore, we have the equality

$$\frac{M'N'}{MN} u^{zp}(N'-1, M'-1) = u(N-1, M-1) = \tilde{u}((N-1)T, (M-1)T)$$

which leads to

$$\forall (k,l) \in \Omega',\ u^{zp}(k,l) \propto \tilde{u}(kT', lT'),\ \text{with } T' = T \times N/N'.$$

Since $N' > N$ and $M' > M$, it comes that $T' < T$, meaning that the signal was zoomed by a factor $z = M'/M = N'/N$, without modifying the Shannon interpolate.

This operation defines the first step to perform before multiplying two discrete images v and w: we first compute the corresponding $\widehat{u}^{zp}$ and $\widehat{v}^{zp}$ using Formula (3.14) and then compute the pixel-wise multiplication. A zoom of 2 ensures that the periodizations of the two spectra do not interfere, however if the image are known to be band-limited, a zoom leading to a size bigger than the (integer) discrete value of $\text{supp}(\widehat{v}) + \text{supp}(\widehat{w})$ is enough. The result of the multiplication of the Gaussian kernels is presented in comparison to the direct calculation in Figure 3.5 and shows that this method enables to compute correctly the spectrum. A zoom of 2 was compulsory in this case because the support of the initial spectrum is the entire domain $\widehat{\Omega}$. The support of the convolution is bigger than $\widehat{\Omega}$; in the case of the direct computation, the energy of the frequency coefficients outside of the initial support, were added to the ones inside $\widehat{\Omega}$, leading to the wrong result.

Remark 11. *The only requirement for creating $\widehat{u}^{zp}$ is that M', N' are integer values, meaning that any zoom $z \in \mathbb{R}$ such that $z = M'/M = N'/N$, with M', N' and M,N integers can be performed.*

Another advantage of this method as a zoom method is that it does not create false values for the unknown frequency coefficients, contrary to some other interpolation methods (see Figure 3.6 where several methods are compared to this one, in space and Fourier domains). This property can be useful for posterior treatment of the image.

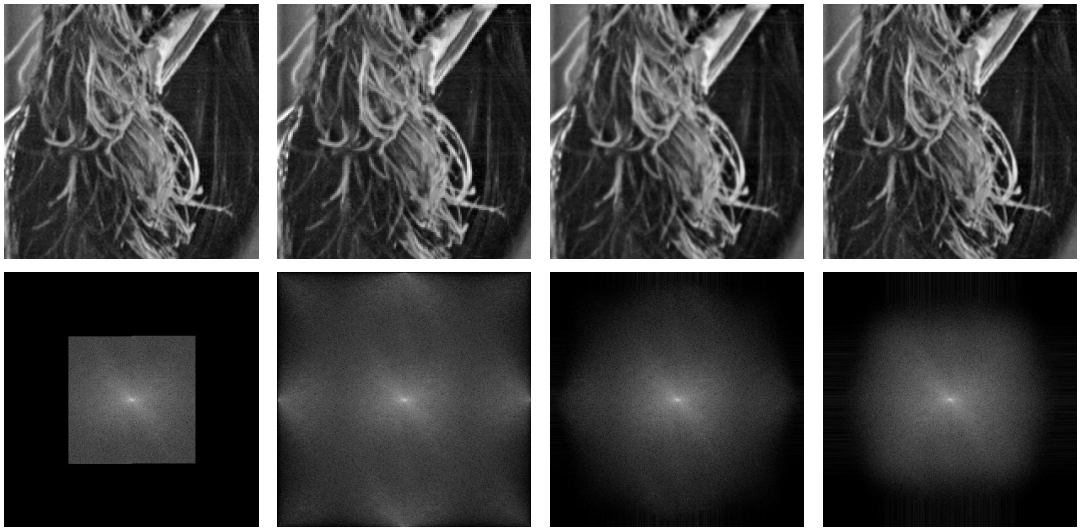

Zero-padding Nearest neighbor Bilinear Spline

Figure 3.6: Comparison of zoom methods; a zoom (of factor 2) on the image of Figure 3.4 was performed, on the first row we present only a crop of the zoomed image (part of her hat); on the second row, we present the Fourier spectrum (in logarithmic scale) of the whole images. The methods used are: zero-padding in the Fourier domain, nearest neighbor interpolation, bilinear interpolation and spline interpolation (order 5). Except for the nearest neighbor interpolation, results in the space domain seem visually quite similar on this image. However, in the Fourier domain, some information was "created" in the three other methods. Zero-padding preserves exactly the spectrum of the original image.

3.2.4 Subsampling and convolution with band-limited signals

According to Formula (3.12) again, we can notice that if the discrete Fourier coefficients of u are zero outside a certain domain $[\![-\rho, \rho]\!]^2$, the interpolate is not modified by taking only the coefficients of the DFT, $(\alpha, \beta) \in [\![-\rho, \rho]\!]^2$. If we denote u_s the image whose discrete Fourier Transform is composed of those of u on the domain $[\![-\rho, \rho]\!]^2$, the number of coefficients in the discrete spectrum is reduced (in comparison to u) creating an image with a different sampling. The sampling of u_s is given by $T' = (T'_x, T'_y)$ with

$$T'_x = T \times \frac{N}{2\rho + 1} > T \text{ and } T'_y = T \times \frac{M}{2\rho + 1} > T.$$

Remark 12. *As we explained before, the PSF φ (as well as the illumination pattern), is band-limited, meaning that the coefficients of its Fourier transform equal*

zero outside of the disk centered on the frequency 0 and of radius f_{max}, the cut-off frequency. Using Formula (3.7), we can compute the discrete cut-off frequency in each direction, p_{max} and q_{max}, given by

$$\frac{2\pi p_{max}}{NT} \geq f_{max}, \ \frac{2\pi q_{max}}{MT} \geq f_{max},$$

so that the discrete frequency coefficients outside of the elliptical domain defined by

$$\left\{(p,q); \left|\frac{p}{p_{max}}\right|^2 + \left|\frac{q}{q_{max}}\right|^2 \leq 1\right\} \text{ with } p_{max} = \left\lceil \frac{f_{max}NT}{2\pi} \right\rceil \text{ and } q_{max} = \left\lceil \frac{f_{max}MT}{2\pi} \right\rceil$$

equal zero. Only the frequency coefficients between $[\![-p_{max}, p_{max}]\!] \times [\![-q_{max}, q_{max}]\!]$ are necessary to compute the multiplication of the spectra, representing the convolution.

What is interesting for the ISM model, is that given the PSF φ and the sample u at a different resolution, the convolution can be performed at the resolution of φ, with no loss of information, for the same reason: φ is band-limited, the frequency coefficients outside of the disk of radius equal to the discrete value of f_{max} are null.

3.2.5 Non-periodic convolution

However, we recall that multiplying the discrete Fourier transforms on $\widehat{\Omega}$ to compute the convolution performs the Ω-periodic convolution. However, the hypothesis of periodicity is not true and can create artifacts, on the border of the image, as shown in Figure 3.7, due to the "copy", the periodization, of the image on each border of the original image. We therefore present how to use the periodic convolution to be able to compute a non-periodic convolution.

In the following, the explanation is described for one-dimensional signal for an ease of read, but could be transposed in two dimensions straightforwards. We recall that the non-periodic convolution, represented by the operator $\circledast$, between u and v both defined on $[\![0, N-1]\!]$ is given by the formula

$$\forall k \in [\![0, 2N-2]\!], \ w(k) = u \circledast v(k) = \sum_{\substack{l \in [\![0,N-1]\!] \\ k-l \in [\![0,N-1]\!]}} u(l)v(k-l). \tag{3.15}$$

Let us now consider the extended signals $\check{u}$ and $\check{v}$, of size $2N-1$, such that

$$\check{u}(k) = \begin{cases} u(k) \text{ if } k < N \\ 0 \quad \text{otherwise} \end{cases} \text{ and } \check{v}(k) = \begin{cases} v(k) \text{ if } k < N \\ 0 \quad \text{otherwise} \end{cases}, \tag{3.16}$$

then we have that $u \circledast v(k) = \check{u} * \check{u}(k)$ with the operator $*$ as defined in Formula (3.6), representing the periodic convolution. By adding some zeros to the original signal, we can use the periodic convolution (that is the one performed multiplying the two spectra obtained by discrete Fourier transforms) to compute the non-periodic one. Since the convolution kernel, in our case the point spread function of the optical device, φ, has a smaller (spatial) support than the biological sample, u, the number of additional zeros should equal the (discrete) size of the support of φ (along each direction). By adding half of this number on each border of the image, the non-periodic convolution is obtained by cropping the center of the image. Figure 3.7 compares the computation with and without the additional zeros.

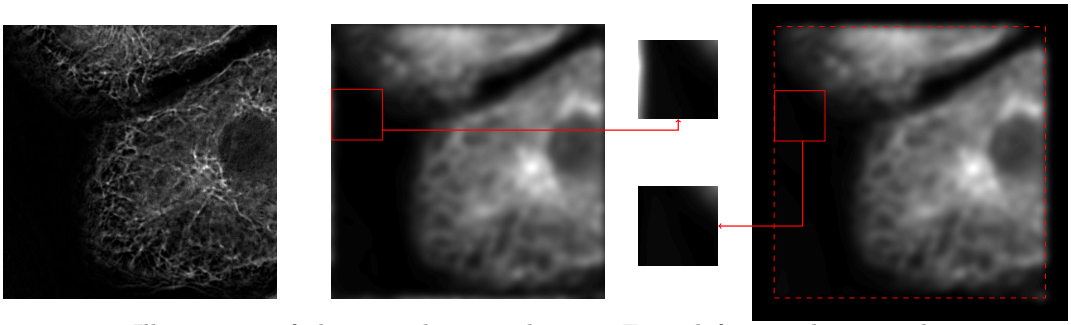

Figure 3.7: Illustration of the periodic convolution. From left to right: initial image - initial image convolved with a Gaussian kernel φ, computing the inverse Fourier transform of the product of the two spectra - crops corresponding to the same area of interest on both results - initial image convolved with the same Gaussian kernel k, with zeros added, divided on both sides, along each direction, before computing the product of the two Fourier spectra, followed by the inverse Fourier transform. The rectangle in dashed line represents the result of the non-periodic convolution, with same size as the initial image. The crop area, chosen on the border of the initial image, shows the effect of the periodic convolution. Even if it is barely visible on the image of the whole sample, due to the fact that these pixels have a lower value in comparison with the rest of the pixels, this phenomenon is noticeable all along the border of the image. The extension with zeros enables to remove the artifact.
Original image from cellimagelibrary.org by Michael Cammer and Phyllis Novikoff.

3.3 Discretization of an ISM method

In the following, using the different definitions of the operations on discretized images developed in the previous section, we describe the discretization of the physical process of the Image Scanning Microscopy, represented by the operator H.

Before going into the description of this discretization, we would like to recall that the images of an ISM method are acquired by a camera. This camera has a (fixed) sampling step of r_c. The only requirement about r_c is that it enables to see the smallest visible details, meaning that it should be smaller than the limit described by Abbe, that is

$$r_c \leq \frac{\lambda}{2NA},$$

for a wavelength λ and an objective with numerical aperture NA.

As explained in Remark 10, the scanning distance between two points should be at least $\lambda/(4NA)$. The scanning points are not necessarily equally distributed on the sample, but we suppose that between two consecutive points, this condition is respected.

Taking $\lambda = 480$nm, $NA = 1$, we then have to take an image every 120 nm, meaning that for imaging a 10µm×10µm area, we need around 7000 scanning positions (meaning 7000 images). On top of that, if we use various illumination patterns, we might need this number of scan points for each of them, leading to several tens of thousands of images. That is the reason why we try to minimize the size of the different operations we present afterwards, so that the implementation needs as less memory as possible and also so that the algorithms using this discretization are as fast as possible.

As explained in Chapter 2, the continuous formulation of an ISM problem is described for a scanning point X_s by

$$\forall x \in \mathbb{R}^2,\ \widetilde{I}_u^s(x, X_s) = \left(\left(\tilde{u}(\cdot) \times \tilde{D}^s(\cdot - X_s)\right) * \tilde{\varphi}(\cdot)\right)(x), \tag{3.17}$$

We suppose that $\tilde{u}$, $\tilde{D}^s$ and $\tilde{\varphi}$ are periodic and band-limited (true for $\tilde{D}^s$ and $\tilde{\varphi}$ which are created within the microscope). Since multiplication and convolution can be written as linear operators, we can find H such that the discretized version of $\widetilde{I}_u^s$, I_u^s can be written as

$$I_u^s = Hu.$$

We now present how to discretize the operator H; using the Shannon interpolate, we can transpose the continuous formulation of H in the discrete domain. The only constraint is the assumption of periodicity on the sample, but we only work on one period.

3.3.1 Description of the operator H

Since we have a sampling step of r_c on the camera, $I_u^s(p,\cdot)$ represents the continuous sample at $p \cdot r_c$, that is

$$\forall p \in Z^2,\ \forall (X_s)_{s\in[\![1,S]\!]},\ I_u^s(p,X_s) = \widetilde{I}_u^s(p \cdot r_c, X_s).$$

The continuous image describing the imaged sample (or more precisely its local density of fluorophores) can be represented with a discrete image $u(k,l)$, $k \in [\![0, N-1]\!]$, $l \in [\![0, M-1]\!]$ thanks to Shannon Theorem. The image u is supposed to be sampled with sampling step of r_u, $r_u < r_c$, since u has a better resolution than I_u^s, it should contain smaller details than $\lambda/(2NA)$ (otherwise, super-resolution is not needed). The discretized operator H enables to compute the images $(I_u^s(p,X_s))_{p\in[\![0,n-1]\!]\times[\![0,m-1]\!],\ s\in[\![1,S]\!]}$ from u. The $(I_u^s(p,X_s))_{p,s}$ are called "micro-images" because their size and resolution are smaller than the ones of u.

If we concatenate all the transposed rows of the image u (creating a one-dimensional signal u^c of size $N \times M$) and if we note (n,m) the sizes of the micro-images obtained, the operator $H : \mathbb{R}^{N\times M} \longrightarrow R^{n\times m\times S}$ can be written matricially as

$$H = \begin{pmatrix} \left[\begin{smallmatrix} h_{0,0} \\ \vdots \\ h_{nm-1,0} \end{smallmatrix}\right] & \textit{impact of } u^c(0) \textit{ on the first micro-image} & \cdots & \left[\begin{smallmatrix} h_{0,N} \\ \vdots \\ h_{nm-1,N} \end{smallmatrix}\right] & \textit{impact of } u^c(N-1) \textit{ on the first micro-image} \\ \vdots & & & \vdots & \\ \left[\begin{smallmatrix} h_{S(n-1),0} \\ \vdots \\ h_{Snm-1,0} \end{smallmatrix}\right] & \textit{impact of } u^c(0) \textit{ on the last micro-image} & \cdots & \left[\begin{smallmatrix} h_{S(n-1),N} \\ \vdots \\ h_{Snm-1,N} \end{smallmatrix}\right] & \textit{impact of } u^c(N-1) \textit{ on the last micro-image} \end{pmatrix}.$$

Discretized sample pixels $(u^c(k))_{k\in[\![0,N\times M-1]\!]}$ (→)

Micro-images pixels (S×n×m) (↓)

In practice, H is never computed as a matrix, because its size is quite big and because it is, in reality, very sparse. The two main operations composing H are the multiplication of the discretized sample with the discretized illumination pattern and the convolution with the discretized PSF. However for the first one, we also need to compute the illumination at the correct resolution and positioned at laser impact X_s. In addition to that, we have to perform a sub-sampling, to reach the camera sampling step, r_c.

In the following, we consider that the laser positions $(X_s)_{s\in[\![1,S]\!]},\ X_s \in \mathbb{R}^2$, are known precisely. They are not necessarily located on one pixel of the discrete image u, requiring a non-integer translation to position the illumination at the exact location of the impact. A discretized version of each illumination pattern, noted D^s, at a sampling rate r_D and size N_D, centered on X_D ($X_D \in \mathbb{R}^2$ can to be made of non integer values, but each coordinate belongs to $[0, N_d - 1]$; for an ease of writing, we suppose that all the illumination patterns are centered on the same point) and a discretized version of the PSF, φ, at a sampling rate r_c (the same as the measured micro-images) and size N_φ (odd number) and supposed centered on the middle of the image are given.

Remark 13. *The term "centered" for the illumination is not totally exact because it implies that it is isotropic which is not always the case, as it will be presented in the next section. It means that the image D^s is the result of the illumination pattern when the laser corresponding to the shape projected in scanning point X_s impacts at position X_D. However we may employ "centered" in the following, always in that sense when it concerns the illumination patterns.*

Remark 14. *If the PSF is given at a different sampling rate then r_c, a spectrum cut can be performed to reach the sampling rate r_c with no loss of information. Anyway, the PSF and the illumination patterns are either calibrated with theoretical formula or obtained thanks to a calibration that is performed using the same camera as for the acquisition. In the first case, the sampling rate can be a parameter of the model, and in the second one, the sampling rate should be directly r_c or proportional to r_c.*

3.3.2 Considerations on the signals

In the following, we consider that all the sizes used during the different operations on the images are the same along both directions, so that it simplifies the writing. In particular, we have for the final micro-images $n = m$. This choice can be questionable if the illumination pattern has a privileged orientation, that is its shape is really bigger in one direction than in the other one, but the calculations could easily be adapted to this case.

We suppose that $\mathrm{supp}(\widehat{\tilde{u}}) \subset [-\pi/r_u, \pi/r_u]^2$. Since the illumination pattern $\widehat{\tilde{D}^s}$ and the PSF $\widehat{\tilde{\varphi}}$ are created within the microscope, they are band-limited, with respective supports $\mathcal{B}(0, f'_{max})$ and $\mathcal{B}(0, f_{max})$, if we take into account that their wavelengths

are not the same. In addition to be band-limited, we assume that each illumination pattern condenses most of its intensity around its impact position. This means that for any discretized illumination pattern, d, with sampling rate r_d, of size N_d, projected at position (X, Y), we can compute an "area of action" of the illumination, centered on (X, Y) and whose radius R_d is defined as

$$R_d = r_d \cdot \widetilde{R}_d \text{ with } \widetilde{R}_d = \min_R \left\{ \frac{\sum\limits_{k\in[\![X-R,X+R]\!],\ l\in[\![Y-R,Y+R]\!]} d(k,l)}{\sum\limits_{k\in[\![0,N_d-1]\!],\ l\in[\![0,N_d-1]\!]} d(k,l)} > \alpha \right\},\ \alpha \in [0.9, 1]. \tag{3.18}$$

This is also true for the PSF, for which we consider that all its energy is condensed in the circle centered on the middle of the PSF and of radius pr_a, where r_a is the Airy radius (in nanometer) and p can be seen as a virtual pinhole, as in the confocal method. This virtual pinhole also permits to remove out of focus light.

Remark 15. *Given a representation of d at resolution r the value in pixel of the radius is given by R_d/r.*

Remark 16. *The hypotheses that the images are both band-limited and with spatial compact support are in reality incompatible. This is an approximation we have to make to be able to perform the calculations.*

3.3.3 Multiplication sample - illumination pattern

Zero-padding and crop of the sample for the multiplication

The multiplication between the sample u and the illumination pattern should be performed at the resolution of u since it has the best resolution. The image of the illumination pattern should then be zoomed to reach the resolution r_u. However, as we mentioned before, the multiplication cannot be performed directly pixel-wise, because there is a risk of aliasing in the spectrum of the resulting image. A first step of zero-padding should be performed. An extension by zeros of the spectrum of u to reach the double of its initial size (that is a resolution of $r_u/2$) assures the correct calculation. However, since we now that the illumination is band-limited, we can compute the discrete value of the frequency cut defined using Equation (3.7), $\rho_{D^s}^{r_u}$, given by

$$\frac{2\pi\rho_{D^s}^{r_u}}{N' r_u} = f'_{max} \Leftrightarrow \rho_{D^s}^{r_u} = N' r_u \frac{f'_{max}}{2\pi},\ N' = \max(N, M).$$

We define u_z for $p = (p_1, p_2) \in [0, N + (2 \times \lceil \rho_{D^s}^{r_u} \rceil] \times [0, M + (2 \times \lceil \rho_{D^s}^{r_u} \rceil]$ by

$$\widehat{u_z}(p_1, p_2) = \begin{cases} \widehat{u}(p_1, p_2) & \text{if } (p_1, p_2) \in [\![-\frac{N}{2}, \frac{N}{2}]\!] \times [\![-\frac{M}{2}, \frac{M}{2}]\!] \\ 0 & \text{otherwise} \end{cases}.$$

By this action of zero-padding, a zoom is performed; its factor z_p is defined by

$$z_p = (N + 2\lceil \rho_{D^s}^{r_u} \rceil + 1)/N$$

and defines the resolution of the produced image u^z: $r_p = r_u/z_p$ ($r_p < r_u$), which will also be the resolution of the zoomed illumination patterns.

Since we supposed that this pattern is also spatially condensed, we do not need to compute the multiplication on the whole domain of u. This permits to define the minimal size N_p, according to the resolution r_p on which the product should be computed. Using Formula (3.18) N_p should respect $N_p \geqslant R_{D^s} \cdot r_p$. For each laser position, a crop of u^z of size N_p is computed. The position of this crop depends on the laser position X_s, since each scan point corresponds to a different area on the image. It is chosen so that the illumination impact is more or less in the middle of the crop, that is setting $C_s \in \mathbb{R}^2$ the top-left corner of the crop on u^z, it is chosen such that

$$C_s = \left\lfloor \frac{X_s}{r_p} - \frac{N_p}{2} \right\rfloor.$$

Translated and zoomed illumination patterns

The image of the illumination pattern should be zoomed to reach the resolution r_p and translated to impact at the exact laser position. Given D^s the discrete distribution, we denote $\tilde{D}^s$ its interpolate, which satisfies $\forall k \in \mathbb{Z},\ \tilde{D}^s(k) = D^s(k)$. We recall that a zoom z of $\tilde{D}^s$, $\tilde{D}^s_z$, is defined by

$$\forall k \in \mathbb{Z}^2,\ \tilde{D}^s_z(k) = \tilde{D}^s\left(\frac{k}{z}\right),$$

and a translation of $\beta \in \mathbb{R}^2$, $\tau_\beta(\tilde{D}^s)$, by

$$\forall k \in \mathbb{Z}^2,\ \tau_\beta(\tilde{D}^s)(k) = \tilde{D}^s\left(k - \beta\right).$$

Combining those two formulas we have that

$$\forall k \in \mathbb{Z}^2,\ \tau_\beta\left(\tilde{D}^s_z(k)\right) = \tilde{D}^s_k\left(\frac{k}{z} - \frac{\beta}{z}\right) = \tilde{D}^s_k\left(\frac{k - \beta}{z}\right), \tag{3.19}$$

meaning that we can compute those operations in one or the other order: either we first translate of β and then zoom the result, or we zoom first and translate of β/z.

However, we cannot compute the illumination pattern on $\mathbb{Z}^2$ as in Formula (3.19); it is computed on a number of pixels $N_p \times N_p$, containing the whole "area of action" of the illumination, as it was defined in Formula (3.18). The value of the zoom z_d to perform on the given distribution D^s is

$$z_d = \frac{r_D}{r_p}.$$

In the zoomed image, at resolution r_p, the center of the distribution is located in $X_D \times z_d$, and needs to be shifted to $(X_s/r_p - C_s)$, that is the position of the exact scanning point, at the correct resolution, on the image cropped with top-left corner C_s. The translation is then defined by $t \in \mathbb{R}^2$ such that

$$t = X_D \times z_d - \left(\frac{X_s}{r_p} - C_s\right).$$

We choose to first perform the zoom using Formula (3.14) and then compute the translation t using Formula (3.13). We can define the DFT of D_z^s, using the discrete value of the cut-off frequency of the initial distribution of size N_d and resolution r_d,

$$\forall p \in \left[\!\left[-\frac{N_p}{2}, \frac{N_p}{2}\right]\!\right]^2, \ \widehat{D_z^s}(p) = \begin{cases} e^{-2i\pi\left(\frac{p_1 t_1}{N_p} + \frac{p_2 t_2}{N_p}\right)} \widehat{D^s}(p) & \text{if } |p| < \left\lceil N_d r_d \frac{f'_{max}}{2\pi} \right\rceil \\ 0 & \text{otherwise} \end{cases}.$$

Now the pixel-wise multiplication can be properly computed, multiplying D_z^s and u_z.

3.3.4 Convolution with the PSF

This result of the multiplication has to be convolved with φ, to create the image I_u^s. We have to be be sure that the domain of computation is large enough to avoid the effect due to periodic convolution, as explained in Subsection 3.2.5.

Link between the sizes of the images for the different operations

As mentioned before, we chose that the sizes of the micro-images are equal in both directions, that is $n \times n$. We also choose that n is odd and then written as

$n = 2n_1 + 1$. n_1 should be chosen so that the whole PSF is inside the micro-image. Since the sampling step is r_c, we have that the minimal value of n_1 is given by

$$n_1 = \left\lceil \frac{pr_a}{r_c} \right\rceil .$$

This size must enable in the Fourier domain to represent all the frequency coefficients smaller than f_{max}; this can be check using Formula (3.7). This micro-image is the result of a convolution, meaning that the pixels contributing to its computation are the one located at less pixels than the discrete value of the radius of the PSF. Performing the convolution on a size $(n+2n_1) \times (n+2n_1)$ and keeping only the middle part, from n_1 to $n+n_1-1$ in each direction, avoids the effect due to periodicity (only present on the bands 0 to $n_1 - 1$ and $n + n_1$ to $n + 2n_1 - 1$) and takes into account all the necessary pixels. In the case where the micro-image is on the border of the captor of the camera, spatial zero-padding, as described in Formula (3.16), has to be performed, in order to reach the size $(n + 2n_1) \times (n + 2n_1)$.

The last constraint is given by the fact that the micro-image used for convolution, of size $2n - 1$ and this image of the discrete multiplication of size N_p correspond to the same image, at two different resolutions, whose factor is given by r_c/r_p. Then the value n and N_p must satisfy

$$2n - 1 = N_p \times \frac{r_c}{r_p} \text{ with } n \geqslant 2 \left\lceil \frac{pr_a}{r_c} \right\rceil \text{ and } N_p \geqslant R_{D^s} \cdot r_p. \tag{3.20}$$

Remark 17. *The values of N_p and r_p, that are not completely fixed but defined by a lower boundary for the first, an upper one for the second, have to be chosen so that $N_p r_c/r_p$ is an integer and odd value.*

Convolution (and sub-sampling)

We recall that φ is sampled at the resolution of the camera, r_c, and we suppose that $N_\varphi = 2n-1$. We choose to compute the convolution as the multiplication of the spectra in the Fourier domain. $\tilde{\varphi}$ is band-limited meaning that all the coefficients of the DFT beyond the discrete value of f_{max} are null. According to Subsection 3.2.4, we can directly sub-sample the product between the crop of u_z and D^s to the resolution of the camera, using spectrum cut, to reach a size of $2n - 1$ (and a resolution of r_c thanks to the first Formula (3.20)). The two discrete spectra are then multiplied to create the image of the (periodic) convolution. As explained in the previous paragraph, a final spatial crop of size $n \times n$ in the middle of the computed

image produces the image corresponding to the non-periodic convolution.

Example: acquiring images with a camera of sampling step $r_c = 100$nm, illuminating with a wavelength $\lambda = 480$nm, and using an objective of numerical aperture $NA = 1$ ($r_c < \lambda/(2NA) \sim 120nm$), we have that $r_a \simeq 313.3$nm. With a pinhole of $p = 1.3$, we compute $n \geq 11$, the other sizes are computed according to the illumination pattern, as presented before.

Remark 18. *We said earlier that the matrix H was sparse; indeed since the illumination patterns are spatially quite compact, their impact at a laser position X on the sampled signal u has consequences only around X. This means that changing one pixel value of the super-resolved image only impacts the micro-images acquired close to this pixel.*

A summary of the steps to compute the micro-images, I_u^s, from the sampled image u is presented in Algorithm 1.

Algorithm 1: Computing Hu from $u = (u(k,l))_{k\in[\![0,N-1]\!],l\in[\![0,M-1]\!]}$

Input - $(X_s)_{s\in[\![1,S]\!]}$, laser impact positions
- $u = (u(k,l))_{k\in[\![0,N-1]\!],l\in[\![0,M-1]\!]}$
- φ at resolution r_c, size $N_\varphi = 2n-1$ and centered
- D^s at resolution r_D, size N_D and corresponding to impact laser in X_D

Output $(MI_s(k,l))_{(k,l)\in[\![0,n-1]\!]^2,\ s\in[\![0,S-1]\!]}$

$u_z \leftarrow$ zero-padding(u, z_p)
for $s \in \{1 \dots S\}$ **do**
  $v_s \leftarrow u_z(C_s : C_s + N_p - 1)$
  $t \leftarrow X_D \times r_d/r_p - (X_s/r_p - C_s)$
  $D_z^s \leftarrow$ zero-padding(D^s, z_d) ▶ Formula (3.14)
  $D_z^t \leftarrow \tau_t(D_z^s)$ ▶ Formula (3.13)
  $v_p \leftarrow v_s \times D_z^t$
  $(\widehat{v_c}(p))_{p\in\mathcal{B}\left(0,\lceil\frac{\pi}{r_c}\rceil\right)} \leftarrow \widehat{v_p}(p)$
  $p \leftarrow \mathcal{F}^{-1}(\mathcal{F}(v_c) \times \mathcal{F}(\varphi))$
  $MI_s \leftarrow p(n_1 : n + n_1 - 1, n_1 : n + n_1 - 1)$
end for
return $(MI_s)_{s\in[\![1,S]\!]}$

3.4 Advantages of singular illumination patterns

Thanks to conical diffraction in biaxial crystal [10], a whole family of unusual-shaped illumination patterns can be created. Some of them are presented in Figure 3.8 and in Figure 3.9, we show that they respect the criterion of spatial consistence of Formula (3.18).

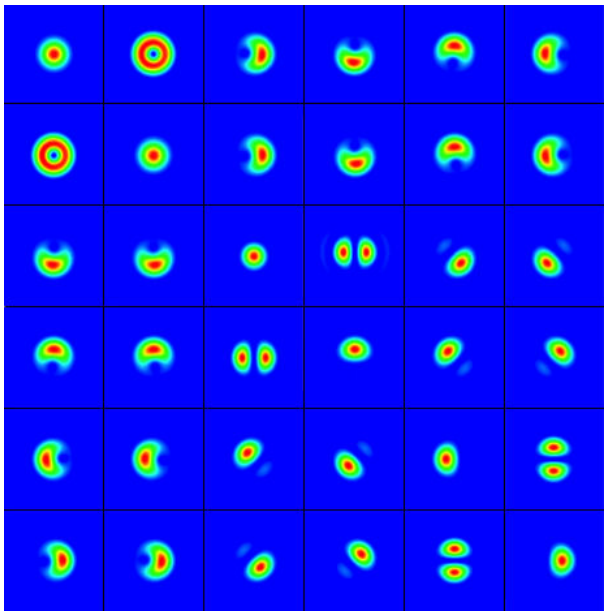

Figure 3.8: Examples of illumination patterns that can be obtained thanks to conical diffraction. Some of them are really similar, only differ by a specific rotation and could be obtained with any angle. Their shapes are quite unusual and some of them have interesting properties in the Fourier domain, as shown in Figure 3.10.

Presented in [22], the BioAxial super-resolution module, which is the one we will simulate in the last Chapter, contains a beam shaper, using conical diffraction. This beam shaper enables to create what we call *half moon* patterns. These patterns are presented in Figure 3.10, in both Fourier and space domains, with 4 angles $\{0, 45, 90, 135\}$ degrees. We can see that their shape in the Fourier domain is atypical, with higher energy along the same axis as the lobes of the half-moons. According to the formula developed in Chapter 2, we can then compare a conventional system with a dual conventional system, using the vertical half-moon, as shown in Figure 3.11. With no doubt, when projecting a half-moon, the dual conventional OTF is better than the conventional: the energy in the frequency coefficients around f_{max} is

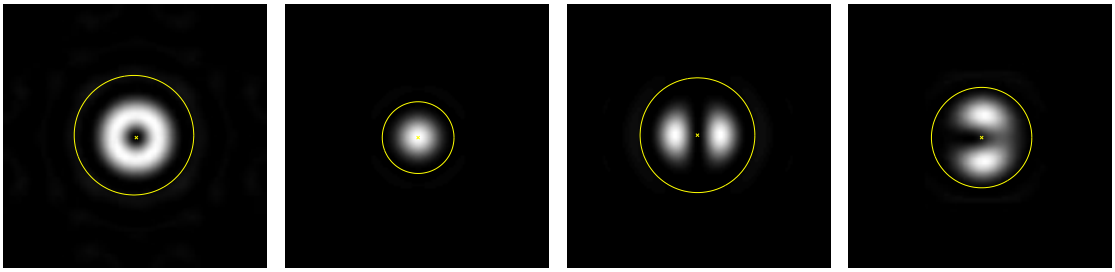

Figure 3.9: Examples of illumination patterns; from left to right: a vortex, having a donut shape, a fundamental, whose shape is very close to the Airy spot, a half-moon, made of two lobes whose orientation can be chosen, and a deformed half-moon. The cross corresponds to the laser impact of each distribution (as we specified, on the last example, for instance, the shape is not isotropic) and the circle in red corresponds to the radius in (3.18) with $\alpha = 0.9$.

higher for half moons. The number and the angles of the half-moons are chosen so that the sum of the spectra recovers almost the disk of radius f_{max}. The advantage of the half-moon patterns in the ISM methods is clear when looking at Formula (2.19), since the value of the illumination pattern close to f_{max} weights the value of $\hat{u}$ close to $2f_{max}$.

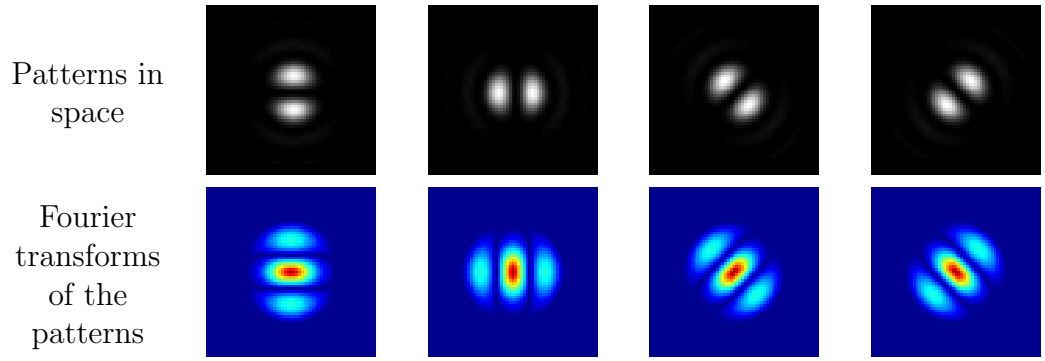

Figure 3.10: In the first line, the four illumination patterns generated by a beam shaper and used by the BioAxial system, called half-moons, are represented. As it can be seen on the module of their Fourier Transforms (second line), the energy in the frequency coefficients along the axis of the half-moons is higher than along the orthogonal axis. The sum of the four Fourier transforms almost covers the whole Fourier domain, explaining why 4 half-moons are used (3 could also be sufficient).

Remark 19. *To be able to compute the image created by a dual conventional system, the laser positions need to be accurate and regular.*

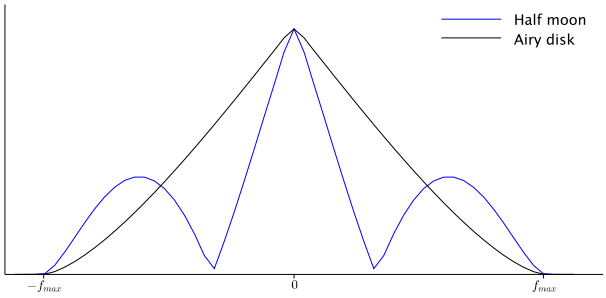

Comparison of the OTFs for conventional and dual conventional.

Figure 3.11: The comparison between the profiles of the spectra of the Airy disk and the vertical half moon clearly shows that near f_{max}, the frequency coefficients of the half moon contain more energy than the corresponding coefficients of the Airy disk. The reconstruction of the dual conventional, whose OTF is the Fourier transform of the half-moon, should produce images that provide a better representation of the frequency coefficients in the direction of the half-moon. However, several of them should be used since their shape is asymmetrical.

3.5 Minimum Variance unbiased estimate

The continuous formulation of the acquisition with Gaussian noise is given, for one illumination pattern D, by

$$\begin{aligned} &I_u(X_s, X_c) = (u \times D(\cdot - X_s)) * \varphi(X_c) + n(X_s, X_c), \quad n(X_s, X_c) \sim \mathcal{N}(0, \sigma) \\ \Leftrightarrow &I_u(X_s, X_c) \sim \mathcal{N}(f(X_s, X_c), \sigma), \end{aligned}$$

with $f(X_s, X_c) = u \times D(\cdot - X_s)) * \varphi(X_c)$.

If we have the equality $N = N_s$, we can write the 4D Discrete Fourier Transform of f as

$$\forall (p, q) \in \widehat{\Omega}^2, \ \widehat{f}(p, q) = \widehat{\varphi}(q)\widehat{D}(-p)\hat{u}(p + q) = \widehat{\alpha}(p, q)\hat{u}(p + q),$$

where $\widehat{\Omega}$ is a discretization of the set of frequencies $[-f_{max} : f_{max}]$. We denote $\widehat{\Omega}'$ the discretization of $[-2f_{max} : 2f_{max}]$.

We propose to compute the optimal estimate for $\widehat{u}$, $\widehat{U}$, in the case of additive Gaussian noise. By optimal we mean that we want an unbiased estimate, of minimal variance and that corresponds, in space, to an image made of real values. $\widehat{U}$ is written as a linear combination of the acquisitions $\widehat{I}_u$. More specifically, the coefficients $r \in \widehat{\Omega}'$

appears when $p+q=r$, so that we can write

$$\forall r \in \widehat{\Omega}',\ \widehat{U}(r) = \sum_{p\in\Omega} \beta^r(p)\widehat{I}_u(p, r-p),\ \beta^r \in \mathbb{C}^{\Omega}.$$

Since $\widehat{U}$ is complex, we use the following definitions,

$$\begin{aligned}
\forall Z \in \mathbb{C},\ \mathbb{E}(Z) &= \mathbb{E}(\mathrm{Re}(Z)) + i\mathbb{E}(\mathrm{Im}(Z)) \\
\forall Z \in \mathbb{C},\ \mathrm{Var}(Z) &= \mathrm{Var}(\mathrm{Re}(Z)) + \mathrm{Var}(\mathrm{Im}(Z)) \\
\forall a \in \mathbb{C}^N,\ Z \in \mathbb{C}^N,\ \mathrm{Var}(\sum_{i=1}^{N} a_i Z_i) &= \sum_{i=1}^{N}\sum_{j=1}^{N} a_i\overline{a_j}\mathrm{Cov}(Z_i, Z_j) \\
\forall (Z_i, Z_j) \in \mathbb{C}^2,\ \mathrm{Cov}(Z_i, Z_j) &= \mathbb{E}\left((Z_i - \mathbb{E}(Z_i))\overline{(Z_j - \mathbb{E}(Z_j))}\right).
\end{aligned}$$

We want that the estimate creates a PSF with real coefficients, in particular it should be symmetrical and $\mathrm{Im}(\widehat{U}(0)) = 0$.

3.5.1 Expression of the β^r for the standards methods

For the conventional, dual conventional and confocal systems, the correspondences with the β^r are direct with the discrete writing of their OTFs.

Conventional and dual conventional

The discrete formulation of the conventional gives that

$$\begin{aligned}
\widehat{U}_{\mathrm{conv}}(r) &= \left(\widehat{\varphi}\widehat{u}\right)(r) = \widehat{D}(0)\widehat{\varphi}(r)\hat{u}(r) \\
&= \sum_{p\in\widehat{\Omega}} \beta^r(p)\widehat{I}_u(p, r-p), \quad \beta^r(p) = \begin{cases} 1 \text{ if } p = 0 \text{ and } r \in \widehat{\Omega} \\ 0 \text{ otherwise} \end{cases}.
\end{aligned}$$

Symmetrically, for the dual conventional, we have

$$\begin{aligned}
\widehat{U}_{\mathrm{conv}^d}(r) &= \left(\check{\widehat{D}}\widehat{u}\right)(r) = \widehat{\varphi}(0)\widehat{D}(-r)\hat{u}(r) \\
&= \sum_{p\in\widehat{\Omega}} \beta^r(p)\widehat{I}_u(p, r-p), \quad \beta^r(p) = \begin{cases} 1 \text{ if } p = r \text{ and } r \in \widehat{\Omega} \\ 0 \text{ otherwise} \end{cases}.
\end{aligned}$$

Confocal

The discrete formulation of the Fourier transform of an image produced by a conventional system is given by

$$\begin{aligned}\widehat{U}_{\text{conf}}(r) &= \widehat{u}(r)\left(\widehat{(D(-\cdot)} * (\widehat{\varphi}(\cdot)\widehat{\mathbf{1}}_{\mathcal{B}(0,R)}(\cdot))\right)(r) \\ &= \widehat{u}(r)\sum_{p\in\widehat{\Omega}} \widehat{D(-p)}\widehat{\varphi}(r-p)\widehat{\mathbf{1}}_{\mathcal{B}(0,R)}(r-p) \\ &= \sum_{p\in\widehat{\Omega}} \beta^r(p)\widehat{I}_u(p, r-p), \quad \beta^r(p) = \widehat{\mathbf{1}}_{\mathcal{B}(0,R)}(r-p).\end{aligned}$$

We recall that in that case, the illumination pattern is the PSF.

3.5.2 Computation of the unbiased estimate of minimal variance - Gaussian case

Unbiased estimate

To create an unbiased estimate, $\widehat{U}(r)$ should satisfy

$$\forall r \in \widehat{\Omega}',\ \mathbb{E}(\text{Re}(\widehat{U}(r))) = \text{Re}(\widehat{u}(r)) \text{ and } \mathbb{E}(\text{Im}(\widehat{U}(r))) = \text{Im}((\widehat{u}(r))).$$

$$\begin{aligned}\mathbb{E}(\text{Re}(\widehat{I}_u(p, r-p)) &= \mathbb{E}\left(\sum_{k,l} I_u(k,l)\cos\left(\frac{2\pi kp}{N} + \frac{2\pi l(r-p)}{N}\right)\right) \\ &= \sum_{k,l} \mathbb{E}(I_u(k,l))\cos\left(\frac{2\pi kp}{N} + \frac{2\pi l(r-p)}{N}\right) \\ &= \sum_{k,l} f(k,l)\cos\left(\frac{2\pi kp}{N} + \frac{2\pi l(r-p)}{N}\right) = \text{Re}\left(\widehat{f}(p, r-p)\right).\end{aligned}$$

Using the same reasoning, we have $\mathbb{E}\left(\text{Im}(\widehat{I}_u(p, r-p)\right) = \text{Im}\left(\widehat{f}(p, r-p)\right)$.

For $r = 0$, this is particular, we want that the imaginary part equals 0 and the real part equals $\hat{u}(0)$. We have that

$$\widehat{I}_u(p,-p) = \alpha(p,-p)\widehat{u}(0) \Leftrightarrow \begin{cases} \mathbb{E}\left(\text{Re}\left(\widehat{I}_u(p,-p)\right)\right) = \text{Re}\left(\widehat{\alpha}_u(p,-p)\right)\widehat{u}(0) \\ \mathbb{E}\left(\text{Im}\left(\widehat{I}_u(p,-p)\right)\right) = \text{Im}\left(\widehat{\alpha}_u(p,-p)\right)\widehat{u}(0). \end{cases}.$$

$$\begin{aligned}\mathbb{E}\left(\mathrm{Re}(\widehat{U}(0))\right) &= \sum_p \mathrm{Re}(\beta^0(p))\mathbb{E}\left(\mathrm{Re}\left(\widehat{I}_u(p,-p)\right)\right) - \mathrm{Im}(\beta^0(p))\mathbb{E}\left(\mathrm{Im}\left(\widehat{I}_u(p,-p)\right)\right)\\ &= \widehat{u}(0)\sum_p \left(\mathrm{Re}(\beta^0(p)\mathrm{Re}\left(\widehat{\alpha}_u(p,-p)\right) - \mathrm{Im}(\beta^0(p)\mathrm{Im}\left(\widehat{\alpha}_u(p,-p)\right)\right)\right)\\ &= \widehat{u}(0)\sum_p \mathrm{Re}(\beta^0(p)\widehat{\alpha}_u(p,-p)).\end{aligned}$$

Equivalently, we have

$$\mathbb{E}\left(\mathrm{Im}(\widehat{U}(0))\right) = \widehat{u}(0)\sum_p \mathrm{Im}(\beta^0(p)\widehat{\alpha}_u(p,-p)).$$

To get $\mathbb{E}\left(\mathrm{Re}(\widehat{U}(0))\right) = \widehat{u}(0)$ and $\mathbb{E}\left(\mathrm{Im}(\widehat{U}(0))\right) = 0$, β^r should satisfy

$$\begin{cases} \sum_p \mathrm{Re}(\beta^0(p)\widehat{\alpha}_u(p,-p)) = 1 \\ \sum_p \mathrm{Im}(\beta^0(p)\widehat{\alpha}_u(p,-p)) = 0. \end{cases}. \tag{3.21}$$

For $r \neq 0$,

$$\begin{aligned}\mathbb{E}(\mathrm{Re}(\widehat{U}(r)) &= \mathbb{E}\left(\mathrm{Re}\left(\sum_p \beta^r(p)\widehat{I}_u(p,r-p)\right)\right)\\ &= \sum_p \mathbb{E}\left(\mathrm{Re}(\beta^r(p))\mathrm{Re}\left(\widehat{I}_u(p,r-p)\right) - \mathrm{Im}(\beta^r(p))\mathrm{Im}\left(\widehat{I}_u(p,r-p)\right)\right)\\ &= \sum_p \mathrm{Re}(\beta^r(p))\mathbb{E}\left(\mathrm{Re}\left(\widehat{I}_u(p,r-p)\right)\right) - \mathrm{Im}(\beta^r(p))\mathbb{E}\left(\mathrm{Im}\left(\widehat{I}_u(p,r-p)\right)\right)\\ &= \sum_p \mathrm{Re}(\beta^r(p))\mathrm{Re}\left(\widehat{f}(p,r-p)\right) - \mathrm{Im}(\beta^r(p))\mathrm{Im}\left(\widehat{f}(p,r-p)\right).\end{aligned}$$

But

$$\mathrm{Re}\left(\widehat{f}(p,r-p)\right) = \mathrm{Re}\left(\widehat{\alpha}(p,r-p)\right)\mathrm{Re}\left(\widehat{u}(r)\right) - \mathrm{Im}\left(\widehat{\alpha}(p,r-p)\right)\mathrm{Im}\left(\widehat{u}(r)\right)$$

and

$$\mathrm{Im}\left(\widehat{f}(p,r-p)\right) = \mathrm{Re}\left(\widehat{\alpha}(p,r-p)\right)\mathrm{Im}\left(\widehat{u}(r)\right) + \mathrm{Im}\left(\widehat{\alpha}(p,r-p)\right)\mathrm{Re}\left(\widehat{u}(r)\right).$$

Finally

$$\begin{aligned}\mathbb{E}(\mathrm{Re}(\widehat{U}(r)) &= \sum_p \mathrm{Re}\left(\widehat{u}(r)\right)\left(\mathrm{Re}(\beta^r(p))\mathrm{Re}\left(\widehat{\alpha}(p,r-p)\right) - \mathrm{Im}(\beta^r(p))\mathrm{Im}\left(\widehat{\alpha}(p,r-p)\right)\right)\\ &\quad - \mathrm{Im}\left(\widehat{u}(r)\right)\left(\mathrm{Re}(\beta^r(p))\mathrm{Im}\left(\widehat{\alpha}(p,r-p)\right) + \mathrm{Im}(\beta^r(p))\mathrm{Re}\left(\widehat{\alpha}(p,r-p)\right)\right)\\ &= \mathrm{Re}\left(\widehat{u}(r)\right)\sum_p \mathrm{Re}\left(\beta^r(p)\widehat{\alpha}(p,r-p)\right) + \mathrm{Im}\left(\widehat{u}(r)\right)\sum_p \mathrm{Im}\left(\beta^r(p)\widehat{\alpha}(p,r-p)\right).\end{aligned}$$

To be unbiased, the value of β^r should respect for $r \neq 0$

$$\begin{cases} \displaystyle\sum_p \mathrm{Re}\left(\beta^r(p)\widehat{\alpha}(p,r-p)\right) = 1 \\ \displaystyle\sum_p \mathrm{Im}\left(\beta^r(p)\widehat{\alpha}(p,r-p)\right) = 0. \end{cases}. \tag{3.22}$$

The development of $\mathbb{E}(\mathrm{Im}(\widehat{U}(r))$ gives the same constraints. The set of constraints defined in (3.21) is in fact equivalent to (3.22) for $r = 0$.

Computation of the variance

We can write the variance of the estimate. It is given by

$$\begin{aligned}\mathrm{Var}\left(U(r)\right) &= \sum_{p\in\Omega}\beta^r(p)\widehat{I}_u(p,r-p)\\ &= \sum_{p\in\widehat{\Omega}}\sum_{p'\in\widehat{\Omega}}\beta^r(p)\overline{\beta^r(p')}\mathrm{Cov}\left(\widehat{I}_u(p,r-p),\widehat{I}_u(p',r-p')\right)\\ &= \sum_{p\in\widehat{\Omega}}\sum_{p'\in\widehat{\Omega}}\beta^r(p)\overline{\beta^r(p')}\mathrm{Cov}\left(\sum_{n,m} I_u(n,m)e^{-\frac{2i\pi np}{N}}e^{-\frac{2i\pi m(r-p)}{N}},\right.\\ &\qquad \left.\sum_{n',m'} I_u(n',m')e^{-\frac{2i\pi n'p'}{N}}e^{-\frac{2i\pi m'(r-p')}{N}}\right).\end{aligned}$$

We suppose that the I_u are independent so that the only remaining term is when $n = n',\ m = m'$, giving

$$\begin{aligned}\mathrm{Var}\left(U(r)\right) &= \sum_{p\in\widehat{\Omega}}\sum_{p'\in\widehat{\Omega}}\beta^r(p)\overline{\beta^r(p')}\sum_{(n,m)\in\Omega} e^{-\frac{2i\pi np}{N}}e^{-\frac{2i\pi m(r-p)}{N}}e^{-\frac{2i\pi np'}{N}}e^{\frac{2i\pi m(r-p')}{N}}\mathrm{Var}\left(I_u(n,m)\right)\\ &= \sum_{(p,p')\in\widehat{\Omega}^2}\beta^r(p)\overline{\beta^r(p')}\sum_{(n,m)\in\Omega}\mathrm{Var}\left(I_u(n,m)\right)e^{-\frac{2i\pi n(p-p')}{N}}e^{-\frac{2i\pi m(p'-p)}{N}}.\end{aligned}$$

In the case where $I_u(X_s, X_c) \sim \mathcal{N}(f(X_s, X_c), \sigma)$, we have that

$$\forall (n,m),\ \mathrm{Var}\left(I_u(n,m)\right) = \sigma^2.$$

We recall this formula, that can be found by computing the sum of a geometric progression

$$\forall y \in \mathbb{R}^*,\ \sum_{k=0}^{N-1} e^{iky} = e^{iy\frac{N-1}{2}} \frac{\sin\left(\frac{Ny}{2}\right)}{\sin\left(\frac{y}{2}\right)}. \tag{3.23}$$

The variance is then written as

$$\mathrm{Var}\left(U(r)\right) = \sum_{(p,p')\in\widehat{\Omega}^2} \beta^r(p)\overline{\beta^r(p')}\sigma^2 \sum_{n=0}^{N-1} e^{-\frac{2i\pi n(p-p')}{N}} \sum_{m=0}^{N-1} e^{-\frac{2i\pi m(p'-p)}{N}}. \tag{3.24}$$

Using Formula (3.23), we have that

$$\sum_{n=0}^{N-1} e^{-\frac{2i\pi n(p-p')}{N}} = e^{\frac{2i\pi(p-p')}{N}\frac{N-1}{2}} \frac{\sin\left(-i\pi(p-p')\right)}{\sin\left(\frac{-i\pi(p-p')}{N}\right)} = 0 \text{ if } p \neq p'.$$

If $p = p'$, Equation (3.24) is really simplified, giving

$$\mathrm{Var}\left(U(r)\right) = N^2\sigma^2 \sum_{p\in\widehat{\Omega}} \beta^r(p)\overline{\beta^r(p)} = N^2\sigma^2\|\beta^r\|^2.$$

Remark 20. *In the previous chapter, we used the property that the mean power spectral density of a Gaussian white noise of variance σ^2 is σ^2 (to estimate the variance of the noise in the SIM method, (2.15)). In the discrete case, we can prove, by separating the computation for real and imaginary parts, that both the real part and the imaginary part of the Discrete Fourier transform of a Gaussian white noise, except the coefficient corresponding to the zero frequency, has a variance of $N\frac{\sigma^2}{2}$, so that we can estimate σ thanks to the DFT coefficients beyond the discrete value of f_{max}. The variance of the zero-coefficient is $N\sigma^2$. This property is illustrated in Figure 3.12 where we compare the histogram of samples from a standard normal distribution and their Fourier transform divided by $\sqrt{\frac{N}{2}}$; we clearly see the similitude between those two.*

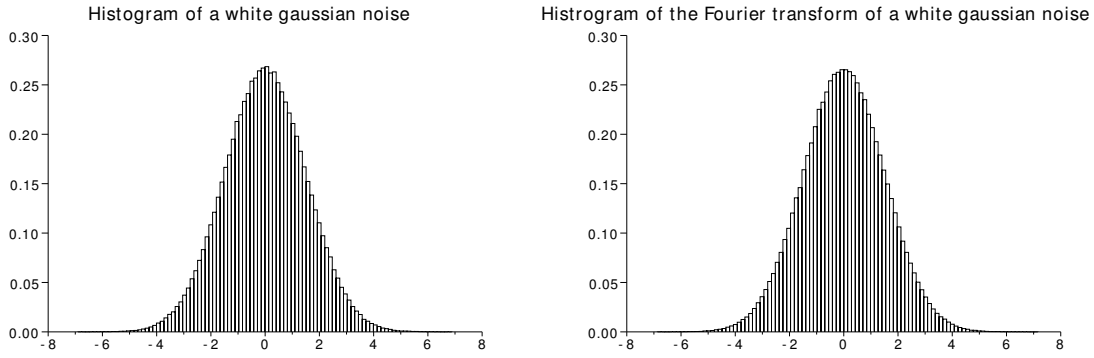

Figure 3.12: Representation of the real part of the DFT of a Gaussian noise; on the left, histogram of a white Gaussian noise $\mathcal{N}(0, 1.5)$, on the right, the real part of its Discrete Fourier Transform. x was created with around 1 million samples of random variables following $\mathcal{N}(0, 1.5)$. For the Discrete Fourier Transform of x (divided by $\sqrt{N/2}$), we kept only the positive coefficients since $\forall p \in \mathbb{Z},\ \widehat{x}(p) = \widehat{x}(-p)$ as x is a real signal. We can notice that the distributions are very close to each other; this confirms that we can use (for instance) the real part of the DFT for the estimation of σ.

Estimate of minimal variance

Minimizing the variance of the estimator in the case of additive Gaussian noise then consists in finding

$$\min_{\beta^r \in \mathcal{C}} \quad N\sigma^2 \sum_r \|\beta^r\|^2,$$

with $\mathcal{C} = \left\{ \mathrm{Re}(\langle \beta^r, \widehat{\alpha^r} \rangle) = 1 \text{ and } \mathrm{Im}(\langle \beta^r, \widehat{\alpha^r} \rangle) = 0 \right\}$, where α^r is the vector $(\alpha(p, r-p))_{p \in \widehat{\Omega}}$. The solution of this problem is simply the projection of 0 onto $\mathcal{C}$, and we have that

$$\beta^r \in \mathcal{C} \Leftrightarrow \langle \beta^r, \overline{\widehat{\alpha^r}} \rangle = 1,$$

whose solution is then given by

$$\beta^r = \frac{\overline{\widehat{\alpha^r}}}{\|\widehat{\alpha^r}\|^2} \Leftrightarrow \forall p \in \widehat{\Omega},\ \beta^r(p) = \frac{\overline{\widehat{\alpha}(p, r-p)}}{\sum_{q \in \widehat{\Omega}} \widehat{\alpha}(q, r-q)^2}.$$

The estimate is then given by

$$\forall r \in \widehat{\Omega}',\ \widehat{U}(r) = \sum_{p \in \widehat{\Omega}} \frac{\overline{\widehat{\varphi}(r-p)\widehat{D}(-p)}}{\sum_{q \in \widehat{\Omega}} \widehat{\varphi}(r-p)^2 \widehat{D}(-p)^2} \widehat{I}_u(p, r-p).$$

Chapter 4

Maximum a posteriori estimate for deconvolution with positivity constraint

Contents

We now consider a simpler inverse problem, the deconvolution, in the case of data corrupted by Gaussian or Poisson noise, under the only constraint of positivity. This is quite a "low" constraint since all images with positive values have the same apriori probability to be the solution. In this chapter, we present a well-known estimate, called Maximum A Posteriori which consists in searching for the most probable image, according to the input data. For both models of noise, we explain how to compute this estimate and present its properties.

We consider that the convolution kernel is known; in this chapter, we always take a Gaussian kernel. The convolution with a Gaussian kernel removes the details of the image, since in the Fourier domain the coefficients of the high frequencies are close to zero (the Gaussian kernel is almost band-limited). The bigger the standard deviation, the more blurry the input image is. An example is shown on Figure 4.1 where the image of Lena is blurred with a Gaussian kernel with standard deviation $\sigma = 3$.

Figure 4.1: Illustration of the convolution: the original image, Lena, on the left is convolved with a Gaussian kernel of standard deviation $\sigma = 3$, on the right. After the convolution the image looks blurry, some separations are not visible anymore (feather of the hat and eyelashes for instance).

4.1 MAP estimation by energy minimization

In the following, we denote x the data we want to recover; we suppose that $x \in \mathbb{R}^\Omega$ where $\mathbb{R}^\Omega$ represents the functions from Ω to $\mathbb{R}$ and we denote $\mathring{x}$ the Ω-periodic function created from x, that is

$$\forall (n_1, n_2) \in \mathbb{Z}^2,\ \forall p = (p_1, p_2) \in \Omega,\ \mathring{x}(p_1 + n_1 N_x, p_2 + n_2 N_y) = x(p_1, p_2),$$

where $\Omega = \{0, \dots, N_x - 1\} \times \{0, \dots, N_y - 1\}$, and thus $|\Omega| = N_x \cdot N_y = N$. The convolution kernel k is also a function from $\mathbb{R}^\Omega$, with its associated Ω-periodic function $\mathring{k}$, whose center is located in $(0, 0)$. Its spatial support, noted S, can be smaller than Ω. The result of the convolution, $k * x$, has a bigger support than x; we denote it Ω' with $|\Omega'| \geq |\Omega| + |S|$ and we have

$$\forall q \in \Omega',\ (k * x)(q) = \sum_{p \in \Omega} \mathring{k}(q - p)\mathring{x}(p) = \sum_{p \in \Omega} \mathring{x}(q - p)\mathring{k}(p). \tag{4.1}$$

Let us denote $y \in \mathbb{R}^{\Omega'}$ the observed data, we have in case of additive Gaussian noise,

$$\forall q \in \Omega',\ y(q) \sim \mathcal{N}((k * x)(q), \sigma^2),\ \sigma^2 \text{ known}$$

and in the case of corruption by Poisson noise,

$$\forall q \in \Omega',\ y(q) \sim \mathcal{P}((k * x)(q)).$$

In the following, we will sometimes use the matrix representation, that is the representation of $k * x$ as the matrix product Hx with $H \in \mathcal{M}_{|\Omega'|,|\Omega|}$, where the image x (and thus y) is represented as a vector, obtained by assembling the transposed rows. H is a circulant matrix whose first line is the values of the kernel k on Ω. Therefore, we have the equality,

$$\forall 1 \leq i \leq |\Omega|',\ (Hx)_i = (k * x)(i_1, i_2),\ \text{with } i_1 = i \bmod N_x \text{ and } i_2 = i - i_1 \times N_x.$$

When using this matrix notation, we will write $(x_i)_{1 \leq i \leq |\Omega|}$ and $(y_i)_{1 \leq i \leq |\Omega'|}$.

Computing the MAP estimate under positivity constraint, that is the most probable positive image given the input data, consists in solving

$$\operatorname*{argmax}_{x \in \mathbb{R}_+^\Omega} p(x|y).$$

We will see that maximizing this posterior density is equivalent to minimizing a specific energy, depending on the type of the noise. This minimum can be computed thanks to the gradient descent method, whose principles are recalled in a first part. In the following, we will use Bayes formula, given by

$$p(x|y) = \frac{p(y|x)p(x)}{p(y)}, \tag{4.2}$$

where $p(x)$ is the prior on the data. In our case, this is the improper prior $p(x) = \mathbf{1}_{x \in \mathbb{R}_+^\Omega}$, but it can be any prior on the result data; the term $p(y)$ does not interfere in the problem since it is independent of x. As mentioned earlier, the chosen prior induces that any positive image have the same probability to be the solution.

4.1.1 Gradient descent method

To compute the gradient of the energies in both case, we compute $\forall h \in \mathbb{R}^\Omega,\ \forall x \in \mathbb{R}^\Omega,\ E(x+h) - E(x)$, since,

$$E(x+h) - E(x) = \langle \nabla E(x), h \rangle + o(h)\,. \tag{4.3}$$

In the case where the function E is convex and differentiable, a well known solution to find its minimum is the gradient descent. It consists in using iteratively the negative of the gradient of the energy as a descent direction: $-\nabla E$. This method enables to reach a local minimum and thus, with the hypothesis of convexity and assuming that E is coercive, a global one. The scheme at each iteration l is given by

$$x^{l+1} = x^l - \gamma_l \nabla E(x^l), \tag{4.4}$$

where $\gamma_l \in]0; +\infty]$ is the step size for iteration l and x^l is the image at the precedent iteration. We have

$$\hat{x}_{MAP} = \lim_{l \to \infty} x^l.$$

The initialization x^0 can be chosen as the input image or as the null image.

4.1.2 Deblurring with MAP - Poisson and Gaussian noise

Gaussian case

In this case, we have $y \sim \mathcal{N}(Hx, \sigma^2 I_n)$ and it comes

$$p(y|x) = \frac{1}{(\sqrt{2\pi})^n \sigma^n} \exp\left(-\frac{\|Hx - y\|^2}{2\sigma^2}\right).$$

Maximum a posteriori computation Bayes Formula (4.2) gives

$$p(x|y) = \frac{p(y|x)p(x)}{p(y)} = \frac{1}{Z}\frac{1}{p(y)} \exp\left(-\frac{\|Hx - y\|^2}{2\sigma^2}\right) \mathbf{1}_{x \in \mathbb{R}^\Omega_+},$$

with Z a normalization constant. Computing the negative logarithm of $p(x|y)$, we obtain

$$\operatorname*{argmax}_{x \in \mathbb{R}^\Omega_+} p(x|y) = \operatorname*{argmin}_{x \in \mathbb{R}^\Omega_+} -\log(p(x|y)) = \operatorname*{argmin}_{x \in \mathbb{R}^\Omega_+} \frac{\|Hx - y\|^2}{2\sigma^2}. \tag{4.5}$$

Let us denote E the convex function defined by

$$\forall x \in \mathbb{R}_+^\Omega,\ E(x) = \frac{1}{2\sigma^2}\|Hx - y\|^2, \tag{4.6}$$

we just proved that looking for the maximum a posteriori under positivity constraint is equivalent to minimizing E under the same constraints.

Gradient of the energy Equation (4.3) with definition of energy (4.6) gives

$$\begin{aligned} 2\sigma^2(E(x+h) - E(x)) &= \langle H(x+h) - y, H(x+h) - y\rangle - \langle Hx - y, Hx - y\rangle \\ &= 2\langle H^*(Hx - y), h\rangle + \langle Hh, Hh\rangle, \end{aligned}$$

leading to

$$\forall x \in R^\Omega,\ \nabla E(x) = \frac{1}{\sigma^2}H^*(Hx - y). \tag{4.7}$$

We need to explicit the operator H^*, which is the adjoint of H but equivalently its transpose since H is real. We recall that $H^* \in \mathcal{M}_{|\Omega|,|\Omega'|}$ is defined by

$$\forall x \in \mathbb{R}^\Omega,\ \forall y \in \mathbb{R}^{\Omega'},\ \langle Hx, y\rangle_{\mathbb{R}^{\Omega'}} = \langle x, H^*y\rangle_{\mathbb{R}^\Omega}.$$

Let us compute $\langle Hx, y\rangle_{\mathbb{R}^{\Omega'}}$ using (4.1)

$$\langle Hx, y\rangle_{\mathbb{R}^{\Omega'}} = \sum_{q\in\Omega'}\sum_{p\in\Omega} x(q-p)k(p)y(q).$$

$$\langle Hx, y\rangle_{\mathbb{R}^{\Omega'}} = \sum_{q\in\Omega'} y(q) \sum_{(q-r)\in\Omega} x(r)k(q-r), \qquad \text{with } r = q - p.$$

Since x and h are Ω-periodic, the second sum (which is on a whole period) can be written as $\sum_{(q-r)\in\Omega} x(r)k(q-r) = \sum_{r\in\Omega} x(r)k(q-r)$, and

$$\begin{aligned} \langle Hx, y\rangle_{\mathbb{R}^{\Omega'}} &= \sum_{q\in\Omega'} y(q) \sum_{r\in\Omega} x(r)k(q-r) \\ &= \sum_{r\in\Omega} x(r) \sum_{q\in\Omega'} y(q)k(q-r) \\ &= \langle x, H^*y\rangle_{\mathbb{R}^\Omega},\ \text{with } (H^*y)_r = \sum_{q\in\Omega'} y(q)k(q-r), \forall r \in \Omega. \end{aligned}$$

In the case of periodic signals, the adjoint operator of H, H^*, is therefore defined $\forall r \in \Omega$ by the operation

$$\sum_{q\in\Omega'} y(q)k(q-r) = \check{k} * y(r),\ \text{with } \forall p \in \mathbb{Z}^2,\ \check{k}(p) = k(-p).$$

Poisson case

In this case, we have $\forall i \in \Omega',\ y(i) \sim \mathcal{P}((Hx)_i + B)$, with B a background constant, and $\forall (i,j) \in \Omega'^2,\ i \neq j$, $y(i)$ and $y(j)$ are independent. It comes

$$\forall i \in \Omega',\ p(y(i)|(Hx)_i) = \frac{((Hx)_i + B)^{y(i)} e^{-(Hx)_i + B}}{y(i)!}.$$

Maximum a posteriori estimate computation Using Bayes formula (4.2) and the fact that the noise is spatially independent, we have

$$p(x|y) = \frac{p(y|x)p(x)}{p(y)} = \frac{1}{Z}\frac{1}{p(y)} \prod_{i \in \Omega'} \frac{((Hx)_i + B)^{y(i)} e^{-(Hx)_i + B}}{y(i)!} \mathbb{1}_{x \in \mathbb{R}_+^\Omega}.$$

Computing the negative logarithm of $p(x|y)$, we have

$$\forall x \in \mathbb{R}_+^\Omega, -\log(p(x|y)) = \sum_{i \in \Omega'} (Hx)_i + B - y(i)\log((Hx)_i + B) + \log(y(i)!) - \log(Z).$$

We define the convex function E as

$$\forall x \in \mathbb{R}_+^\Omega,\ E(x) = \sum_{1 \leq i \leq |\Omega'|} (Hx)_i - y_i \log((Hx)_i + B). \tag{4.8}$$

We proved to following equivalence

$$\underset{x \in \mathbb{R}_+^\Omega}{\operatorname{argmax}}\, p(x|y) = \underset{x \in \mathbb{R}_+^\Omega}{\operatorname{argmin}}\, E(x). \tag{4.9}$$

Gradient of the energy The energy can be matricially written as

$$E(x) = (Hx)^t \mathbf{1}_{\mathbb{R}^{\Omega'}} - y^t \log(Hx + B\mathbf{1}_{\mathbb{R}^{\Omega'}}),$$

with $\mathbf{1}_{\mathbb{R}^{\Omega'}}$ the vector of $\mathbb{R}^{\Omega'}$ composed of ones and the logarithm a pixel-wise logarithm (as well as the quotients below are pixel-wise). Equation (4.3) gives

$$\begin{aligned} E(x+h) - E(x) &= (H(x+h))^t \mathbf{1}_{\mathbb{R}^{\Omega'}} - y^t \log(H(x+h) + B\mathbf{1}_{\mathbb{R}^{\Omega'}}) \\ &\quad -((Hx)^t \mathbf{1}_{\mathbb{R}^{\Omega'}} - y^t \log(Hx) + B\mathbf{1}_{\mathbb{R}^{\Omega'}}) \\ &= (Hh)^t \mathbf{1}_{\mathbb{R}^{\Omega'}} - y^t \log\left(\mathbf{1} + \frac{Hh}{Hx + B\mathbf{1}_{\mathbb{R}^{\Omega'}}}\right) \\ &= (Hh)^t \mathbf{1}_{\mathbb{R}^{\Omega'}} - y^t \frac{Hh}{Hx + B\mathbf{1}_{\mathbb{R}^{\Omega'}}} + o(h)\,. \end{aligned}$$

By definition, the first terms gives $(Hh)^t \mathbf{1}_{\mathbb{R}^{\Omega'}} = \left\langle H^t \mathbf{1}_{\mathbb{R}^{\Omega'}}, h \right\rangle_{\mathbb{R}^{\Omega}}$. For the second term, we have, since the quotient is pixel-wise

$$\begin{aligned} y^t \frac{Hh}{Hx + B\mathbf{1}_{\mathbb{R}^{\Omega'}}} &= \sum_{1 \leq i \leq |\Omega'|} y_i \frac{(Hh)_i}{(Hx)_i + B} = \sum_{i \in \Omega} \frac{y_i}{(Hx)_i} (Hh)_i \\ &= \left\langle \frac{y}{Hx + B\mathbf{1}_{\mathbb{R}^{\Omega'}}}, Hh \right\rangle_{\mathbb{R}^{\Omega}} = \left\langle H^t \frac{y}{Hx + B\mathbf{1}_{\mathbb{R}^{\Omega'}}}, h \right\rangle_{\mathbb{R}^{\Omega}}, \end{aligned}$$

leading to

$$\nabla E(x) = H^t \left(\mathbf{1}_{\mathbb{R}^{\Omega'}} - \frac{y}{Hx + B\mathbf{1}_{\mathbb{R}^{\Omega'}}} \right). \tag{4.10}$$

4.1.3 Algorithms to compute MAP estimate

A well known algorithm for minimizing a function on a convex set is the projected gradient; it consists in applying Formula (4.4) and at each iteration projecting the result on the set of constraints. In the case of the positivity constraint, it consists in thresholding to zero any negative value. For instance, the fixed step gradient method takes $\gamma_l = \gamma,\ \forall l \in \mathbb{N}$ in Formula (4.4), that is the step is constant at each iteration, chosen so that the energy decreases. This algorithm is described in Algorithm 2.

Algorithm 2: Projected gradient algorithm with fixed step (N iterations)

Inputs $x_0 \in \mathbb{R}_+^{\Omega}$, initialization, L, Lipschitz constant for ∇f, N number of iterations
Output x, approximation of $\hat{x}_{MAP}$

$x \leftarrow x_0$
for k in $[\![1, N]\!]$ **do**
  grad$E = \nabla E(x)$ ▶ Using Formula (4.7) or (4.10)
  $x = \max(0, x - \text{grad}E/L)$
end for
return x

Unfortunately, this algorithm is very slow due to the high dimension of x, that is $|\Omega|$ (in the case of images, it corresponds to the number of pixels), and does not converge in practice for image deblurring, leading to a result that does not properly estimate $\hat{x}_{MAP}$. In [87], Nesterov presents optimal schemes to solve problems such as (4.5) or (4.9). It has been proven in [122] that when the problem can be written

as

$$\operatorname*{argmin}_{u\in\mathbb{R}^\Omega} E(u) + \psi(u),$$

with $\psi(u)$ the characteristic function of a convex set (in our case, this is true, setting $\psi(u) = \mathbb{1}_{R_+^\Omega}(u)$), an adaptation of Nesterov Algorithm can be used. This implementation, like the projected gradient, requires to compute only once per iteration the gradient of the function E. The algorithm is summarized in Algorithm 3, two projections are required and the initialization should belong to the set of constraints. As presented in Figure 4.2, the convergence is really faster than the projected gradient. More precisely, comparing the two function representations, it seems impossible that the energy of projected gradient reaches the one of Nesterov in a finite amount of time. As in the gradient descent, there is a descent step, called L in the algorithm, that should be chosen so that the energy decreases.

Algorithm 3: Nesterov algorithm

Inputs $x_0 \in \mathbb{R}_+^p$, initialization, L, Lipschitz constant for ∇f, N number of iterations
Output x, approximation of $\hat{x}_{MAP}$

$g \leftarrow 0$
for k in $[\![0, N-1]\!]$ **do**
  $\text{grad}E \leftarrow \nabla E(x)$
  $y \leftarrow \max(0, x - \frac{\text{grad}E}{L})$
  $g \leftarrow g + \frac{k+1}{2}\text{grad}E$
  $v \leftarrow \max(0, x_0 - \frac{g}{L})$
  $x \leftarrow \frac{2}{k+3}v + \frac{k+1}{k+2}y$
end for
return x

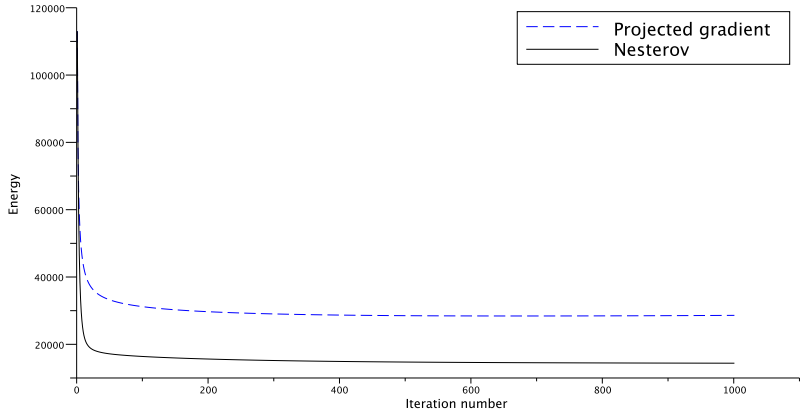

Figure 4.2: Comparison of the evolution of the energy during 1000 iterations for both projected Gradient with constant step and Nesterov algorithm on the same image (the one represented in the next section in Figure 4.3) with the same step ($1/L$ in the algorithms) in the algorithm. According to the general decreasing shape of the energy sequence for the projected gradient, we can guess that the minimum computed by Nesterov algorithm is unreachable in practice for the projected gradient algorithm.

4.2 The Night sky effect: an artifact of the MAP

In the following, several results are presented, computed thanks to Algorithm 3, on quite sparse images, obtained by a fluorescence microscope or simulated according to structures often observed in microscopy. On all these simulations, we can observe an artifact called *night sky* ([14], [57]) on the converged results (Figures 4.3 and 4.5) that is $\hat{x}_{MAP}$ is made of isolated point sources, loosing continuity of the intensity distributions. If this can seem interesting if the sample is really made of isolated structures (such as proteins in microscopy), we also see this artifact on expected constant zone or on filaments, as it is shown in Figure 4.3, where the center is almost a constant area and the other part of the image quite thin filaments. We can explain the apparition of the night sky by the fact that deconvolution tends to create very high frequencies (the energy in the Fourier domain is quite high for the high frequency coefficients), and that, with the positivity constraint, which is quite a weak constraint, oscillations between very large and null values appear in the domain of the image, maintaining locally an average close to the real image.

4.2.1 Examples

We present two examples,

— first, an image of fibroblast in Figure 4.3 that mixes, as mentioned before, quite thin filaments and in the middle an almost constant area. The night sky is visible on all parts of the image, constant and more sparse, as it can be observed on the little crops made on some regions of interest. An idea is to convolve this MAP estimate with a kernel such that the night sky disappears; however, as presented in Figure 4.4, it is impossible to find a kernel such as the night sky totally disappears **and** deconvolution is still visible

— second, in Figure 4.5, we present the results on some synthetic curves, created by drawing randomly points on random curves. The density of points on the curves, its thickness and a standard deviation for the curvature are defined, creating a random set of points according to these parameters. Finally a very small PSF is applied at each position of the set to create an image with continuous structures. Their structure is aimed at modeling biological structures such as microtubules. The MAP estimate presents as before night sky, and we see that the recovered values are not representative of the initial signal. On top of that, in Figure 4.5, the modulus of the Fourier transforms are also represented. We can see that the night sky phenomenon is also noticeable in the Fourier domain where the energy in the high frequency coefficients of

the Fourier transform is very high (more than in classical spectra).

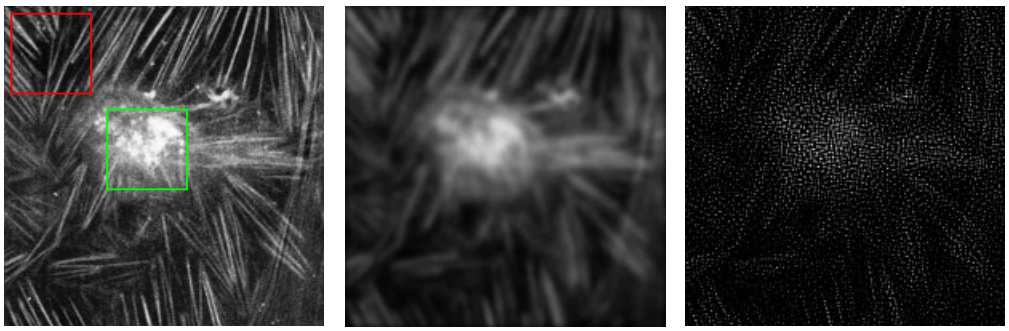

Ground truth | Input image (Noisy and blurry ground truth) | MAP estimate

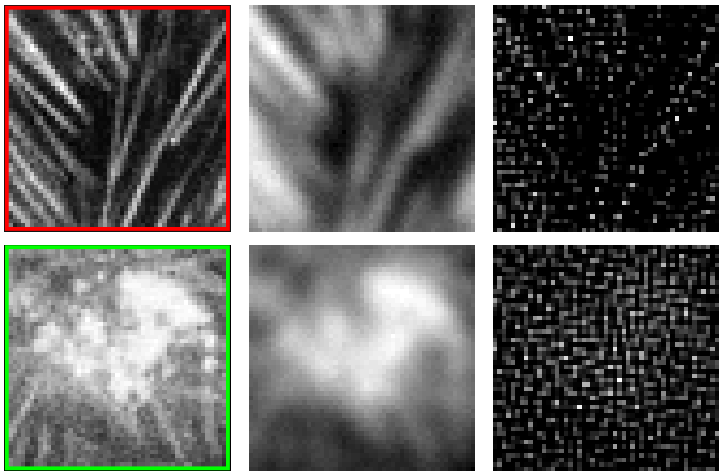

Ground truth | Input | MAP

Figure 4.3: Illustration of the night sky effect; the original image (a fibroblast) (on the left) was convolved with a Gaussian kernel of standard deviation 2 and a Gaussian noise of standard deviation 2 was added (in the middle); Nesterov algorithm (presented in Algorithm 3) was used to estimate the image minimizing the energy (on the right). We can see the night-sky effect on the MAP estimate; we chose two different regions on the original image to show this artifact. On the first one, filaments, whose separations cannot be all distinguished after convolution (input data), are made of separated points in the MAP estimate, loosing totally the continuity of the structures. On the second one, we focus on a quite constant area in the original image; it is also reconstructed with oscillations between null and very high values. The MAP estimate is really not satisfactory. *Ground truth image from cellimagelibrary.org by Don W. Fawcett and Elias Lazarides is licensed under CC BY-NC-ND 3.0 - a threshold of 30 (to get a really black background) and a frequency cut were performed to a crop of the original image.*

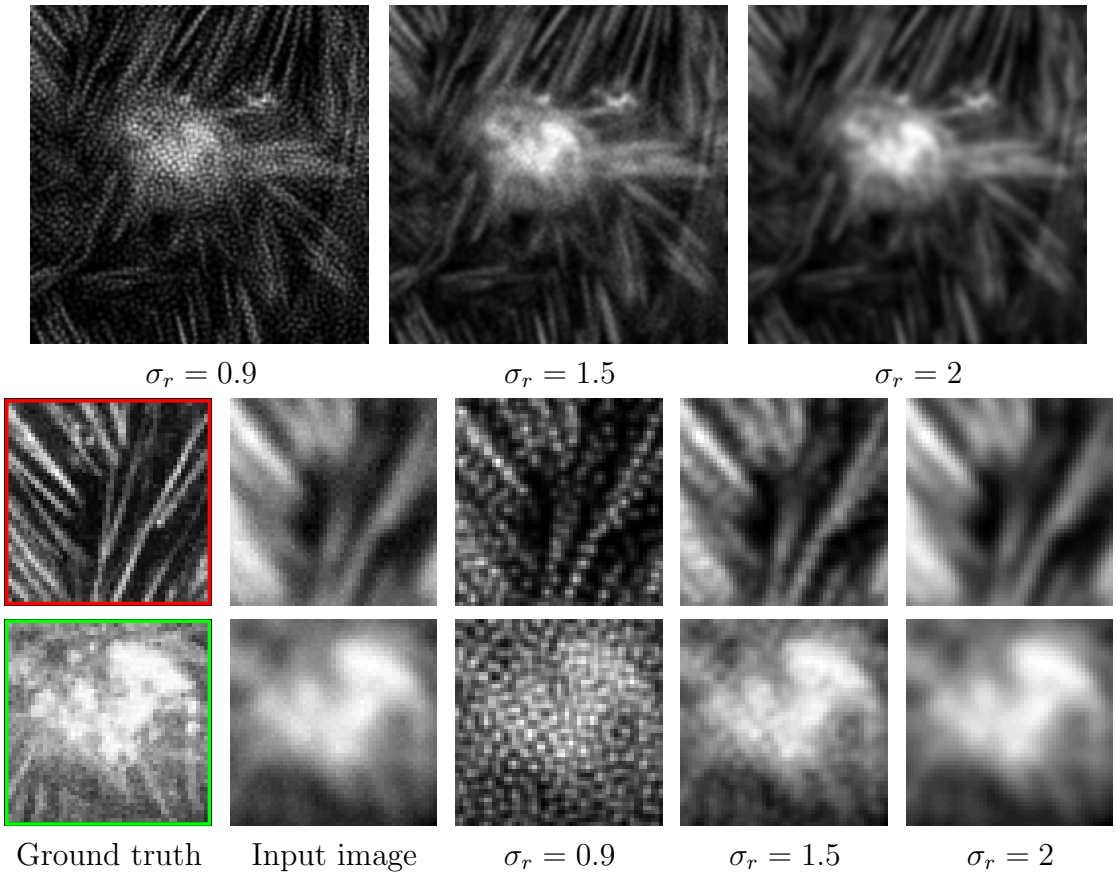

Figure 4.4: Post-convolution of the MAP estimate from Figure 4.3 (with a zoom on the same regions of interest). We could think that a convolution of the MAP estimate would create an interesting estimate, however, the standard deviation that enables to completely remove the night sky artifact is larger or similar to the standard deviation of the kernel, which therefore removes any deconvolution effect. We can see the convolution of the MAP estimate with 3 Gaussian kernels of standard deviations equal to 0.9, 1.5 and 2. With $\sigma_r = 0.9$ the night sky is still very visible and with $\sigma_r = 1.5$ the continuity is recovered but we still see oscillations between small and high intensities, as if the intensities were not homogeneous on the filament. With $\sigma_r = 2$, of course, the signal is very close to the input one, but less noisy.

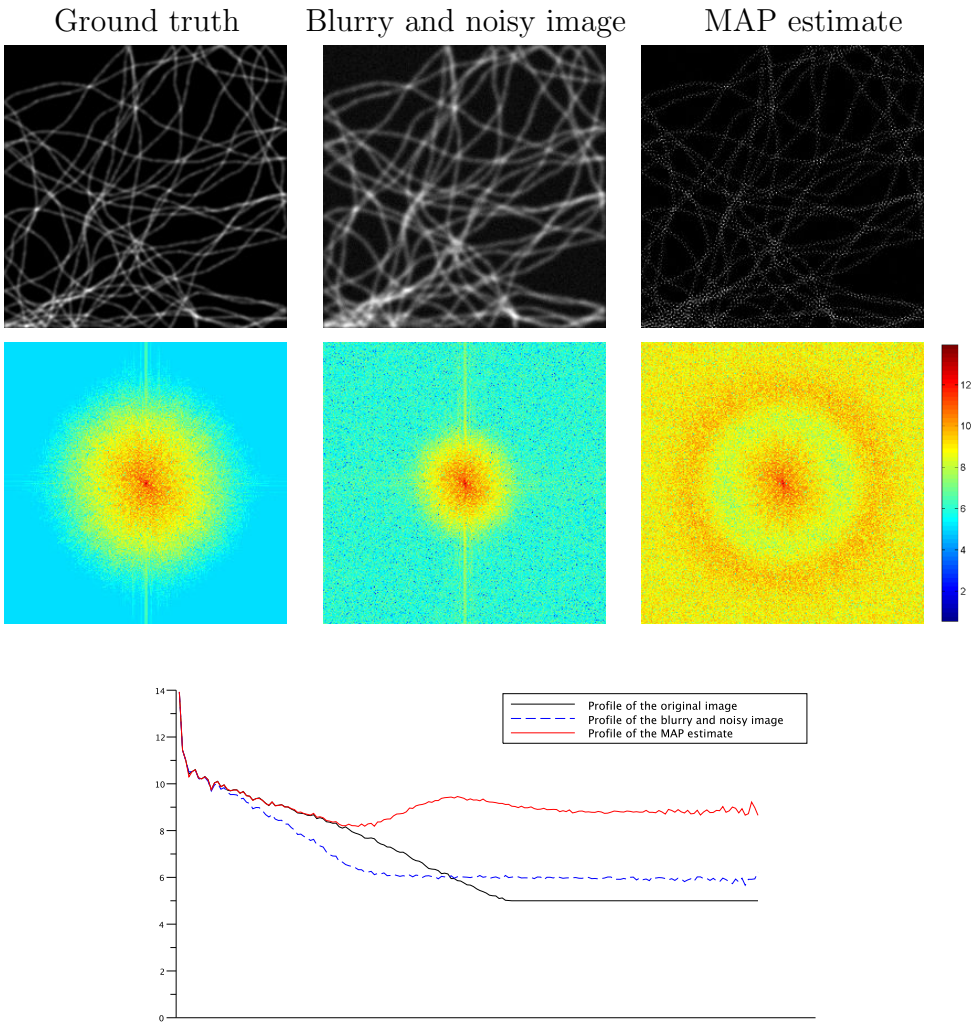

Figure 4.5: Illustration of the night sky effect in space and Fourier domains. From left to right: original image (curves randomly drawn in the image) and its Fourier transform - original image convolved (Gaussian kernel, of standard deviation 1.5), corrupted by a Gaussian noise of standard deviation 2 and its Fourier Transform - MAP estimate at convergence and its Fourier Transform. The modulus of the Fourier transforms are represented, in logarithmic scale, as well as their average radial profiles, below. Visually on the reconstruction in the space domain, it is clear that continuity is lost and that the values of the pixels of the estimate are not representative of the real values: this is the night sky artifact. In the Fourier domain, we can see that the Fourier transform and the profile are not common: normally it gradually decreases, as the one from the original image; for the MAP estimate, we see that the values do not respect this scheme; this is because the noise is over-fitted, creating energy in the high frequency coefficients.

4.2.2 Non converged images

We can notice that with Nesterov Algorithm, the night sky only appears after several iterations, as it can be seen in Figure 4.6, presenting the result at different times, as well as their corresponding energy. The result image tries to explain the data x as well as the noise n; we can think that during the first iterations, the result fits more the data (than the noise) and after it fits more and more the noise, creating the night sky artifact. This means that, during the iterations, some intermediate results are night-sky free and less blurry and noisy than the input image. In Figure 4.7, we present the evolution of the energy and the distance between the iterate and the ground truth image; this distance decreases during the first iterations but then drastically increases before stabilization. The values taken are very large compared to the energy ones.

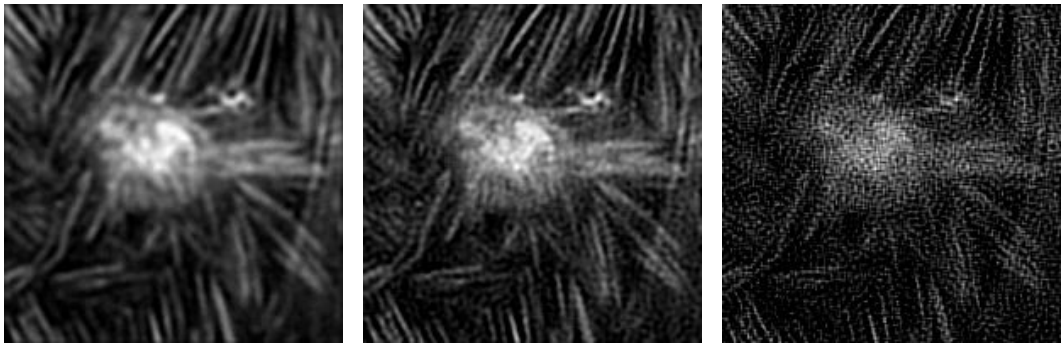

10^{th} Iteration
$E = 190252,9083$

50^{th} Iteration
$E = 138607,3312$

250^{th} Iteration
$E = 124155,3757$

Figure 4.6: Images obtained during the iterations 10, 50 and 250 of Nesterov algorithm for the image of Figure 4.3. We can notice that for the 10^{th} iteration, there is no night sky. Artifacts appear more and more at each step: for the 50^{th} iteration, we can see that the structures are changing, oscillations of intensity can be seen, on the filaments for instance, leading to the night sky, alternating null and positive values, with the positive values increasing gradually. Visually the estimated result is better at the 10^{th} iteration, however its energy is really higher than the minimum, so that we are wondering if the energy is a relevant criteria.

We can recall that this is not the only algorithm known to create artifact by over-fitting the noise after several iterations; indeed Richardson-Lucy algorithm, mostly used in presence of Poisson noise, is very often stopped after a few iterations because the reconstructions are visually better than at the end of the algorithm. We briefly recall the principle of this algorithm; Richardson-Lucy algorithm [77][95] was developed for the deconvolution of images corrupted by Poisson noise. Given the Poisson

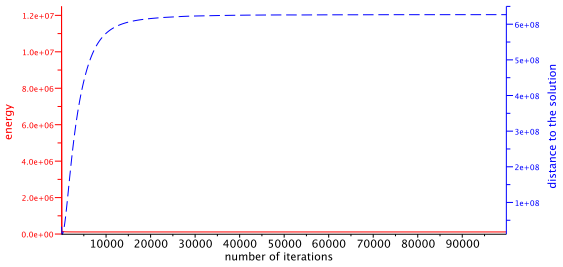

Evolution of energy and distance between the result at each iteration and the ground truth

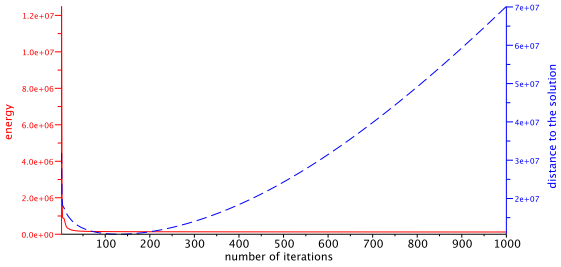

Zoom on the first 1000 iterations

Figure 4.7: Evolution of the energy and the distance to the ground truth according to iterations: in blue is drawn $\|Hx^k - y\|^2$ and in red $\|x^k - x\|^2$, where x^k is the result of iteration k by Nesterov algorithm; the data is the one from 4.6. As seen before, the energy decreases during iterations. On the contrary, the L^2 distance between the estimate and the ground truth decreases during the first iterations but then drastically increases, we can suppose that the last iteration without night-sky is around this minimum.

energy in Formula (4.8),

$$E(u) = \sum_i (Hx)_i - y_i \log((Hx)_i + B),$$

the gradient is defined by

$$\nabla E(u) = H^t \left(\mathbf{1}_{\mathbb{R}^{\Omega'}} - \frac{y}{Hx + B\mathbf{1}_{\mathbb{R}^{\Omega'}}} \right), \tag{4.11}$$

where, as before, the division and the logarithm are element-wise operations and the notation $\mathbf{1}_{\mathbb{R}^{\Omega'}}$ refers to the vector of $\mathbb{R}^{\Omega'}$ made of only 1. Since the energy is convex in x, the solution of the minimization can be obtained by setting the value of each component of the gradient to zero, that is,

$$\forall l \in \{1, \dots, |\Omega|\}, \ \sum_{k=1}^{|\Omega'|} H_{k,l} - \sum_{k=1}^{|\Omega'|} y_k \frac{H_{k,l}}{\sum_{i=1}^{|\Omega|} H_{k,i} x_i + B} = 0. \tag{4.12}$$

Assuming that the PSF is normalized, and using the fact that H is circulant, we then replace $\sum_k H_{k,l} = 1$ in (4.12) and multiply by x_l on each side of the equation.

The image x appears like the solution of a fixed point problem that can be solved by iterating on x with the scheme

$$\forall n \in \mathbb{N},\ \forall l \in \{1, \dots, |\Omega'|\},\ x_l^{n+1} = x_l^n \sum_{k=1}^{|\Omega'|} y_k \frac{H_{k,l}}{\sum_{i=1}^{|\Omega|} H_{k,i} x_i + B}. \tag{4.13}$$

An interesting property of this model is that, given a positive initialization, the result at each iteration remains positive (this can be seen in Formula (4.13) where the input data as well as the PSF are positive functions).

Ideally, the number of iterations is chosen so that convergence is reached; this can be done using, for instance, the criteria $\|x^{n+1} - x^n\| < \varepsilon \|x^n\|$, for ε chosen, quite small, to stop the iterations. However, as we mentioned before and as it can be seen in [120] for instance as well as in Figure 4.8, the fit of the noise is amplified when increasing the number of iterations. Thus, most of the time, the algorithm is stopped after a few iterations.

4.2.3 Analysis of the night sky effect

To better understand the night sky phenomenon, we made several simulations by changing the noise perturbing the data. First, we can notice that the night sky effect happens even for a very small amount of noise, as it can be seen in Figure 4.9, where a noise of 0.1 was added to the initial image and night sky appears on the MAP estimate image. The only case where it does not happen is when the input data is the convolved but noise-free image.

Given any estimator $\hat{x}$ of the sample x, we can exhibit a bias-variance decomposition, of the estimation error. We recall that for an estimator $\hat{\theta}$ of $\theta \in \mathbb{R}$, we have

$$B(\hat{\theta}) = \mathbb{E}(\hat{\theta} - \theta)$$

is the bias and represents the expectation of the difference between the estimate and the real data, and

$$\mathrm{Var}(\hat{\theta}) = \mathbb{E}(\hat{\theta}^2) - \mathbb{E}(\hat{\theta})^2$$

is the variance of the estimator.

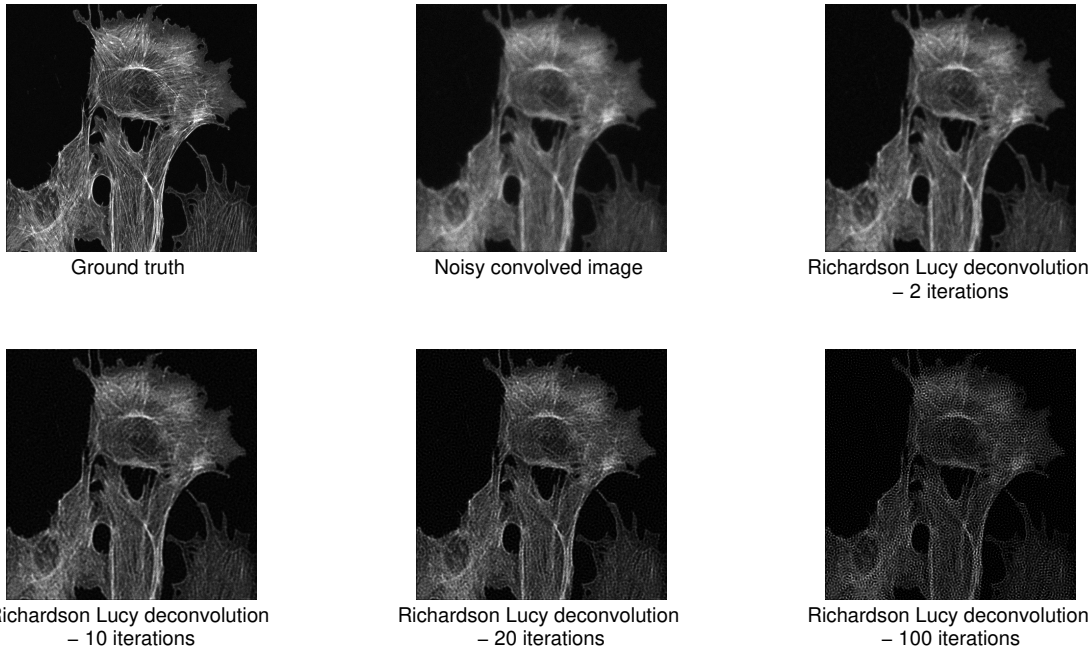

Figure 4.8: Evolution of Richardson-Lucy deconvolution result for an image of cells from cow lungs obtained by fluorescence microscopy. On the first line, from left to right, images represent the ground truth - the ground truth convolved with an Airy disk and corrupted by Poisson noise (maximum amount of photons is 250) - result from Richardson-Lucy algorithm with 2 iterations; on the second line, results from Richardson-Lucy algorithm with respectively 10 - 20 - 100 iterations. Because of the convolution (second image), some features of the original image disappeared. With 2 iterations of RL algorithm, the image still looks blurry. The result given for 10 iterations seems in fact the best because for 20 and 100 some artifacts appear (getting worse with the number of iterations), due to an over fitting of the noise. When using Richardson-Lucy algorithm, the kept image is rarely the converged image, because it contains a lot of artifacts; the iterations are generally stopped before the algorithm fits more the noise than the data.
Ground truth image from cellimagelibrary.org by Tina Cavalho - public domain.

The bias can be seen as an estimation of the average error and the variance consists more in the additional error due to the noise realization. The expectation of the error in our case is given by

$$\mathbb{E}\left(\|y - H\hat{x}\|^2\right) = \sum_{i=1}^{N} \mathbb{E}((y_i - (H\hat{x})_i)^2),$$

and we have

$$\begin{aligned}\mathbb{E}((y_i - (H\hat{x})_i)^2) &= \mathbb{E}\left((y_i - (Hx)_i + (Hx)_i - (H\hat{x})_i)^2\right) \\ &= \mathbb{E}\left((y_i - (Hx)_i)^2\right) + \mathbb{E}\left(((H\hat{x})_i - (Hx)_i)^2\right) \\ &\quad + 2\mathbb{E}\left((y_i - (Hx)_i)((Hx)_i - (H\hat{x})_i)\right).\end{aligned}$$

And since $\mathbb{E}((Hx)_i) = \mathbb{E}(y_i) = (Hx)_i$,

$$\begin{aligned}\mathbb{E}\left((y_i - (Hx)_i)((Hx)_i - (H\hat{x})_i)\right) &= \mathbb{E}(y_i(Hx)_i) - \mathbb{E}((Hx)_i^2) - \mathbb{E}(y_i(H\hat{x})_i) + \mathbb{E}((Hx)_i(H\hat{x})_i) \\ &= (Hx)_i^2 - (Hx)_i^2 + (Hx)_i\mathbb{E}((H\hat{x})_i) - (Hx)_i\mathbb{E}((H\hat{x})_i) \\ &= 0.\end{aligned}$$

Using the equality $\mathbb{E}(Z^2) = \mathrm{Var}(Z) + (\mathbb{E}(Z))^2$,

$$\begin{aligned}\mathbb{E}\left(((H\hat{x})_i - (Hx)_i)^2\right) &= \mathrm{Var}((H\hat{x})_i - (Hx)_i) + (\mathbb{E}((H\hat{x})_i - (Hx)_i))^2 \\ &= \mathrm{Var}((H\hat{x})_i) + B((H\hat{x})_i)^2.\end{aligned}$$

Since $\mathbb{E}\left((y_i - (Hx)_i)^2\right) = \mathbb{E}\left(n_i^2\right) = \sigma^2$, we finally have

$$\mathbb{E}((y_i - (H\hat{x})_i)^2) = \sigma^2 + \mathrm{Var}((H\hat{x})_i) + B((H\hat{x})_i)^2.$$

We can therefore write that

$$\mathbb{E}\left(\|y - H\hat{x}\|^2\right) = N\sigma^2 + \mathrm{tr}(\mathrm{Cov}((H\hat{x}))) + \|B((H\hat{x}))\|^2,$$

where Cov represents the covariance matrix of $H\hat{x}$ and tr its trace, that is

$$\mathrm{tr}(\mathrm{Cov}((H\hat{x}))) = \sum_i \mathrm{Var}((H\hat{x})_i).$$

We are wondering if the night sky is more a bias or variance issue. To answer this question, we create several images, with different realizations of the noise, but with the same characteristics, that is

$$\forall k \in \mathbb{N},\ y^k = (Hx) + n^k,\ \text{with } n^k \sim \mathcal{N}(0, \sigma),\ \sigma \text{ fixed}.$$

The MAP estimate is computed thanks to Nesterov algorithm for each set, giving $\hat{x}^k_{MAP}$, the MAP estimate for each one of the realization of the noise. On each one of the images, we observe some night sky effect, meaning that it systematically happens. Therefore, its apparition is a bias of the method (see Figure 4.9 for two examples of images obtained as MAP estimate). However, as it can be seen on those

two images, the night sky is not exactly the same; more precisely, we averaged the MAP estimates for the different realizations, the night sky does not totally disappear but it is really reduced, as it can be seen in Figure 4.9 also, comparing the average on 100, 1000 and 10000 results. With no doubt averaging the result with different realizations diminishes the night sky (last image of Figure 4.9). The filaments are still not totally continuous, and we cannot know if an infinite number of realizations would make the night sky totally disappear. However, this clearly shows that the night sky is mostly a variance effect.

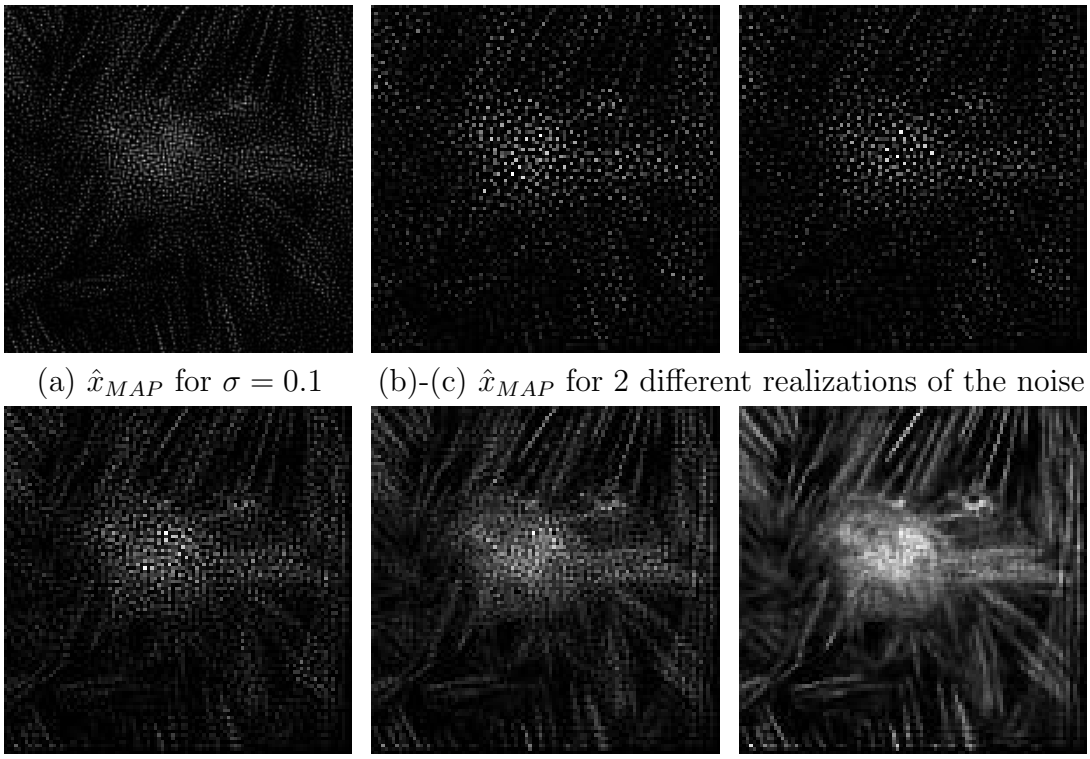

(a) $\hat{x}_{MAP}$ for $\sigma = 0.1$ (b)-(c) $\hat{x}_{MAP}$ for 2 different realizations of the noise

(d) Average of $\hat{x}^k_{MAP}$, $k = 100$ (e) Average of $\hat{x}^k_{MAP}$, $k = 1000$ (f) Average of $\hat{x}^k_{MAP}$, $k = 10000$

Figure 4.9: Experiments on night sky: in (a) we notice that even for a quite small noise, standard deviation of 0.1, the MAP estimate suffers from night sky. On the other images are presented the experiments averaging the MAP estimates obtained for several realizations of the noise on the same ground truth image; (b)-(c) show two reconstructions obtained with two different realizations of the noise, they both have very visible night sky, but we can see that the intense points do not seem to be all at the same positions. And, indeed, the averaged images (c)-(d)-(e) for 100, 1000 and 10000 MAP estimates show more and more the structures of the fibroblast. The last one is not totally continuous, but the night sky is really not visible anymore; this means that the night sky is mainly a variance issue.

4.3 Plausibility of the result

Given x, the ground truth, the observation y is written as $y = Hx + n$, with $n \sim \mathcal{N}(0, \sigma^2)$. Let us denote $\tilde{x}$ the estimate of x obtained by any algorithm; thanks to this estimate, an estimate of the noise, $\tilde{n}$, is computed by

$$\tilde{n} = y - H\tilde{x}.$$

We are wondering, if this noise estimate is plausible. In [88] for instance, it is shown that the distributions of both the MAP estimate and the noise one are biased.

In the following, we only focus on additive Gaussian noise; trying to minimize $\|y - H\tilde{x}\|^2$ is totally equivalent, as said in Chapter 2 by Parseval equality, to minimize $\|\hat{y} - \widehat{H\tilde{x}}\|^2$ which by definition consists in minimizing a sum made of the differences between the coefficients of the discrete Fourier Transforms of the input data and those of the estimate after application of the operator H. However, in the case of deconvolution, the operator H strongly attenuates high frequency coefficients, so that the estimate $\tilde{x}$ can afford non consistent energy in the high frequency coefficients, since they will have a very small impact after the convolution, and thus do not affect $\|\hat{y} - \widehat{H\tilde{x}}\|^2$, as shown in Figure 4.10. The idea of the method is to find at which moment (and then which iteration of the Nesterov algorithm) the solution is only fitting noise, and no more the signal itself.

4.3.1 Estimation of the plausibility

To estimate the plausibility of $\tilde{n}$, we focus on the plausibility of its squared L^2 norm $\|\tilde{n}\|^2$: if it is too low to be plausible, according to the known property of the noise degrading the image, the iterations are stopped and the result is given by the previous iteration. If M is the total number of pixels of the image y, each pixel of the image $y - H\tilde{x}$ is a realization of the noise. By definition, the real noise n satisfies $\forall i \in \Omega,\ n(i) \sim \mathcal{N}(0, \sigma^2)$, so that

$$\frac{\|n\|^2}{\sigma^2} \sim \chi_2(M),$$

where $\chi_2(M)$ is the chi-squared distribution with M degrees of freedom, which can be approximated for M quite large by $\mathcal{N}(M, 2M)$, giving

$$\frac{Z - 1}{\sqrt{\frac{2}{M}}} \sim \mathcal{N}(0, 1), \text{ with } Z = \frac{1}{M}\frac{\|n\|^2}{\sigma^2}.$$

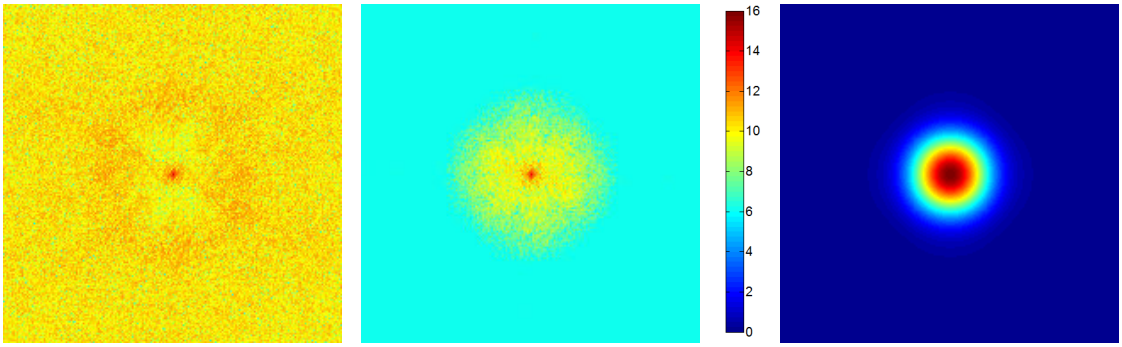

DFT iteration 501 Nesterov algorithm | DFT after convolution with a Gaussian kernel | DFT of the Gaussian kernel

Figure 4.10: Effect of the convolution on an iterate obtained during Nesterov algorithm: on the left, we see the modulus of the discrete Fourier transform, in logarithmic scale, of the image obtained during iteration 501 of Nesterov algorithm (with night sky starting to appear, explaining the unusual distribution of energy of the Fourier transform), in the middle, the modulus of the Fourier transform, in logarithmic scale, with the same color-map as the first one, of the image obtained after convolution with a Gaussian kernel, whose modulus of the Fourier transform is represented on the right. We can see that after convolution the high frequency coefficients are very low compared to the original ones. Since the energy only depends on the image after convolution, the night sky artifact is not really controlled by the energy.

We have

$$\forall z \in \mathbb{R},\ \mathbb{P}(Z > z) = \mathbb{P}\left(\frac{Z-1}{\sqrt{\frac{2}{M}}} > \frac{z-1}{\sqrt{\frac{2}{M}}}\right). \tag{4.14}$$

Given $D \sim \mathcal{N}(0, \sigma^2)$, we recall that

$$\forall d \in \mathbb{R},\ \mathbb{P}(D > d) = \frac{1}{2}\mathrm{erfc}\left(\frac{d}{\sqrt{2}}\right),$$

where erfc is the complementary error function, so that (4.14) becomes

$$\forall z \in \mathbb{R},\ \mathbb{P}(Z > z) = \frac{1}{2}\mathrm{erfc}\left((z-1)\frac{\sqrt{M}}{2}\right).$$

Given a fixed value of α (usually quite small), the value t such that $\mathbb{P}(\|n\|^2 >$

$t) = 1 - \alpha$ satisfies

$$\mathbb{P}\left(Z > \frac{t}{M\sigma^2}\right) = 1 - \alpha,$$
$$\frac{1}{2}\mathrm{erfc}\left(\left(\frac{t}{M\sigma^2} - 1\right)\frac{\sqrt{M}}{2}\right) = 1 - \alpha.$$

The value of t is thus defined by

$$t = \left(\mathrm{erfc}^{-1}\left(2(1-\alpha)\right) \times \frac{2}{\sqrt{M}} + 1\right) \times M\sigma^2. \tag{4.15}$$

The idea of the plausibility criterion is to check at each iteration k of the algorithm, proposing image $\tilde{x}^k$ that $\tilde{n}^k = y - H\tilde{x}^k$, the estimate of the noise, is plausible. We consider that the proposal is plausible if $\mathbb{P}(\|n\|^2 < \|\tilde{n}\|^2) > \alpha$. The critical value for $\|\tilde{n}\|^2$ can be computed using Formula (4.15). The L^2 distance of the estimate of the noise equals

$$\|\tilde{n}^k\|^2 = \|y - H\tilde{x}^k\|^2,$$

and is exactly the energy multiplied by $2\sigma^2$. This means that the plausibility criterion does not require additional computation. It can only be a supplementary condition on the continuation of the algorithm: it should stop when the energy is below the critical value t, according to the chosen value of α.

4.3.2 Adaptation of the algorithm

As mentioned, the only change in the algorithm is an additional condition on the energy value; the value of t is computed once at the beginning of the algorithm. At each iteration, there is a check that the energy is not smaller than t, leading to Algorithm 4.

Remark 21. *This criterion can also be adapted to a projected gradient algorithm, or any other algorithm, adding a condition on the energy value at each iteration.*

Algorithm 4: Nesterov algorithm using plausibility criterion

Inputs $x_0 \in \mathbb{R}_+^\Omega$, initialization, L, Lipschitz constant for ∇f, N_i number of iterations, α, such that $\mathbb{P}(\|n\|^2 > \|\tilde{n}\|^2) \sim 1-\alpha$, σ, standard deviation of the Gaussian noise applied to the data
Output x_{old}, last plausible estimate obtained estimating $\hat{x}_{MAP}$

$g \leftarrow 0$,
$t \leftarrow (\text{erfc}^{-1}(2(1-\alpha))\frac{2}{\sqrt{M}} + 1)M\sigma^2$
$x \leftarrow x_0$
$E \leftarrow E(x)$
$k \leftarrow 0$
while $k < N_i$ **and** $2\sigma^2 E < t$ **do**
  $x_{old} \leftarrow x$
  $\text{grad}E \leftarrow \nabla E(x)$
  $y \leftarrow \max(0, x - \frac{\text{grad}E}{L})$
  $g \leftarrow g + \frac{k+1}{2}\text{grad}E$
  $v \leftarrow \max(0, x_0 - \frac{g}{L})$
  $x \leftarrow \frac{2}{k+3}v + \frac{k+1}{k+2}y$
  $E \leftarrow E(x)$
  $k \leftarrow k+1$
end while
return x_{old}

4.3.3 Results with plausibility criterion

This criterion was tested with Nesterov algorithm for several images, among the ones presented before. In Figure 4.11 are compared the blurry and noisy images with the real MAP estimate obtained with Algorithm 3 (presenting night sky in all cases) and the last plausible iteration generated by Algorithm 4. The algorithm stops before the apparition of the night sky for the 3 of them, and a real gain of sharpness can be observed. In Figure 4.12, a profile shows a better separation after deconvolution but also the appearance of details that were not visible on the blurry image, meaning that some deblurring was performed.

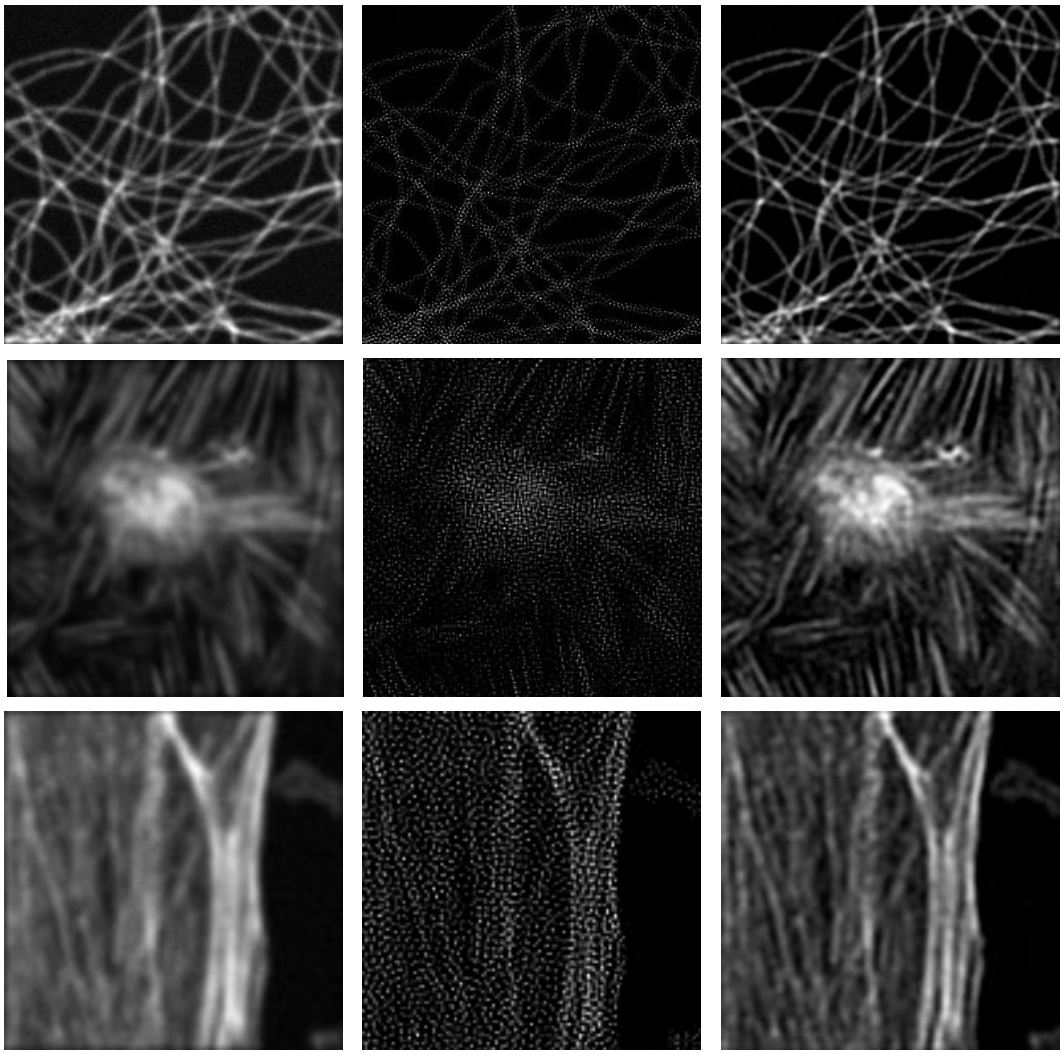

Input image MAP estimate Last plausible result

Figure 4.11: Illustration of the plausibility criterion on several images. From left to right: original blurry and noisy image (Gaussian noise) - MAP estimate (converged result of Nesterov algorithm) with night sky - last plausible result obtained during Nesterov algorithm estimating the MAP estimate. With no doubt the last image shows a gain of sharpness in comparison to the first one, curves are thiner, even if not all separations are visible. We can observe that the criteria permits the algorithm to stop before the presence of night sky.

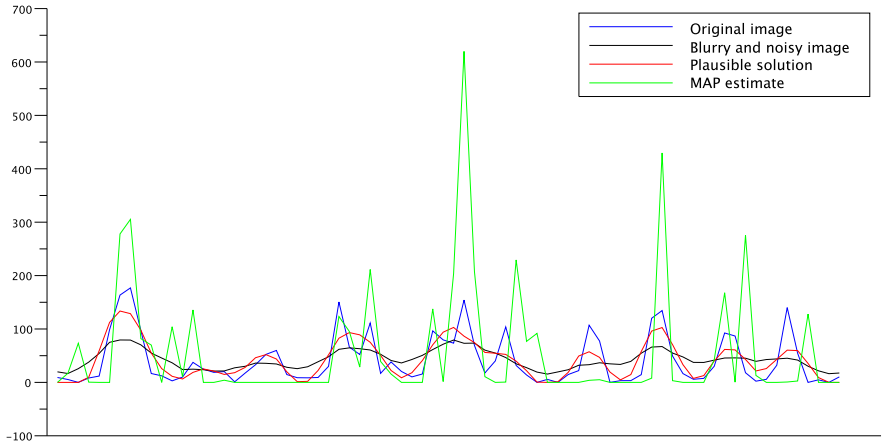

Figure 4.12: Cross-section from fibroblast image (image in the middle of Figure 4.11), on a line made of separated filaments. The comparison between the original image, the blurry/noisy one and the plausible estimate clearly shows that some deblurring was performed; indeed the separations are stronger in the plausible estimate, and we can also see some separations that had been hidden destroyed by the convolution. The real MAP estimate is made of distributions of Dirac, with very high intensities, not representative of the original signal.

Chapter 5

Emitters-Least-Square Error estimator - Application to deconvolution with positivity constraint

Contents

In [76], the Least-Square Error (LSE) estimate, computed by

$$\hat{x}_{LSE} = \int_{\mathbb{R}^n} p(x|y)xdx = \frac{\int_{\mathbb{R}^n} e^{-E_y(x)}xdx}{\int_{\mathbb{R}^n} e^{-E_y(x)}dx} = \mathbb{E}(x|y), \tag{5.1}$$

with $y \in \mathbb{R}^n$ the noisy version (Gaussian noise) of $x \in \mathbb{R}^n$ that we want to recover. This approach is different from the Maximum A Posteriori estimate, which computes "the" image that minimizes the energy; this minimum may not be totally representative of the posterior density.

The integrals in (5.1), computed on a space of large dimension (n is the number of pixels of the image), require special tools to be estimated. Indeed, methods using regular sampling (such as rectangles method) are not possible with such a huge dimension. We use Monte Carlo Markov chain, MCMC, methods with the algorithm of Metropolis-Hastings. We briefly recall the principles and convergence properties of MCMC and of Metropolis-Hastings algorithm, which enables to generate a chain with a chosen stationary distribution. Then, we adapt the computation of the LSE estimate in the case of deconvolution with positivity constraint. Finally, we define an estimate more adapted to sparse images, called Emitters-Least-Square Error (E-LSE) estimate.

We recall that, in the following, we are dealing with images whose rows are assembled to create a vector of size n. We may sometimes refer to Ω, the set of pixels of x, the image to recover; it satisfies $|\Omega| = n$, so that the integrals on $\mathbb{R}^n$ and on $\mathbb{R}^\Omega$ are equivalent. y is defined on Ω', with $|\Omega'| = p > n$.

5.1 Brief recall on MCMC methods

A MCMC, for Monte Carlo Markov chain, is a method allowing to sample a probability distribution, using Markov chains. Indeed, if we know how to sample from the probability density law $\exp(-E_y(x))/Z$, we know how to estimate the expectation of this law, and thus how to compute $\widehat{x}_{LSE}$. We recall that a Markov chain is a discrete random process, whose next state uniquely depends on the current state, and is independent from its past ones. We focus on Metropolis-Hastings algorithm that defines a Markov chain, with a given stationary distribution, by using a transition procedure divided in two phases: a proposal of a new state and an acceptance or rejection of this state. We briefly present the principle of this method and focus on how to implement Metropolis-Hastings algorithm in practice to approximate the

estimate (5.1). In this formula, the space of definition of the integrals is $\mathbb{R}^n$. However, when computing numerically the estimate, the set of states is finite. For this reason, and because Markov chains with a finite state space are really easier to address theoretically, in the following, we present the definitions and properties in the case of finite state space. Remark 22 will, however, briefly consider the continuous case.

5.1.1 Definitions

Definition 1. *Given a set I, called the state space, a random process $(\gamma_k)_{k\geqslant 0} \in I^{\mathbb{N}}$ is a Markov chain with initial distribution μ if, for any $i_0, \ldots, i_{k+1} \in I$,*

- $\mathbb{P}(\gamma_0 = i_0) = \mu(i_0)$,
- $\mathbb{P}(\gamma_{k+1} = i_{k+1} | \gamma_0 = i_0, \ldots, \gamma_k = i_k) = \mathbb{P}(\gamma_{k+1} = i_{k+1} | \gamma_k = i_k)$.

Definition 2. *The Markov chain (γ_k) is said to be homogeneous if*

$$\forall k \in \mathbb{N},\ \forall (i,j) \in I \times I,\ \mathbb{P}(\gamma_{k+1} = i | \gamma_k = j) = \mathbb{P}(\gamma_1 = i | \gamma_0 = j).$$

If I is finite (let us set $I = \{1, 2, \ldots, K\}$), we can define the transition matrix $P = (p_{i,j})_{1\leq i,j\leq K}$, with

$$p_{i,j} = \mathbb{P}(\gamma_1 = i | \gamma_0 = j).$$

The Markov Chain (γ_k) is then fully characterized by the initial distribution μ and the transition matrix P.

Definition 3. *We say that a Markov chain is irreducible if each one of its states communicates with each other, that is each state is accessible from each other one.*

Definition 4. *A Markov chain (γ_k) with transition matrix P is said to have $\pi = (\pi_i)_{i\in I}$ as a stationary distribution if $\pi = \pi P$.*

5.1.2 Main theorem

The convergence theorem in the case of finite states space can then be expressed as (see for instance [45]),

Theorem 1. *Given an irreducible Markov chain, $(\gamma_k)_{k\geq 0}$, with stationary distribution π, defined on a finite state space I, we have*

$$\forall f : I \to \mathbb{R},\ \frac{1}{N}\sum_{k=1}^{N} f(\gamma_k) \underset{N\to+\infty}{\longrightarrow} \sum_{i\in I} f(i)\pi(i)\ \ a.s.$$

This means that we can approximate the value of $\sum_{i\in I} f(i)\pi(i)$, which can be an approximation of $\int_{\mathbb{R}^n} f(x)\pi(x)dx$, with the average value of the $f(\gamma_k)$ for $1 \leq k \leq N$.

Remark 22. *The convergence theorem can be expressed in a continuous framework as (see for instance [81] and [75] for the exact definition of the properties of the chain): given $(\gamma_k)_{k=1,\dots,N}$ an Harris-recurrent chain (i.e irreducible, with a stationary measure, π, and for all A with $\pi(A) > 0$, the chain will visit A infinitely often, whatever the first state of the chain is), we have*

$$\forall f \in L^1(\pi),\ \frac{1}{N}\sum_{k=1}^{N} f(\gamma_k) \underset{N\to+\infty}{\longrightarrow} \int f(x)\pi(dx)\ a.s.\ ,$$

meaning that the integral of a function $f \in L^1(\pi)$ can be approximated with the average value of the $f(\gamma_k)$ for $1 \leq k \leq N$.

In Formula (5.1), π is the measure with density

$$p(x) = \frac{e^{-E_y(x)}}{\int_{\mathbb{R}^n} e^{-E_y(z)}dz} = \frac{1}{Z}e^{-E_y(x)}, \tag{5.2}$$

where Z is simply a normalizing factor. We thus need to know how to create a Harris-recurrent chain with stationary measure π, which can be done using Metropolis-Hastings algorithm.

5.1.3 Metropolis-Hastings algorithm

The algorithm of Metropolis-Hastings, first created by Metropolis in the 1950's [80] and improved by Hastings in the 1970's [51], enables to create a chain with stationary distribution π. Its density p is used in a phase of acceptance/rejection of a proposed state of evolution for the chain. Here, we present the discrete version of the algorithm [45], which will be the one used to approximate the estimates.

Given a proposal distribution $q(\cdot|\cdot)$ and a Markov chain γ_k, with an initial measure γ_0, we define its transition matrix P as follows

$$P(\gamma_k, \gamma_{k+1}) = \begin{cases} \rho(\gamma_k, \gamma_{k+1})q(\gamma_k|\gamma_{k+1}) & \text{if } \gamma_k \neq \gamma_{k+1} \\ \sum_v (1 - \rho(\gamma_k, v))q(v|\gamma_k)dv & \text{otherwise} \end{cases},$$

with

$$\rho(\gamma_k, \gamma_{k+1}) = \begin{cases} \min\left(\dfrac{p(\gamma_{k+1})}{p(\gamma_k)}\dfrac{q(\gamma_k|\gamma_{k+1})}{q(\gamma_{k+1}|\gamma_k)}, 1\right) & \text{if } p(\gamma_k)q(\gamma_{k+1}|\gamma_k) > 0 \\ 1 & \text{if } p(\gamma_k)q(\gamma_{k+1}|\gamma_k) = 0 \end{cases}.$$

Then, if γ_0 is chosen such that its support belongs to the one of π, π is a stationary distribution for γ_k.

This leads to an algorithm with the following steps

— compute $\gamma_{k+1/2} \sim q\left(\gamma_{k+1/2}|\gamma_k\right)$

— if $p(\gamma_{k+1/2})q\left(\gamma_k \left|\gamma_{k+1/2}\right.\right) > p(\gamma_k)q\left(\gamma_{k+1/2}\left|\gamma_k\right.\right)$ then $\gamma_{k+1} = \gamma_{k+1/2}$
otherwise $\gamma_{k+1} = \begin{cases} \gamma_{k+1/2} & \text{with probability } p = \min\left(\frac{p(\gamma_{k+1/2})}{p(\gamma_k)}\frac{q(\gamma_k|\gamma_{k+1/2})}{q(\gamma_{k+1/2}|\gamma_k)}, 1\right) \\ \gamma_k & \text{with probability } 1-p \end{cases}$

The proposal distribution q should respect some criteria:

— it should be easy to implement,

— jumps between two states of the chain should not be too "big",

— the parameters should be chosen so that the proposal is not rejected too often (otherwise convergence can be quite long), but not accepted too often either; without entering into details (which can be found in [76]), an optimal proposal distribution should be chosen so that the acceptance rate, that is the number of times the proposal $\gamma_{k+1/2}$ is accepted with respect to the total number of proposed changes, is around 0.234 [20].

In our case, the proposal distribution is also chosen to ensure the positivity of the solution, the only constraint on the solution. More precisely, in the case of the LSE estimate, q, which enables to go from image $u = (u_i)_{i\in\{1,\dots,n\}}$ to $u' = (u'_i)_{i\in\{1,\dots,n\}}$, is chosen as follows

$$q(u'|u) = \frac{1}{n}\sum_{i=1}^{n}\left(\prod_{j\neq i}\delta_{u_j}(u'_j)\right)\frac{1}{2\alpha}\mathbb{1}_{|\log(u_i)-\log(u'_i)|\leq\alpha}, \tag{5.3}$$

that is, between two states of the chain, up to one pixel value is modified. The choice $|\log(u_i) - \log(u'_i)| \leq \alpha$ ensures to preserve the positivity, given a positive initialization, since we have $u'_i = e^{\beta}u_i,\ \beta \sim \mathcal{U}_{[-\alpha,\alpha]}$.

Remark 23. *The function $q(\cdot, u)$ is a probability density on the set defined by*

$$\bigcup_{i=1}^{n} \left\{ \begin{pmatrix} \vdots \\ u_{i-1} \\ \lambda \\ u_{i+1} \\ \vdots \end{pmatrix}, \ |\log(\lambda) - \log(u_i)| \leq \alpha \right\}.$$

Remark 24. *In the algorithm proposed by Metropolis-Hastings, only the ratio of $p(\gamma_k)$ and $p(\gamma_{k+1})$ needs to be computed and since they have the same normalizing factor, Z, defined in (5.2), there is no need to estimate Z.*

5.1.4 Parameters for the computation of the estimate

In the following, the chosen function f is the coordinate function, that is $f_z : x \mapsto x(z)$ for each pixel z; it is square integrable with respect to π. According to Theorem 1, an estimation of the gray level $\hat{x}_{LSE}$ can be approximated by averaging the results of the function f for all the states of an irreducible chain with stationary distribution π. First we cannot have an infinite number of states for the chain, meaning that we need to fix a number of iterations, called N_i. It has to be chosen large enough, so that the result correctly approximates the estimate (convergence is reached) and does not depend much on the initialization.

However, since, from one state to another, no more than one pixel has been modified, with our choice of proposal distribution, we decide that each iteration k, with $1 \leq k \leq N_i$ is decomposed into n_i sub-iterations. In the following, for the LSE, we set $n_i = |\Omega| = n$, so that, in average, each pixel has been modified during one iteration. At each chain γ_k we associate Υ_k, defined by

$$\forall k \in \{1, \ldots, N_i\}, \ \Upsilon_k = \gamma_{kn_i}, \tag{5.4}$$

and we use Υ_k for the computation of the estimates.

Instead of using all the states of the produced chain, that is the Υ_k, $1 \leq k \leq N_i$, a method called *burn-in* is used (see [75] for instance) which consists in averaging all the iterations produced after iteration b, which is called the burn-in parameter. b has to be chosen so that the stationary regime of the chain is more or less reached, and enables that the initialization does not impact the final result. The approximation

of the estimate is then given by

$$\frac{1}{N_i - b} \sum_{k=b+1}^{N_i} f(\Upsilon_k),$$

and an optimal way to find b is proposed in [75]. In our case, it will be fixed. Most of the time, we chose $b = N_i/2$.

In [75] again, we can find a convergence criteria using two Markov chains, γ_n and γ'_n, with their corresponding Υ_n and Υ'_n as defined in (5.4). The following equality can be proven, for b and N_i large enough

$$\left\| \frac{1}{N_i - b} \sum_{k=b+1}^{N_i} f(\Upsilon_k) - \hat{x}_{LSE} \right\|_2 \simeq \frac{1}{\sqrt{2}} \left\| \frac{1}{N_i - b} \sum_{k=b+1}^{N_i} (f(\Upsilon'_k) - f(\Upsilon_k)) \right\|_2 .$$

Then to obtain a precision of ε, one can stop when

$$\frac{1}{N_i - b} \sum_{k=b+1}^{N_i} (f(\Upsilon'_k) - f(\Upsilon_k)) \leq 2\varepsilon,$$

and the estimate is given by

$$\frac{1}{2} \left(\frac{1}{N_i - b} \sum_{k=b+1}^{N_i} (f(\Upsilon'_k) - f(\Upsilon_k)) \right)$$

and is expected to lie at a maximum value of ε from $\hat{x}_{LSE}$.

However, in the case of deblurring and especially with the estimate E-LSE that we present at the end of this chapter, the chains sometimes get blocked in a configuration; the changes between two states become either less frequent or are not very significant. That is the reason why, in order to speed up the algorithm, we generalize this idea to several chains, N_c. Given N_c computed chains $(\gamma_k^l)_{1 \leq k \leq N_i,\ 1 \leq l \leq N_c}$, and their corresponding (Υ_k^l), the estimate is given by

$$\frac{1}{N_c} \sum_{l=1}^{N_c} \frac{1}{N_i - b} \sum_{k=b+1}^{N_i} f(\Upsilon_k^l).$$

5.2 Least-Square Error Estimate

The Maximum A Posteriori estimate, although it is a natural choice, is not really representative of the posterior density; in [52], the authors explain that this estimate is only depending on the mode location, whatever its probability is. With the posterior expectation, we expect to generate an estimate that describes better the posterior density. The idea of using this kind of estimate in image processing is not new, it has been studied in the 1990's by Besag in [16] for instance.

5.2.1 Denoising with Least-Square Error estimate

Gaussian denoising with Total variation prior

As mentioned before, $\hat{x}_{LSE}$ was proposed for Gaussian denoising. The full model and its properties can be found in [75]. The Total Variation (TV) operator was used as a prior, giving the following definition of $\hat{x}_{LSE}$

$$\hat{x}_{LSE} = \frac{\int_{\mathbb{R}^n} \exp\left(-\frac{\|x-y\|^2+\lambda TV(x)}{2\sigma^2}\right) x dx}{\int_{\mathbb{R}^n} \exp\left(-\frac{\|x-y\|^2+\lambda TV(x)}{2\sigma^2}\right) dx}, \tag{5.5}$$

with λ the regularization parameter. First proposed in [96] for image restoration, the Maximum A Posteriori estimate with TV prior can be computed really quickly thanks to Chambolle algorithm [24]; however it is known to present an artifact called *staircasing*. This artifact is characterized by the fact that a (noisy) linear signal will have a piecewise constant $\hat{x}_{MAP}$ estimate and not linear as expected. On the contrary, the computation of the expectation of the posterior density (5.5) totally avoids this artifact, emphasizing that $\hat{x}_{MAP}$ may not be the most representative estimate. In that case, the LSE seems to be a better representation.

Poisson denoising

First, we propose to compute the LSE estimate, $\hat{x}_{LSE}$, in the case of Poisson denoising, without regularization, only positivity, induced by the Poisson assumption. Given $(x_k)_{k\in[\![1,n]\!]}$, with $x_k > 0$, and $y_k \in \mathbb{N}$ defined by

$$\forall k \in [\![1,n]\!]\,,\ y_k \sim \mathcal{P}(x_k),$$

the energy associated to the denoising problem is given by Formula (4.8), with $H = I$, that is

$$\forall x \int \mathbb{R}^n,\ E_y(x) = \sum_{j=1}^{n} x_j - y_j \log(x_j). \tag{5.6}$$

The value of the estimate given by Formula (5.1) is therefore given by

$$\hat{x}_{LSE} = \frac{\displaystyle\int_{\mathbb{R}_+^n} \exp\left(-\sum_{j=1}^{n} x_j + y_j \log(x_j)\right) x dx}{\displaystyle\int_{\mathbb{R}_+^n} \exp\left(-\sum_{j=1}^{n} x_j + y_j \log(x_j)\right) dx},$$

and is explicit. Let us first compute the numerator, we have

$$I = \int_{\mathbb{R}_+^n} e^{-E_y(x)} x dx = \int_{\mathbb{R}_+^n} \exp\left(-\sum_{j=1}^{n} x_j + y_j \log(x_j)\right) dx_1 \cdots dx_n$$

and using exponential function properties,

$$I = \left(\int_{\mathbb{R}_+^{n-1}} \left(\prod_{j\neq k} x_j^{y_j}\right) \exp\left(-\sum_{j\neq k} x_j\right) \left(\int_{\mathbb{R}_+} \left(x_k^{y_k+1}\right) e^{-x_k} dx_k\right) dx_1 \cdots dx_{k-1} dx_{k+1} \cdots dx_{n-1} \right)_{1\leq k\leq n}.$$

We can recognize the Gamma function defined as

$$\forall t \in \mathbb{R},\ \Gamma : t \longmapsto \int_0^{+\infty} x^{t-1} \exp(-x) dx,$$

giving

$$\int_{\mathbb{R}_+^n} x e^{-E_y(x)} dx = \left(\prod_{j\neq k} \Gamma(y_j) \times \Gamma(y_k + 1) \right)_{1\leq k\leq n}.$$

Using the property of Gamma function, $\forall t \in \mathbb{R},\ \Gamma(t+1) = t\Gamma(t)$, we have

$$\int_{\mathbb{R}_+^n} x e^{-E_y(x)} dx = \begin{pmatrix} \vdots \\ \prod_{j=1}^{n} \Gamma(y_j) \times (y_k + 1) \\ \vdots \end{pmatrix}_{1 \leq k \leq n} . \tag{5.7}$$

An identical computation for the denominator leads to

$$\int_{\mathbb{R}_+^n} e^{-E_y(x)} dx = \begin{pmatrix} \prod_{j=1}^{n} \Gamma(y_j) \\ \vdots \\ \prod_{j=1}^{n} \Gamma(y_j) \end{pmatrix}, \tag{5.8}$$

so that the ratio (5.7) / (5.8), gives

$$\forall k \in [\![1, n]\!]\,,\ (\hat{x}_{LSE})_k = y_k + 1. \tag{5.9}$$

Computing the LSE estimate on data corrupted by Poisson noise leads to a bias of 1 on the input data. Therefore, the use of this estimate on such data will not give an interesting denoising result; however, it shows that, numerically, the chain created thanks to Metropolis-Hastings algorithm converges to the correct estimate. We propose to create a chain defined by

$$\gamma_{k+1} = \begin{cases} \gamma_{k+1/2} = \gamma_k + (e^{Z_k} - 1)\gamma_k(X_k)\delta_{X_k} & \text{if } A_k > Y_k \\ \gamma_k & \text{else} \end{cases}, \tag{5.10}$$

with $Z_k \sim \mathcal{U}_{[-\alpha,\alpha]}$ ($\alpha > 0$ fixed), $Y_k \sim \mathcal{U}_{[0,1]}$, $X_k \sim \mathcal{U}_\Omega$, (X_k, Y_k, Z_k) independent random variables and

$$A_k = \frac{p(\gamma_{k+1/2})}{p(\gamma_k)} \frac{q(\gamma_k|\gamma_{k+1/2})}{q(\gamma_{k+1/2}|\gamma_k)}. \tag{5.11}$$

For a Poisson distributed noise, we have that $p(\gamma_k) = 1/Z \exp\left(-E_y(\gamma_k)\right)$, with E_y defined as in (5.6), that is

$$p(\gamma_k) = \frac{1}{Z} \exp\left(\sum_{j=1}^{n} x_j - y_j \log(x_j) \right).$$

Since $p(\gamma_{k+1/2})$ differs from $p(\gamma_k)$ by only the value of the pixel X_k (which may change from $\gamma_k(X_k)$ to $\gamma_k(X_k)e^{Z_k}$), we can isolate the contribution of this pixel in both chains, leading to the following difference between the energies,

$$\begin{aligned} E_y(\gamma_{k+1/2}) - E_y(\gamma_k) &= \left(\gamma_k(X_k)e^{Z_k} - y_{X_k}\log(\gamma_k(X_k)e^{Z_k})\right) \\ &\quad - \left(\gamma_k(X_k) - y_{X_k}\log(\gamma_k(X_k))\right) \\ &= \gamma_k(X_k)\left(e^{Z_k}-1\right) - y_{X_k}\left(\log\left(\frac{\gamma_k(X_k)e^{Z_k}}{\gamma_k(X_k)}\right)\right) \\ &= \gamma_k(X_k)\left(e^{Z_k}-1\right) - y_{X_k}Z_k, \end{aligned}$$

leading to

$$\frac{p(\gamma_{k+1/2})}{p(\gamma_k)} = \frac{e^{-E_y(\gamma_{k+1/2})}}{e^{-E_y(\gamma_k)}} = \exp\left(-\gamma_k(X_k)\left(e^{Z_k}-1\right) + y_{X_k}Z_k\right).$$

Concerning the proposal distribution, q, which enables to go from image $u = (u_i)_{i\in\{1,\dots,n\}}$ to $u' = (u'_i)_{i\in\{1,\dots,n\}}$, it is chosen as in Formula (5.3), that is, between two states of the chain, up to one pixel value is modified. The choice of multiplying the intensity by $\exp(Z_k)$ with $Z_k \sim \mathcal{U}_{[-\alpha,\alpha]}$ in Formula (5.10) ensures to preserve the positivity, given a positive initialization.

Given, like in Formula (5.10), that the chosen pixel to modify is X_k, the ratio $q(\gamma_{k+1/2}|\gamma_k)/q(\gamma_k|\gamma_{k+1/2})$ in (5.11) can then be written using the proposal distribution defined in (5.3), as

$$\frac{q(\gamma_k|\gamma_{k+1/2})}{q(\gamma_{k+1/2}|\gamma_k)} = \frac{\gamma_{k+1/2}(X_k)}{\gamma_k(X_k)} = e^{Z_k}. \tag{5.12}$$

Using Metropolis-Hastings as it was presented in Subsection 5.1.3, the probability p is written, in the case of denoising data with Poisson distributed noise, as

$$p = \frac{p(\gamma_{k+1/2})}{p(\gamma_k)}\frac{q(\gamma_k|\gamma_{k+1/2})}{q(\gamma_{k+1/2}|\gamma_k)} = \exp\left(Z_k - \gamma_k(X_k)\left(e^{Z_k}-1\right) + y_{X_k}Z_k\right),$$

with $Z_k \sim \mathcal{U}_{[-\alpha;\alpha]}$.

The burn-in method, as well as the control of convergence presented in Subsection 5.1.4, are used to produce the estimation of $\hat{x}_{LSE}$. We use two independent Markov

chains, γ_n and γ'_n, their corresponding Υ_n and Υ'_n given by (5.4), and compute the estimate as

$$\hat{x}_{LSE} \simeq \frac{1}{2}\left(\frac{1}{N_i - b + 1}\sum_{k=b+1}^{N_i}\Upsilon_k + \frac{1}{N_i - b + 1}\sum_{k=b+1}^{N_i}\Upsilon'_k\right), \tag{5.13}$$

and stop for N_i such that

$$\left\|\frac{1}{N_i - b + 1}\sum_{k=b+1}^{N_i}\Upsilon_k - \frac{1}{N_i - b + 1}\sum_{k=b+1}^{N_i}\Upsilon'_k\right\|_2 \leq 2\varepsilon. \tag{5.14}$$

The result given by (5.13) with $\varepsilon = 0.1$ can be seen in Figure 5.1. It reflects the theoretical Formula (5.9): a bias of 1 is visible between the input data and $\hat{x}_{LSE}$. The algorithm of Metropolis-Hastings, adapted to create one chain according to this scheme and used to generate the result, is presented in Algorithm 5. To make the algorithm converge faster, we chose to initialize the chain with the input vector y.

Algorithm 5: Computation of one chain (N_i iterations of n sub-iterations) in the case of denoising $y \in \mathbb{R}^n$, data corrupted with Poisson noise

Inputs $y \in \mathbb{R}^n$, input data, γ_0 s.t. $\gamma_0 = y$ initialization, N_i, number of iterations, α scaling parameter

Output Γ one of the chain used for the approximation of the LSE estimate

$k \leftarrow 0$
repeat
  draw $x \in \mathcal{U}_{[\![1,n]\!]}$
  draw $\beta \in \mathcal{U}_{[-\alpha;\alpha]}$
  $\gamma_{k+1/2} \leftarrow \gamma_k + \gamma_k(x)(1 - e^{\beta})\delta_e$
  $p \leftarrow \min\left(\exp\left(\beta(1 + y(x)) - \gamma_k(x)\left(e^{\beta} - 1\right)\right), 1\right)$
  $\gamma_{k+1} \leftarrow \begin{cases} \gamma_{k+1/2} & \text{with probability } p \\ \gamma_k & \text{with probability } 1 - p \end{cases}$
  $k \leftarrow k + 1$
until $k = N_i \times n$
$\Gamma = \frac{1}{N_i - b + 1}\sum_{k=b+1}^{N_i}\gamma_{k \times n}$
return Γ

(a) Ground truth (b) Input data (c) LSE estimate

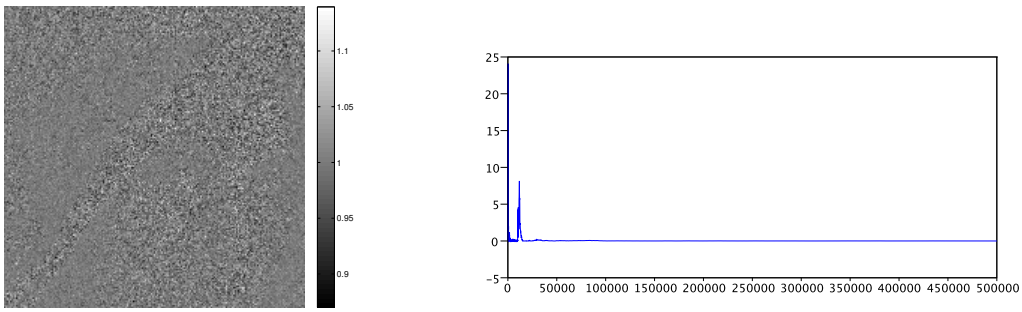

(d) Difference between LSE result and input data (e) Evolution of $\|\hat{x}_{LSE}(i) - (y(i)+1)\|_2$ for one pixel during iterations

Figure 5.1: Illustration of denoising with the LSE estimate on data corrupted by Poisson noise; (a) ground truth, (b) ground truth corrupted by Poisson noise, (c) LSE estimate (use of 2 chains, results computed by Formula (5.13), around $500,0000$ iterations to obtain convergence as in (5.14) for $\varepsilon = 0.2$), (d) image of the difference between the input data and the LSE estimate and (e) representation of $\|\hat{x}_{LSE}(i) - (y(i)+1)\|_2$ for one pixel. Visually, the LSE estimate is not better than the input image. This is logical since it simply introduces a bias of 1. However we see that the created model converges to the correct estimate (5.9). First, it can be seen on the image of the difference whose pixels are all around 1 (mean of 0.9997, variance of 7.2569e-04); secondly, the convergence of $\|x^k(i) - (y(i)+1)\|_2$, where $x^k(i)$ is the value of the estimate at iteration k, with $x^0(i) = y(i)$, varies a lot at the beginning of the algorithm, with the exploration of different states of the chain, but then stabilizes close to 0, meaning $x^k(i) \simeq (y(i)+1)$.

5.2.2 LSE estimate for deblurring

The LSE estimate can be adapted to the problem of deconvolution under positivity constraints. $\hat{x}_{LSE}$ is defined by integrating (5.1) on $\mathbb{R}^n_+$, using the model of deconvolution. The energy $E_y(x)$ can be either the Gaussian one or the Poisson one;

we recall them from Chapter 4, $\forall i \in \{1, \cdots, p\}$, $p > n$,

$$y_i \sim \mathcal{P}((Hx)_i) \Leftrightarrow \forall x \in \mathbb{R}^n,\ E_y(x) = (Hx)^t \mathbf{1}_{\mathbb{R}^p} - y^t \log(Hx), \tag{5.15}$$
$$y_i \sim \mathcal{N}((Hx)_i, \sigma^2) \Leftrightarrow \forall x \in \mathbb{R}^n,\ E_y(x) = \frac{\|Hx - y\|^2}{2\sigma^2},$$

and π is defined, as before, by $p(x) = 1/Z \exp(-E_y(x))$.

The algorithm is exactly the same as Algorithm 5, except for the acceptance probability. The state $k+1/2$ of the chain, when X_k is the modified pixel, is written, as before, as

$$\gamma_{k+1/2} = \gamma_k + \gamma_k(X_k)(e^\beta - 1)\delta_{X_k},\ \beta \sim \mathcal{U}([-\alpha, \alpha])$$

and the ratio of the proposal distributions is the same as in the case of denoising. However the difference between old and new energy is a bit different, because of the convolution. Let us denote S_φ the spatial support of the convolution kernel φ

$$S_\varphi = \text{supp}(\varphi),\ \text{with } |S_\varphi| = K,$$

with $K \ll n$ in most cases. One needs to recompute all the pixel values for pixels belonging to the support of the kernel centered on X_k (that is only for K pixels). In both cases of noise, the difference between $H\gamma_k$ and $H\gamma_{k+1/2}$ is given by

$$H\gamma_{k+1/2} = H\gamma_k + \gamma_k(X_k)(e^\beta - 1)\varphi(\cdot - X_k).$$

This means that for each iteration, the computation of the convolved proposal, $H\gamma_{k+1/2}$, is made by adding to the current convolved chained, $H\gamma_k$, the weighted kernel at the position X_k. The weight is given by the difference between the proposed and the old value.

The nature of the noise only impacts the acceptance probability. Let us first compute in both case $\delta E = E_y(\gamma_{k+1/2}) - E_y(\gamma_k)$. In the case of data corrupted by Poisson noise, we have

$$\delta E = \sum_{(i-X_k)\in S_\varphi} \gamma_k(X_k)(e^\beta - 1)\varphi(i - X_k) - y_i \log\left(\frac{(H\gamma_k)_i + \gamma_k(X_k)(e^\beta - 1)\varphi(i - X_k)}{(H\gamma_k)_i}\right), \tag{5.16}$$

and in the case of Gaussian noise,

$$\delta E = \sum_{(i-X_k)\in S_\varphi} ((H\gamma_{k+1/2})_i - y_i)^2 - ((H\gamma_k)_i - y_i)^2. \tag{5.17}$$

The difference between the energies is used for the computation of p,

$$p = \frac{p(\gamma_{k+1/2})}{p(\gamma_k)} \frac{q(\gamma_k|\gamma_{k+1/2})}{q(\gamma_{k+1/2}|\gamma_k)} = \exp\left(-(E_y(\gamma_{k+1/2}) - E_y(\gamma_k))\right) e^{\beta}, \tag{5.18}$$

where the first term is given by Formulas (5.16) and (5.17), depending on the noise, and the ratio of proposal distributions comes from Formula (5.12).

In this case, the LSE estimate is approximated using N_c chains, γ_k^l, by

$$\hat{x}_{LSE} \simeq \frac{1}{N_c} \sum_{l=1}^{N_c} \frac{1}{N_i - b} \sum_{k=b+1}^{N_i} \gamma_k^l.$$

In Figure 5.2, we present the influence of the scaling parameter α on the acceptance rate: as expected, a very small value gives so small changes that the new state is very often accepted and on the contrary, a big value reduces drastically the acceptance rate since the gap between two values rises. In the following, we took a value of α such that the acceptance rate is between 20 and 30% once it is stabilized. The value of α depends on input image (its values, the applied noise...).

In Figure 5.3 are presented results with the two kinds of noise. They both present night sky artifact, like the MAP estimate. Indeed, when looking at the final states of the different chains, we can see that most of them present the artifact, and therefore, so does their average.

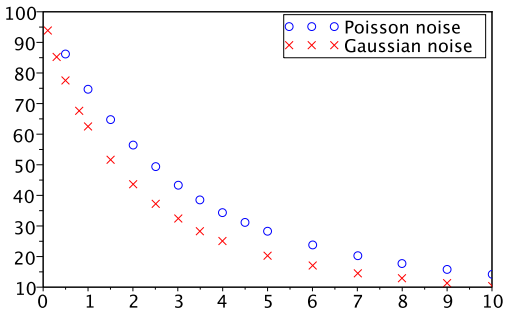

(a) Averaged final acceptance rates according to the value α

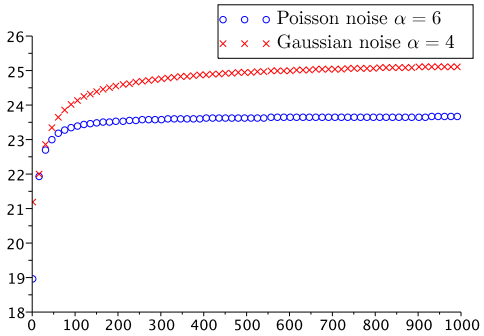

(b) Evolution of the averaged rates according to iterations

Figure 5.2: (a) Mean value of the final acceptance rates according to the values of the scaling parameter α (the proposition of the new intensity of the pixel being multiplied by e^{β}, $\beta \sim \mathcal{U}([-\alpha, \alpha])$) and (b) evolution of the averaged acceptance rates during the iterations for the values of scaling giving the "optimal" final rate according to [20] (close to 0.234), that is $\alpha = 4$ in the Gaussian case, $\alpha = 6$ in the Poisson one. These values were computed using around 5000 chains. As expected, for a small value, which creates very small changes of intensity, the acceptance rates are quite high, and they decrease when α increases. We can notice on (b) that the acceptance rates in the first iterations are quite low and then almost stabilize.

The variance error estimation per pixel, which can be computed by

$$\frac{1}{\sqrt{N_c}\sqrt{n}} \left\| \sum_{i=1}^{N_c} \left(\frac{1}{(N_i - b)N_c} \sum_{k=b}^{N_i} (\gamma_k^i)^2 - \frac{1}{(N_i - b)} \left(\frac{1}{N_c} \sum_{k=b}^{N_i} \gamma_k^i \right)^2 \right) \right\|_2, \tag{5.19}$$

is represented in Figure 5.5 and can be used to control convergence.

5.2.3 Energy weighting

As seen in the previous Chapter, the non converged MAP gives better results than the real estimate, avoiding the night sky effect. This gives the idea of computing, instead of $\hat{x}_{LSE}$,

$$\hat{x}_{LSE}^{\lambda} = \frac{\displaystyle\int_{\mathbb{R}^{\Omega}} x e^{-\lambda E_y(x)} dx}{\displaystyle\int_{\mathbb{R}^{\Omega}} e^{-\lambda E_y(x)} dx}, \tag{5.20}$$

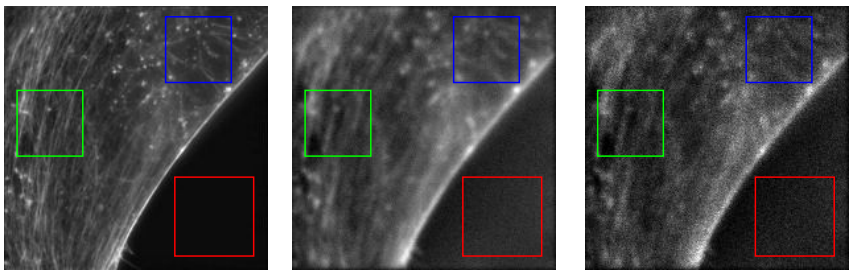

(a) Ground truth (b) Convolution and Gaussian noise (c) Convolution and Poisson noise

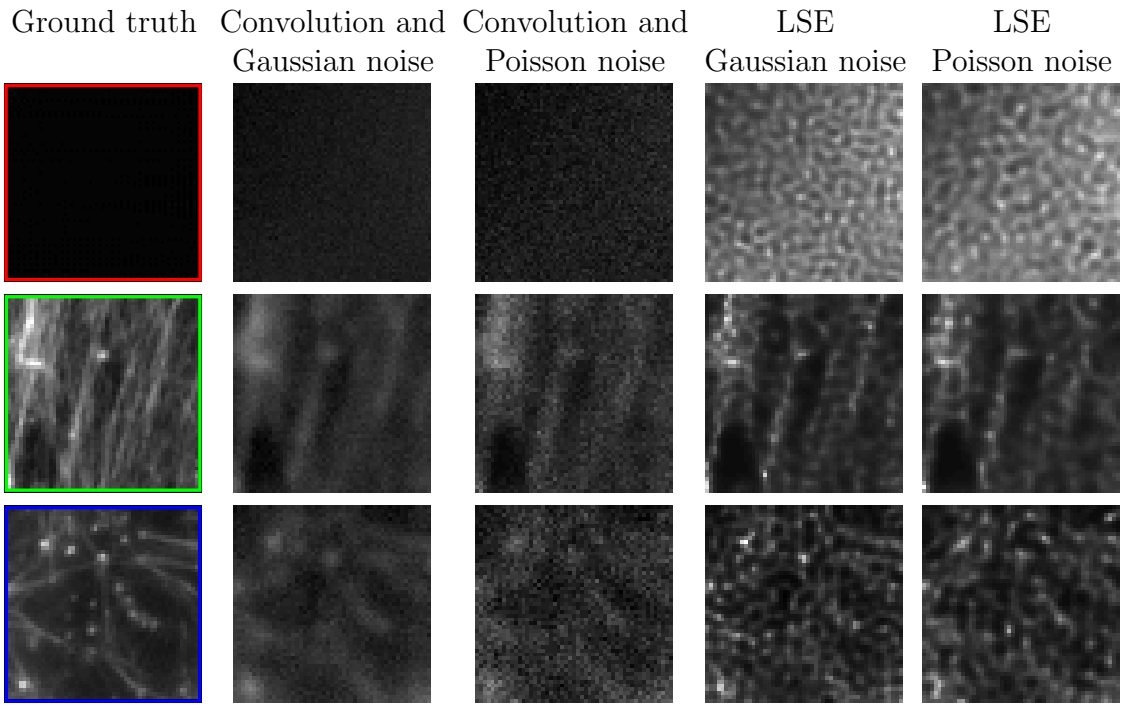

Figure 5.3: Illustration of the Least-Square Error estimate in the cases of Poisson and Gaussian noise. On top, the ground truth image (a) has been blurred with a Gaussian kernel with standard deviation 2; Gaussian noise, with standard deviation 2, was added (b) or Poisson noise was applied (c) and LSE estimates were approximated. In order to see precisely the results, we chose three regions, drawn on the original images. The results on these regions are represented below, compared with the original image and the convolutions. It is clear that in both cases the night sky effect was not removed thanks to this estimate. The almost constant black background is recovered as a texture, the filaments have lost their continuities. On top of that the biological elements looking like dots were not really separated.

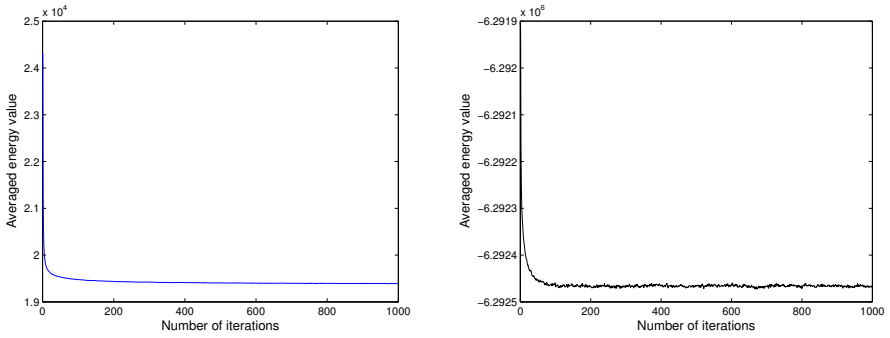

Gaussian energy Poisson energy

Figure 5.4: Evolution of the (averaged) energies in both case, according to the number of iterations, is shown below. Results were obtained with $1,000$ iterations, averaging the last quarter of the iterations; around $4,000$ chains were used. Energies in both cases decrease very fast during the first iterations and then stabilize.

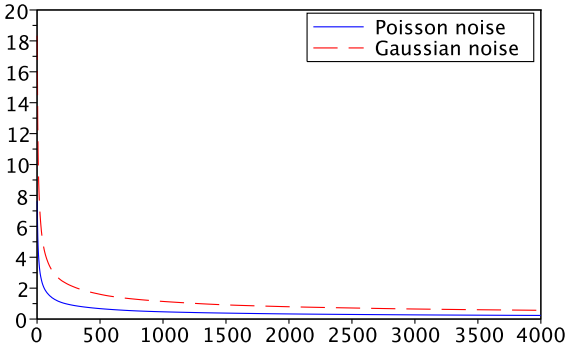

Figure 5.5: Evolution of the averaged variance error estimation per pixel, given by Formula (5.19), for both Poisson and Gaussian LSE-estimate from images of Figure 5.3 is represented according to the number of chains. The error decreases drastically during the 500 to $1,000$ first chains but would require a very large number of chains to totally stabilize; indeed, we can see that it continues to decrease even after 3000 chains (but quite slowly).

which consists in a weighting of the energy. This formula can be used for both models of noise. We present the results of this estimate on three values of λ in Figure 5.6, as well as a zoom on the regions of interest for $\lambda = 0.001$ in Figure 5.7. As expected by its definition, a very big value of λ leads to a result very close to the MAP estimate, whereas a very small one creates a blurry image with no gain of resolution, since

the probability of acceptation becomes more dependent on the intensities of emitters than the energy, according to Formula (5.18). The results with $\lambda = 0.001$ are very close to the result obtained with the plausibility criteria proposed in the previous chapter. Concerning the implementation, it is totally equivalent to the classical LSE, just replacing the computation of E by λE each time the total or partial energy is computed.

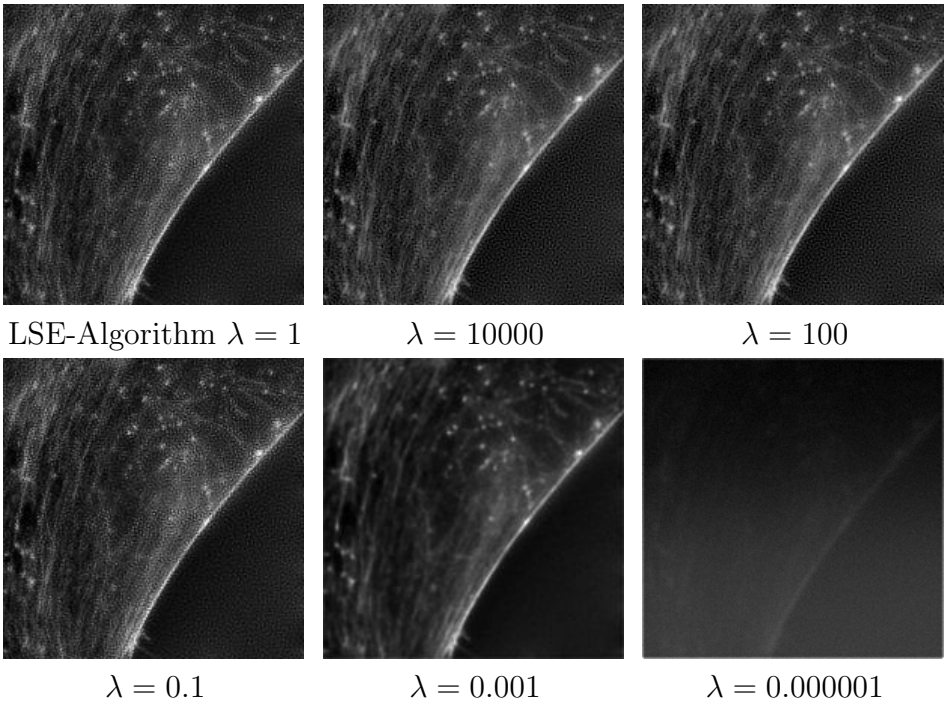

Figure 5.6: Influence of the energy weighting in the case of data corrupted by Gaussian noise: (5.20) was computed for several values of λ from 0.000001 to 10000. The night sky effect is noticeable on the images down to $\lambda = 0.001$ where the reconstruction is artifact free and more resolved than the input image (see 5.7 for a comparison with the real and input data, on the same regions as Figure 5.3). A too small value of λ, as it was predicted, creates an image with no details, where the structures are not even visible anymore.

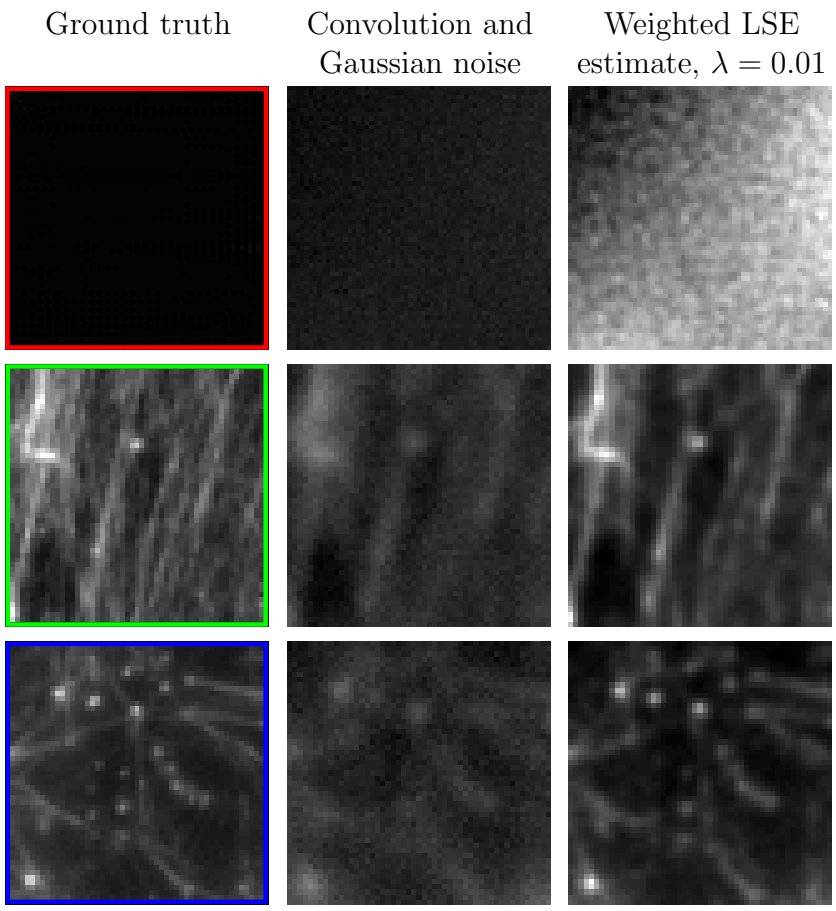

Figure 5.7: Zoom on the same regions as Figure 5.3 for $\lambda = 0.001$ (which seems the best compromise between deblurring and no artifact in Figure 5.6). We see that on the constant area, the artifactual texture created by the LSE estimate is less visible, even if the image is not constant either. The deblurring on filaments was quite efficient, comparing with the input image, as well as the dots; however some structures seem to have disappeared or are really less intense than in the original image.

5.3 Emitters-Least-Square Error Estimate

5.3.1 Definition of the Emitters-Least-Square Error estimate

In order to take into account the sparsity of the result image (particularly true in the case of microscopy, since the image is supposed to be obtained thanks to a finite number of excited fluorophores), we propose to compute the Least-Square Error estimate, but on the restricted set of images $C \subset \mathbb{R}^{\Omega}$ defined by

$$C = \left\{ x \in \mathbb{R}^{\Omega} \middle| x = \sum_{e=1}^{N_e} \lambda_e \delta_{p_e} \, , \lambda_e \in \mathbb{R}, p_e \in \Omega \right\}, \tag{5.21}$$

with $N_e < n = |\Omega|$. This means that we consider that the latent image can be written as a sum of weighted Dirac distributions, located on some pixels of the result image. It may be noticed that this definition does not prevent several emitters from sharing the same position. The E-LSE estimate, $\hat{x}_{E-LSE}$, is defined as

$$\hat{x}_{E-LSE} = \frac{\displaystyle\int_C x e^{-E_y(x)} dx}{\displaystyle\int_C e^{-E_y(x)} dx}.$$

Due to the structure of C and the definition of the Poisson energy in (5.15), we decided to add a background constant, B, in the Poisson model, that is

$$\forall i \in \{1, \cdots, p\}, \; y_i \sim \mathcal{P}((Hx)_i + B),$$

leading to the Poisson energy

$$E_y(x) = \sum_{i=1}^{p} (Hx)_i + B - v_i \log((Hx)_i + B).$$

Adding a background value is very convenient in the case of Poisson noise, especially when dealing with sparse images because it will prevent the logarithmic term from exploding [119]. Moreover it can help modeling images with a constant background but no information. Most of the time, in our cases, it is chosen quite small (< 0.1), so that it does not affect the computed intensities.

In the previous chapters, we considered that the solution x was band-limited; in the following, it satisfies $x \in C$, where C is defined by (5.21). The computation is

then a bit different. The convolution, with the kernel φ, can be written as

$$\forall i \in \{1, \cdots, p\},\ (Hx)_i = \sum_{e=1}^{N_e} \lambda_e \varphi(i - p_e). \tag{5.22}$$

This means that $Hx = \sum_e \lambda_e \varphi(\cdot - p_e)$, so that the image of the convolution is in fact a sum of weighted copies of the kernel φ: the intensities of the emitters, λ_e, define the weights and their positions, p_e, the centers of the replicated kernels.

5.3.2 Initialization of the emitter positions

The number of emitters N_e is user defined, according to the input data. All the chains generated during the algorithm have the same number of emitters. In order to have "interesting" positions (that is quite close to the ones of the final solution) from the very start of the algorithm, we chose to draw the initial positions using the input data as a distribution of probability. Indeed, with this method, the chosen positions should rarely belong to very dark zones of the image, where emitters are less needed. More precisely, given $\tilde{y} = (\tilde{y}_i)_{i=1,\dots,p}$, normalization of y_i, that is

$$\forall i \in \{1, \dots, p\},\ \tilde{y}_i = \frac{y_i}{\sum_{i=1}^{p} y_i},$$

we decide that the probability of choosing pixel i as a position for initialization, X, is given by $\mathbb{P}(X = i) = \tilde{y}_i$.

To draw the positions according to $\tilde{y}$, we use the cumulative distribution function of X, F_X whose definition is

$$\forall i \in \{1, \dots, p\},\ F_X(i) = \sum_{1 \le k \le i} \tilde{y}_k,$$

and given a uniform variable $U \sim \mathcal{U}_{[0,1]}$, we have that

$$\forall i \in \{1, \dots, p\},\ \mathbb{P}(F_X(i-1) < U \le F_X(i)) = \mathbb{P}(F_X(i)) - \mathbb{P}(F_X(i-1)) = \tilde{y}_i.$$

This means that in order to generate the N_e positions with the desired law, we can draw N_e uniform variables on $[0, 1]$, U_e, and choose the positions p_e as

$$\forall e \in \{1, \cdots, N_e\},\ \mathbb{P}(F_X(p_e - 1) < U_e \le F_X(p_e)).$$

5.3.3 Optimization of the initial emitter intensities

Once the N_e positions are computed, the intensities are initialized with value 1, so that the expectation of the initialization is the input image. However 1 may be not the optimal value for the emitter intensities. For this reason, we decide to optimize this value at the beginning of the algorithm by looking for the constant A that minimizes $E_y(Ax)$. We present the result for both Gaussian and Poisson noise distributions. In the first case, the computation is direct, whereas in the second one, it requires to use a fixed point method, for instance Newton's method.

Gaussian energy

The energy for Ax can be written as

$$E_y(Ax) = \|H(Ax) - y\|_2^2 = \sum_{i=1}^{p} (A(Hx)_i - y_i)^2,$$

leading to

$$\begin{aligned}\frac{d}{dA}(E_y(Ax)) &= \sum_{i=1}^{p} 2((H(Ax))_i - y_i)(Hx)_i \\ &= 2A\sum_{i=1}^{p}((Hx)_i)^2 - 2\sum_{i=1}^{p} y_i(Hx)_i,\end{aligned}$$

and then we have the equivalence

$$\frac{d}{dA}(E_y(Ax)) = 0 \iff A = \frac{\sum_{i=1}^{p} y_i(Hx)_i}{\sum_{i=1}^{p}((Hx)_i)^2}.$$

The optimal initialization in the Gaussian case is obtained by multiplying each emitter intensity by the value of A defined above.

Poisson energy

In the Poisson case, because of the B term added in the logarithm, the expression is not explicit and we propose to use Newton's method to find the optimal value, A^*. Note that this methods converges in a few iterations. A^* is given by

$$A^* = \min_{A \in \mathbb{R}^+} E_y(Ax).$$

Setting $F(A) = E_y(Ax) = \sum_{i=1}^{p}((H(Ax))_i + B) - y_i \log((H(Ax))_i + B)$, we have

$$F'(A) = \sum_{i=1}^{p}(Hx)_i - \frac{y_i(Hx)_i}{(H(Ax))_i + B} = \sum_{i=1}^{p}(Hx)_i \left(1 - \frac{y_i}{(H(Ax))_i + B}\right). \quad (5.23)$$

A^* corresponds to the zero of (5.23), which cannot be computed directly. Using Newton's method, we define the sequence A_k, with

$$\forall k \in \mathbb{N},\ A_{k+1} = A_k - \frac{F'(A_k)}{F''(A_k)}. \quad (5.24)$$

The computation of F'' gives

$$F''(A) = \sum_{i=1}^{p} \frac{((Hx)_i)^2 y_i}{((H(Ax))_i + B)^2}.$$

To be able to use Newton's method, one needs that $\forall k,\ F''(A_k) \neq 0$; the denominator is never 0 thanks to the additional B term. For the numerator, the condition is

$$\exists i \in \{1, \dots, p\},\ (Hx)_i > 0 \text{ and } y_i > 0.$$

The first value of the sequence A_0 should respect $F'(A_0) \neq 0$, otherwise Equation (5.24) gives $\forall k \in \mathbb{N},\ A_{k+1} = A_k = A_0$. Due to convexity of the function, if the minimum respects $F'(A^*) \geq 0$, the method converges if A_0 satisfies $A_0 \geq A^*$.

An illustration of the fast convergence of this method can be seen in Figure 5.8 where the image from Figure 5.3 was initialized with different numbers of emitters and the optimal constant was computed using (5.24). We can see that the optimized constant significantly decreases the initial energy, avoiding this step during the Metropolis-Hastings algorithm. In Figure 5.9 is drawn an example of the energy function in the case of Poisson model according to the constant value.

5.3.4 Metropolis-Hastings for computation of the E-LSE estimate

The principle is the same as for the LSE estimate, except that the proposal distribution q should enable an emitter to change its position; we denote $\mathcal{V}(p_e)$ the

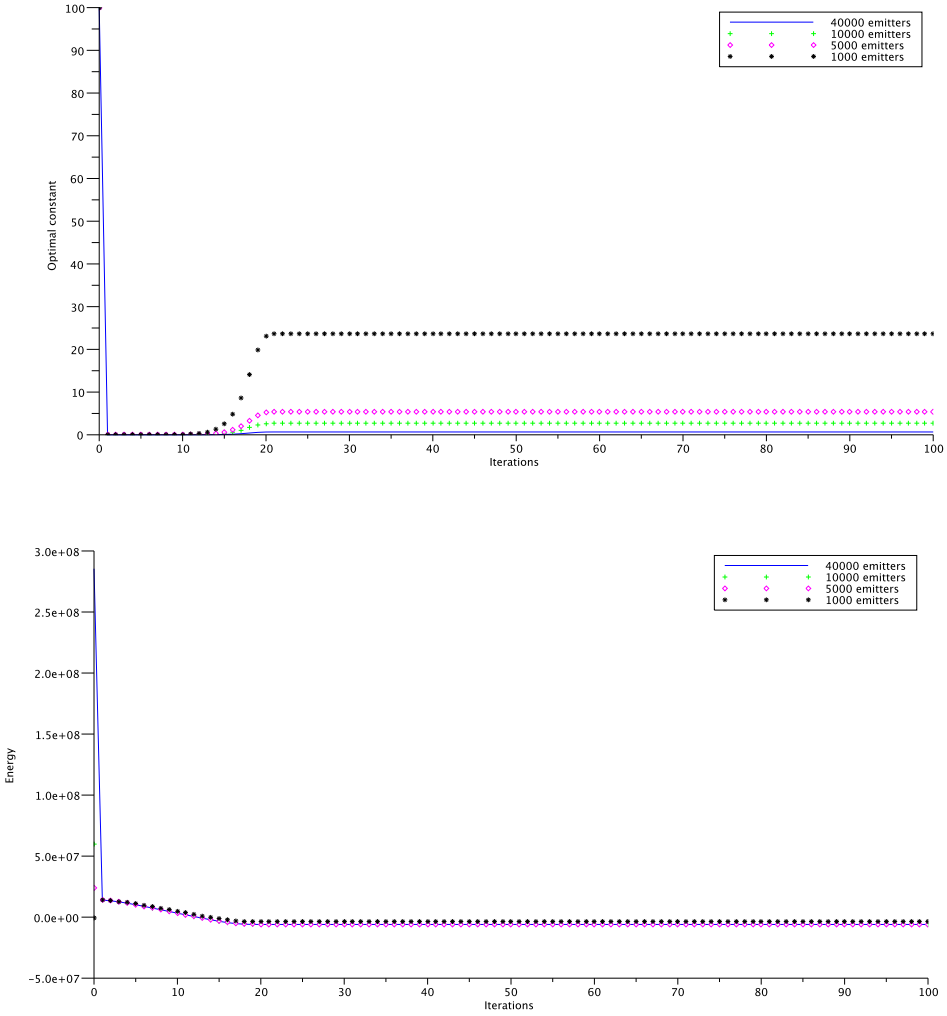

Figure 5.8: Illustration of Newton's method to find A^*: on top the evolution of the value of the constant A_k during the iterations and at the bottom the evolution of the energy $E_y(A_k x)$ during the iterations. The image of Figure 5.3 (200 pixels $\times$ 200 pixels) was initialized with $1,000$, $5,000$, $10,000$ and $40,000$ emitters and Newton's method described by formula (5.24) was used for 100 iterations, with initialization $C_0 = 100$ (100 photons for one emitter being considered as bigger than the expected value). We can see that the algorithm converges in very few iterations (the ratio $|(A_{k+1} - A_k)/A_k|$ is smaller than 10^{-10} after 20 iterations for the four initializations) and that the energy is significantly reduced by this operation, leading to a faster convergence of the algorithm.

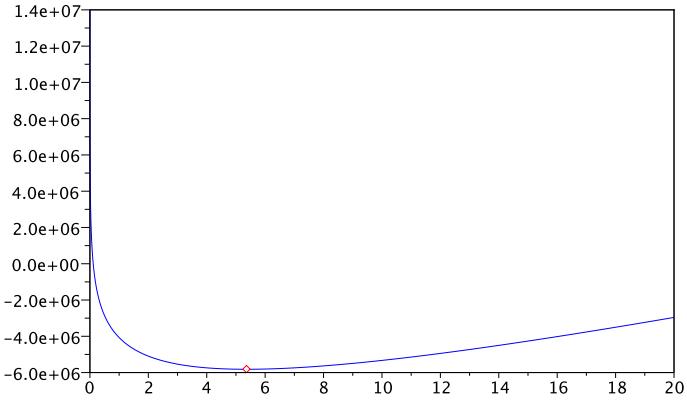

Figure 5.9: Plot of a function $F(A) = E_y(Ax)$ (the one corresponding to the Poisson case in Figure 5.8, for 10000 emitters) for $A \in [0:20]$. The function is convex, the red dot represents the minimal value and was correctly computed thanks to Newton's method in less than 20 iterations (Figure 5.8).

set of positions the emitter e can access from p_e. Given $u = \sum \lambda_e \delta_{p_e}$ and $u' = \sum \lambda'_e \delta_{p'_e}$ the proposal distribution q is chosen as

$$q(u'|u) = \frac{1}{N_e} \sum_{e=1}^{N_e} \left(\prod_{e \neq f} \delta_{\lambda_e}(\lambda'_e) \delta_{p_e}(p'_e) \right) \frac{1}{|\mathcal{V}(p_f)|} \mathbb{1}_{p'_f \in \mathcal{V}(p_f)} \frac{1}{2\alpha} \mathbb{1}_{|\log(\lambda_f) - \log(\lambda'_f)| \leq \alpha},$$

meaning that two states of the chain only differ by one emitter, whose position or intensity or both have been modified; once again the positivity is ensured, given a positive initialization, thanks to the multiplication of the intensity by an exponential value, e^β, $\beta \sim \mathcal{U}([-\alpha, \alpha])$. To respect the requirement on the proposal distribution that the jump between two states should not be too big, we chose for $\mathcal{V}$ the 8 direct neighbors as well as the current position, so that, since the positions are located on pixels of the image,

$$\mathbb{1}_{p'_f \in \mathcal{V}(p_f)} = \mathbb{1}_{|p'_f - p_f| \leq \sqrt{2}}.$$

We set δ_x and δ_y the motion in each direction ($-1 \leq \delta_x, \delta_y \leq 1$ when we take the 8 neighbors); when the new x coordinate (respectively y coordinate) is outside the support of the image, δ_x is replaced by $-\delta_x$ (respectively δ_y by $-\delta_y$).

From the definition of the proposal distribution, it comes that $\gamma_{i+1/2}$ can be

written as

$$\gamma_{i+1/2} = \gamma_i - \lambda_e \delta_{p_e} + e^{\beta} \lambda_e \delta_{p_f},\ \beta \sim \mathcal{U}([-\alpha, \alpha]),$$

where emitter e was moved from p_e to p_f and whose intensity went from λ_e to $e^{\beta}\lambda_e$.

Using (5.22), we have that

$$H\gamma_{i+1/2} = H\gamma_i - \lambda_e \varphi(\cdot - p_e) + e^{\beta} \lambda_e \varphi(\cdot - p_f),\ \beta \sim \mathcal{U}([-\alpha, \alpha]),$$

meaning that the computation of the convolved proposal, $H\gamma_{i+1/2}$, can be obtained by removing from the current convolved chain, $H\gamma_i$, the kernel centered in p_e and weighted by λ_e and adding the kernel centered in p_f and weighted by $e^{\beta}\lambda_e$. Between $H\gamma_{i+1/2}$ and $H\gamma_i$, only the pixels belonging to the union of two domains, each one of the size of the PSF support, S_φ, are modified: the first one centered on p_e, the second one on p_f. We denote S the union of these two domains.

The Poisson energy in the case of emitters is written as

$$E_y(\gamma_k) = \sum_{i=1}^{n} \sum_{e=1}^{N_e} \lambda_e \varphi(i - p_e) - y_i \log \left(\sum_{e=1}^{N_e} \lambda_e \varphi(i - p_e) + B \right),$$

giving a difference of energy of

$$\begin{aligned} E_y(\gamma_{k+1/2}) - E_y(\gamma_k) = \lambda_e & \left(e^{\beta} \sum_{i \in S} \varphi(i - p_f) - \sum_{i \in S} \varphi(i - p_e) \right) \\ & - \sum_{i \in S} y_i \left(\log \left(\frac{\sum\limits_{e' \neq e} \lambda_{e'} \varphi(i - p_{e'}) + e^{\beta} \lambda_e \varphi(i - p_f) + B}{\sum\limits_{e'=1}^{N_e} \lambda_{e'} \varphi(i - p_{e'}) + B} \right) \right). \end{aligned} \tag{5.25}$$

For a Gaussian noise distribution, we have

$$\begin{aligned} E_y(\gamma_{k+1/2}) - E_y(\gamma_k) = \sum_{i \in S} & \left(\left(\sum_{e' \neq e} \lambda_{e'} \varphi(i - p_{e'}) + e^{\beta} \lambda_e \varphi(i - p_f) - y_i \right)^2 \right. \\ & \left. - \left(\sum_{e'=1}^{N_e} \lambda_{e'} \varphi(i - p_{e'}) - y_i \right)^2 \right). \end{aligned} \tag{5.26}$$

In the case of E-LSE, we define an iteration N_i as a set of N_e sub-iterations (instead of $n = |\Omega|$ for the LSE), so that, in average, each emitter changes value and/or position once. The algorithm for N_e sub-iterations is given by Algorithm 6; the acceptance probability is the same as for the LSE.

Algorithm 6: Computation of one chain (N_i iterations of N_e sub-iterations) in the case of deblurring $y \in \mathbb{R}^n$; the energy term, E_y, should be computed using Formula (5.25) or (5.26), depending on the nature of the noise model (Gaussian or Poisson)

Inputs $\tilde{y} \in \mathbb{R}^p$, input data, $\tilde{y} \in \mathbb{R}^p$, normalized input data, N_e, number of emitters, α, scaling parameter
Output Γ one chain used to approximate the E-LSE estimate

$k \leftarrow 0$
initialize γ_0: draw $(p_e)_{e=1,\cdots,N_e}$ positions using $\tilde{y}$ as density probability
find the optimal constant A^* and initialize each $(\lambda_e)_{e=1,\cdots,N_e}$ with A^*
repeat
  draw $e \sim \mathcal{U}_{[\![1,N_e]\!]}$
  draw $\beta \sim \mathcal{U}_{[} -\alpha; +\alpha]$
  draw $p_f \sim \mathcal{U}_{\mathcal{V}(p_e)}$, with $\mathcal{V}(p_e) = \left\{p_f \in \Omega, |p_e - p_f| \leq \sqrt{2}\right\}$
  $\gamma_{k+1/2} \leftarrow \gamma_k - \lambda_e \delta_{p_e} + e^{\beta} \lambda_e \delta_{p_f}$
  $p \leftarrow \min\left(\exp\left(\beta - (E_y(\gamma_{k+1/2}) - E_y(\gamma_k))\right), 1\right)$
  $\gamma_k \leftarrow \begin{cases} \gamma_{k+1/2} & \text{with probability } p \\ \gamma_k & \text{with probability } 1-p \end{cases}$
  $k \leftarrow k + 1$
until $k = N_e \times N_i$
$\Gamma = \frac{1}{N_i - b + 1} \sum_{k=b+1}^{N_i} \gamma_{k \times N_e}$
return Γ

5.3.5 Parameters and results

As in the case of classical LSE estimate, we need to choose the number of chains and iterations, as well as the burn-in parameter, so that the computation is fast and the stationary state of the chains is approximately reached when starting averaging. But we also have an additional parameter, which is the number of emitters, N_e.

The parameter N_e has to be chosen large enough so that it can represent the whole signal in each chain but not too big, since it should be smaller than the number of pixels of the image (otherwise the model of emitters is less meaningful). It is not an easy parameter to calibrate, as shown in Figure 5.10, where the original image is made of two Dirac distributions (with a constant background of 5 photons). Indeed we could have hoped that only two emitters could be able to separate the Dirac distributions (the peak intensity is 200 times bigger than the background); however, numerous chains put one of their two emitters between the two Dirac distributions, because this is where the signal is the best explained, getting intensity from both Dirac distributions, when another emitter represents the background. Ten emitters enable to describe better the signal.

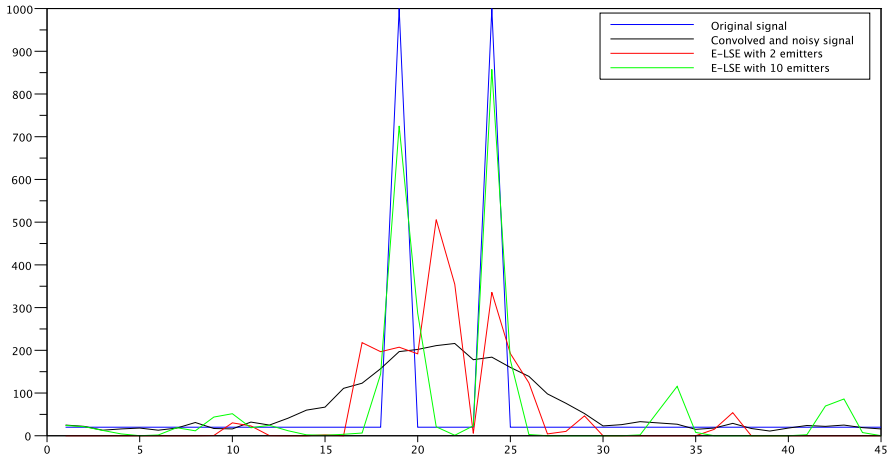

Figure 5.10: Illustration of the complexity for the choice of the number of emitters on a one-dimensional example. In blue the original signal is made of two Dirac distributions with very high intensities compared to the rest of the signal; the separation between these distributions are not visible anymore after convolution. With two emitters, we expect the emitters to choose the peaks as positions; however a lot of chains stabilize in a state where one of the emitters is between the two peaks, getting energy from both of them. With 10 emitters, the Dirac distributions are correctly recovered but we also see small peaks in the constant background.

We have to keep in mind that in the case of the E-LSE estimate, each chain is not made of the pixels of the image but of a set of positions and intensities. To create the final image, we decide to apply a PSF, φ^r at each position returned by the chain, that is $\hat{x}_{E-LSE}$ is approximated using N_c chains, $\Gamma_k^l = ((p_e^l)_k, (\lambda_e^l)_k)$ (such

that $\Gamma_k^l = \gamma_{kN_e}^l$), by

$$\frac{1}{N_c}\sum_{l=1}^{N_c}\frac{1}{N_i - b}\sum_{k=b+1}^{N_i}\sum_{e=1}^{N_e}(\lambda_e^l)_k\varphi^r(\cdot - (p_e^l)_k). \tag{5.27}$$

Of course, φ^r has to be chosen so that the blur it introduces is smaller than the initial blur; in the case where φ, the convolution kernel, is a Gaussian kernel of standard deviation σ, φ^r can be chosen as a Gaussian kernel too with standard deviation σ' such that $\sigma' < \sigma$. In Figure 5.11, we present the E-LSE estimate on simulated curves, with a number of emitters higher than the number of non-zero coefficients in the original image, using several σ' as standard deviation of the PSF φ^r. We can see that for any σ' smaller than σ, the same artifact of non uniformity as in the LSE can be seen; because of the convolution, it does not look like the night sky of the MAP or LSE but this is the same phenomenon, the filaments are not continuous, as the original ones, but they seem to be made of beads. We could think first that this is due to a too low number of emitters, however as shown in Figure 5.12, increasing this parameter does not impact that much the result (except when it is really too small, 2000 emitters in the example).

The artifact can be explained by the fact that the positions of the emitters tend to be the same on all the chains, as we can see on Figure 5.13 where the normalized impact cards are drawn. They were obtained by incrementing the value of one pixel by 1 each time the position of an emitter used to compute the estimate is on this pixel. Clearly, two positions, next to each other on the filaments, are not equally chosen by the algorithm, creating the night sky effect. On this figure, we can also notice that the final chains are quite different, at least by their energies, as proven by the histogram.

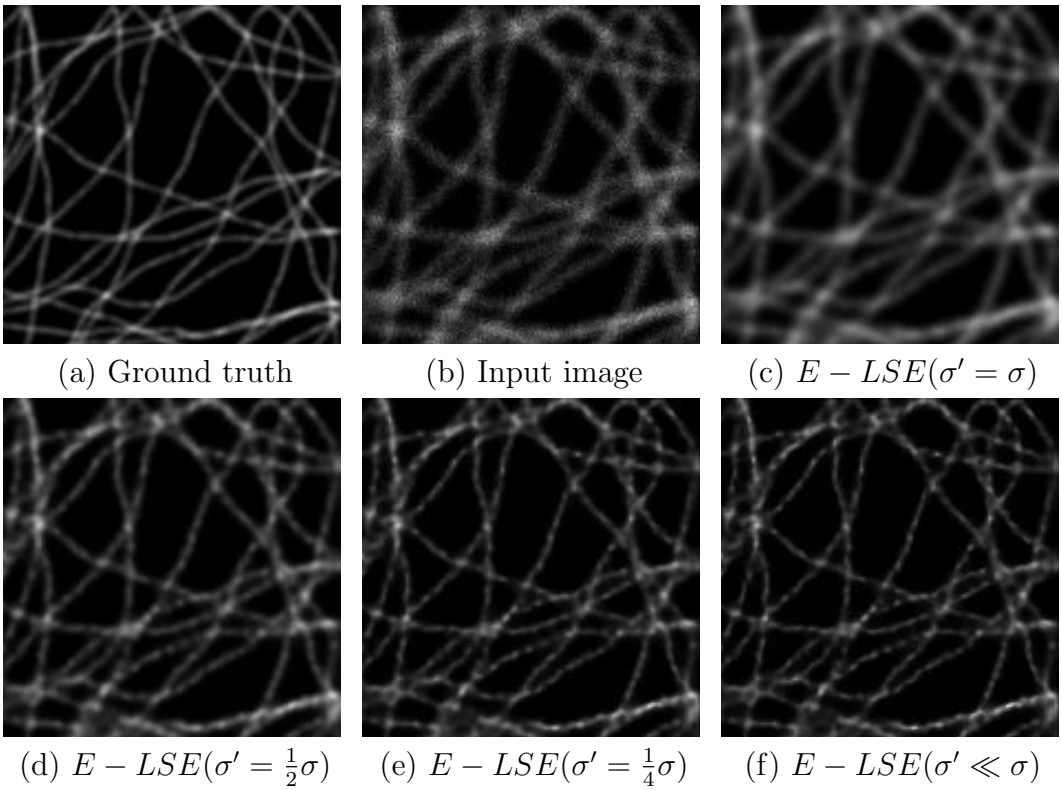

(a) Ground truth (b) Input image (c) $E - LSE(\sigma' = \sigma)$

(d) $E - LSE(\sigma' = \frac{1}{2}\sigma)$ (e) $E - LSE(\sigma' = \frac{1}{4}\sigma)$ (f) $E - LSE(\sigma' \ll \sigma)$

Figure 5.11: Representation of $\hat{x}_{E-LSE}$ according to the standard deviation of the PSF, φ_r, applied on the set of positions, obtained by MCMC algorithm. In (a), we see the ground truth data and in (b) this image convolved and corrupted with Poisson noise. Algorithm 6 was used to approximate $\hat{x}_{E-LSE}$, with a number of emitters greater than the real number of non null pixels in the ground truth image (with Poisson noise, so that the black background remains black). We show the convolution afterwards, using Formula (5.27), using 4 values of standard deviation; the first in (b) equals the one of the convolution performed on the ground truth, the image is then a less noisy version of the input data. Decreasing this standard deviation, we see the night sky artifact appearing (d)-(e)-(f), creating filaments with non constant values. The night sky is less visible than in the case of the MAP or the LSE due to the convolution, however the result is not satisfactory either (crops are presented in Figure 5.12).

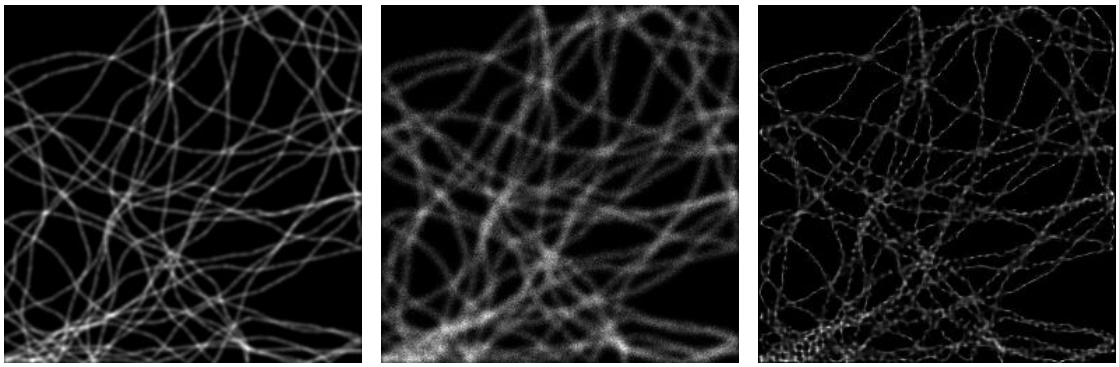

Ground truth Input image 2000 emitters

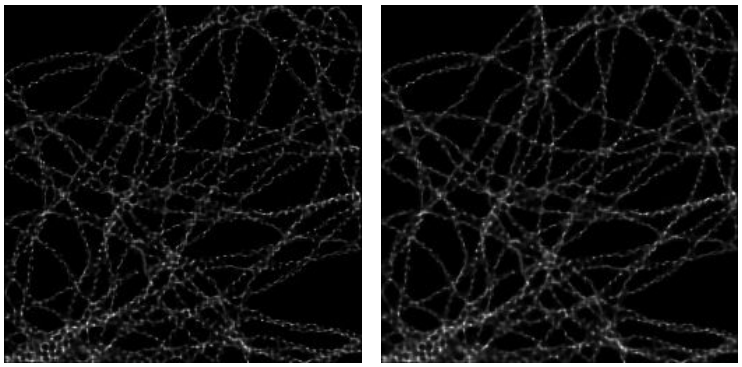

5000 emitters 10000 emitters

Figure 5.12: Illustration of the E-LSE estimate according to the number of emitters. Results are presented in the case of the Poisson noise model, but are equivalent for Gaussian noise. The image contains around 10000 pixels, but only half of them has a really significant value. We can see that whatever the number of emitters, the night sky is present. In the case of 2000 emitters there is clearly a lack of emitters: filaments are very thin. In the other cases, results are quite equivalent.

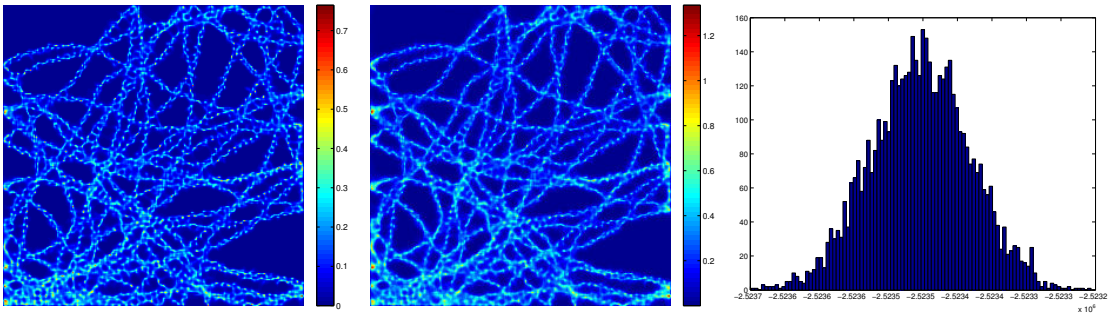

Impact map for 5000 emitters | Impact map for 10000 emitters | Histogram of energies for 10000 emitters

Figure 5.13: Averaged impacts maps for 5000 and 10000 emitters (left) and histogram of the energy distribution for 10000 emitters (right). The impact cards were obtained by computing for each pixel the average number of emitter at this position in the final chains. Comparing those two for 5000 and 10000 emitters, we see that exactly the same areas are covered by the emitters; this means that adding emitters did not help to model additional structures, emitters simply aggregate on the filaments. The histogram shows the repartition of the energies at the end of the chains; even if the range is quite tight, it may be noted that the night sky artifact is not specific to the minimum of the energy only (that is the MAP estimate).

Like for the LSE estimate, we computed the weighted E-LSE, defined by the same Formula as (5.20), except that the integration is computed on the set C defined by (5.21). Results are presented in Figure 5.14, where we can see that $\lambda = 0.01$ totally removes the artifact but the image still seems very blurry; the filaments are however thiner than the original ones and the noise is less visible. For $\lambda = 0.1$, the result is visually better than the E-LSE estimate, but some parts of the filaments still present the artifact. It is very difficult to choose λ when the image is made of heterogeneous structures, as shown on Figure 5.15, where some thin filaments surround a more dense tissue: when the filaments have a better aspect ($\lambda = 0.01$, with 5000 emitters), the tissue is still reconstructed as if it was non-continuous. Using 20000 emitters, we loose the notion of sparsity induced by the use of C (N_e should be smaller than $|\Omega|$) but we see anyway that the results are not really better.

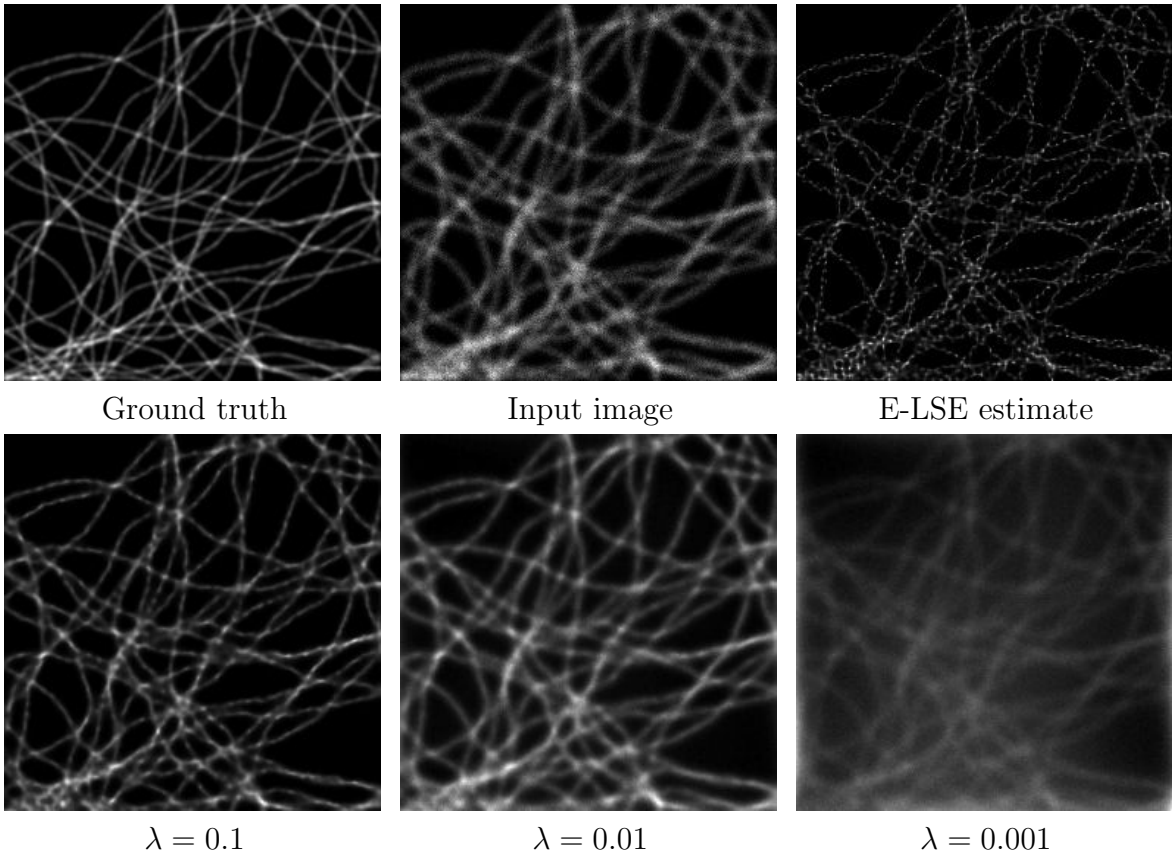

Figure 5.14: Results with the weighted energy in (5.20), integrating on the set C, with $|C| = 5000$. It can be seen that the night sky artifact disappears when minimizing a weighted energy and this method gives a very reasonable result on this example for $\lambda = 0.1$, with $\lambda = 0.01$, a full disappearance of the artifact can be noticed, but the image still appears to be blurry (even if the comparison with the input image shows some deconvolution on the filaments). This is getting worse with the diminution of λ.

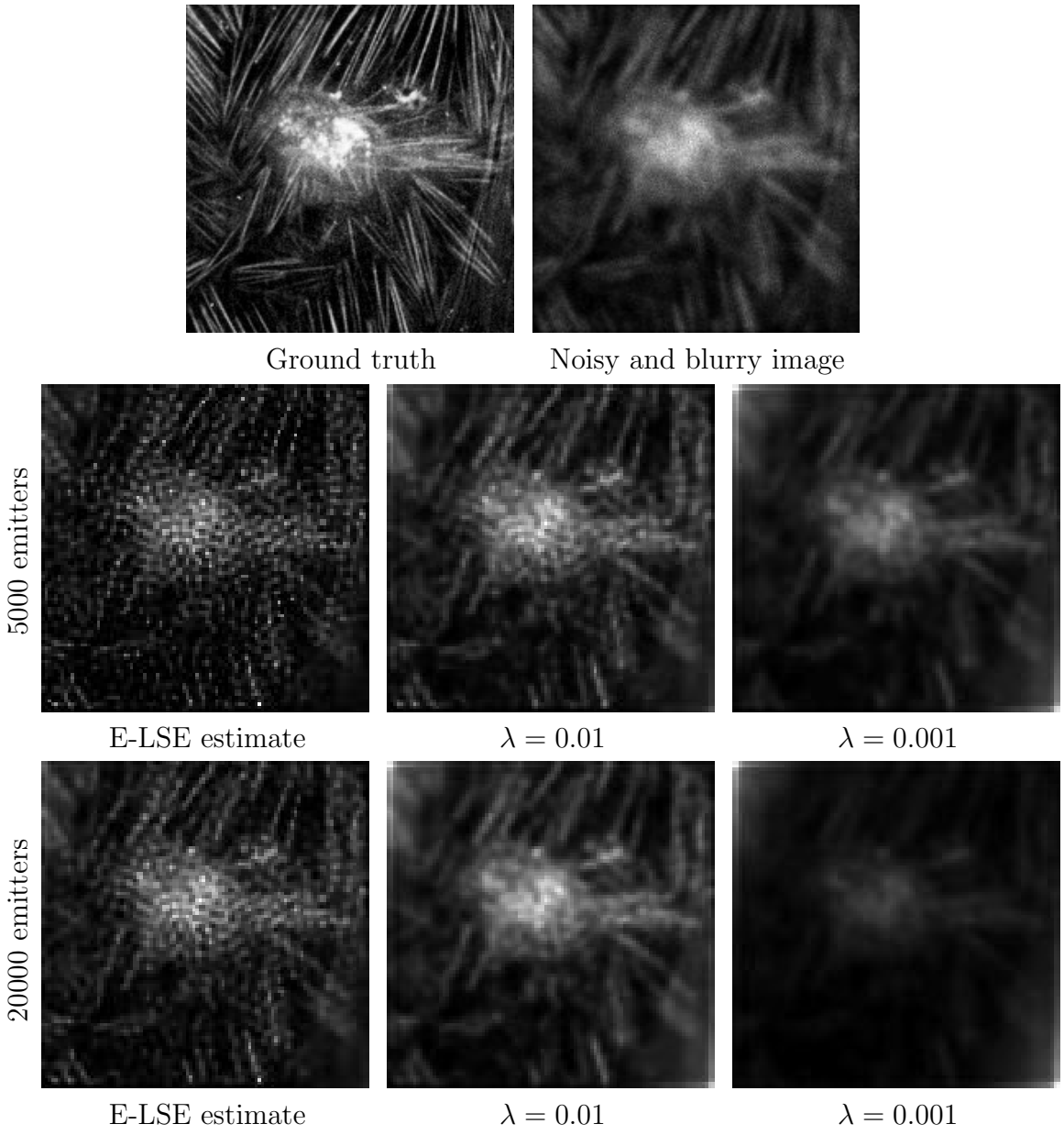

Figure 5.15: E-LSE with weighted energy on a more complex image; the original image is an image 100×100 pixels. We present the results with the original E-LSE estimate and with a weighting of the energy. A real compromise between the correct reconstruction of the filaments, with deconvolution compared to the original image, and the central tissue cannot really be found. Using 20000 emitters, we cannot see really better result, and using twice more emitters than the number of pixels, on an image with real black background (a threshold was performed and with Poisson noise, the background remains black), is not really consistent with the definition of the E-LSE, where the number of emitters is supposed to be smaller than the number of pixels.

Chapter 6

Maximum A Posteriori and Emitters-Least-Square Error estimates for Image Scanning Microscopy

Contents

Since the 1980's, super-resolution algorithms exist, inspired by deconvolution methods. As mentioned, for the SIM Method, a simple Wiener filter is used, but the problem could also be resolved using a Bayesian framework. This chapter begins with a state of art concerning methods currently used in super-resolution. Even if, as mentioned in Chapter 4, Richardson-Lucy algorithm is quite old (1972) and known for its artifacts when pushing iterations, it has been used widely used in microscopy with and without regularization; concerning these regularizations, they are also very classical ones, Total Variation or Tikhonov. Most of the presented methods works on the widefield or confocal images, that is a representation of the whole sample. Our approach is slightly different because it models the scanning of the sample and works with all the image created as described in Chapter 3, called as before the micro-images.

Then, we present the Maximum A Posteriori implementation for the operator H described in Chapter 3 composed of multiplication, sub-sampling and deconvolution. As in the case of deconvolution only, in Chapter 4, a gradient descent method can be used to approximate this estimate, using the adjoint of H. Two assumptions on the super-resolved image are made: its positivity and its bandlimitedness. This second condition ensures that not only the computed solution (that is at the chosen resolution) is positive, but its Shannon interpolate also is. Both of these constraints constitute convex sets of images, and hence so does their intersection. Nesterov algorithm was implemented to compute the MAP estimate, with a dual Forward-Backward scheme for the projection on the set of constraints. Artifacts can appear on the reconstruction images, especially when iterating a lot, which can be indispensable to gain resolution.

As we mentioned several times, microscopy images can be quite sparse images, depending on the density of fluorophores (and the biological tissues they are fixed on). For this type of images, we present the adaptation of the E-LSE for the operator H. The model for the super-resolved image is slightly different from the MAP: we consider that the data to recover (the super-resolved image) can be written as a weighted sum of Dirac distributions; we present how the E-LSE estimate can be approximated via MCMC taking advantage of this modeling. We present some results where the E-LSE estimate is an artifact-free images, compared to the MAP estimate. Most of the time, we present the conventional image as a comparison, as defined in Chapter 2, by Formula (2.20); in the discrete case, it is obtained by summing all the micro-images at the positions they were acquired on the camera.

In this chapter, we consider that the PSF as well as the illumination patterns are exactly known. This is a strong hypothesis, which requires a very good calibration of the optical system beforehand. Concerning PSF estimation, the reader can refer to [117] for estimation with real data or [112] for a precise theoretical model. Some blind deconvolution methods have been developed in microscopy too, for instance [29] (where a model is chosen for the PSF with unknown parameters that are estimated at the same time as the reconstruction) or [18], adapted from [41] for microscopy, where Richardson-Lucy algorithm is used on both sample and PSF to estimate those two simultaneously.

In the following, u is the super-resolved image, and we have $u \in \mathbb{R}^{\Omega}$, where as before, $\mathbb{R}^{\Omega}$ represents the functions from Ω to $\mathbb{R}$, with $\Omega = \{0, \dots, N_x - 1\} \times \{0, \dots, N_y - 1\}$, $|\Omega| = N_x \cdot N_y = N$, so that we might also write $u \in \mathbb{R}^N$. Except in the first section or if stated otherwise, the notation (x, y) will be used for the coordinates of a pixel in u. The input data v is of size $n_x \times n_y \times S$, where S is the total number of laser positions; we denote $\Omega^c = \{0, \dots, n_x - 1\} \times \{0, \dots, n_y - 1\}$, with $|\Omega^c| = n_x \cdot n_y = n$. We may also refer to the k^{th} micro-image of the input data using the notation v^k with $v^k \in \Omega^c$. H is the operator computing from the super-resolved image u the micro-images, thus $H \in \mathcal{M}_{|\Omega^c| \times S, |\Omega|}$. When using the notation with matrix, we consider u and v as vectors, obtained concatenating their transposed rows.

6.1 Super-Resolution in microscopy

First to introduce deconvolution in microscopy, Agard [5][4] proposed optical sectioning (which consists in removing signal coming from other z-plans especially one above and one below, estimated thanks to acquisitions on those plans too), associated with an iterative method ensuring that the proposed image at each iteration convolved with the PSF of the device gets closer to the input data.

As mentioned in the introduction, the best way to describe the noise in the case of low level of photons is clearly Poisson noise [7][6]; however a large literature about deconvolution in the case of Gaussian noise existed before super-resolution. Since for a photon number, λ, higher than 15, the approximation $\mathcal{P}(\lambda) \sim \mathcal{N}(\lambda, \lambda)$ is considered satisfactory, some algorithms were developed modeling noise with Gaussian approximation, and in particular using Tikhonov regularization. We briefly present some of these algorithms and a generalized version of Richardson-Lucy algorithm, specific to Poisson noise as said in Chapter 4, that can be applied to the ISM inverse problem.

6.1.1 Gaussian approximation with Tikhonov regularization

Tikhonov regularization (seen in deconvolution in [115] and used in microscopy in [13] for instance, on confocal images) has been used in microscopy, leading to the minimization problem

$$\underset{u\in\mathbb{R}^p}{\operatorname{argmin}} \|Au - v\|^2 + \lambda\|Cu\|^2, \tag{6.1}$$

λ being the regularization parameter, C the regularization matrix and the first term corresponds, as seen in Chapter 4, to the energy associated to a Gaussian noise. The analytical solution of this problem is explicit,

$$(A^tA + \lambda C^tC)^{-1}A^tv,$$

but does not take advantage of the positivity assumption. Two well known methods have been developed minimizing (6.1) with the positivity constraint, namely the Iterative Constraint Tikhonov-Miller (ICTM) algorithm [117] and the Carrigton algorithm [23]. They differ by the way they compute the minimum: for the first one, a projection on the set of positive results is performed at each iteration, whereas for the second one, the positivity constraint is directly integrated in the function to minimize; both create super-resolved images whose frequency components have energy outside of $\mathcal{B}(0, f_{max})$.

6.1.2 Richardson-Lucy algorithm in microscopy

The idea of using Richardson-Lucy algorithm for optical imaging was first proposed by Holmes in [58]. However, as presented in Chapter 4, this algorithm is known to amplify noise when increasing the number of iterations, which is the reason why it is either stopped after very few iterations, or used with a regularization term.

In [32], the well known Total Variation, TV, is proposed as a regularization, using Richardson-Lucy too, on confocal images. Results on both simulated and real data (corrupted by Poisson noise), comparing classical Richardson-Lucy algorithm with the TV regularization, show sharper edges with the regularization and intensity less oscillating inside dense and homogeneous areas. However, as pointed in the article and as we mentioned before, one drawback of the total variation is the staircasing effect. In [65], Richardson-Lucy algorithm is generalized for any operator H, and then could be used on the ISM one, where, given an initialization for the super-resolved

image, u^0, the sequence

$$u^{k+1} = u^k \frac{H^t \frac{v}{Hu^k+B}}{H^t \mathbf{1}_{\mathbb{R}^{n\times S}}}, \tag{6.2}$$

where the divisions are element-wise, is supposed to converge towards the minimizer of argmin $E(u)$, where u is the super-resolved image, v the set of input (sub-resolved) images.

Remark 25. *We can notice that Formula (6.2) is equivalent to (4.13) in the case of deconvolution, since we defined that the kernel was normalized; in that case*

$$H^t \mathbf{1}_{\mathbb{R}^{n\times S}} = \mathbf{1}_{\mathbb{R}^{n\times S}}$$

giving the result since the division is element-wise.

This algorithm was used in microscopy in 2015 in [113], on an ISM technique. Once again, if the operator H is positive, positivity will be preserved given a positive initialization. Next section focuses on the transposition of the operator as described in Chapter 3. The sequence (6.2) can therefore be implemented and at the end of this chapter, this estimate is compared to the MAP and E-LSE ones.

6.2 Maximum A Posteriori estimate

6.2.1 Problem formulation for Image Scanning Microscopy

The energy in the case of data corrupted by Poisson noise for an ISM operator is written as

$$\underset{u\in\mathbb{R}^\Omega}{\operatorname{argmin}} \sum_{i\in(\Omega^c)^S} (Hu)_i - v_i \log((Hu)_i + B). \tag{6.3}$$

This energy is minimized with two priors on the result image u,

— u is positive, that is $u \in C_1$ with $C_1 = \left\{u \in \mathbb{R}^\Omega_+\right\}$, a convex set,

— u is band-limited, that is $u \in C_2$ with $C_2 = \left\{u \in \mathbb{R}^\Omega \,|\mathrm{supp}(\hat{u}) \subset \mathcal{B}(0,R)\right\}$, C_2, a convex set too; this condition can also be written as $\hat{u} \in C_2'$, with $C_2' = \left\{v \in R^\Omega \,|\mathrm{supp}(v) \subset \mathcal{B}(0,R)\right\}$.

We define $\mathcal{K} = C_1 \cap C_2$, convex set as well.

For any set A, its characteristic function i_A is defined as

$$i_A(x) = \begin{cases} 0 & \text{if } x \in A \\ +\infty & \text{else} \end{cases},$$

the two priors lead to the following minimization

$$\underset{u \in \mathbb{R}^\Omega}{\operatorname{argmin}} \sum_{i \in (\Omega^c)^S} (Hu)_i - v_i \log((Hu)_i + B) + i_{\mathcal{K}}(x). \tag{6.4}$$

Nesterov algorithm was used to approximate the MAP estimate as described in Algorithm 7, where $\Pi_{\mathcal{K}}$ denotes the projection on the convex set $\mathcal{K}$, ε the precision to reach and N_{iter} a maximum number of iterations. Since Nesterov algorithm performs better when the input data u_0 is close to the solution, a classical projected Gradient descent (with fixed step and check on the decreasing of the energy to validate this step) is computed beforehand for a few iterations and the result is used to initialize Nesterov algorithm.

Algorithm 7: Maximum a posteriori estimate computation for a system of Image Scanning Microscopy

Inputs $u_0 \in \mathbb{R}^\Omega$, first estimate, N_{iter}, maximum number of iterations, λ, descent step, ε, tolerance
Output u, MAP estimate

$k \leftarrow 0$
$u \leftarrow u_0$
$g_0 \leftarrow 0$
repeat
  $y \leftarrow \Pi_{\mathcal{K}}\left(u - \lambda \nabla E(u)\right)$
  $g \leftarrow g + \frac{k+1}{2} \nabla E(u)$
  $z \leftarrow \Pi_{\mathcal{K}}\left(u_0 - \lambda g\right)$
  $u_{\text{old}} \leftarrow u$
  $u \leftarrow \frac{k+1}{k+3} y + \frac{2}{k+3} z$
  $k \leftarrow k + 1$
until $k < N_{iter}$ and $\|u - u_{\text{old}}\| / \|u_{\text{old}}\| > \varepsilon$
return u

Remark 26. *The initialization for the gradient descent is most of the time taken as the null image, so that during the first step of the gradient descent, a scaling step is performed, where the data and the reconstruction are multiplied by a constant λ which*

equals the ratio between the sum of all the input images ($\sum_{i,s} v_i^s$) and the sum of all the simulated micro-images, created from the first iteration of the gradient descent. This λ is also used in the following of the algorithm as the descent step.

Remark 27. *Most of the time, the value of R (in C_2) is chosen as a multiple of Abbe's limit, that is*

$$R = n \times \frac{4\pi NA}{\lambda}, n \in \mathbb{N}^*. \tag{6.5}$$

According to Formula (2.19), proving that a factor of resolution 2 can be reached for an ISM method, we can take $n = 2$. In case of sparsity of the solution, n can be greater than 2.

To be able to implement Algorithm 7, one should be able to implement the computation of both the projection on $\mathcal{K}$ and the gradient of the energy, $\nabla E(u_k)$, at each iteration.

The projection on $\mathcal{K}$ is performed using a Dual Backward scheme, as explained in [28]; several other methods presented in this article were implemented, including the "natural" iterated alternate projection algorithm. This method also called POCS (Projections Onto Convex Sets, see [38] for instance) is easy to implement, with the following scheme,

$$\forall k \in \mathbb{N},\ u_{k+1} = \Pi_{C_1}(\Pi_{C_2}(u_k)),\ u_0 \in \mathbb{R}^\Omega,$$

and quite fast. However as explained in [9], this algorithm converges to an element of $\mathcal{K}$ but does not guarantee that this element is the orthogonal projection of u_k on $\mathcal{K}$. The Dual Backward scheme seems to be a good compromise between time consumption and precision of the result (the sequence converges faster on our problem than other methods presented in [28] and requires less parameters).

To compute the gradient ∇E, which is defined by (4.11), we explicit the computation of the adjoint of H. Of course, the image $H^t \mathbf{1}_{\mathbb{R}^{n\times s}}$ is computed only once, at the beginning of the algorithm. As described in Chapter 3, H can be decomposed in very simple operations, each one can be transposed, creating at the end the adjoint operator.

6.2.2 Practical computation of the estimator

Transposition of the operator H in the ISM model

We recall (Chapter 3) that the operator of the ISM model can be written as

$$\forall z \in \mathbb{R}^2,\ I_u(z, X_s) = \left((u(\cdot) \times D^s(\cdot - X_s)) * \varphi(\cdot)\right)(z),$$

where u is the super-resolved image we want to recover, D^s the illumination pattern, projected at laser impact X_s, for the s^{th} image and φ the PSF of the system. This operation can be written under matrix form as seen in Chapter 3. One micro-image, corresponding to illumination index s, noted I_u^s, can be obtained from the sampled image $u \in \mathbb{R}^\Omega$, decomposing each step, as

$$I_u^s = LM^sCu, \tag{6.6}$$

where (unless stated otherwise, the notations for sizes are the ones that were used in Chapter 3 for the precise description of the simulation of H):

— $C \in \mathcal{M}_{N_x \times N_y, N_p \times N_p}$ is the crop operator,
— $M^s \in \mathcal{M}_{N_p \times N_p, N_p \times N_p}$ is the diagonal operator computing the multiplication with the (translated/zoomed) illumination pattern,
— $L \in \mathcal{M}_{N_p \times N_p, n_x \times n_y}$ is the down-sampling and convolution operator, which are performed in the Fourier domain.

We note $m = (I_u^s)_{s \in \{1,\dots,S\}}$, $m \in \mathbb{R}^{n_x \times n_y \times S}$ the vector concatenating all the micro-images.

The energy using the notation (6.6) is given by

$$E(u) = \sum_{i=1}^{n_x \times n_y \times S} m_i - v_i \log(m_i + B).$$

To explicit H^*, $H^* : R^{\Omega^c \times S} \longrightarrow \mathbb{R}^\Omega$, we can first compute the adjoint of the operator that enables to create I_u^s. By using property of the adjoint operator, it is given by $C^*M^{s*}L^*$; we note m_s^u the image in Ω created by $m_s^u = C^*M^{s*}L^*I_u^s$. Then, according to the structure of the matrix H^*,

$$H^*m = \sum_{s=1}^{S} m_s^u.$$

Crop We recall that the top left corner for the crop of u for the micro-image of index s is noted (c_x^s, c_y^s). The matrix C extracts the values of u in the rectangle of top-left corner (c_x^s, c_y^s) and bottom-right corner $(c_x^s + N_p, c_y^s + N_p)$.

Supposing that we create a one-dimensional vector u by concatenating its transposed rows, we can explicit C. Defining (i_c, j_c) the indexes of the crop image ($i_c \in \{0, \dots, N_p - 1\}$, $j_c \in \{0, \dots, N_p - 1\}$) (so that any column index of C, between 1 and $N_p \cdot N_p$, can be written as $1 + i_c + N_p \times j_c$), the matrix $C = (C_{IJ})$ with $I \in [\![1, N_x \cdot N_y]\!]$, $J \in [\![1, N_p \cdot N_p]\!]$, is defined by

$$C_{IJ} = \begin{cases} 1 & \text{if } J = 1 + i_c + N_p \times j_c \text{ and } I = 1 + (c_x^s + i_c) + (c_y^s + j_c)N_x \\ 0 & \text{else} \end{cases},$$

so that each row of C contains only one non-null value, 1, at the position of the pixel to keep.

The transpose of this matrix $C^t (= C^*)$, defined by inversing the roles of columns and rows, replaces a matrix of size $N_p \times N_p$ at the position of the initial crop, that is from (c_x^s, c_y^s) to $(c_x^s + N_p, c_y^s + N_p)$.

Multiplication Since M^s is a diagonal matrix, composed of real values, the operator and its transpose are identical; we have, $\forall s \in \{1, \dots, S\}$, $M^{s*} = M^s$.

Convolution and sub-sampling As mentioned in Chapter 3, the computation of $\hat{u}$, the DFT of $u \in \mathbb{R}^\Omega$, can be written in matrix form (see (3.5)). Since we are dealing with two-dimensional signals, the matrix is not as simple as the one in (3.5), but we can still write $\hat{u} = Fu$, where F has to take into account the two dimensions. We note F^{-1} the matrix representing the inverse transform, and we recall that $F^{-1} = 1/|\Omega| F^*$. In the following, we will use the notation $F_{N_p \times N_p}$ to describe the DFT operator on the set of images of size $N_p \times N_p$ and $F_{n_x \times n_y}$ on the set Ω^c.

The operator L describes the convolution as well as the down-sampling, performed by frequency cut; we can write

$$L = F_{\Omega^c}^{-1} C' P F_{N_p \times N_p},$$

$P \in \mathcal{M}_{N_p \times N_p, N_p \times N_p}$ is the multiplication with the DFT of the PSF (whose spectrum has been extended by 0 to reach size $N_p \times N_p$) and $C' \in \mathcal{M}_{N_p \times N_p, n_x \times n_y}$ is the frequency cut at the resolution (and size) of Ω^c. C' is similar to the crop matrix C

presented before; we can conclude that the transposition of C', $C'^* \in \mathcal{M}_{n_x \times n_y, N_p \times N_p}$, is simply the extension of the discrete Fourier spectrum by zeros.

The matrix P is diagonal since it represents the multiplication; it contains the coefficients of the discrete Fourier transform (that is potentially complex numbers), so that $P^* = P^{\mathrm{H}}$.

We finally have $L^{\mathrm{T}} \in \mathcal{M}_{n_x \times n_y, N_p \times N_p}$ defined by

$$L^{\mathrm{T}} = F^*_{N_p \times N_p} P^{\mathrm{H}} C'^* (F^{-1}_{\Omega^c})^* = \frac{N_p \cdot N_p}{|\Omega_c|} F^{-1}_{N_p \times N_p} P^{\mathrm{H}} C'^* F_{\Omega^c},$$

meaning that the operator L^{T}, applied to an image of size $n_x \times n_y$ computes its DFT, extends its spectrum with zeros to reach size $N_p \times N_p$, multiply by the conjugate of the DFT of the PSF and apply the inverse DFT.

Computation of the gradient thanks to H^*

An adaptation of the formula of Chapter 4 in the case of Poisson Noise gives that the gradient of the energy equals, using element-wise division,

$$\nabla E(u) = H^t \mathbf{1}_{\mathbb{R}^{n \times S}} - \frac{H^t v}{Hu + B}, \tag{6.7}$$

Algorithm 8 summaries every step of the computation of the transposed operator. At each iteration, supposing that the transposed operator applied to the micro-images made of ones (first term of (6.7)) is precomputed in the memory, the computation of the negative gradient (6.7) is performed subtracting this result to the result of the function of Algorithm 8 whose input is the quotient (element-wise division) of the input data and the micro-images generated during the current iteration of the algorithm.

Algorithm 8: Function computing the transposed operator, H^*

Inputs $\tilde{w} \in \mathbb{R}^{\Omega^c \times S}$

Output tr_im $\in \mathbb{R}^{\Omega}$ equals to $H^* \tilde{v}$

for $s \in \{1, ..., S\}$ **do**

fft_im $\leftarrow C'^* F_{\Omega^c} \tilde{w}$ ▶ Zero-padding to reach size N_p

fft_im $\leftarrow P^{\mathrm{H}}$fft_im ▶ Element-wise multiplication

im $\leftarrow \frac{N_p N_p}{n_x n_y} F^{-1}_{N_p \times N_p}$fft_im ▶ Image in the space domain

im $\leftarrow$ im $\times D_s$ ▶ Element-wise multiplication

tr_im$((c_x^s, c_y^s) \rightarrow (c_x^s + N_p, c_y^s + N_p)) \leftarrow$ tr_im$((c_x^s, c_y^s) \rightarrow (c_x^s + N_p, c_y^s + N_p))$ + im

▶ Add of the image at its correct location on the transpose image

end for

return tr_im

Computation of the projection

Based on [28], we chose the *Dual forward-backward splitting* method, that proposes to compute, given a proposal $r \in \mathbb{R}^{\Omega}$ and a matrix L such that $L \times L^{\mathrm{H}} = I$,

$$\underset{u \in \mathbb{R}^{\Omega}}{\operatorname{argmin}}\, h(u) + g(Lu) + \frac{1}{2}\|u - r\|^2. \tag{6.8}$$

The proposed algorithm requires a computation of the proximal operators on both h and γg. We briefly remind the definition of this operator; for a proper convex function f, $f : \mathbb{R}^{\Omega} \longmapsto \mathbb{R}$, it is defined as

$$\forall r \in \mathbb{R}^{\Omega},\ \operatorname{prox}_f(r) = \underset{u \in \mathbb{R}^{\Omega}}{\operatorname{argmin}}\, f(u) + \frac{1}{2}\|u - r\|^2,$$

but we mostly used the summary table at the end of [28] for the computation, and in particular the fact that the proximal operator of a characteristic function on a set A equals to the projection on this set A. Algorithm 9 presents the Dual forward-backward splitting for a minimization problem as in (6.8).

Algorithm 9: Resolution of the problem (6.8) using dual forward-backward splitting algorithm

Inputs $r \in \mathbb{R}^{\Omega}$, image to be projected, N_{proj}, maximum number of iterations, $\kappa \in]0, \min(1, 1/\|L\|^2)]$, ε, tolerance
Output y, estimate of the solution of (6.8)

$k \leftarrow 0$
$y \leftarrow r$
repeat
  $z \leftarrow \text{prox}_h\left(r - L^{\text{H}} y\right)$
  $\gamma \in [\kappa, 2/\|L\|^2 - \kappa]$
  $\lambda \in [\kappa, 1]$
  $y_{\text{old}} \leftarrow y$
  $y \leftarrow y + \lambda(\text{prox}_{\gamma g^*}(y + \lambda L x) - y)$
  $k \leftarrow k + 1$
until $k < N_{\text{proj}}$ and $\|y - y_{\text{old}}\|/\|y_{\text{old}}\| > \epsilon$
return y

Using this algorithm to solve (6.4), the functions and matrix in (6.8) can be chosen as follows:

— r is the proposal from Nesterov algorithm (which can be neither positive nor band-limited),
— h ensures positivity of the solution that is $h = i_{C_1}$,
— L is the discrete operator of the Fourier Transform divided by $\sqrt{|\Omega|}$, to ensure $LL^{\text{H}} = I$ (meaning that L^{H} is the discrete operator of the Inverse Fourier Transform, also divided by $\sqrt{|\Omega|}$),

$$L = \frac{1}{\sqrt{|\Omega|}} F, \; L^{\text{H}} = \frac{1}{\sqrt{|\Omega|}} F^*,$$

— g ensures that the solution is band-limited that is $g = i_{C_2'}$.

Using the DFT matrix for L really eases the choice of the constants in the Algorithm (9); indeed, the spectral norm of the DFT matrix is equal to $\sqrt{|\Omega|}$, so that $\|L\|^2 = 1$. Therefore, we choose $\lambda = \gamma = 1$ for each iteration.

For h, the proximal operator only consists on the projection on C_1 (true for any characteristic function as mentioned before). This means that, practically, prox_h

consists in keeping the positive values of u and set to zero the negative ones. Identically, the proximal operator of g consists in a projection on the set of band limited images. This is done practically by multiplying by 0 all off-band coefficients of the Discrete Fourier Transform of the image.

The Dual forward-backward splitting adapted to (6.4) is then described in Algorithm 10.

Algorithm 10: Projection onto $\mathcal{K}$

Inputs $r \in \mathbb{R}^{\Omega}$, image to be projected onto $\mathcal{K}$, N_{proj}, maximum number of iterations, ε, tolerance
Output y, projection of r onto $\mathcal{K}$

$k \leftarrow 0$
$y \leftarrow r$
repeat
  $z \leftarrow \Pi_{C_1}\left(r - L^{\mathrm{H}} y\right)$
  $y_{\text{old}} \leftarrow y$
  $y \leftarrow \Pi_{C_2'}\left(y + Lz\right)$
  $k \leftarrow k + 1$
until $k < N_{\text{proj}}$ and $\|y - y_{\text{old}}\| / \|y_{\text{old}}\| > \epsilon$
return y

It has be proven in [27] that, if the set $\mathcal{K}$ is not empty, any sequence generated by Algorithm 10 converges to the solution of (6.8).

In Figure 6.1 is shown the comparison between the spectra computed by Nesterov algorithm before and after projection. The image generated by Algorithm 10 is positive and band-limited; we can see that the Discrete Fourier coefficients are quite similar for the low frequencies before and after projection, but that the higher coefficients have been smoothed.

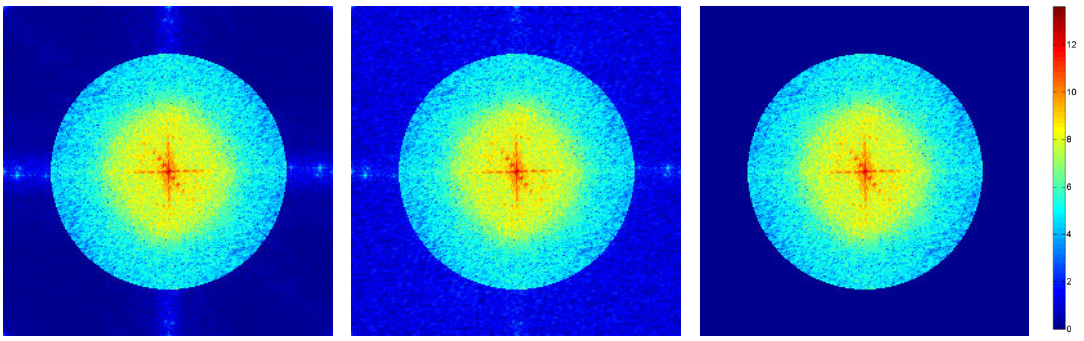

Before projection Projection on C_1 Projection on $\mathcal{K}$

Figure 6.1: Illustration of the projection on the modulus of the Fourier transforms (logarithmic scale); on the left, the image to be projected (obtained by Nesterov or Gradient descent algorithm), it is almost band-limited however its values in the space domain are in the interval $[-0.5522, 86.4379]$. A projection on the set of positive images, C_1, represented by the image in the middle, creates energy in the high frequency coefficients of the DFT (this energy is however lower than the one of the low frequencies). The application of Algorithm 10 enabled to create a positive and band-limited image, as it can be seen on the image on the right, whose values are in the interval $[0, 86.4371]$.

6.2.3 Some results

Before presenting some results, we recall that the illuminations projected on the sample in the case of simulated or real data are the half-moons presented in Chapter 3, made of two lobes and whose Fourier transform presents frequency coefficients with higher energy for the frequencies close to f_{max}.

This Algorithm was successfully used for biological purposes, we can refer to [43] (study of neurotransmitters), [93] (study of the movement of viruses within infected cells) or [91] (study of the mitochondrial fission in mammalian cells). In [22], a comparison between the SIM and BioAxial system (that is an ISM method projecting the half-moons as illumination patterns and computing the MAP estimate) clearly shows a better separation on micro-tubules using the second technique.

Here we present two examples, one on simulated data and one on real data

— in Figure 6.2, simulations were made on an image of neurons, the gain of resolution is undeniable; however, not all the separations visible on the ground truth are visible on the MAP estimate, and intensity variations are less represented (some structures are really more bright in the ground truth image and this is less visible in the MAP),

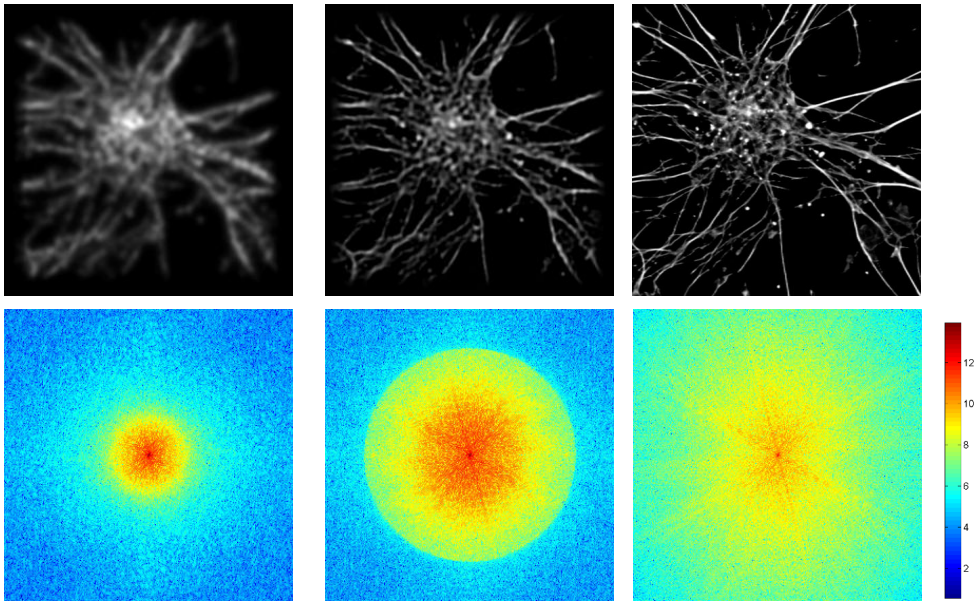

(a) Conventional image (b) MAP Estimate (c) Ground truth

Figure 6.2: Illustration of the Maximum A Posteriori reconstruction algorithm on simulated data for a super-resolution ISM system. On the first row, results in the space domain, on the second in the Fourier domain (logarithmic scale). From left to right: (a) conventional image zoomed by zero padding in Fourier domain (energy $\sim -4.2451310 \times 10^7$), (b) result of Nesterov algorithm for 200 iterations (energy $\sim -4.4015619 \times 10^7$), (c) ground truth at the resolution of the MAP. The comparison between the three results (in both spaces) clearly shows that the MAP estimate provides more information than the conventional image. We can notice that the intensity ratios are not perfectly well represented by the algorithm.
Image of motor neurons from cellimagelibrary.org by Gist Croft & Mackenzie Weygandt for 2009 Olympus BioScapes Digital Imaging Competition is licensed under CC BY-NC-ND 3.0

— in Figure 6.3 and 6.4 (real data), the MAP estimate reveals, over the iterations, the structure of a chromatid, made of wound strands of DNA. This gain of resolution is of course also visible on the Fourier Transform of the images, as shown in Figure 6.5. The cross-section really shows the evolution of the separation according to iterations.

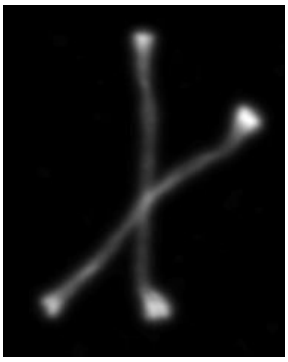

(a) Zoomed Conventional image

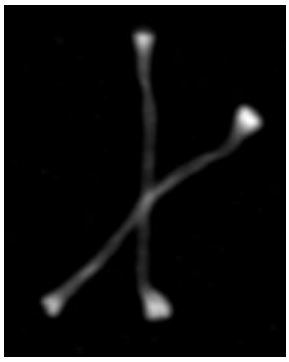

(b) Input image for Nesterov algorithm

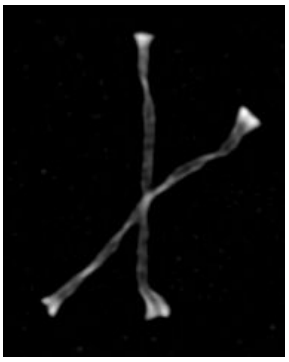

(c) Image after 100 iterations

(d) Image after 473 iterations

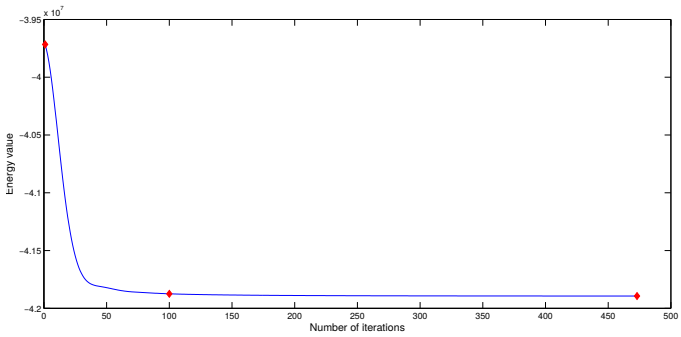

(e) Evolution of the energy with respect to the number of iterations

Figure 6.3: Illustration of the Maximum A Posteriori reconstruction algorithm on real data. From top to bottom, left to right: (a) conventional image, (b) input image for Nesterov algorithm (obtained after 27 iterations performed with a classical gradient descent), (c) result of Nesterov algorithm for 100 iterations, (d) result of Nesterov algorithm for 473 iterations, (e) evolution of the energy during the iterations (the red markers denote the iterations chosen for this figure). With no doubt, the separation between the stands of DNA composing the chromatid becomes more and more visible when increasing the number of iterations. A cross-section line confirming this can be seen in Figure 6.4.
Courtesy of J. Matthew Kofron, Cincinati Children's, USA

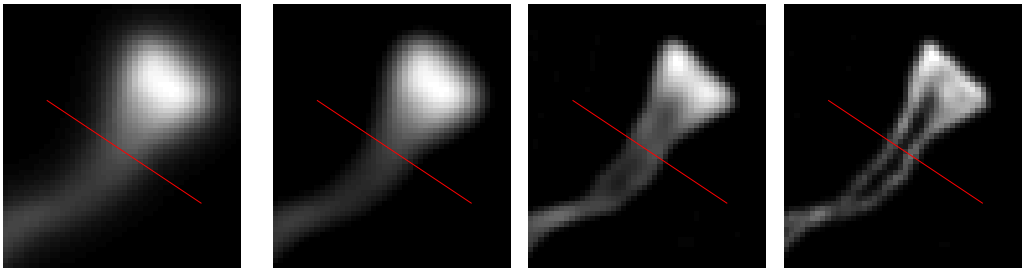

Conventional image 1^{st} iteration 100^{th} iteration 473^{th} iteration

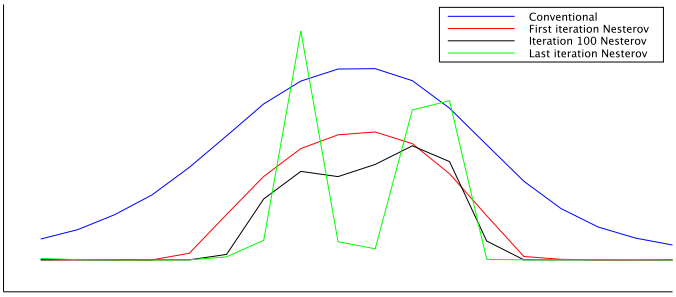

Figure 6.4: Zoom on the images of Figure 6.3 with the red cross section plotted below. With no doubt, the iterations of the algorithm improve the separation between the two strands; it starts being visible when the number of iterations reaches 100 but more iterations are required to really obtain a clear separation.

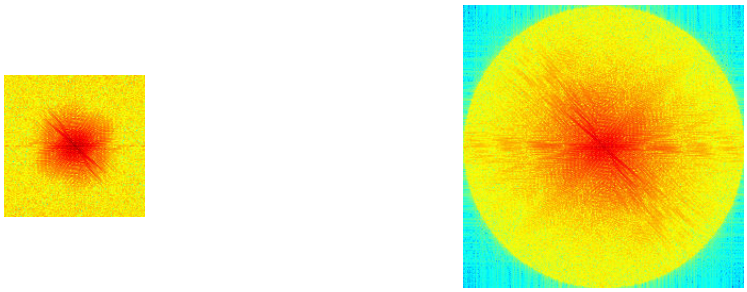

Spectrum conventional image Spectrum MAP estimate

Figure 6.5: Representation in logarithmic scale of the module of the Discrete Fourier Transforms of the conventional image (whose resolution is twice the one of the MAP reconstruction) and the MAP estimate at 473 iterations. We notice that the low frequency coefficients are quite similar between the two images; the final image has non-zero coefficients beyond the disk whose radius is the cut-off frequency, which explains the better resolution.

6.3 E-LSE Estimate

6.3.1 Application to Image Scanning Microscopy model

The idea of modeling the image as a set of emitters has been proposed in [63] (for single-molecule microscopy) or [31] (for widefield imaging) for instance, but to our knowledge not in a super resolution application for a scanning system.

Let us recall the definition of $\hat{u}_{E-LSE}$,

$$\hat{u}_{E-LSE} = \frac{\int_C e^{-E_v(u)} u du}{\int_C e^{-E_v(u)} du}, \text{ with } C = \left\{ u \in \mathbb{R}^{\Omega} \middle| u = \sum_{e=1}^{N_e} \lambda_e \delta_{p_e} \, , \lambda_e \in \mathbb{R}^+, p_e \in \Omega \right\}.$$

In the case of super-resolution reconstruction, we consider that the super-resolved image u is a sum of weighted Dirac functions. Concerning the intensities of the emitters, as before, they are supposed to be positive and the positions are supposed to belong to the set of pixels of the reconstruction, Ω (also called the grid of reconstruction). This grid is supposed to be f times thiner than the camera grid, on which the input data v were acquired.

The definition of the ISM model (3.17), $\forall z \in \mathbb{R}^2, \ \forall s \in \{1, ..., S\}$,

$$\tilde{I}_u(z, X_s) = \left((u(\cdot) \times D^s(\cdot - X_s)) * \tilde{\varphi}(\cdot) \right)(z),$$

where S is the number of laser positions and $(X_s)_{s=1,...,S}$ the positions of the laser impacts can be computed in the case $u \in C$. We denote $\tilde{I}^s_u(z) = \tilde{I}_u(z, X_s)$ that corresponds to the micro-images predicted, also called the model in the following. We have with $u = \sum_e \lambda_e \delta_{p_e}$,

$$\tilde{I}^s_u(z) = \int_{\mathbb{R}^2} \sum_{e=1}^{N_e} \lambda_e \delta_{p_e}(Z) D^s(Z - X_s) \tilde{\varphi}(z - Z) dZ$$

$$\tilde{I}^s_u(z) = \sum_{e=1}^{N_e} \lambda_e D^s(p_e - X_s) \tilde{\varphi}(z - p_e),$$

whose exact discretization for a factor of resolution f, using the PSF φ discretized at the resolution of the camera, by

$$\forall p \in \mathbb{Z}^2, \ I^s_u(p) = \tilde{I}^s_u(pf) = \sum_{e=1}^{N_e} \lambda_e D^s(p_e - X_s) \varphi\left(p - \frac{p_e}{f}\right). \tag{6.9}$$

In the case of the E-LSE, the computation of the micro-images is not performed as presented in Chapter 3, but using Formula (6.9); this means that for each emitter composing u, its influence is added to the pixels of the micro-images, multiplying the intensity of this emitter with the distribution value at the position of the emitter and convolving with the PSF centered on the emitter position.

We remind that we denote $\Omega^c = \{0, \dots, n_x - 1\} \times \{0, \dots, n_y - 1\}$. The energy associated to the problem can then be written as

$$\begin{aligned} E_v(u) = & \sum_{s=1}^{S} \sum_{i \in \Omega^c} \left(\sum_{e=1}^{N_e} \lambda_e D^s \left(p_e - X_s\right) \varphi \left(i - \frac{p_e}{f} \right) \right. \\ & \left. - v_i^s \log \left(\sum_{e=1}^{N_e} \lambda_e D^s \left(p_e - X_s\right) \varphi \left(i - \frac{p_e}{f} \right) + B \right) \right), \end{aligned} \tag{6.10}$$

with B the constant background value, as defined for the E-LSE in deconvolution.

6.3.2 Metropolis Hastings adaptation

As described in Chapter 5, the incremental function is

$$q(u'|u) = \frac{1}{N_e} \sum_{e=1}^{N_e} \left(\prod_{e \neq f} \delta_{\lambda_e}(\lambda'_e) \delta_{p_e}(p'_e) \right) \frac{1}{|\mathcal{V}(p_f)|} \mathbb{1}_{p'_f \in \mathcal{V}(p_f)} \frac{1}{2\alpha} \mathbb{1}_{|\log(\lambda_f) - \log(\lambda'_f)| \leq \alpha}, \tag{6.11}$$

that is, as before, at each iteration, only one emitter, f, is changed: its intensity, its position or both. The proposed position is chosen in the neighborhood of the current emitter, noted $\mathcal{V}(p_f)$. The proposed intensity, as before, obtained by the multiplication with a positive value (using the exponential to provide at each step a positive value, given a positive initialization). In the following, and as in Chapter 5, the chosen neighborhood consists in the 8 direct neighbors (in the super-resolved image) and the current position.

We recall that the state $i + 1/2$ of the chain can then be written as

$$\gamma_{i+1/2} = \gamma_i - \lambda_e \delta_{p_e} + e^{\beta} \lambda_e \delta_{p_f}, \ \beta \sim \mathcal{U}([-\alpha, \alpha]), \tag{6.12}$$

and that the acceptance probability p is given by

$$p = \frac{\pi\left(\gamma_{i+1/2}\right)}{\pi\left(\gamma_i\right)} \frac{q\left(\gamma_i | \gamma_{i+1/2}\right)}{q\left(\gamma_{i+1/2} | \gamma_i\right)} = \frac{e^{-E_v\left(\gamma_{i+1/2}\right)}}{e^{-E_v(\gamma_i)}} \frac{\lambda'_e}{\lambda_e} = e^{-\left(E_v(\gamma_{i+1/2}) - E_v(\gamma_i)\right)} e^{\beta}. \tag{6.13}$$

In the case of deconvolution, the initialization of the emitter positions was done using the input data as distribution of probability; in the case of super-resolution, we have chosen to use the (normalized) conventional image as distribution of probability. This conventional image is first zoomed by zero-padding (and projected on the set of positive functions if the zero-padding creates negative values) at the final resolution chosen for the super-resolved image, so that the produced positions are directly on the correct grid, Ω.

Most of the time, in the following, we do not refer to a number of emitters for the super-resolved image, but to a density of emitters, density that is user-defined, and can be estimated by looking at the conventional image. A density of 1 means that, on the conventional image, we consider that, in average, one emitter per pixel is needed to be able to represent correctly the signal.

Concerning the sizes, the zoomed micro-images are of size $fn_x \times fn_y$ (in red in Figure 6.6). We recall that one pixel value of the predicted micro-images I_u^s is computed with all the pixel values of the super-resolved image u within a disk of radius R_φ centered on this pixel, where R_φ is the upper integer value of the radius of the zoomed PSF.

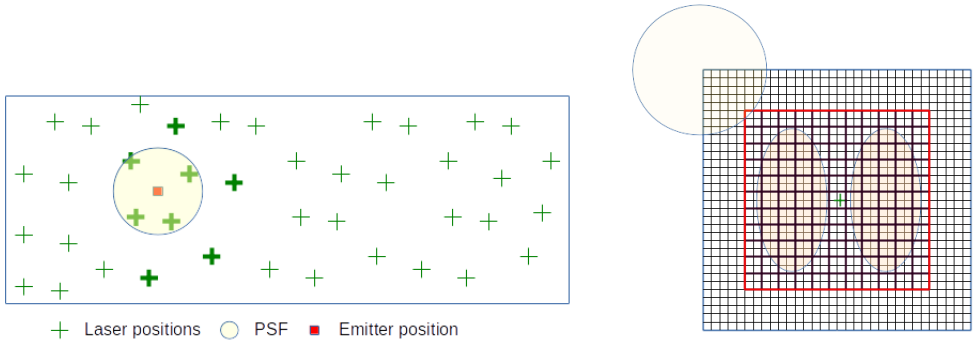

Figure 6.6: On the left, we can see a representation of the reconstruction with the laser positions represented as green crosses. Given an emitter located on a pixel (red square on the figure), the pixels influenced by a change on this emitter are located within the (zoomed) PSF, supposed to be spatially limited and represented in yellow. The micro-images to be computed again are the ones containing at least one pixel within the yellow disk. They correspond to the laser positions in bold. On the right is represented, in red, a zoomed micro-image. The illumination pattern (a half moon), in yellow, is centered on the laser position represented by a green cross. In blue is displayed the square of pixels impacting the micro-image; indeed, due to the convolution with the PSF (yellow disk on the top left corner of the blue square) any pixel located at less than one radius of the zoomed PSF will impact the pixels of the micro-image.

As shown in Figure 6.6, the pixels of the reconstruction influencing the pixels of one micro-image model are the ones located at less than R_φ, the radius of the PSF, of any pixel of this micro-image. The area of influence of the zoomed micro-image s is then delimited by the top-left corner $(c_x^s - R_\varphi, c_y^s - R_\varphi)$ and the bottom-right corner $(c_x^s + fn_x + R_\varphi, c_y^s + fn_y + R_\varphi)$. To make computations easier, the size of the zoomed illumination patterns is the size of this area of influence. The initial laser impact position X_s in the zoomed micro-image becomes $X_s + R_\varphi$ in this referential. The computation of the zoomed illumination pattern at the correct position is performed thanks to the formula from Chapter 3,

$$\forall k \in \mathbb{Z}^2,\ \mathcal{D}^s(k) = \tilde{d}^s\left(\frac{k - \tau_s}{f}\right), \tag{6.14}$$

where $\tilde{d}^s$ is the calibrated illumination pattern at resolution r_d, whose impact is located on pixel (X_d, Y_d) and $\tau_s = (X_s + R_\varphi) \times r_d/f - X_d$ is the translation (at the resolution of the calibrated illumination pattern) performed so that the zoomed illumination pattern is located at the correct laser impact position. Both zoom and translation are performed using Fourier transforms, as explained in Chapter 3.

As presented in the case of deconvolution, the change of one emitter does not require to recompute all the model (that is the predicted micro-images), but only a part of them. However this is not as simple as the deconvolution case since we treat several (micro-)images, at a resolution different from the reconstruction's one. As shown in Figure 6.6 and explained in Chapter 5, the range of action of one emitter is determined by the size of the PSF, centered on this pixel. Using, as before, the notation (c_x^s, c_y^s) for the top left corner of the zoomed micro-image and R_φ the integer radius of the zoomed PSF, the set of indices of the images impacted by a change of emitter e is given by

$$\mathcal{I}_{p_e} = \left\{ t \in \{1, ..., S\} \,\middle|\, \exists (x,y) \in [\![c_x^t, c_x^t + fn_x]\!] \times [\![c_y^t, c_y^t + fn_y]\!] \,,\ |p_e - (x,y)| \leq R_\varphi \right\},$$

that is any micro-image whose zoomed version contains at least one pixel in the disk of center p_e and radius R_φ. For two positions p_1 and p_2, we define the set of indexes of micro-images to recompute in the case of a movement of the emitter from p_1 to p_2 by

$$\mu_{\mathcal{I}}(p_1, p_2) = \mathcal{I}_{p_1} \cup \mathcal{I}_{p_2}.$$

Concerning the computation of the ratio of the probabilities, as shown in Formula (6.13), we just need the difference between the energy associated to the current

chain and the energy associated to the proposed chain, created by the change of one emitter. The energy expression, given by (6.10), shows that only the micro-images that are modified need to be taken into account; the contribution of the other images is identical in both cases so that their values do not impact the computation of the energy differences. In the end, for an emitter migrating from p_1 to p_2, (6.10) needs to be computed only for $s \in \mu_{\mathcal{I}}(p_1, p_2)$. Thus, we define a partial energy $E_v^p(x, \mu_{\mathcal{I}}(p_1, p_2))$ which computes the energy on theses indices. For an emitter moving from p_e to p_f, Formula (6.13) becomes

$$p = \exp\left(-\left(E_v(\gamma_{i+1/2}) - E_v(\gamma_i)\right)\right) e^{\beta}$$
$$p = \exp\left(-(E_v^p(\gamma_{i+1/2}, \mu_{\mathcal{I}}(p_e, p_f)) - E_v^p(\gamma_i, \mu_{\mathcal{I}}(p_e, p_f))\right) e^{\beta}$$

6.3.3 Practical computation of the estimate

Definition of Ω

We recall that we set (c_x^s, c_y^s), where $s \in \{1, \ldots, S\}$ represents the number of the micro-image, as the top left corner of the zoomed micro-image. Each input micro-image is of size $n \times n$. Since this image is a zoom of a micro-image recorded on the camera, c_x^s/f and c_y^s/f are integer values. The coordinates of the zoomed region of interest are obtained by searching for the maximum and minimum values of the region of interest on the camera and multiply them by the factor of zoom used f. This define where the measurement was recorded on the camera; however for computing the whole reconstruction, we need to extend this region of measurement of half a Airy radius on each border (and in each direction), because of the convolution with the PSF; we therefore set

$$m_x = f \cdot \min_{s\in\{1,\ldots,S\}} \left(\frac{c_x^s}{f}\right) - \left\lceil \frac{r_a}{2fr_c} \right\rceil, \qquad m_y = f \cdot \min_{s\in\{1,\ldots,S\}} \left(\frac{c_y^s}{f} + n\right) - \left\lceil \frac{r_a}{2fr_c} \right\rceil$$
$$M_x = f \cdot \max_{s\in\{1,\ldots,S\}} \left(\frac{c_x^s}{f} + n\right) + \left\lceil \frac{r_a}{2fr_c} \right\rceil, \quad M_y = f \cdot \max_{s\in\{1,\ldots,S\}} \left(\frac{c_y^s}{f} + n\right) + \left\lceil \frac{r_a}{2fr_c} \right\rceil,$$

where $r_a/2fr_c$ represents the rounded up integer value of half the Airy radius (r_a is its value in nm, r_c the pixel size of the camera, and therefore fr_c the pixel size of the reconstruction). The emitters can then take their positions in $\{m_x, \ldots, M_x\} \times \{m_y, \ldots, M_y\}$. The sizes of Ω, (N_x, N_y), are then given by $N_x = M_x - m_x + 1$ and $N_y = M_y - m_y + 1$. We recall that we set $|\Omega| = N = N_x \times N_y$.

Computation of one iteration

We present in Algorithm 11 the computation of one iteration of the Metropolis-Hastings algorithm adapted to the E-LSE estimate; as in the previous chapter, one iteration consists in a number of proposals corresponding to the number of emitters.

Algorithm 11: Computation of one chain for the E-LSE estimate in the case of an ISM system

---

Inputs $y \in \mathbb{R}^{\Omega^c}$, input data, N_e, number of emitters, α, scaling parameter, N_i number of iterations
Output Γ one chain used to approximate the E-LSE estimate

initialize $\gamma_0 = (\lambda_e^0, p_e^0)_{e \in [\![1, N_e]\!]}$, that is draw the N_e emitter positions and intensities using a probability density function built from the normalized zoomed conventional image
for $i \in \{0, \dots, N_i \times (N_e - 1\}$ **do**
  draw $e \sim \mathcal{U}_{[\![1,N_e]\!]}$
  draw $\beta \sim \mathcal{U}_{[-\alpha;+\alpha]}$
  draw $p_f \sim \mathcal{U}_{\mathcal{V}(p_e)}$, with $\mathcal{V}(p_e) = \left\{p_f \in \Omega, |p_e - p_f| \leq \sqrt{2}\right\}$
  $\gamma_{i+1/2} \leftarrow \gamma_i - \lambda_e^i \delta_{p_e^i} + e^\beta \lambda_e^i \delta_{p_f}$
  $E_1 \leftarrow E_v^p(\gamma_i, \mu_{\mathcal{I}}(p_e^i, p_f))$ ▶ partial energy for γ_i
  for $s \in \mu_{\mathcal{I}}(p_e^i, p_f)$ **do**
    compute $I^s_{\gamma_{i+1/2}}$, the micro-image built in $\gamma_{i+1/2}$ for laser position s
  end for
  $E_2 \leftarrow E_v^p(\gamma_{i+1/2}, \mu_{\mathcal{I}}(p_e^i, p_f))$ ▶ partial energy for $\gamma_{i+1/2}$.
  $p \leftarrow e^{-(E_2 - E_1)} e^\beta$
  $\gamma_{i+1} \leftarrow \begin{cases} \gamma_{i+1/2} & \text{with probability } p \\ \gamma_i & \text{with probability } 1-p \end{cases}$
end for
$\Gamma = \frac{1}{N_i - b} \sum_{k=b+1}^{N_i} \lambda_e^{kN_e} \delta_{p_e^{kN_e}}$

Computation of the micro-images

Using the linearity of H and the definition of $\gamma_{i+1/2}$ (Formula (6.12)), we obtain

$$H\gamma_{i+1/2} = H\gamma_i - H\lambda_e^i \delta_{p_e^i} + He^\beta \lambda_e^i \delta_{p_f},$$

meaning that we only need to compute the action of the operator H on weighted Dirac distributions. Computing Formula (6.9) with $u = \lambda_e \delta_{p_e}$, we have

$$\forall p \in \mathbb{Z}^2,\ I_u(p, X_s) = \lambda_e D_k(p_e - X_s)\varphi\left(p - \frac{p_e}{f}\right). \tag{6.15}$$

Since the grid of reconstruction is f times thiner than the grid of the camera, one pixel on the camera represents $f \times f$ pixels on the reconstruction grid. The PSF is given at the resolution of the camera. Given one emitter, localized on this reconstruction grid, its position in a (un-zoomed) micro-image can be written as $(i, j) + (k, l) \times 1/f$, with (i, j) and (k, l) integer values and $(k, l) \in [\![0, f - 1]\!]^2$. This means that the PSF applied to this point needs to be shifted to correspond to this position (last term of Formula (6.15)). Since the chosen zoom factor f is rarely greater than 4, we decided to store the $f \times f$ translated PSF (f in each direction, translated of a factor $(k/f, l/f)$, $(k, l) \in [\![0, f - 1]\!]^2$); the choice of the translated PSFs is done for each emitter, according to its position within the non-zoomed pixel. An example with $f = 2$, where an un-zoomed pixel represents 4 zoomed pixels and then 4 PSFs are possible, is shown in Figure 6.7.

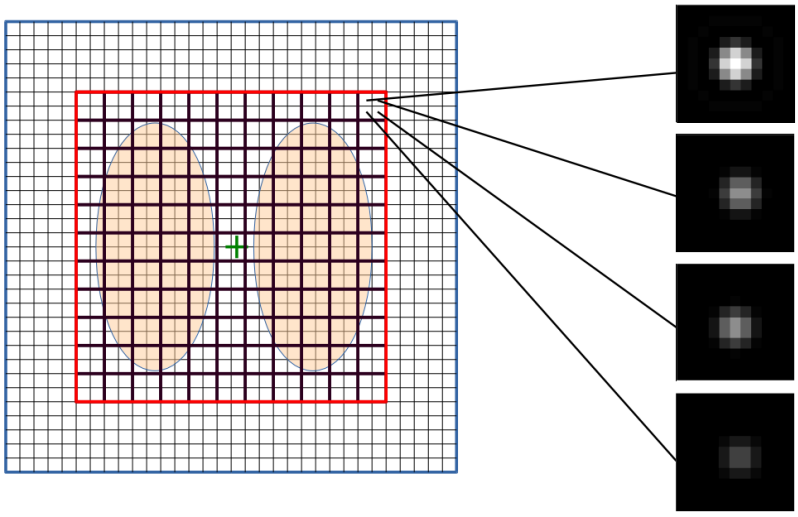

Figure 6.7: Illustration of the choice of the PSF according to the pixel on the zoomed image. In red is the real zoomed micro-image, in blue as in Figure 6.6 the set of pixels impacting this micro-image. We chose a zoom factor $f = 2$. This means that each pixel of the real micro-image, got on the camera (squares in bold), represents four pixels on the zoomed micro-image. According to the position of the emitter within these four possibilities, a different PSF is used; each of them is normalized. The first one is the one given as the "standard" PSF, the three others are obtained by shifting this PSF of $1/f$ (here 0.5) in one or both directions. These f^2 PSF are precomputed before starting the Metropolis–Hastings algorithm.

In the following, we consider that the PSF is a 4-dimensional table, the two first dimensions represent the translation index along x and y directions and the two remaining dimensions represent the position in the (translated) PSF image (corresponding to camera pixels); this table is computed once at the beginning of the program. The size of the PSF and its translated versions has been set at $3n_x \times 3n_y$ so that any crop of size $n_x \times n_y$ around the "real" PSF (that is the signal of interest of the PSF, considered of size $n_x \times n_y$) can be performed.

Knowing the illumination patterns at the correct resolution given by Formula (6.14), the computation of the micro-image s for one emitter on one pixel of the super-resolved image consists in

— finding the (integer) position of the emitter in the zoomed micro-image number s, noted (e_x, e_y),
— computing the intensity of the emitter in the micro-image by multiplying the intensity of the emitter with the intensity of the distribution in (e_x, e_y),
— finding the correct PSF (translation and position) according to the position of the emitter in the real micro-image,
— multiplying this PSF by the intensity of step 2.

This computation of the micro-images is shortened in Algorithm 12.

Algorithm 12: Computation of the micro-image s for an emitter e of position (p_x^e, p_y^e) in Ω and intensity λ_e

$(e_x, e_y) \longleftarrow (c_x^s - p_x^e, c_y^s - p_y^e)$ ▶ position in the zoomed micro-image
$d \longleftarrow \mathcal{D}^s(e_x, e_y) \times \lambda_e$
$(x_s, y_s) \longleftarrow \left(\left\lfloor \frac{x}{f}, \frac{y}{f} \right\rfloor\right)$
$(t_x, t_y) \longleftarrow (e_x - x_s f, e_y - y_s f)$
mi $\longleftarrow d \times PSF(t_x, t_y, (x_s, y_s) - \left\lfloor \frac{n_x}{2}, \frac{n_y}{2} \right\rfloor \longrightarrow (x_s, y_s) + (n_x, n_y))$
return mi.

To store the micro-image model, we need a table of the same size as the input data, containing the values of the micro-images associated to the current set of emitters. We decided to create in fact two of them, to store the current micro-images (created by the chain number i) but also the "proposed" micro-images (the ones associated to chain $i+1/2$). This prevents from computing again the old micro-images if the proposition of Metropolis-Hastings is rejected (which happens in more than half the cases), but requires to duplicate the table. During the iterations, a binary table of size S indicates for each laser position, which micro-image is the correct

current one. This also means that a rejection of the proposal during Metropolis-Hastings only consists in changing the values of this binary table, for the impacted micro-images that were recomputed, to the other value.

Remark 28. *The idea of using positions that are not exactly on a pixel of reconstruction has been considered, however it requires to recompute for each emitter the PSF translated at this exact position, instead of just having a fixed number of (translated) PSF; this action would make the algorithm much slower than the current one, and that is the reason why it was not implemented.*

As in the previous chapter, the E-LSE estimate is obtained using several chains, whose results are averaged, and a convolution with a small Gaussian kernel is performed. The pixel size of the reconstruction defines the discrete frequency cut of the reconstruction f^u_{max}; according to [125] the Airy disk can be approximated by a Gaussian with parameter $\sigma \sim 0.33 r_a$, with r_a the Airy radius whose definition was given in Chapter 3. We then choose the Gaussian kernel approximating the PSF of a system of frequency cut f^u_{max} for the final convolution. As it can be seen in Figure 6.8, the Gaussian profile does not perfectly fit the Airy profile, but the approximation is reasonable for the convolution.

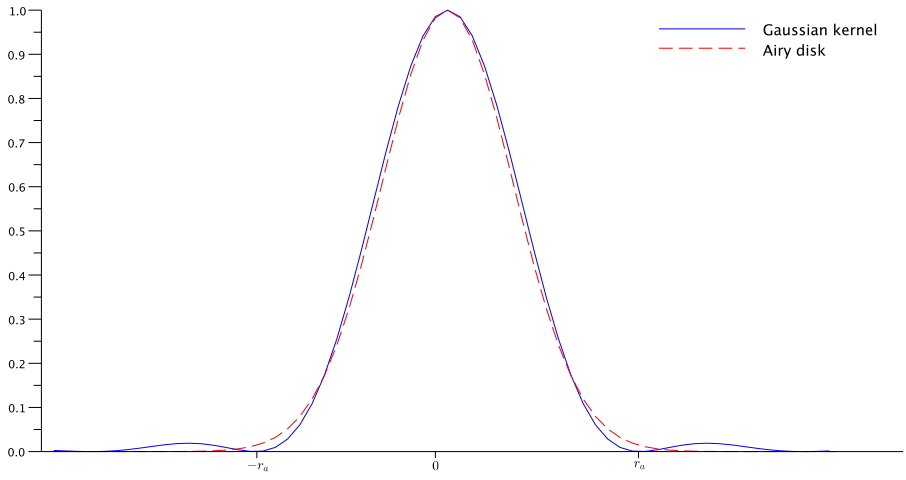

Figure 6.8: Comparison of the Airy profile and the Gaussian profile for σ chosen as $\sigma \sim 0.33 r_a$. Even if the rebound of the Airy profile cannot be represented by a simple Gaussian, we see that this approximation is really reasonable and that the result of the convolution should be quite close.

6.3.4 Memory optimization for time-saving

As mentioned several times, the MCMC methods are very time-consuming, creating the result image in a quite long time. However, by the definition of the algorithm, we can notice that the chains are independent and could be computed in parallel, in order to accelerate the code. In return, it requires that each thread possesses its own (double) table of micro-images, corresponding binary table, list of emitters and reconstruction image. That is the reason why some choices had to be made to reduce the memory used by the algorithm. We focus on two of them.

First, we did not keep, for each pixel of the reconstruction, all the indexes of the micro-images to re-compute for an emitter on this position, but created patches on the reconstruction, of size 5 by 5 pixels for a zoom of value 2, containing the union of the micro-images indexes to re-compute for all the pixels of the area. Depending on the pixel size and the scan step the results are not exactly the same, but between 5% and 15 % of the images are re-computed whereas it is not necessary. In contrast, the savings in memory are quite impressive: for a set of around $12,000$ micro-images, representing an area of 5μm$\times 5\mu$m, with a camera pixel size around 100 nm and a scanning step of 100 nm, theses changes enable to use from more than 5 gigabytes to less than 100 megabytes when using 5 by 5 pixels patches (on a reconstruction of effective size around 190×100, $f = 2$).

Another change that was chosen was not to store all the illumination patterns, zoomed and translated. Indeed the $\mathcal{D}^s$ from Formula (6.14) were stored for all $s \in \{1, \dots, S\}$. This is a large amount of memory, especially when the zoom is bigger or equal to 4; in this case, the size of the illumination patterns can exceed 1 gigabyte. An alternative was tried: zoom these patterns, by zero-padding in Fourier domain, at a higher factor, $z_{\mathcal{D}}$, than the one required by the reconstruction, f times thinner than the micro-images, and then estimate the illumination pattern value by bilinear interpolation. Given $\mathcal{D}^s$, the zoomed illumination pattern of factor $z_{\mathcal{D}}$ for laser position s, it satisfies

$$\forall (m,n) \in \mathbb{Z}^2,\ \mathcal{D}^s(m,n) = \tilde{d}^s(m/z_{\mathcal{D}}, n/z_{\mathcal{D}}),$$

where $\tilde{d}^s$ is the calibrated illumination pattern of center (x_d, y_d). The center of the zoomed illumination pattern $\mathcal{D}^s$ is thus located in $(x_d \times z_{\mathcal{D}}, y_d \times z_{\mathcal{D}})$. For an emitter e, localized in (p_x^r, p_y^r) on the reconstruction grid, its position is still an integer in any zoomed micro-image s, with coordinates (p_x^s, p_y^s), such that $(p_x^s, p_y^s) = (p_x^r - c_x^s, p_y^r - c_x^y)$, with (c_x^s, c_y^s) the top left corner of the zoomed micro-image number s. However, the

center of the distribution in the zoomed micro-image number s, given by (X_s, Y_s), is most of the time a non-integer value. The computation of d, the value of the pattern at the emitter position, consists in finding the value of the distribution at a distance $(p_x^s - X_s, p_y^s - Y_s)$ from the center of the distribution. The coordinates of the emitter in this referential are given by $(p_x, p_y) = (x_d \times f, y_d \times f) - (p_x^s - X_s, p_y^s - Y_s)$.

In the illumination pattern $\mathcal{D}^s$ zoomed at $z_\mathcal{D} > f$, the bilinear interpolation computing d is given, using the positions $p'_x = p_x \times f/z_\mathcal{D}$, $p'_y = p_y \times f/z_\mathcal{D}$, by the formula

$$\begin{aligned} d = \; & \mathcal{D}^s\left(\lfloor p'_x \rfloor, \lfloor p'_y \rfloor\right) + (p_x - \lfloor p'_x \rfloor)\,\delta_{1,0}\left(\mathcal{D}^s\left(\lfloor p'_x \rfloor, \lfloor p'_y \rfloor\right)\right) \\ & + \left(p_y - \lfloor p'_y \rfloor\right)\delta_{0,1}\left(\mathcal{D}^s\left(\lfloor p'_x \rfloor, \lfloor p'_y \rfloor\right)\right) \\ & + (p_x - \lfloor p'_x \rfloor)\left(p_y - \lfloor p'_y \rfloor\right)\left(\delta_{1,0}\left(\mathcal{D}^s\left(\lfloor p'_x \rfloor, \lfloor p'_y \rfloor\right)\right) + \delta_{0,1}\left(\mathcal{D}^s\left(\lfloor p'_x \rfloor, \lfloor p'_y \rfloor\right)\right)\right) \end{aligned} \tag{6.16}$$

where $\delta_{i,j}\left(\mathcal{D}^s\left(\lfloor p'_x \rfloor, \lfloor p'_y \rfloor\right)\right) = \mathcal{D}^s\left(\lfloor p'_x \rfloor + i, \lfloor p'_y \rfloor + j\right) - \mathcal{D}^s\left(\lfloor p'_x \rfloor, \lfloor p'_y \rfloor\right)$ and $\lfloor \cdot \rfloor$ denotes the lower integer part function.

In Figure 6.9, we compare the direct (old) computation with this new one, with two different values of $z_\mathcal{D}$: 8 and 16 for a real factor of resolution $f = 4$. Before, the illumination patterns were zoomed to the correct resolution and translated to the exact laser impact position in the zoomed referential (details are in Chapter 3); with this new method, they are computed using Formula (6.16). We plotted a cross-section on the lobes of one half-moon, when the illumination pattern is obtained with the original method (in black) and the bilinear one with $z_\mathcal{D} = 8$ and $z_\mathcal{D} = 16$. We can notice that for $z_\mathcal{D} = 16$ the cross-sections of old and new versions are visually the same, which is not the case with $z_\mathcal{D} = 8$. With no doubt using a zoom of 16 enables to be close enough to the old computation with high saving in memory area.

In that case, the second step of Algorithm 12 is slightly different; it implements Formula (6.16) instead of extracting the value from a pre-computed table.

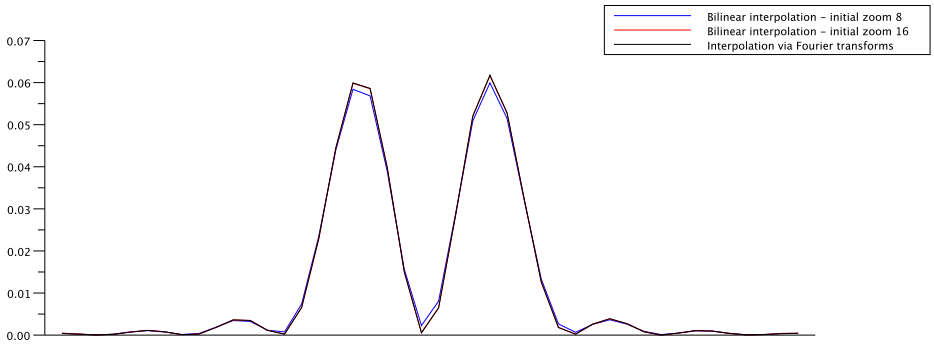

Figure 6.9: Illustration of the illumination pattern's interpolation by a cross section on the lobes of an half-moon: one illumination pattern was chosen, computed using zero-padding and subpixelic translation via Fourier transform (initial choice of computation) and by bilinear interpolation on a pre-zoomed illumination pattern with zoom of values 8 and 16 using Formula (6.16). Clearly, choosing an initial zoom of 16 and the bilinear interpolation, we should not deteriorate the results, since the profiles are very close. In memory, we only keep one version of each illumination pattern zoomed instead of the S (S can be bigger than 10000) already repositioned patterns.

Using Intel Xeon Phi Processors [1] for the computation, we moved from one chain in about 30 minutes to 240 chains in about 50 minutes. This is true for quite small data set because the memory on these cards is limited to 8 Go; for bigger data sets, the maximum number of chains in parallel is limited by the amount of memory required by each thread.

6.3.5 Illumination reconstruction

When finding the solution of the inverse problem $v = Hu$ (meaning $\forall i, v_i = \sum_k h_{ik} u_k$), u represents a fluorophore density on each pixel. However the acquisition is not "uniform" on the whole sample, in the sense that some pixels of the reconstruction appear in more micro-images than others (in particular, the pixels on the border can be illuminated only once per illumination pattern and very weakly). This favors the aggregate of emitters on the border of the reconstruction domain with possibly very high intensities. A first attempt to correct that was to create a map of authorized/unauthorized emitter positions, based on the number of impacted micro-images per pixel of the reconstruction. In Figure 6.10 (a), we can see a representation of this number for each pixel. A threshold relative to the maximum

1. The acquisition of Xeon Phi SE8X at the end of 2015 considerably sped up the computation of the E-LSE estimate, enabling to easily parallelize (use of OpenMP) the chains computation, in the best case, depending on the size of the data, 244 chains can be computed in parallel.

number of impacted micro-images enables to create the map of authorized emitter positions; we chose 10%. The reconstruction associated to this authorized position map is presented also in Figure 6.10 (c); we can clearly see that some pixels on the border have erratic values, because of their smaller impact on the energy.

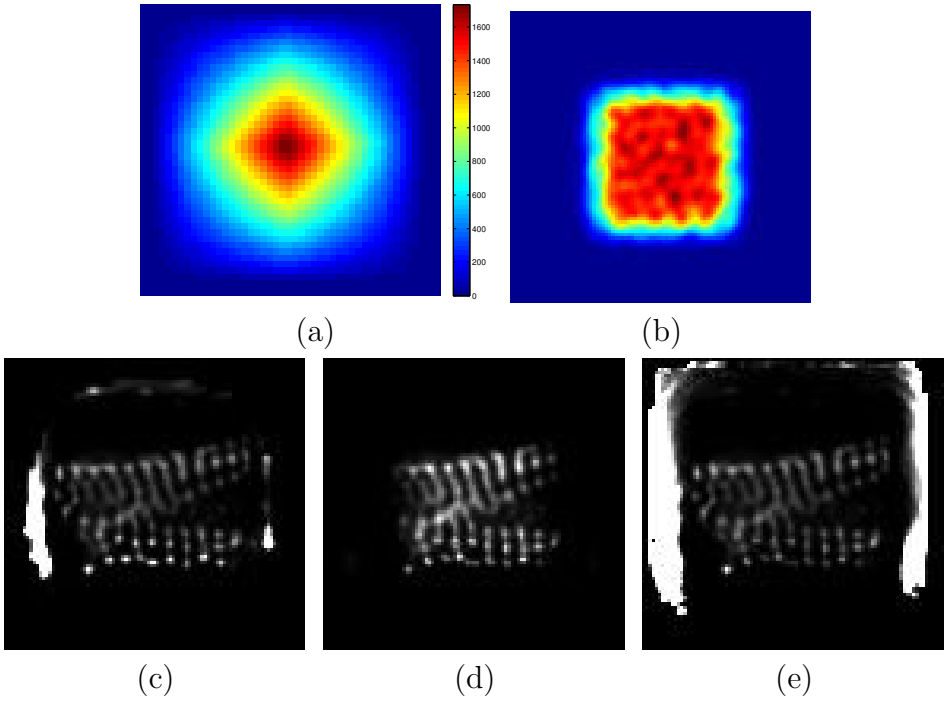

Figure 6.10: Illustration of the illumination reconstruction: (a) image representing the number of impacted micro-images per reconstruction pixel, (b) image representing the values of the c_k (that is the illumination in each pixel of the reconstruction), (c) result of the algorithm with the matrix H and the authorized emitter position map (thresholded so that we may see the reconstruction, a ratio of almost 200 is observed between the middle and the border of the reconstruction), (d) result of the algorithm with matrix H', (e) result of the algorithm with matrix H' re-multiplied afterwards by the image of the c_k (thresholded too). As it can be seen on the two images on the top, all pixels of the reconstruction do not have the same influence on the micro-images. The reconstruction with H' does not prevent the emitters from moving to the border, as it can be seen on the image (e),however they take very smaller values. The drawback is of course that some structures next to the border that may have been correctly reconstructed disappear in this reconstruction, because their level of illumination is too low.

Remark 29. *The introduction of this map is not without consequences on the algorithm, since we need to take into account for each pixel of the reconstruction its*

number of "eligible" neighbors and add it in the acceptance computation. Indeed in Formula (6.11), we considered that each pixel has the same number of neighbors, simplifying the term $|\mathcal{V}(\cdot)|$. Given that an emitter goes from (p_e, λ_e) to (p'_e, λ'_e), the incremental function becomes

$$\frac{q((p_e,\lambda_e)|(p'_e,\lambda'_e))}{q((p'_e,\lambda'_e)|(p_e,\lambda_e))} = \frac{|\mathcal{V}(p_e)|}{|\mathcal{V}(p'_e)|}\frac{\lambda'_e}{\lambda_e}.$$

In fact, if a pixel is illuminated but returns only a very few number of photons, we can consider that the result associated to this pixel will be quite unstable, making the matrix unstable too and then ill-conditioned (see Remark 30). Some solutions were tested to deal with this issue, as adding a penalization to the energy. Finally, we decided to reconstruct, instead of the density of fluorophores, the emitted light in each point, u'. The problem becomes

$$\forall i \in \{1, ..., n \times S\},\ v_i = \sum_{k=1}^{N} h_{ik}u_k = \sum_{k=1}^{N} \frac{h_{ik}}{c_k}u'_k \Leftrightarrow v_i = \sum_{k=1}^{N} h'_{ik}u'_k,$$

with $c_k = \sum_i h_{ik}$ the illumination in each pixel, that is the light created in the micro-images by one fluorophore of intensity 1 localized on this pixel, k.

Remark 30. *Given a rectangular matrix A, its condition number is the ratio between its highest and lowest singular values, that are the square roots of the eigenvalues of A^tA. We suppose that A is a well-conditioned matrix, of size $n \times p-1$, we construct the matrix A' of size $n \times p$ defined by*

$$A' = \begin{pmatrix} & \begin{pmatrix} 0 \\ \vdots \\ \varepsilon \\ \vdots \\ 0 \end{pmatrix} \\ A & \end{pmatrix},\ \textit{with } \varepsilon \textit{ such that } a'_{i,p} = \varepsilon,\ i \in \{1, \dots, n\},$$

we have that

$$A'^tA' = \begin{pmatrix} & A^t & \\ 0 & \dots \ \varepsilon \ \dots & 0 \end{pmatrix} \begin{pmatrix} & \begin{pmatrix} 0 \\ \vdots \\ \varepsilon \\ \vdots \\ 0 \end{pmatrix} \\ A & \end{pmatrix} = \begin{pmatrix} A^tA & \varepsilon a_{q,\cdot} \\ \varepsilon a_{q,\cdot} & \varepsilon^2 \end{pmatrix} = \begin{pmatrix} A^tA & 0 \\ 0 & 0 \end{pmatrix} + \mathcal{O}(\varepsilon)\,.$$

Since A is supposed well-conditioned, the ratio between its highest and lowest singular values is close to 1. However, we can see that the eigenvalues of $A'^t A'$ tend to the ones of $A^t A$ with supplementary value 0 when ε tend to 0. This drastically increases the condition number of the matrix, and then the stability of the linear system.

In Figure 6.10, image (b), each pixel k represents the value of c_k and we see a ratio of almost 200 between the smaller and bigger values. Each column of the new matrix H' is obtained by normalizing each column of H, meaning that $\sum_i h'_{i,j} = 1$. The results are interesting, removing big values on the border, even if emitters still move there, as it can be seen on the last image (c). However, one drawback is that the area of the real reconstruction domain is smaller.

6.3.6 Comparison of results according to the parameters

In the following, we present the different results obtained when changing the density of emitters (Figure 6.11) and also the evolution according to number of iterations and chains (Figures 6.12 and 6.13). In addition to the final images (and some profiles), we present the average of the energies during the iterations, and the average of the acceptance rate (see Figure 6.14). We can see that a minimum number of emitters is compulsory to be able to represent correctly the whole signal (in particular separation between elements, as it was emphasized in Chapter 5); indeed, if the number of emitters is too small, the created structures are very thin, not representative of the real signal. On the contrary, a high density does not help to gain resolution. This can be guessed looking at the energy curves in Figure 6.14, where the final reconstructions with three last densities have quite close energies. Concerning the time of execution, the results were obtained respectively in 1 hour, 6 hours, 12 hours and 1 day using 4 Intel Xeon Phi Processors in parallel (working each one by batch of 240 chains). To get a result in a reasonable amount of time, some parameters (such as the number of iterations, chains and the burn-in state) should be optimized, but also sometimes a compromise on the number of emitters and then the quality.

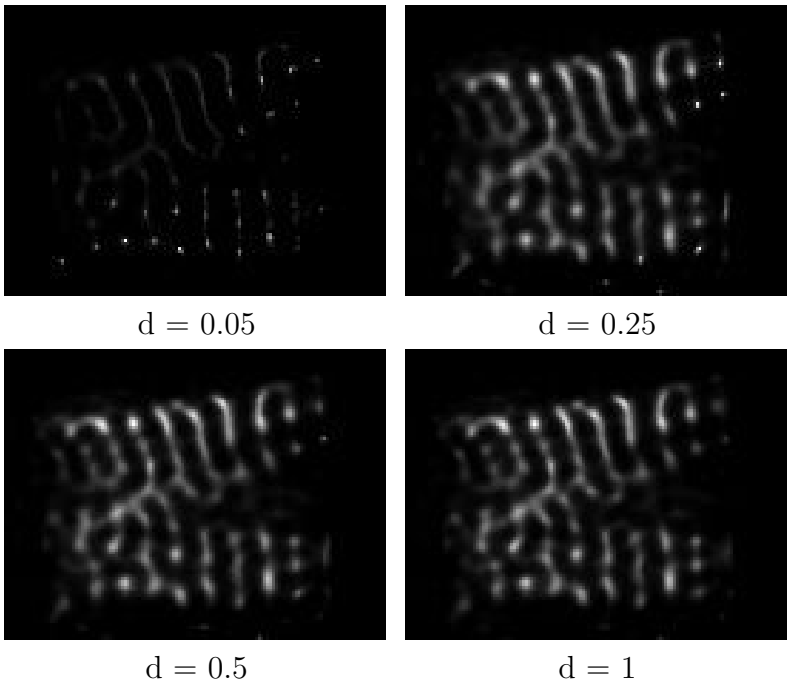

Figure 6.11: Comparison of E-LSE estimates obtained with different densities of emitters: from left to right, top to bottom: 0.05, 0.25, 0.5 and 1. It is clear that a density of 0.05 is not high enough to represent the whole signal, making impossible some separations and creating very thin structures. Between the other three reconstructions, we see that the results are quite similar (as shown on the plot below too). The time for creating the chains is proportional to the number of emitters, so that a choice has to be done to get the best quality, in a quite reasonable time.

6.4 Comparison of the algorithms on simulated data

We present two figures of comparison on simulated data; in the first one, Figure 6.15, a representation of chromosomes was chosen for simulations; on the ground truth, we can clearly see, at several places, the separation between the chromatids (showing the shape of an X, as it is often drawn in biological schema, whose different parts are called arms). The MAP estimate cannot resolve them, contrary to the E-LSE one, and on the MAP estimate the structure of the chromosomes is a bit distorted, like if it was made of round particles. In Figures 6.16 and 6.17, we can see that the generalization of Richardson-Lucy from sequence (6.2) creates structures with holes, not representative at all of the real structures. The resolution of MAP and E-LSE estimates on this image are quite similar; the E-LSE estimate seems a

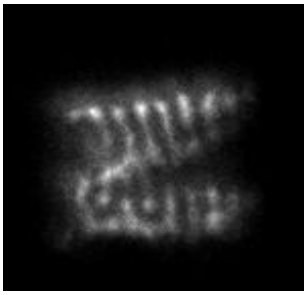

(a) 2^{nd} iteration

(b) 40^{th} iteration

(c) 100^{th} iteration

(d) 200^{th} iteration

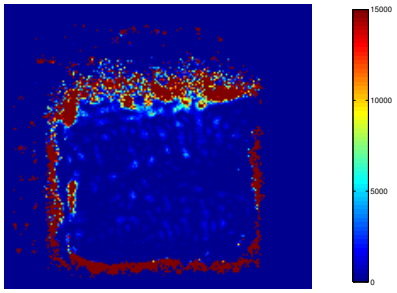

(e) L^2 distance between 2^{nd} iteration and final result

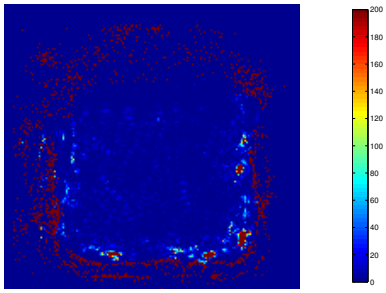

(f) L^2 distance between 40^{th} iteration and final result

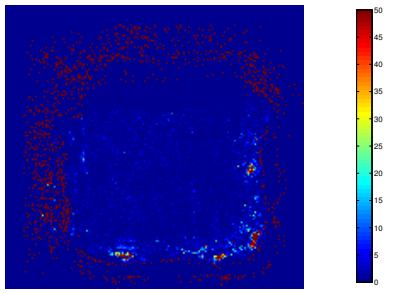

(g) L^2 distance between 100^{th} iteration and final result

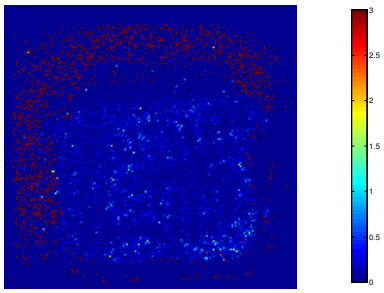

(h) L^2 distance between 199^{th} iteration and final result

Figure 6.12: Results of the E-LSE according to the number of iterations for a density of 0.5: in (a) to (d) are represented the averages of the $5,040$ chains according to the number of iterations (one iteration consisting in N_e changes) and in (e) to (h) the L^2 distances between the results after 2, 40, 100, 199 iterations and the final one (200 iterations). The scale is different on each one of these figure to emphasize the difference for all of them. Visually, differences are hard to see between the reconstructions after 100 iterations. The representations of the L^2 distances really enable to see the evolution of those differences: at each iteration, the borders pixel values are quite different value from those of the final image, but at the beginning we clearly see that the difference is also on the structures. At the end of the iterations, the significant difference are mainly on the border and a little bit in the background.

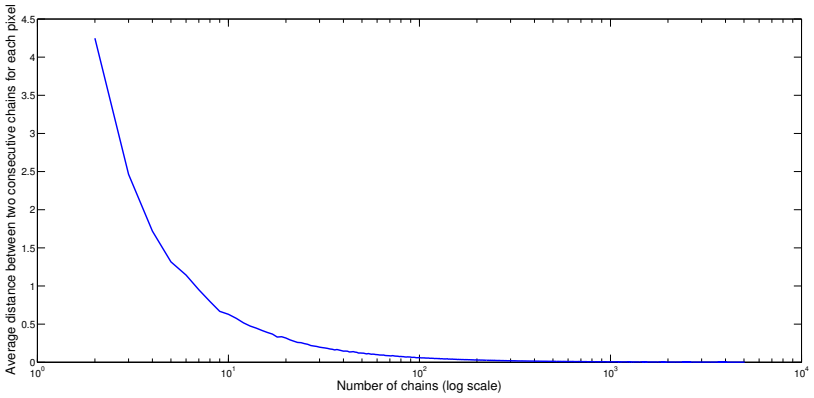

(a) Evolution of the average difference

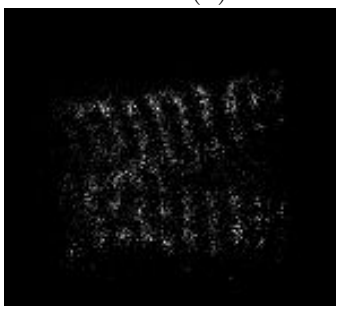

(b) 7 chains, $\bar{d} = 1$

(c) 202 chains, $\bar{d} = 0.1$

(d) 565 chains, $\bar{d} = 0.01$

(e) 1366 chains, $\bar{d} = 0.005$

Figure 6.13: Influence of the number of chains. The first plot (a) represents the evolution, in logarithmic scale, of the average difference between two consecutive reconstructions (adding one chain at the global average) per pixel, that is $\bar{d} = 1/M\sqrt{\sum_x(\gamma^{i+1}(x) - \gamma^i(x))^2}$, with M the number of effective pixels. The presented images correspond, to (b) $\bar{d} = 1$ (7 chains), (c) $\bar{d} = 0.1$ (202 chains), (d) $\bar{d} = 0.01$ (565 chains) and (e) $\bar{d} = 0.005$ (1366 chains). The final distance is $\bar{d} = 0.0012$. Comparing the result with $1,366$ chain and the result with $5,040$ (Figure 6.11), we see that we could have stopped before $5,040$ and still get a good resolution, and thus gain some time.

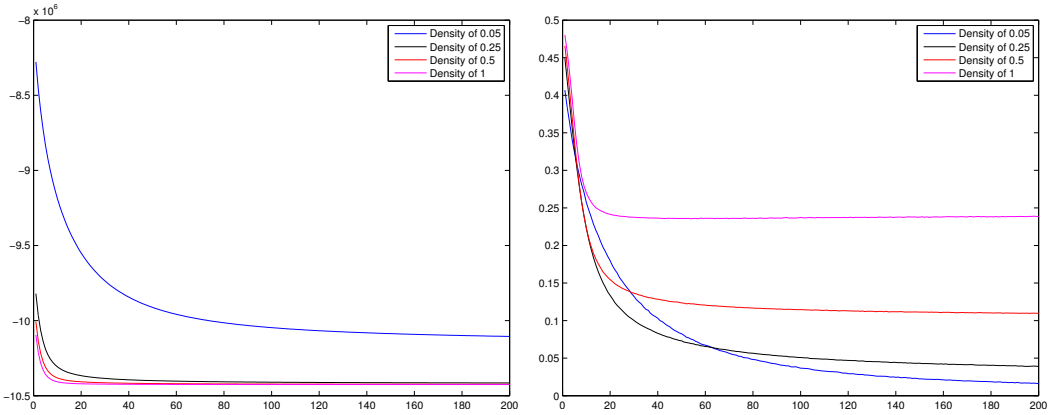

(a) Evolution of the energies (b) Evolution of the acceptance rate

Figure 6.14: Evolution of the energy (a) and the acceptance rate (b) during the iterations of the E-LSE algorithm, according to the initial density of emitters. On the energy plot, we can see that densities 0.25, 0.5 and 1 have energies that are quite close (it is logical that with more emitters the energy is smaller, because the reconstruction is more precise) contrary to the case of density 0.05, where some emitters are probably missing, preventing the correct representation of the biological sample. Concerning acceptance rates, we notice that the more emitters on the image, the higher the acceptance rate is; but in all cases, the rate levels off at some point. For a small amount of emitters however, it is very close to 0, meaning that a very few number of changes are accepted. With a higher number of emitters, the rate stabilizes earlier in the iterations.

bit better for separation but create structures a bit thiner than they really are. Observing the low intensity levels (by saturating the intensity on display), it is clear that the E-LSE estimate is artifact-free compared to the MAP estimate.

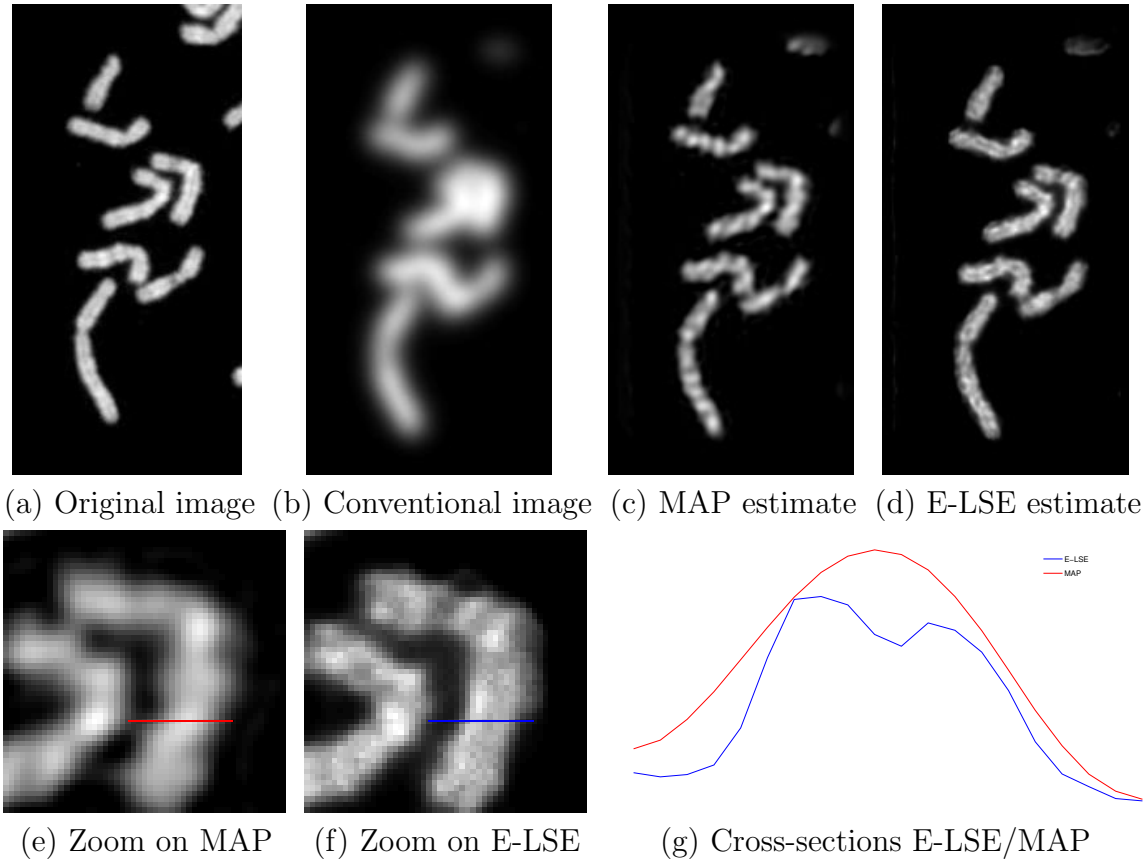

(a) Original image (b) Conventional image (c) MAP estimate (d) E-LSE estimate

(e) Zoom on MAP (f) Zoom on E-LSE (g) Cross-sections E-LSE/MAP

Figure 6.15: Comparison of the E-LSE and MAP estimates on an image of chromosomes; the original image (a) really shows the shape of chromosomes, with a separation of chromatids. In the conventional image (b), these details and some separations are totally lost. On both estimates,the separation between chromosomes are equivalently recovered; however, the MAP estimate (c) is "beaded", as if the chromosomes were made of round particles and the separation between chromatids are not visible at all. The E-LSE estimate (d) is not perfect, but represents better the reality and some separation between chromatides are visible, as it can be confirmed on the zooms (e)-(f) and cross-sections (g). The beaded effect is also a bit visible on the E-LSE estimate, which makes sense because some of the final chains may be close to the MAP estimate. These results were obtained simulating on a real image of fluorescence microscopy the system BioAxial, as described in Chapter 3 and with the half moons as illuminations patterns.
Image of chromosomes available on the site commons.wikimedia.org and licensed under CC BY-NC-ND 3.0

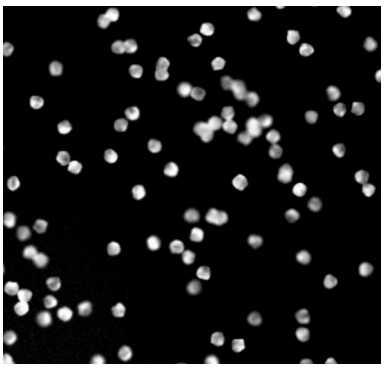

(a) Original image

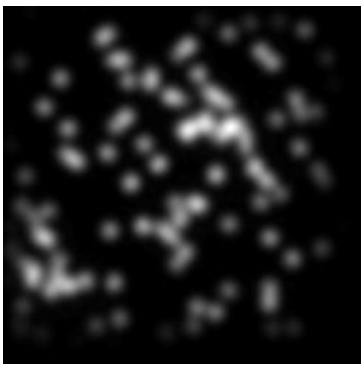

(b) Conventional image

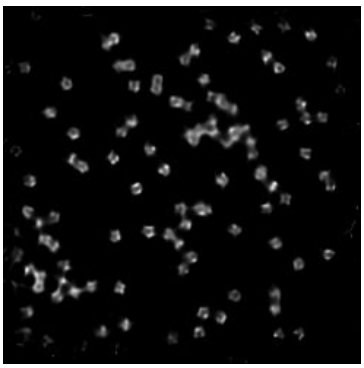

(c) Generalized RL Estimate

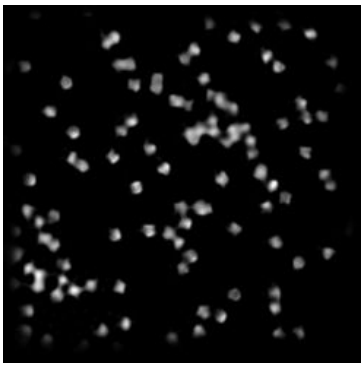

(d) MAP estimate

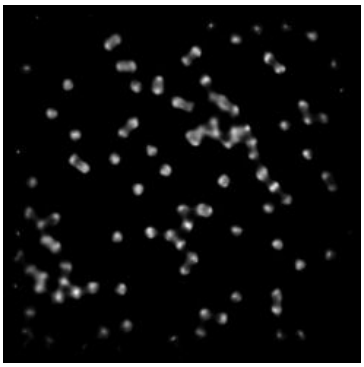

(e) E-LSE Estimate

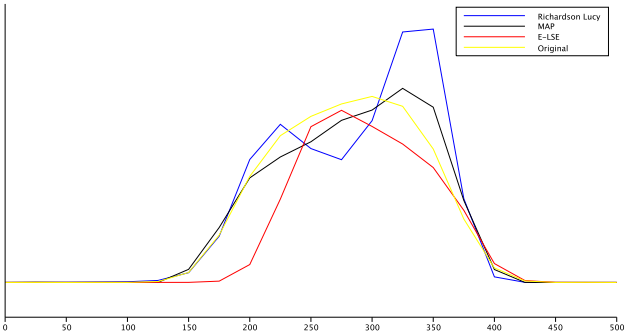

(f) Plot of one nucleus

Figure 6.16: Comparison of reconstructions on simulations (using an image representing synthetic nuclei, image (a)) for a super-resolution ISM system. The conventional image is represented in (b) and we compare several reconstructions: (c) Generalized Richardson-Lucy estimate computed thanks to Formula (6.2), (d) MAP estimate computed with Nesterov algorithm, (e) E-LSE estimate with a density of 0.25. (f) presents the cross-section of one nucleus for each one of the reconstruction, in comparison to the original one. We clearly see on this plot, as well as on the big image, that the Richardson Lucy estimate creates "holes" in the structures, that are in fact solid structures as it can be seen on the original image. The E-LSE seems the best estimate in terms of shape; however we can see that it makes structures thinner than they really are. These results were obtained simulating on a real image of fluorescence microscopy the system BioAxial, as described in Chapter 3 and with the half moons as illuminations patterns.
Image of synthetic nuclei from cellimagelibrary.org by P. Ruusuvuori - Original image was thresholded, convolved with a Gaussian kernel ($\sigma = 1$), cropped and un-zoomed by frequency cut.

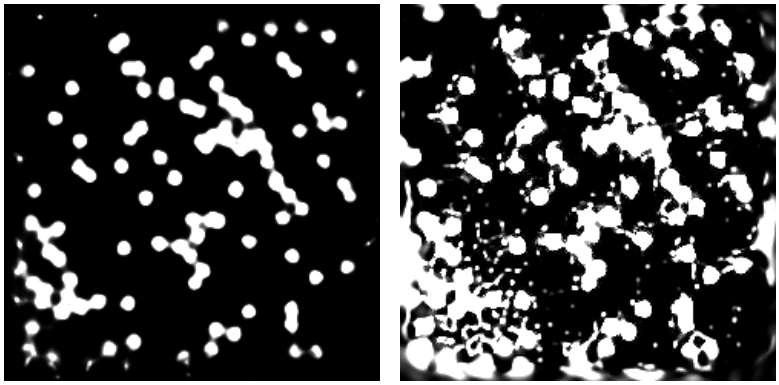

(a) E-LSE estimate (b) MAP estimate

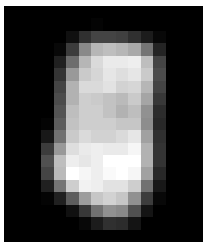

(c) MAP

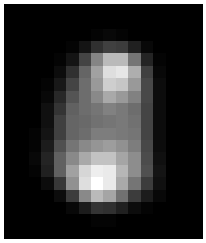

(d) E-LSE

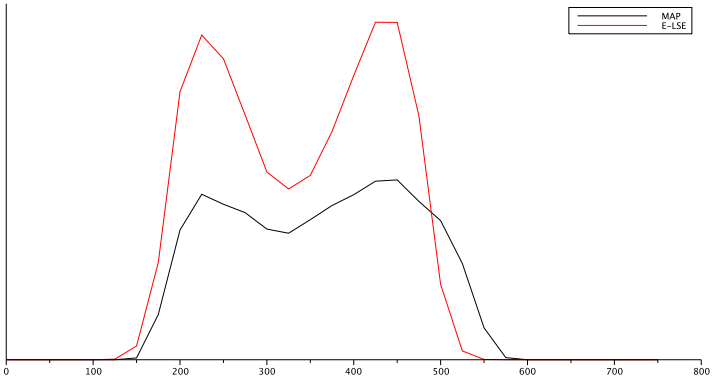

(e) Cross-section of the separation on images (c) and (d)

Figure 6.17: Comparison of E-LSE and MAP estimates: on top, saturated images from Figure 6.16, (a)-(b), zoom on the reconstruction MAP and LSE (c)-(d) for one of the same bead and plot of the separation between those two (e). From the saturated images, we clearly see that the image produced by the E-LSE really has less artifacts. Indeed even if they are not visible when the image is not saturated, some points are present in the background of the MAP estimate, which is a reconstruction artifact since the background of the ground truth is perfectly black. This is a very interesting property of the E-LSE estimate, in particular if one wants to apply post-processing on the super resolved data (for instance counting the nuclei in the image). On top of that, the profile clearly shows a better separation on some beads; the ratio between the peak and the cavity between the peaks is 1.4 for the MAP and 3.5 for the E-LSE.

Chapter 7

Conclusion

7.1 Super-resolution as an inverse problem

As we explained and showed all along the chapters, every optical system has a limited resolution, its limit depending on the wavelength and the objective used by the imaging system. These two parameters have ranges of values preventing from visualizing smaller objects than around 160 nanometers, in optimal conditions (that is illuminating with a small wavelength but in the visible spectrum and using an objective with a large numerical aperture). However, some biological phenomena are only observable at a much lower scale (for instance the fusion of membranes, or the action of proteins) requiring the development of super-resolution systems surpassing this limit. We showed in Chapter 2 that a system of Image Scanning Microscopy, ISM, which is the type of system that is considered in this thesis, can recover some frequency coefficients above this frequency limit.

In this thesis, we focused on two inverse problems under constraint of positivity: the deconvolution and the inverse problem generated by a system of ISM. The positivity constraint is quite a weak constraint, since all images whose pixels have positive intensities have the same a-priori probability to be the solution. However, it is particularly adapted to fluorescence microscopy. The purpose of super-resolution is to observe at a thiner scale, to see the phenomena and real shapes of biological elements. Enforcing an a priori on the image to recover could lead to false biological conclusions. Super-resolution systems are expected to support the biologist, either to confirm his theoretical hypotheses or to help him explore a dynamic biological

process. His confidence as well as his knowledge (possible artifacts, parameters of the algorithm) of the system are essential.

7.2 E-LSE and MCMC methods

Using estimates such as the (Emitters)-Least-Square Error, approximated with MCMC techniques, was not as successful as expected in deconvolution under positivity constraint, the night-sky effect created by Nesterov algorithm approximating the MAP estimate is not removed by computing the expectation of the posterior density. This kind of methods had presented very interesting results in Gaussian denoising, which motivated our choice. In the case of additive Gaussian noise, we proposed a criteria, based on the properties of this additive noise, to obtain a range of values for the energy that is "plausible"; this criterion gave very good results, stopping the iterations in Nesterov algorithm before the apparition of the night sky. The calculation of this criterion should be adapted to the more complicated case of Poisson noise.

As we mentioned several times, the MCMC methods are very time-consuming. This is a real issue for an industrial application; the acquirement of Phi Cards during this thesis was a real accelerator as mentioned in Chapter 6, but the parameters of density, number of iterations and chains have to be chosen so that the result is obtained in a reasonable amount of time, which is still several hours.

7.3 Practical aspects and three-dimensional acquisition and reconstruction

In this thesis, we only focused on the image to recover; we have considered known the Point Spread Function (PSF) as know, as well as the illumination patterns and the laser impact position. In practice, this requires for the first computation a calibration; this one can be done by imaging beads smaller than the diffraction limit for instance but also requires a dedicated algorithm. On top of that, in 1995, Van der Voor [117] pointed out that the PSF could be space variant. Concerning the laser positions, we need to know, for each recorded image, at which position exactly the laser hits the sample. This is not always easy since the galvanometric mirrors handling the movement of the laser are most of the time constantly running (and

not stopping at each point of the scan). Of course the accuracy of these parameters strongly determines the final quality of the super-resolved image.

In the last chapter, the results with the E-LSE estimate on an ISM system prove that this estimate can, in some situations, lead to a better-resolved image. The presented results were obtained on simulated data, with exact laser positions and calibrated illumination patterns identical to the one used in the scanning. Unfortunately, on real data, the E-LSE estimate tend to bring no or very little resolution improvement over the MAP estimate, even if it presents sometimes thinner structures and/or sharper separations. This can also be linked to the fact that we are reconstructing a planar image (the biological sample is supposed to be in the focus plane), whereas the biological sample is actually not flat, meaning that some light collected by the camera comes from planes above and below. That is the reason why an important step for super-resolution is three-dimensional acquisitions and reconstructions. If both presented reconstruction algorithms can be quite easily adapted, there are some issues in term of acquisitions, calibrations and computation time. Acquiring three-dimensional data means acquiring images obtained with several slightly different positions of the focused plan. This is not an easy task for several reasons; first the time of acquisition for one slice is an important aspect because there is a risk of drift of the sample. Another issue is the bleaching of the sample, meaning that the acquisition at each slice could require a different amount of light to get results of the same quality, because the intensity of fluorophores decreases with the number of excitations. Last but not least, the calibration process, that is computing both the PSF and the illumination pattern becomes a more complex task because of the needs for 3D acquisitions and the optical aberrations due to lenses, which also need to be modeled. For the adaptation of the E-LSE estimate, since the algorithm is quite time-consuming, this would require first to drastically accelerate the proposed algorithm (by the use of GPU cards for instance); however the implementation is straightforward, each emitter would just have a three dimensional position instead of a two dimensional one, and each slice should be part of the modeling. The MAP estimate could also be easily implemented, looking for the 3D object that is the more plausible given the data on each plan.

7.4 Neural networks for super-resolution

The recent enthusiasm for neural networks creates new opportunities for super-resolution. They have proven their good efficiency in single image super-resolution for several years, as it has been shown for instance by Dong [34] [35]. In most cases,

the training is performed learning on patches, which are given to the network in low and high resolution. In 2016, in [66], a different approach is proposed: the network is used to predict the high-frequency components only, and the super-resolved image is the result of the addition between the image of the high-frequency components and the interpolated input image. The use of neural network in microscopy is more recent. In [86], a neural network is used to compute a super-resolved image with STORM acquisitions; the network is trained to be able to perform super-resolution on images with a higher density of excited proteins than usually (for this method), which could lead to a reduction of the acquisition time. In [121], the authors compute the super-resolved image from a widefield image, with a ground-truth being a widefield image too, but acquired with a better objective. The results are quite impressive, even on structures which were not directly learned by the network.

In the case of ISM reconstructions, because of the high dimension and complexity of the problem, a mathematical model nevertheless seems necessary; however a combination of this model and a neural network could lead to a more robust system. However, an issue associated to the use of a neural network would be the amount of necessary data for training. Of course, simulated data can be used (and the whole discretization of the problem, as it was studied in Chapter 3, is very helpful), but there is also a need for real data (large data-sets of labeled microscopic images), which is more difficult to perform.

Bibliography

[1] E. Abbe. Beiträge zur Theorie des Mikroskops und der mikroskopischen Wahrnehmung. *Archiv für mikroskopische Anatomie*, 9(1):413–418, 1873.

[2] R. Abergel, C. Louchet, L. Moisan, and T. Zeng. Total variation restoration of images corrupted by poisson noise with iterated conditional expectations. In *International Conference on Scale Space and Variational Methods in Computer Vision*, pages 178–190. Springer, 2015.

[3] R. Abergel and L. Moisan. The Shannon total variation. *Journal of Mathematical Imaging and Vision*, 59(2):341–370, 2017.

[4] D.A. Agard, Y. Hiraoka, P. Shaw, and J.W. Sedat. Fluorescence microscopy in three dimensions. *Methods in cell biology*, 30:353–377, 1989.

[5] D.A. Agard and J.W. Sedat. Three-dimensional architecture of a polytene nucleus. *Nature*, 302(5910):676–681, 1983.

[6] C. Aguerrebere, J. Delon, Y. Gousseau, and P. Musé. Study of the digital camera acquisition process and statistical modeling of the sensor raw data. *HAL*, September 2012.

[7] J. Art. Photon detectors for confocal microscopy. In *Handbook of biological confocal microscopy*, pages 251–264. Springer, 2006.

[8] G. Ball, J. Demmerle, R. Kaufmann, I. Davis, I.M. Dobbie, and L. Schermelleh. SIMcheck: a toolbox for successful super-resolution structured illumination microscopy. *Scientific reports*, 5:15915, 2015.

[9] H.H. Bauschke, J.M. Borwein, and A.S. Lewis. The method of cyclic projections for closed convex sets in Hilbert space. *Contemporary Mathematics*, 204:1–38, 1997.

[10] M.V. Berry. Conical diffraction asymptotics: fine structure of Poggendorff rings and axial spike. *Journal of optics A: Pure and applied optics*, 6(4):289, 2004.

[11] M.V. Berry and M.R. Jeffrey. Conical diffraction: Hamilton's diabolical point at the heart of crystal optics. *Progress in Optics*, 50:13–50, 2007.

[12] M. Bertero and P. Boccacci. Image restoration methods for the Large Binocular Telescope (LBT). *Astronomy and Astrophysics Supplement Series*, 147(2):323–333, 2000.

[13] M. Bertero, P. Boccacci, G.J. Brakenhoff, F Malfanti, and H.T.M. Van der Voort. Three-dimensional image restoration and super-resolution in fluorescence confocal microscopy. *Journal of microscopy*, 157(1):3–20, 1990.

[14] M. Bertero, P. Boccacci, G. Desiderà, and G. Vicidomini. Image deblurring with poisson data: from cells to galaxies. *Inverse Problems*, 25(12):123006, 2009.

[15] M. Bertero, P. Brianzi, and E.R. Pike. Super-resolution in confocal scanning microscopy. *Inverse Problems*, 3(2):195, 1987.

[16] J. Besag. Digital image processing: Towards bayesian image analysis. *Journal of Applied statistics*, 16(3):395–407, 1989.

[17] E. Betzig, G.H. Patterson, R. Sougrat, O.W. Lindwasser, S. Olenych, J.S. Bonifacino, M.W. Davidson, J. Lippincott-Schwartz, and H.F. Hess. Imaging intracellular fluorescent proteins at nanometer resolution. *Science*, 313(5793):1642–1645, 2006.

[18] D.S.C. Biggs. 3D deconvolution microscopy. *Current Protocols in Cytometry*, pages 12–19, 2010.

[19] P. Bildstein. Filtres actifs. *Editions radio*, 1972.

[20] L.A. Breyer and G.O. Roberts. From metropolis to diffusions: Gibbs states and optimal scaling. *Stochastic Processes and their Applications*, 90(2):181–206, 2000.

[21] A. Buades, B. Coll, and J.-M. Morel. The staircasing effect in neighborhood filters and its solution. *IEEE transactions on Image Processing*, 15(6):1499–1505, 2006.

[22] J. Caron, C. Fallet, J.-Y. Tinevez, L. Moisan, L.P. Braitbart, G.Y. Sirat, and S.L. Shorte. Conical diffraction illumination opens the way for low phototoxicity super-resolution imaging. *Cell adhesion & migration*, 8(5):430–439, 2014.

[23] W.A. Carrington. Image restoration in 3-D microscopy with limited data. In *OE/LASE'90, 14-19 Jan., Los Angeles, CA*, pages 72–83. International Society for Optics and Photonics, 1990.

[24] A. Chambolle. An algorithm for total variation minimization and applications. *Journal of Mathematical imaging and vision*, 20(1):89–97, 2004.

[25] K.R. Chi. Super-resolution microscopy: breaking the limits. *Nature Methods*, 6(1):15–18, 2009.

[26] J. Chung, E. Haber, and J. Nagy. Numerical methods for coupled super-resolution. *Inverse Problems*, 22(4):1261, 2006.

[27] P.L. Combettes, Đ. Dũng, and B.C. Vũ. Dualization of signal recovery problems. *Set-Valued and Variational Analysis*, 18(3-4):373–404, 2010.

[28] P.L. Combettes and J.-C. Pesquet. Proximal splitting methods in signal processing. In *Fixed-point algorithms for inverse problems in science and engineering*, pages 185–212. Springer, 2011.

[29] J.-A. Conchello and Q. Yu. Parametric blind deconvolution of fluorescence microscopy images: preliminary results. In *Proceedings-SPIE the international society for optical engineering*, pages 164–174. SPIE international society for optical, 1996.

[30] J. Demmerle, C. Innocent, A.J. North, G. Ball, M. Müller, E. Miron, A. Matsuda, I.M. Dobbie, Y. Markaki, and L. Schermelleh. Strategic and practical guidelines for successful structured illumination microscopy. *Nature protocols*, 2017.

[31] T. Dertinger, R. Colyer, G. Iyer, S. Weiss, and J. Enderlein. Fast, background-free, 3D super-resolution optical fluctuation imaging (SOFI). *Proceedings of the National Academy of Sciences*, 106(52):22287–22292, 2009.

[32] N. Dey, L. Blanc-Feraud, C. Zimmer, P. Roux, Z. Kam, J.-C. Olivo-Marin, and J. Zerubia. Richardson–Lucy algorithm with total variation regularization for 3D confocal microscope deconvolution. *Microscopy research and technique*, 69(4):260–266, 2006.

[33] D.C. Dobson and F. Santosa. Recovery of blocky images from noisy and blurred data. *SIAM Journal on Applied Mathematics*, 56(4):1181–1198, 1996.

[34] C. Dong, C. Change Loy, K. He, and X. Tang. Learning a deep convolutional network for image super-resolution. In *European Conference on Computer Vision*, pages 184–199. Springer, 2014.

[35] C. Dong, C. Change Loy, K. He, and X. Tang. Image super-resolution using deep convolutional networks. *IEEE transactions on pattern analysis and machine intelligence*, 38(2):295–307, 2016.

[36] D.L. Donoho. Compressed sensing. *IEEE Transactions on information theory*, 52(4):1289–1306, 2006.

[37] G. Dupuis. La super-résolution. *Photoniques*, (62):42–47, 2012.

[38] R. Escalante and M. Raydan. *Alternating projection methods*, volume 8. Society for Industrial and Applied Mathematics, 2011.

[39] J.N. Farahani, M.J. Schibler, and L.A. Bentolila. Stimulated emission depletion (STED) microscopy: from theory to practice. *Microscopy: science, technology, applications and education*, 2(4):1539–1547, 2010.

[40] S. Farsiu, M.D. Robinson, M. Elad, and P. Milanfar. Fast and robust multiframe super resolution. *IEEE transactions on image processing*, 13(10):1327–1344, 2004.

[41] D.A. Fish, J.G. Walker, A.M. Brinicombe, and E.R. Pike. Blind deconvolution by means of the Richardson–Lucy algorithm. *Journal of the Optical Society of America*, 12(1):58–65, 1995.

[42] C. Fox and G.K. Nicholls. Exact map states and expectations from perfect sampling: Greig, porteous and seheult revisited. In *AIP Conference Proceedings*, volume 568, pages 252–263. AIP, 2001.

[43] A.M. Getz, F. Xu, F. Visser, R. Persson, and N.I. Syed. Tumor suppressor menin is required for subunit-specific nachr $\alpha 5$ transcription and nachr-dependent presynaptic facilitation in cultured mouse hippocampal neurons. *Scientific Reports*, 7, 2017.

[44] J.W. Goodman. *Introduction to Fourier optics*. Roberts and Company Publishers, 2005.

[45] G. Grimmett and D. Stirzaker. *Probability and random processes*. Oxford university press, 2001.

[46] M.G.L. Gustafsson. Surpassing the lateral resolution limit by a factor of two using structured illumination microscopy. *Journal of microscopy*, 198(2):82–87, 2000.

[47] M.G.L. Gustafsson. Nonlinear structured-illumination microscopy: wide-field fluorescence imaging with theoretically unlimited resolution. *Proceedings of the National Academy of Sciences of the United States of America*, 102(37):13081–13086, 2005.

[48] M.G.L. Gustafsson, L. Shao, P.M. Carlton, C.J.R. Wang, I.N. Golubovskaya, W.Z. Cande, D.A. Agard, and J.W. Sedat. Three-dimensional resolution doubling in wide-field fluorescence microscopy by structured illumination. *Biophysical journal*, 94(12):4957–4970, 2008.

[49] J. Hadamard. Sur les problèmes aux dérivées partielles et leur signification physique. *Princeton university bulletin*, pages 49–52, 1902.

[50] W.R. Hamilton. Third supplement to an essay on the theory of systems of rays. *Transactions of the Royal Irish Academy*, 17(part 1):1–144, 1837.

[51] W.K. Hastings. Monte Carlo sampling methods using Markov chains and their applications. *Biometrika*, 57(1):97–109, 1970.

[52] R. Havard and M.A. Hurn. Loss functions for Bayesian image analysis. *Scandinavian Journal of Statistics*, 24:103–114, 1997.

[53] R. Heim, A.B. Cubbitt, and R.Y. Tsien. Improved green fluorescence. *Nature*, 373(6516):663–664, 1995.

[54] B. Hein, K.I. Willig, and S.W. Hell. Stimulated emission depletion (STED) nanoscopy of a fluorescent protein-labeled organelle inside a living cell. *Proceedings of the National Academy of Sciences*, 105(38):14271–14276, 2008.

[55] R. Heintzmann and C.G. Cremer. Laterally modulated excitation microscopy: improvement of resolution by using a diffraction grating. In *BiOS Europe'98*, pages 185–196. International Society for Optics and Photonics, 1999.

[56] S.W. Hell and J. Wichmann. Breaking the diffraction resolution limit by stimulated emission: stimulated-emission-depletion fluorescence microscopy. *Optics letters*, 19(11):780–782, 1994.

[57] I.C. Hernández, M. Castello, L. Lanzanò, M. d'Amora, P. Bianchini, A. Diaspro, and G. Vicidomini. Two-photon excitation STED microscopy with time-gated detection. *Scientific reports*, 6:19419, 2016.

[58] T.J. Holmes. Maximum-likelihood image restoration adapted for noncoherent optical imaging. *Journal of the Optical Society of America*, 5(5):666–673, 1988.

[59] B. Huang, M. Bates, and X. Zhuang. Super-resolution fluorescence microscopy. *Annual review of biochemistry*, 78:993–1016, 2009.

[60] W. Huang and Y. Zheng. MMSE reconstruction for 3D freehand ultrasound imaging. *Journal of Biomedical Imaging*, 2008:2, 2008.

[61] J. Huff. The Airyscan detector from ZEISS: confocal imaging with improved signal-to-noise ratio and super-resolution. *Nature methods*, 12(12), 2015.

[62] J. Huff. The Fast mode for ZEISS LSM 880 with Airyscan: high-speed confocal imaging with super-resolution and improved signal-to-noise ratio. *Nature Methods*, 13(11), 2016.

[63] S. Hugelier, J.J. De Rooi, R. Bernex, S. Duwé, O. Devos, M. Sliwa, P. Dedecker, P.H.C. Eilers, and C. Ruckebusch. Sparse deconvolution of high-density super-resolution images. *Scientific reports*, 6:21413, 2016.

[64] N. Hurley and S. Rickard. Comparing measures of sparsity. *IEEE Transactions on Information Theory*, 55(10):4723–4741, 2009.

[65] M. Ingaramo, A.G. York, E. Hoogendoorn, M. Postma, H. Shroff, and G.H. Patterson. Richardson–Lucy deconvolution as a general tool for combining images with complementary strengths. *ChemPhysChem*, 15(4):794–800, 2014.

[66] J. Kim, J. Kwon Lee, and K. Mu Lee. Accurate image super-resolution using very deep convolutional networks. In *Proceedings of the IEEE Conference on Computer Vision and Pattern Recognition*, pages 1646–1654, 2016.

[67] V.L. Kolossov, M. Sivaguru, J. Huff, K. Luby, K. Kanakaraju, and H.R. Gaskins. Airyscan super-resolution microscopy of mitochondrial morphology and dynamics in living tumor cells. *Microscopy Research and Technique*, 2017.

[68] K. Korobchevskaya, H. Colin-York, B.C. Lagerholm, and M. Fritzsche. Exploring the potential of Airyscan microscopy for live cell imaging. In *Photonics*, volume 4, page 41. Multidisciplinary Digital Publishing Institute, 2017.

[69] P. Křížek, T. Lukeš, M. Ovesnỳ, K. Fliegel, and G.M. Hagen. Simtoolbox: a matlab toolbox for structured illumination fluorescence microscopy. *Bioinformatics*, 32(2):318–320, 2015.

[70] A. Lal, C. Shan, and P. Xi. Structured illumination microscopy image reconstruction algorithm. *IEEE Journal of Selected Topics in Quantum Electronics*, 22(4):50–63, 2016.

[71] G. Landi and E.L. Piccolomini. A projected Newton-CG method for nonnegative astronomical image deblurring. *Numerical Algorithms*, 48(4):279–300, 2008.

[72] H. Lantéri and C. Theys. Restoration of astrophysical images: the case of Poisson data with additive Gaussian noise. *EURASIP Journal on Applied Signal Processing*, 2005:2500–2513, 2005.

[73] B.O. Leung and K.C. Chou. Review of super-resolution fluorescence microscopy for biology. *Applied spectroscopy*, 65(9):967–980, 2011.

[74] H. Lloyd. On the phenomena presented by light in its passage along the axes of biaxal crystals. *The Transactions of the Royal Irish Academy*, pages 145–157, 1831.

[75] C. Louchet. *Modèles variationnels et bayésiens pour le débruitage d'images: de la variation totale vers les moyennes non-locales*. PhD thesis, Université Paris Descartes, 2008.

[76] C. Louchet and L. Moisan. Total variation denoising using posterior expectation. In *Proceedings of the 16th European Signal Processing Conference (EUSIPCO)*, pages 1–5. IEEE, 2008.

[77] L.B. Lucy. An iterative technique for the rectification of observed distributions. *The Astronomical Journal*, 79:745, 1974.

[78] T. Lukeš, G.M. Hagen, P. Křížek, Z. Švindrych, K. Fliegel, and M. Klíma. Comparison of image reconstruction methods for structured illumination microscopy. In *SPIE Photonics Europe*, pages 91293J–91293J. International Society for Optics and Photonics, 2014.

[79] A. Marquina and S.J. Osher. Image super-resolution by TV-regularization and Bregman iteration. *Journal of Scientific Computing*, 37(3):367–382, 2008.

[80] N. Metropolis, A.W. Rosenbluth, M.N. Rosenbluth, A.H. Teller, and E. Teller. Equation of state calculations by fast computing machines. *The journal of chemical physics*, 21(6):1087–1092, 1953.

[81] S.P. Meyn and R.L. Tweedie. *Markov chains and stochastic stability*. Springer Science & Business Media, 2012.

[82] J. Min, C. Vonesch, H. Kirshner, L. Carlini, N. Olivier, S. Holden, S. Manley, J.C. Ye, and M. Unser. FALCON: fast and unbiased reconstruction of high-density super-resolution microscopy data. *Scientific reports*, 4, 2014.

[83] L. Moisan. Periodic plus smooth image decomposition. *Journal of Mathematical Imaging and Vision*, 39(2):161–179, 2011.

[84] K.I. Mortensen, L.S. Churchman, J.A. Spudich, and H. Flyvbjerg. Optimized localization analysis for single-molecule tracking and super-resolution microscopy. *Nature methods*, 7(5):377–381, 2010.

[85] C.B. Müller and J. Enderlein. Image scanning microscopy. *Physical review letters*, 104(19):198101, 2010.

[86] E. Nehme, L.E. Weiss, T. Michaeli, and Y. Shechtman. Deep-storm: super-resolution single-molecule microscopy by deep learning. *Optica*, 5(4):458–464, 2018.

[87] Y. Nesterov. Gradient methods for minimizing composite objective function. *Math. Program*, 140(1):125–161, 2013.

[88] M. Nikolova. Model distortions in Bayesian MAP reconstruction. *Inverse Problems and Imaging*, 1(2):399, 2007.

[89] F. Orieux, E. Sepulveda, V. Loriette, B. Dubertret, and J.-C. Olivo-Marin. Bayesian estimation for optimized structured illumination microscopy. *IEEE Transactions on image processing*, 21(2):601–614, 2012.

[90] K. O'Holleran and M. Shaw. Optimized approaches for optical sectioning and resolution enhancement in 2d structured illumination microscopy. *Biomedical optics express*, 5(8):2580–2590, 2014.

[91] A. Pagliuso, T.N. Tham, J.K. Stevens, T. Lagache, R. Persson, A. Salles, J.-C. Olivo-Marin, S. Oddos, A. Spang, P. Cossart, et al. A role for septin 2 in Drp1-mediated mitochondrial fission. *EMBO reports*, page e201541612, 2016.

[92] S.C. Park, M.K. Park, and M.G. Kang. Super-resolution image reconstruction: a technical overview. *IEEE signal processing magazine*, 20(3):21–36, 2003.

[93] D.M. Portilho, R. Persson, and N. Arhel. Role of non-motile microtubule-associated proteins in virus trafficking. *Biomolecular concepts*, 7(5-6):283–292, 2016.

[94] T. Quan, Shaoqun Z., and Z.-L. Huang. Localization capability and limitation of electron-multiplying charge-coupled, scientific complementary metal-oxide semiconductor, and charge-coupled devices for superresolution imaging. *Journal of biomedical optics*, 15(6):066005–066005, 2010.

[95] W.H. Richardson. Bayesian-based iterative method of image restoration. *Journal of the Optical Society of America*, 62(1):55–59, 1972.

[96] L. I. Rudin, S. Osher, and E. Fatemi. Nonlinear total variation based noise removal algorithms. *Physica D: Nonlinear Phenomena*, 60(1):259–268, 1992.

[97] H. Rue. New loss functions in Bayesian imaging. *Journal of the American Statistical Association*, 90(431):900–908, 1995.

[98] M.J. Rust, M. Bates, and X. Zhuang. Sub-diffraction-limit imaging by stochastic optical reconstruction microscopy (storm). *Nature methods*, 3(10):793–796, 2006.

[99] L. Schermelleh, R. Heintzmann, and H. Leonhardt. A guide to super-resolution fluorescence microscopy. *The Journal of cell biology*, 190(2):165–175, 2010.

[100] P.J. Sementilli Jr. *Suppression of artifacts in super-resolved images.* PhD thesis, 1993.

[101] C.E. Shannon. Communication in the presence of noise. *Proceedings of the IRE*, 37(1):10–21, 1949.

[102] C.J.R. Sheppard. Super-resolution in confocal imaging. *Optik*, 80(2):53–54, 1988.

[103] C.J.R. Sheppard, S.B. Mehta, and R. Heintzmann. Superresolution by image scanning microscopy using pixel reassignment. *Optics letters*, 38(15):2889–2892, 2013.

[104] C.J.R. Sheppard, S. Roth, R. Heintzmann, M. Castello, G. Vicidomini, R. Chen, X. Chen, and A. Diaspro. Interpretation of the optical transfer function: Significance for image scanning microscopy. *Optics Express*, 24(24):27280–27287, 2016.

[105] O. Shimomura, F.H. Johnson, and Y. Saiga. Extraction, purification and properties of aequorin, a bioluminescent protein from the luminous hydromedusan, aequorea. *Journal of cellular and comparative physiology*, 59(3):223–239, 1962.

[106] H. Shroff, C.G. Galbraith, J.A. Galbraith, H. White, J. Gillette, S. Olenych, M.W. Davidson, and E. Betzig. Dual-color superresolution imaging of genetically expressed probes within individual adhesion complexes. *Proceedings of the National Academy of Sciences*, 104(51):20308–20313, 2007.

[107] J.D. Simpkins and R.L. Stevenson. An introduction to super-resolution imaging. *Chapter*, 16:555–578, 2012.

[108] G.Y. Sirat. Method and device for superresolution optical measurement using singular optics, February 2 2016. US Patent 9,250,185.

[109] D.L. Snyder, C.W. Helstrom, A.D. Lanterman, R.L. White, and M. Faisal. Compensation for readout noise in CCD images. *Journal of the Optical Society of America*, 12(2):272–283, 1995.

[110] D.L. Snyder, M.I. Miller, L.J. Thomas, and D.G. Politte. Noise and edge artifacts in maximum-likelihood reconstructions for emission tomography. *IEEE transactions on medical imaging*, 6(3):228–238, 1987.

[111] M.S. Soskin, V.N. Gorshkov, M.V. Vasnetsov, J.T. Malos, and N.R. Heckenberg. Topological charge and angular momentum of light beams carrying optical vortices. *Physical Review A*, 56(5):4064, 1997.

[112] P.A. Stokseth. Properties of a defocused optical system. *Journal of the Optical Society of America*, 59(10):1314–1321, 1969.

[113] F. Ströhl and C.F. Kaminski. A joint Richardson—Lucy deconvolution algorithm for the reconstruction of multifocal structured illumination microscopy data. *Methods and Applications in Fluorescence*, 3(1):014002, 2015.

[114] Y. Terui. Image processing for structured illumination microscopy. In *Information Optics (WIO), 2015 14th Workshop on*, pages 1–3. IEEE, 2015.

[115] A.N. Tikhonov, A.V. Goncharsky, and M. Bloch. *Ill-posed problems in the natural sciences*. Mir Moscow, 1987.

[116] A. Turpin, Y.V. Loiko, T.K. Kalkandjiev, and J. Mompart. Conical refraction: fundamentals and applications. *Laser & Photonics Reviews*, 2016.

[117] H.T.M. Van der Voort and K.C. Strasters. Restoration of confocal images for quantitative image analysis. *Journal of Microscopy*, 178(2):165–181, 1995.

[118] G.M.P. Van Kempen. *Image restoration in fluorescence microscopy*. Delft University Press, 1999.

[119] G.M.P. Van Kempen and L.J. Van Vliet. Background estimation in nonlinear image restoration. *Journal of the Optical Society of America*, 17(3):425–433, 2000.

[120] G.M.P. Van Kempen, L.J. Van Vliet, P.J. Verveer, and H.T.M. Van Der Voort. A quantitative comparison of image restoration methods for confocal microscopy. *Journal of Microscopy*, 185(3):354–365, 1997.

[121] H. Wang, Y. Rivenson, Y. Jin, Z. Wei, R. Gao, H. Gunaydin, L. Bentolila, and A. Ozcan. Deep learning achieves super-resolution in fluorescence microscopy. *bioRxiv*, page 309641, 2018.

[122] P. Weiss, L. Blanc-Féraud, and G. Aubert. Efficient schemes for total variation minimization under constraints in image processing. *SIAM journal on Scientific Computing*, 31(3):2047–2080, 2009.

[123] H. Yang, Y. Zhang, Y. Xiao, F. Gao, J. Chang, T. Wei, and S. Jiang. Generation and comparison of donut-shaped depletion beams in STED microscopy. *Optik-International Journal for Light and Electron Optics*, 127(8):3735–3739, 2016.

[124] R. Yuste. Fluorescence microscopy today. *Nature methods*, 2(12):902–904, 2005.

[125] B. Zhang, J. Zerubia, and J.-C. Olivo-Marin. Gaussian approximations of fluorescence microscope point-spread function models. *Applied optics*, 46(10):1819–1829, 2007.